

**MECHANICAL AND MICROSTRUCTURAL  
CHARACTERIZATION OF DISSIMILAR JOINT OBTAINED BY  
GMAW USING COLD METAL TRANSFER (CMT)**

THESIS

*submitted to*

DELHI TECHNOLOGICAL UNIVERSITY

*For the award of the degree of*

**DOCTOR OF PHILOSOPHY  
IN  
MECHANICAL ENGINEERING**

*By*

**YASHWANT KOLI**

(2K17/Ph.D/ME/56)

*Under the supervision of*

**Dr. N. Yuvaraj**

(Department of Mechanical  
Engineering, DTU)

**Prof. Vipin**

(Department of Mechanical  
Engineering, DTU)

**Prof. S. Aravindan**

(Department of Mechanical  
Engineering, IIT-D)



**DEPARTMENT OF MECHANICAL ENGINEERING  
DELHI TECHNOLOGICAL UNIVERSITY  
(Formerly Delhi College of Engineering)**

**Main Bawana Road, Shahabad Daultpur, Delhi - 110042, India**

**February 2021**

# CERTIFICATE

---

This is to certify that the thesis entitled “**Mechanical and Microstructural Characterization of dissimilar joint obtained by GMAW using Cold Metal Transfer (CMT)**” submitted to the Delhi Technological University , Delhi -110042, is fulfillment of the requirements for the award of degree of Doctorate in Philosophy in Mechanical Engineering embodies the original research work carried out by **Mr. YASHWANT KOLI**, Enrollment No: 2K17/Ph.D/ME/56 under my supervision. This work has not been submitted in part or full for any other degree or diploma of this or any other University.

**DR. N. YUVARAJ**

Department of Mechanical Engineering  
Delhi Technological University, Delhi.

**PROF. VIPIN**

Department of Mechanical Engineering  
Delhi Technological University, Delhi.

**PROF. S. ARAVINDAN**

Department of Mechanical Engineering  
Indian Institute of Technology, Delhi.

# DECLARATION

---

I certify that the work which is being presented in this thesis entitled “**Mechanical and Microstructural Characterization of dissimilar joint obtained by GMAW using Cold Metal Transfer (CMT)**” in the partial fulfillment of requirement for the award of degree of Doctorate in Philosophy submitted in the Department of Mechanical Engineering at Delhi Technological University, is an authentic record of my own work carried out during a period from August 2017 to February 2021, under the supervision of **DR. N. YUVARAJ** and **PROF. VIPIN**, Department of Mechanical Engineering, Delhi Technological University, Delhi and **PROF. S. ARAVINDAN**, Department of Mechanical Engineering, Indian Institute of Technology, Delhi. The matter presented in this thesis has not been submitted in any other University/Institute for the award of any degree or diploma.

(**YASHWANT KOLI**)

Roll No: 2K17/Ph.D/ME/56

# ACKNOWLEDGEMENT

---

I am greatly indebted to my supervisor **Dr. N. Yuvaraj** and **Prof. Vipin**, Department of Mechanical Engineering, Delhi Technological University, Delhi, for his invaluable guidance, constant inspiration, numerous suggestions and continued support throughout this research work. I am profoundly grateful to him with reverence for helping me with necessary information and equipment & materials as well.

With great pleasure, I wish to express my deep sense of reverence and gratitude to my supervisor **Prof. S. Aravindan**, Department of Mechanical Engineering, Indian Institute of Technology, Delhi for his perpetual planned and inspiring guidance, constructive criticism, encouragement, concrete suggestions, advice and invaluable support rendered to me during every stage of this research work and even during pandemic times of corona (COVID-19). He is a great thinker for looking new perceptions and ways to understand the reality around us. I would not have imagined having a better advisor and mentor for my research work. The door of his office was always open whenever I ran into a trouble spot or had a doubt about my research or writing. He not only guided me but also endowed me with the capacity to guide myself in future.

With great humbleness, I sincerely thank **Prof. R.S. Mishra**, Dean, Mechanical, Production & Industrial and Automobile Engineering, for his insightful comments and constant encouragement. SRC Committee members and faculty members of Department of Mechanical Engineering, Delhi Technological University for their suggestions and support throughout the research work.

I would also thank with much appreciation the people whose help and support was a great asset; the technical staff at DTU, namely, Mr. Net Ram, Mr. Lalan Kumar Sinha, Mr. Manjeet Singh, Mr. Sunil, Mr. Sanjeev Kumar, Mr. Amit, and Mr. Francis who provided great help for conducting the experiments and material characterization; Mr. Sandeep for their help in conducting the XRD studies, Mr. Tek Chand for his help in



revealing the microstructures, Mr. Rajesh Bohra for his help and assistance in doing the temperature analysis from thermal imaging camera.

Finally I dedicate my work to my Parents. My sincere thanks to my father Mr. Bhawani Shankar and my mother Mrs. Dropati Devi for their support and blessings that greatly helped me carrying out this research work.

**YASHWANT KOLI**

# ABSTRACT

---

This research work focuses on a comparative study on weld bead geometries of three different welding techniques: Cold Metal Transfer (CMT), Metal Inert Gas Pulse Synergic (MIG P) and MIG Manual Standard (MIG M). Bead-on-plate tests were performed using ER4043 (AlSi5%) as a filler material on the 3.18 mm thick plates of AA6061-T6. Current (80 A, 100 A and 120 A) and welding speed (7.5, 10.5 and 13.5 mm/sec) were used as input process parameters while shielding gas flow rate and contact tip to workpiece distance (CTWD) were maintained constant as 15 l/min and 10mm respectively. The weld beads processed by all the three techniques are compared by analysing the weld bead geometry. Microstructural characterization is carried out using optical microscopy and Field Emission Scanning Electron Microscope (FESEM). CMT has high dilution and penetration with low heat input. Compared to MIG P and MIG M, CMT shows a drastic reduction in residual stresses. Multi-response mathematical model is established for prediction of weld bead geometry in CMT, MIG P and MIG M welding of AA6061-T6 using ER4043 (AlSi5%) as a filler material. Central composite face-centered design (CCFCD) under response surface methodology (RSM) is employed to develop the design matrix for conducting the experiments. The developed model is employed in finding the optimal process parameters for good weld bead aesthetics. Current (I) and welding speed (S) are opted as input process parameters for response output such as penetration, dilution and heat input. This model is proficient to forecast the main effects and interactive effects of two factor of the opted welding process parameters. Results show that higher current values with low welding speed results in deeper penetration, high amount of dilution with higher heat input and vice versa. With lower heat input, CMT has high dilution and penetration with respect to MIG P and MIG M welding. The optimal process parameters are 92.518A and 7.50mm/sec for CMT, 109.418A and 10.873mm/sec for MIG P, 110.847A and 11.527mm/sec for MIG M with 61.11%, 68.80% and 72.6% desirability, respectively. Predicted output values generated from regression model equation obtained from welding process parameters are very close and sometimes overlaid on actual output that obviously demonstrates the suitability of the second order regression equations. A

good amount of penetration and dilution with low heat input is required for better joint efficiency.

The requirements projected by many industries for stronger, lighter, more efficient and cost-effective combined alloys in the welding of two dissimilar materials or dissimilar thickness. The current industry trend is the coalescence of various aluminium alloys of varying thicknesses. CMT welding process was used for joining of AA6061-T6 and AA6082-T6 using ER4043 filler wire and inspected the effect of different process parameters on mechanical properties of welded butt joints. Current (I), welding speed or travel speed (TS) and gas flow rate (Q) are the input welding process parameters that are to be optimized. Different heat input is studied w.r.t welding speed, current and gas flow rate. Heat inputs ranging from 100+, 200+ and 300+ J/mm is achieved at constant welding speed of 9, 7 and 5 mm/sec respectively at variable currents and flow rates. Bead geometry variables such as penetration (P), reinforcement (R) and contact angle (CA) are distinguished at different heat inputs. Mechanical properties such as tensile test and microhardness for different heat input were investigated. Microstructural characterization of base metal (BM), fusion line (FL) and weld metal (WM) is carried out. High-Resolution X-ray Diffraction (HR-XRD) technique based on  $\cos\alpha$  method is used for residual stress measurements at different heat inputs. Tensile fractured surfaces were examined by FESEM and energy-dispersive X-ray spectroscopy (EDX). Butt joints of various different process parameters were fabricated with the help of full factorial CCFCD under RSM to optimize the tensile properties, microhardness and residual stresses. Grey relation analysis (GRA) with Principal component analysis (PCA) is incorporated with CCFCD for finding out the optimal process parameter by considering multi-response parameters simultaneously. ANOVA was executed to interpret the impact of process parameters on the mechanical properties of the weldments. Results showed that the most dominant process parameter was found to be the welding speed. The optimal process parameter obtained via GRA-PCA technique is I3-TS1-Q1 (I - 100 A, TS - 5 mm/sec and Q - 14 L/min having heat input 352 J/mm) which produces 226 MPa of ultimate tensile strength, 12.6 % of elongation, 68.7 HV of microhardness and -152.3 MPa of compressive residual

stress. Desirability of optimality level obtained through CCFCD was 65.99 % and significantly improved to 97.07 % through GRA-PCA.

Nowadays, to enhance the structural efficiency, ultrasonic vibrations are combined with other manufacturing processes such as welding. It gives considerable advantages in terms of improved mechanical properties, adequate surface strength, improved material flow and uniform grain growth etc. Ultrasonic assisted cold metal transfer (U-CMT) welding is performed to fabricate the joints and improvements in mechanical properties and microstructural modifications are studied. Non-destructive technique (NDT) such as radiography technique (RT) is used to test weld consistency. Results revealed improved weld bead geometry with the aid of ultrasonic vibrations for the same welding parameters. The tensile strength and micro-hardness are enhanced. Samples with ultrasonic vibration experiences grain refining as compared to without vibration samples. As compared with CMT, U-CMT joints are rich in Al-Si eutectic structure. Al-Si structure is in globular form with reduced porosity level.

# TABLE OF CONTENTS

---

CERTIFICATE .....	i
DECLARATION .....	ii
ACKNOWLEDGEMENT .....	iii
ABSTRACT.....	v
TABLE OF CONTENTS.....	viii
LIST OF FIGURES .....	xiii
LIST OF TABLES .....	xix
NOMENCLATURE .....	xxi
<b>CHAPTER 1 : INTRODUCTION</b>	
<b>1.1 INTRODUCTION</b> .....	1
1.1.1 Aluminium Alloys .....	6
1.1.2 Motivation.....	7
<b>1.2 CMT MECHANISM</b> .....	7
<b>1.3 OVERVIEW OF THE THESIS</b> .....	9
<b>1.4 SUMMARY</b> .....	11
<b>CHAPTER 2 : LITERATURE REVIEW</b>	
<b>2.1 INTRODUCTION</b> .....	12
<b>2.2 CMT WELDING OF DISSIMILAR MATERIALS</b> .....	12
2.2.1 Aluminium and Steel .....	12
2.2.2 Magnesium and Aluminium alloy .....	14
2.2.3 Titanium and other materials .....	17
2.2.4 Tailor Welded Blanks (TWB).....	17

2.2.5	Aluminium alloys.....	18
<b>2.3</b>	<b>COMPARISON WITH OTHER WELDING TECHNIQUES.....</b>	<b>44</b>
2.3.1	MIG Welding-Brazing.....	44
2.3.2	TIG Welding-Brazing.....	44
2.3.3	LASER + MIG Welding-Brazing.....	44
<b>2.4</b>	<b>SHIELDING GAS.....</b>	<b>45</b>
2.4.1	Argon.....	46
2.4.2	Helium.....	46
2.4.3	Carbon-di-oxide.....	47
<b>2.5</b>	<b>RESEARCH GAP.....</b>	<b>48</b>
<b>2.6</b>	<b>RESEARCH OBJECTIVES.....</b>	<b>48</b>
<b>2.7</b>	<b>FLOW CHART FOR PRESENT WORK.....</b>	<b>49</b>
<b>2.8</b>	<b>SUMMARY.....</b>	<b>49</b>
<b>CHAPTER 3 : EXPERIMENTAL SETUP &amp; PROCEDURE</b>		
<b>3.1</b>	<b>MATERIAL SELECTION.....</b>	<b>51</b>
3.1.1	Substrate / Base Material.....	51
3.1.2	Filler Material.....	55
<b>3.2</b>	<b>SAMPLE PREPARATION.....</b>	<b>56</b>
3.2.1	Macrostructure Characterization.....	56
3.2.2	Microstructure Characterization.....	57
3.2.3	Microhardness.....	58
3.2.4	Tensile Testing.....	59
3.2.5	Residual Stress.....	60
<b>3.3</b>	<b>EXPERIMENTAL MACHINES.....</b>	<b>60</b>
3.3.1	CMT Machine.....	60

3.3.2	Tensile Testing Machine.....	63
3.3.3	Microhardness Machine.....	65
3.3.4	Optical Microscopy.....	67
3.3.5	Vision Inspection Machine .....	69
3.3.6	Field Emission Gun Scanning Electron Microscope .....	71
3.3.7	X-Ray Diffraction .....	72
3.3.8	Residual Stress Measurement Machine .....	75
<b>3.4</b>	<b>OPTIMIZATION OF CMT PROCESS PARAMETERS.....</b>	<b>76</b>
3.4.1	Response Surface Methodology .....	76
3.4.2	Grey Relation Analysis (GRA).....	78
3.4.3	Principal Component Analysis (PCA).....	80
3.4.4	GRA-PCA Hybrid Technique.....	81
3.4.5	Process Parameters.....	82
3.4.6	The limits of the process parameter and design matrix .....	84
<b>3.5</b>	<b>EXPERIMENTAL PROCEDURE.....</b>	<b>85</b>
3.5.1	Bead-on-Plate.....	85
3.5.2	CMT Butt Joint .....	87
3.5.3	Ultrasonic Assisted CMT (U-CMT) Butt Joint .....	91
<b>3.6</b>	<b>TEMPERATURE PROFILE.....</b>	<b>92</b>
<b>3.7</b>	<b>SUMMARY.....</b>	<b>95</b>
<b>CHAPTER 4 : RESULTS AND DISCUSSION ON BEAD-ON-PLATE</b>		
<b>4.1</b>	<b>INTRODUCTION.....</b>	<b>96</b>
<b>4.2</b>	<b>OPTIMIZATION OF PROCESS PARAMETERS.....</b>	<b>98</b>
4.2.1	Introduction.....	98
4.2.2	Experimental results for Bead-on-Plate .....	99

4.2.3 Mathematical Model Equation.....	101
4.2.4 Checking the adequacy of the model for penetration, dilution and heat input .....	105
4.2.5 Process Parameter Optimization .....	118
4.2.6 Confirmation Test .....	121
<b>4.3 MACROSTRUCTURE OF WELD BEAD .....</b>	<b>122</b>
4.3.1 Consequence of welding parameters on bead dimensions.....	125
4.3.2 Consequence of different welding techniques on bead dimensions .....	126
<b>4.4 MICROSTRUCTURAL ANALYSIS.....</b>	<b>126</b>
<b>4.5 EFFECT BY PROCESS PARAMETERS .....</b>	<b>132</b>
4.5.1 Effect on dilution (D) and heat input (H).....	132
4.5.2 Effect on penetration.....	135
4.5.3 Effect of residual stress .....	136
<b>4.6 SUMMARY.....</b>	<b>140</b>
<b>CHAPTER 5 : RESULTS AND DISCUSSION ON CMT BUTT JOINTS</b>	
<b>5.1 INTRODUCTION.....</b>	<b>141</b>
<b>5.2 OPTIMIZATION OF PARAMETERS FOR WELDED JOINTS.....</b>	<b>142</b>
5.2.1 Introduction.....	142
5.2.2 Mathematical Model Equations .....	145
5.2.3 Checking the adequacy of the model .....	145
5.2.4 Process parameter optimization using hybrid technique .....	156
5.2.5 Confirmation Test .....	161
<b>5.3 MICROSTRUCTURAL ANALYSIS ON CMT BUTT WELD .....</b>	<b>162</b>
<b>5.4 MECHANICAL PROPERTIES ON CMT BUTT WELD.....</b>	<b>169</b>
5.4.1 Ultimate Tensile Strength .....	169



5.4.2	Microhardness .....	172
5.4.3	Residual Stress .....	174
<b>5.5</b>	<b>SUMMARY .....</b>	<b>177</b>
<b>CHAPTER 6 : RESULTS AND DISCUSSION ON U-CMT BUTT JOINTS</b>		
<b>6.1</b>	<b>INTRODUCTION .....</b>	<b>178</b>
<b>6.2</b>	<b>COMPARISON BETWEEN CMT AND U-CMT BUTT JOINTS .....</b>	<b>179</b>
6.2.1	Effect of ultrasonic vibrations on weld bead dimensions .....	179
6.2.2	Effect of ultrasonic vibrations on the microstructure .....	182
6.2.3	Effect of ultrasonic vibrations on the microhardness .....	185
6.2.4	Effect of ultrasonic vibrations on tensile strength .....	188
6.2.5	Effect of ultrasonic vibrations on porosity.....	193
<b>6.3</b>	<b>SUMMARY.....</b>	<b>194</b>
<b>CHAPTER 7 : CONCLUSIONS AND SCOPE FOR FUTURE WORK</b>		
<b>7.1</b>	<b>CONCLUSIONS .....</b>	<b>195</b>
7.1.1	Bead-on-Plate.....	195
7.1.2	CMT Butt Joining .....	196
7.1.3	Ultrasonic-Assisted CMT Butt Joining.....	197
<b>7.2</b>	<b>SCOPE FOR FUTURE WORK .....</b>	<b>198</b>
<b>REFERENCES.....</b>		<b>199</b>
<b>LIST OF PUBLICATIONS .....</b>		<b>212</b>
<b>CURRICULUM VITAE.....</b>		<b>214</b>

# LIST OF FIGURES

<b>Fig. 1.1</b> Advantages and disadvantages for GMAW process .....	3
<b>Fig. 1.2</b> Comparison between GMAW and CMT welding process.....	4
<b>Fig. 1.3</b> Current and voltage waveform (a) during GMAW (b) during CMT .....	5
<b>Fig. 1.4</b> CMT welding process .....	9
<b>Fig. 2.1</b> Demonstration of weld bead with and without shielding gas .....	45
<b>Fig. 2.2</b> Comparison between Argon and Helium as shielding gas.....	47
<b>Fig. 2.3</b> Flow chart of present research work .....	49
<b>Fig. 3.1</b> Substrate material as purchased .....	51
<b>Fig. 3.2</b> Microstructural images by optical microscope (a) AA6061-T6 (b) Magnified view of AA6061-T6 (c) AA6082-T6 (d) Magnified view of AA6082-T6.....	52
<b>Fig. 3.3</b> Stress vs strain curve of substrate material .....	53
<b>Fig. 3.4</b> XRD plots (a) AA6061-T6 (b) AA6082-T6.....	54
<b>Fig. 3.5</b> FESEM images (a) AA6061-T6 (b) AA6082-T6.....	55
<b>Fig. 3.6</b> (a) Cold mounting of Filler wire (b) Microstructure at 0.2mm (c) Microstructure at 0.1mm (d) Microstructure at 50 $\mu$ m of filler wire .....	56
<b>Fig. 3.7</b> Macrostructure specimen of the weld bead .....	57
<b>Fig. 3.8</b> Steps of sample preparation for microstructure characterization .....	58
<b>Fig. 3.9</b> Microhardness indentation on aluminium sample.....	59
<b>Fig. 3.10</b> Tensile Specimen as per ASTM E8 .....	60
<b>Fig. 3.11</b> TPS400i CMT machine.....	61
<b>Fig. 3.12</b> Tensile machine (Model: Tinius Olsen H50KS).....	64
<b>Fig. 3.13</b> Microhardness testing machine (Struers Duramin-40) .....	65
<b>Fig. 3.14</b> Olympus GX41 compact inverted metallurgical microscope .....	67
<b>Fig. 3.15</b> Sipcon multi sensor CNC inspection system .....	69
<b>Fig. 3.16</b> Field Emission Gun Scanning Electron Microscope (FEG-SEM) (Model: FEI QUANTA 3D FEG).....	71

<b>Fig. 3.17</b> X-Ray diffraction (Model: BRUKER D8 ADVANCED).....	73
<b>Fig. 3.18</b> Pulstec $\mu$ -X360n Full 2D High-Resolution X-ray Diffraction (HR-XRD) machine .....	75
<b>Fig. 3.19</b> Fixture setup for bead-on-plate experiments .....	86
<b>Fig. 3.20</b> Fixture setup for CMT butt joints.....	87
<b>Fig. 3.21</b> Experimental setup for CMT butt joints.....	88
<b>Fig. 3.22</b> (a) Ultrasonic setup (b) Ultrasonic Probe (c) Generator .....	92
<b>Fig. 3.23</b> Temperature setup (a) K-type thermocouple and thermostat method (b) Thermal imaging camera method.....	93
<b>Fig. 3.24</b> Thermal imaging camera images of welded S-10 sample at various points (a) Line 0 (b) Line 1 (c) Line 2 (d) Line 3 (e) Line 4 (f) Line 5 .....	94
<b>Fig. 3.25</b> Temperature profile of welded sample at variable lines marked on the image.	95
<b>Fig. 4.1</b> Weld Bead geometry .....	97
<b>Fig. 4.2</b> Schematic diagram (3-D) of weld bead dimensions .....	97
<b>Fig. 4.3</b> Predicted vs Actual graphs for CMT.....	104
<b>Fig. 4.4</b> Predicted vs Actual graphs for MIG P .....	104
<b>Fig. 4.5</b> Predicted vs Actual graphs for MIG M .....	105
<b>Fig. 4.6</b> Interaction curve of input and output parameters for CMT .....	112
<b>Fig. 4.7</b> Interaction curve of input and output parameters for MIG P .....	113
<b>Fig. 4.8</b> Interaction curve of input and output parameters for MIG M.....	114
<b>Fig. 4.9</b> 3-D surface plot of interaction between input and output parameters for CMT	115
<b>Fig. 4.10</b> 3-D surface plot of interaction between input and output parameters for MIG P .....	116
<b>Fig. 4.11</b> 3-D surface plot of interaction between input and output parameters for MIG M .....	116
<b>Fig. 4.12</b> Desirability curve of CMT, MIG P and MIG M .....	120
<b>Fig. 4.13</b> Macro-images of CMT weld bead.....	122
<b>Fig. 4.14</b> Macro-images of MIG P weld bead .....	123
<b>Fig. 4.15</b> Macro-images of MIG M weld bead .....	124

<b>Fig. 4.16</b> (A) No crack on CMT 120 A; Crack formation on bead on plate (B) MIG P (120 A) (C) MIG M (120 A) .....	124
<b>Fig. 4.17</b> Variation in macro-images of bead geometry for variable welding speeds (7.5mm/sec, 10.5mm/sec and 13.5mm/sec) at constant current of 80A for CMT process .....	125
<b>Fig. 4.18</b> Variation in macro-images of bead geometry for variable current (80A, 100A and 120A) at constant welding speed of 13.5mm/sec for CMT process .....	125
<b>Fig. 4.19</b> Variation in macro-images of bead geometry for different welding techniques (CMT, MIGP and MIG M) at constant current (100A) and welding speed (13.5mm/sec) .....	126
<b>Fig. 4.20</b> Vision inspection image A, B and C of CMT 80 A, 100 A and 120 A respectively at 10.5 mm/sec. Optical microscope image (a) BM (b & c) FZ (d) WZ .....	128
<b>Fig. 4.21</b> Vision inspection image D, E and F of MIG P for 80 A, 100 A and 120 A respectively at 10.5 mm/sec. Optical microscope image (a) BM (b & c) FZ (d) WZ ....	129
<b>Fig. 4.22</b> Vision inspection image G, H and I of MIG M for 80 A, 100 A and 120 A respectively at 10.5 mm/sec. Optical microscope image (a) BM (b & c) FZ (d) WZ ....	130
<b>Fig. 4.23</b> FESEM images of fusion zone of CMT 100 A at (a) 50 $\mu$ m scale and (b) 30 $\mu$ m scale.....	131
<b>Fig. 4.24</b> XRD and EDX plots for (a) CMT-100, (b) MIG P-100 and (c) MIG M-100.	132
<b>Fig. 4.25</b> Comparison of heat input (J/mm) between CMT, MIG P and MIG M.....	133
<b>Fig. 4.26</b> Comparison of dilution (%) between CMT, MIG P and MIG M.....	134
<b>Fig. 4.27</b> Dilution (%) vs heat input (J/mm) between CMT, MIG P and MIG M.....	134
<b>Fig. 4.28</b> Comparison of penetration (mm) between CMT, MIG P and MIG M .....	135
<b>Fig. 4.29</b> Penetration (mm) vs heat input (J/mm) between CMT, MIG P and MIG M..	136
<b>Fig. 4.30</b> Residual stresses induced on different position of the specimen .....	137
<b>Fig. 4.31</b> Residual stress profile vs alpha angle for CMT, MIG P and MIG M at different positions for 100A and 10.5mm/sec process parameters.....	138
<b>Fig. 4.32</b> Microhardness vs FWHM .....	139
 <b>Fig. 5.1</b> Macro-images of the weld bead at various ranges of heat input .....	141
<b>Fig. 5.2</b> Weld bead geometry as per heat input .....	142

<b>Fig. 5.3</b> UTS graphs (a) Interaction curve (b) Contour graph (c) Predicted vs actual (d) 3-D surface plot.....	147
<b>Fig. 5.4</b> Elongation graphs (a) Interaction curve (b) Contour graph (c) Predicted vs actual (d) 3-D surface plot.....	149
<b>Fig. 5.5</b> Microhardness graphs (a) Interaction curve (b) Contour graph (c) Predicted vs actual (d) 3-D surface plot .....	151
<b>Fig. 5.6</b> Residual graphs (a) Interaction curve (b) Contour graph (c) Predicted vs actual (d) 3-D surface plot.....	153
<b>Fig. 5.7</b> Model reliability (a) UTS (b) Elongation (c) Microhardness (d) Residual stress .....	154
<b>Fig. 5.8</b> Optimal process parameters, responses and their desirability with using CCFCDD of RSM.....	155
<b>Fig. 5.9</b> Screen plots of response with 4 principal components .....	157
<b>Fig. 5.10</b> Residual plots for GRG .....	160
<b>Fig. 5.11</b> Optimal process parameters, responses and their desirability with using GRA-PCA technique .....	161
<b>Fig. 5.12</b> Macro-image of welded sample indicating the points.....	162
<b>Fig. 5.13</b> Microstructures at the indicated positions for 163 J/mm heat input .....	163
<b>Fig. 5.14</b> Microstructures at the indicated positions for 227 J/mm heat input .....	164
<b>Fig. 5.15</b> Microstructures at the indicated positions for 369 J/mm heat input .....	165
<b>Fig. 5.16</b> FESEM images at 163 J/mm (80A-9mm/sec-14L/min) (a)&(b) FL of AA6061-T6 side (c)&(d) FL of AA6082-T6 side (e) & (f) Weldment (WM) .....	167
<b>Fig. 5.17</b> EDX spectroscopy of sample (Magnesium wt. %) .....	167
<b>Fig. 5.18</b> Experiment 2 <sup>nd</sup> with 80A-9mm/sec-18L/min (168J/mm) plots (a) XRD (b) EDX .....	168
<b>Fig. 5.19</b> Tensile specimen (a) before UTM (b) after UTM.....	169
<b>Fig. 5.20</b> Tensile strength and elongation curve vs heat input .....	170
<b>Fig. 5.21</b> Stress vs strain curve .....	171
<b>Fig. 5.22</b> Fractography FESEM image (a) Sample 3 (90A-9mm/sec-16L/min) (183 J/mm) (b) Sample 10 (100A-7mm/sec-16L/min) (245 J/mm).....	171
<b>Fig. 5.23</b> Microhardness at various position.....	172

<b>Fig. 5.24</b> Microhardness vs heat input.....	173
<b>Fig. 5.25</b> Residual stress at various positions .....	175
<b>Fig. 5.26</b> Debye ring (3D), Distortion and profile of residual stress at various heat input (a) 163 J/mm (b) 227 J/mm (c) 369 J/mm.....	176
<b>Fig. 6.1</b> Cross-sectional view of welded samples indicating weld width (left side is AA6082-T6 and right side is 6061-T6) (a) CMT (b) U-CMT.....	180
<b>Fig. 6.2</b> Effect of ultrasonic vibrations on CMT and U-CMT welded Joints (a) Weld width (b) Weld depth penetration (c) Contact angle.....	181
<b>Fig. 6.3</b> Macro-image of weld bead consisting of various points for microstructural analysis .....	182
<b>Fig. 6.4</b> Microstructure of sample 7 (CMT) (a) Interface of AA6082-T6/weld bead (b) Weld bead (c) Interface of weld bead/AA6061-T6 .....	183
<b>Fig. 6.5</b> Microstructure of U-CMT (a) Interface of AA6082-T6/weld bead (b) Weld bead (c) Interface of weld bead/AA6061-T6.....	184
<b>Fig. 6.6</b> Grain size distributions at the weld bead (a) CMT (b) U-CMT.....	185
<b>Fig. 6.7</b> (a) FESEM image of CMT welded weld bead (b) FESEM image of U-CMT welded weld bead .....	185
<b>Fig. 6.8</b> Microhardness of CMT and U-CMT of sample 7 and 8 respectively (a) Perpendicular ( $V_1V_2$ ) to cross-section of weld bead (b) Parallel ( $H_1H_2$ ) to cross-section of weld bead .....	186
<b>Fig. 6.9</b> Average weld bead microhardness values for CMT and U-CMT.....	187
<b>Fig. 6.10</b> Fracture location of tensile specimens (a) CMT (b) U-CMT.....	189
<b>Fig. 6.11</b> Tensile strength of welded samples for with and without ultrasonic vibrations welded samples .....	189
<b>Fig. 6.12</b> Stress vs strain curve (a) All CMT samples (b) CMT and U-CMT comparison .....	190
<b>Fig. 6.13</b> FESEM image of tensile fractured surface (a) CMT sample 7 (90A-9mm/sec) (b) U-CMT sample 8 (90A-9mm/sec).....	191

<b>Fig. 6.14</b> EDX image tensile fractured surface of CMT (a) & (b) spectrum 9 (c) & (d) spectrum 11 .....	192
<b>Fig. 6.15</b> EDX image tensile fractured surface of U-CMT (a) & (b) spectrum 23 (c) & (d) spectrum 24 .....	193
<b>Fig. 6.16</b> Radiography weld image of (a) CMT process (S-7) (b) U-CMT process (S-8) .....	194

# LIST OF TABLES

<b>Table 2.1</b> Welding parameters of CMT welding process.....	20
<b>Table 2.2</b> Major conclusions on dissimilar materials using CMT .....	29
<b>Table 2.3</b> Experimental results for butt joint using CMT welding process .....	36
<b>Table 2.4</b> Experimental results for lap joint using CMT welding process.....	40
<b>Table 3.1</b> Chemical compositions (wt%) obtained by chemical spectroscopy of substrate materials as per ASTM standards .....	52
<b>Table 3.2</b> Mechanical properties of substrate material .....	53
<b>Table 3.3</b> Chemical composition (wt.%) of filler wire as per ASTM standards.....	55
<b>Table 3.4</b> Specification of CMT machine .....	61
<b>Table 3.5</b> Specification of Tensile Testing Machine.....	64
<b>Table 3.6</b> Specification of Microhardness testing machine (Struers Duramin-40).....	66
<b>Table 3.7</b> Specifications of Optical Microscope .....	68
<b>Table 3.8</b> Specification of Vision Inspection Machine .....	70
<b>Table 3.9</b> Specification of FESEM machine .....	72
<b>Table 3.10</b> Specification of XRD machine .....	74
<b>Table 3.11</b> Specification of Residual stress machine .....	76
<b>Table 3.12</b> Process parameters for bead-on-plate experiments for CMT, MIG P and MIG M with their levels .....	85
<b>Table 3.13</b> Design of experiments for CMT butt joints .....	85
<b>Table 3.14</b> Central composite design matrix for bead-on-plate experiment .....	86
<b>Table 3.15</b> Central composite design matrix for CMT butt joints .....	88
<b>Table 3.16</b> Experimental table with increasing heat input as per CCFC matrix .....	89
<b>Table 3.17</b> Experimental welding parameters for different welding process and weld geometry .....	91
<b>Table 4.1</b> Experimental results for CMT .....	100
<b>Table 4.2</b> Experimental results for MIG P .....	100



<b>Table 4.3</b> Experimental results for MIG M.....	101
<b>Table 4.4</b> ANOVA table of full quadratic model for Penetration in CMT .....	106
<b>Table 4.5</b> ANOVA table of full quadratic model for Penetration in MIG P.....	107
<b>Table 4.6</b> ANOVA table of full quadratic model for Penetration in MIG M .....	108
<b>Table 4.7</b> ANOVA table of full quadratic model for Dilution in CMT .....	108
<b>Table 4.8</b> ANOVA table of full quadratic model for Dilution in MIG P.....	109
<b>Table 4.9</b> ANOVA table of full quadratic model for Dilution in MIG M .....	109
<b>Table 4.10</b> ANOVA table of full quadratic model for Heat Input in CMT .....	110
<b>Table 4.11</b> ANOVA table of full quadratic model for Heat Input in MIG P .....	110
<b>Table 4.12</b> ANOVA table of full quadratic model for Heat Input in MIG M.....	111
<b>Table 4.13</b> Model reliability for CMT .....	117
<b>Table 4.14</b> Model reliability for MIG P .....	117
<b>Table 4.15</b> Model reliability for MIG M.....	118
<b>Table 4.16</b> Criteria of optimal parameters .....	118
<b>Table 4.17</b> Optimization result for optimal parameters .....	119
<b>Table 4.18</b> Confirmation test.....	121
<b>Table 5.1</b> Experimental design matrix as per CCFCFCD using RSM along with results ..	144
<b>Table 5.2</b> ANOVA table for response 1: UTS .....	146
<b>Table 5.3</b> ANOVA table for response 2: Elongation .....	148
<b>Table 5.4</b> ANOVA table for response 3: Microhardness .....	150
<b>Table 5.5</b> ANOVA table for response 4: Residual stress .....	152
<b>Table 5.6</b> Normalizing and deviation sequence table for GRA .....	156
<b>Table 5.7</b> Eigen analysis of the Correlation Matrix .....	157
<b>Table 5.8</b> Eigenvectors, principal components and contribution .....	157
<b>Table 5.9</b> GRC, GRG and Rank table with PCA .....	158
<b>Table 5.10</b> Main effects on mean GRG with PCA.....	159
<b>Table 5.11</b> ANOVA table results for GRG with PCA weights.....	160
<b>Table 5.12</b> Confirmation runs with GRA-PCA.....	161

# NOMENCLATURE

---

<b>AA</b>	Aluminium Association
<b>Al</b>	Aluminium
<b>ALC</b>	Arc Length Correction
<b>ANN</b>	Artificial Neural Network
<b>ANOVA</b>	Analysis of variance
<b>ASTM</b>	American Society for Testing Materials
<b>BCP</b>	Background Current Phase
<b>BHN</b>	Brinell Hardness Number
<b>BM</b>	Base Metal
<b>CAV</b>	Constant Arc Voltage
<b>CCFCD</b>	Central composite face centered design
<b>CCRD</b>	Central Composite Rotatable Design
<b>CMT</b>	Cold Metal Transfer
<b>CO</b>	Carbon Monoxide
<b>CO<sub>2</sub></b>	Carbon Di-Oxide
<b>CSC</b>	Conventional Short Circuit
<b>CTWD</b>	Contact Tip To Workpiece Distance
<b>Cu</b>	Copper
<b>DCEN</b>	Direct Current Electrode Negative
<b>DCEP</b>	Direct Current Electrode Positive
<b>DCRP</b>	Direct Current Reverse Polarity
<b>DE</b>	Design Expert
<b>DOE</b>	Design of Experiments
<b>DPC</b>	Digital Process Control
<b>EDM</b>	Electrical Discharge Machine
<b>EDS</b>	Energy Dispersive Spectrometer
<b>EDX</b>	Energy Dispersive X-ray

<b>EMF</b>	External Magnetic Field
<b>EN-CMT</b>	Electrode Negative Cold Metal Transfer
<b>EP-CMT</b>	Electrode Positive Cold Metal Transfer
<b>FESEM</b>	Field Emission Scanning Electron Microscope
<b>FL</b>	Fusion Line
<b>FSW</b>	Friction Stir Welding
<b>FZ</b>	Fusion Zone
<b>GA</b>	Genetic Algorithm
<b>GMAW</b>	Gas Metal Arc Welding
<b>GRA</b>	Grey Relation Analysis
<b>GRC</b>	Grey Relation Coefficient
<b>GRG</b>	Grey Relation Grade
<b>GTAW</b>	Gas Tungsten Arc Welding
<b>HAZ</b>	Heat Affected Zone
<b>HR-XRD</b>	High-Resolution X-ray Diffraction
<b>IMC</b>	Inter-Metallic Compounds
<b>IML</b>	Inter-Metallic Layer
<b>Mg</b>	Magnesium
<b>MIG</b>	Metal Inert Gas
<b>MIG M</b>	Metal Inert Gas Manual Standard
<b>MIG P</b>	Metal Inert Gas Pulse Synergic
<b>NDT</b>	Non-Destructive Technique
<b>OCV</b>	Open Circuit Voltage
<b>PCA</b>	Principal Component Analysis
<b>PCP</b>	Peak Current Phase
<b>PDC</b>	Pulse Dynamic Correction
<b>PWHT</b>	Post Weld Heat Treatment
<b>RSM</b>	Response Surface Methodology
<b>RT</b>	Radiography Technique
<b>SAW</b>	Submerged Arc Welding

<b>SCP</b>	Short Circuiting Phase
<b>SEM</b>	Scanning Electron Microscope
<b>SMAW</b>	Shielded Metal Arc Welding
<b>THI</b>	Thermal Heat Input
<b>TIG</b>	Tungsten Inert Gas
<b>U-CMT</b>	Ultrasonic Assisted Cold Metal Transfer
<b>UTM</b>	Universal Testing Machine
<b>UTS</b>	Ultimate Tensile Strength
<b>VHN</b>	Vickers Hardness Number
<b>VP-CMT</b>	Variable Polarity Cold Metal Transfer
<b>WFS</b>	Wire Feed Speed
<b>WM</b>	Weld Zone / Weld Metal
<b>XRD</b>	X-Ray Diffraction

# CHAPTER 1 : INTRODUCTION

---

## 1.1 INTRODUCTION

Amongst the numerous manufacturing technologies, fusion welding has been conceded as an essential empowering technology to enhance the pioneering and sustainable manufacturing [Allison and Scudamore, 2014]. A solitary product without joining process is hard to manufacture because of some technological limitations. Assembling using several components of the products is typically done and fusion practices are dynamic in fabrication to deliver product function and rise process proficiency [Tseng & Hu, 2014].

Joining different metals or different alloys of metals offers the competence to use benefits of various materials which offer distinctive solutions to engineering requirements [Taban et al., 2010]. Fusion of different materials drastically reduce the weight of the fabricated product and curtail the cost of production as well, without negotiating the safety and structural requirements. The dissimilar fusion weld must acquire satisfactory tensile and ductility test results so that the joint will be successful [Ghosh et al., 2017]. Subsequently, joining processes for dissimilar materials have received significant consideration in the current years. Till now dissimilar materials or dissimilar alloys have been joined by different welding processes which include fusion joining in electric arc welding such as, ‘Gas Metal Arc Welding’ (GMAW)/ ‘Metal Inert Gas’ (MIG), ‘Gas Tungsten Arc Welding’ (GTAW), ‘Shielded Metal Arc Welding’ (SMAW), ‘Submerged Arc Welding’ (SAW), solid state welding like ‘Pressure Welding’, ‘Explosion Welding’, ‘Friction Welding’ [Satyanarayana et al., 2005], ‘Diffusion Welding’, ‘Brazing’, and ‘Soldering’. A challenge which comes under fusion joining of unlike metals in arc welding is large size of ‘Heat Affected Zone’ (HAZ) and selection of appropriate filler material [Martinsen et al., 2015]. The large size of HAZ will lead to a sizable region of brittle inter-metallic compounds (IMC) when welding of unlike materials. Tendency to fracture will increase as large zone of brittle IMC are formed. Selection of suitable filler material is mandatory because the mechanical properties and microstructure characterization is perceived in the weld zone where the filler material is deposited.

Among the above-mentioned welding processes, MIG welding is a flexible process which is considerably used in fusion of a range of ferrous and non-ferrous metals as it advances the superiority of the weldment [Ibrahim et al., 2012]. GMAW/MIG is not only proficient in improving gap-bridging ability but it correspondingly also compensate the loss of alloy elements during welding [Hu et al., 2016]. Mostly this welding method is used for automotive applications [Ahsan et al., 2016]. Nowadays, the automotive industry is moving towards environmental sustainability and to improve passenger safety. To fabricate car body components for the vehicle chassis and passenger compartment, different grades of steel were joined together using various welding techniques [Májlinger et al., 2016]. There are certain imperfections in the GMAW/MIG by which some materials are not perfectly welded. Conventional Short Circuit (CSC) welding method is one of the crucial mode of metal transfer in GMAW for joining of thin sheets. This enables the liquid droplet detachment from filler wire, which is due to Lorentz forces (electromagnetic forces) and gravitational forces. During the short-circuiting phase of the transfer cycle, the transfer of a single molten droplet of electrode occurs, i.e., where electrical short circuit is established. The electrode's physical interaction with the molten weld pool takes place, and the amount of short-circuiting events will occur up to 200 times per second. The current supplied by the source of welding power raises, followed by an increase in the magnetic force exerted at the end of the electrode. The electromagnetic field surrounding the electrode provides the force that squeezes the molten droplet from the end of the electrode (more commonly known as a pinch force). It is most commonly applied to thin materials because of the low thermal heat input (THI) associated with short-circuiting transfer. The problems that the CSC facing is that the 'high short circuit current' and 'timing of short circuit is uncontrollable' which causes high heat input and spatter respectively. These difficulties can be minimized by cold metal transfer (CMT) welding which is an advanced variant of GMAW as shown in Fig. 1.1. However, fusion techniques must overcome the two significant challenges in order to acquire appropriate dissimilar joints. Firstly, due to lot of differences in physical, chemical and mechanical properties such as microhardness, melting point, corrosion potential, thermal conductivity, coefficient of thermal expansion and insignificant weldability between two different materials. Therefore, it is very hard to obtain sound weld using conventional welding methods. Secondly, high thermal heat input

in conventional arc welding (GMAW, GTAW etc.) which directly influences the brittle inter-metallic compounds (IMCs) by broadening the Intermetallic layer (IML) that drastically degrades the mechanical properties of the weld joint [Dong, 2012 and Lin et al., 2010].

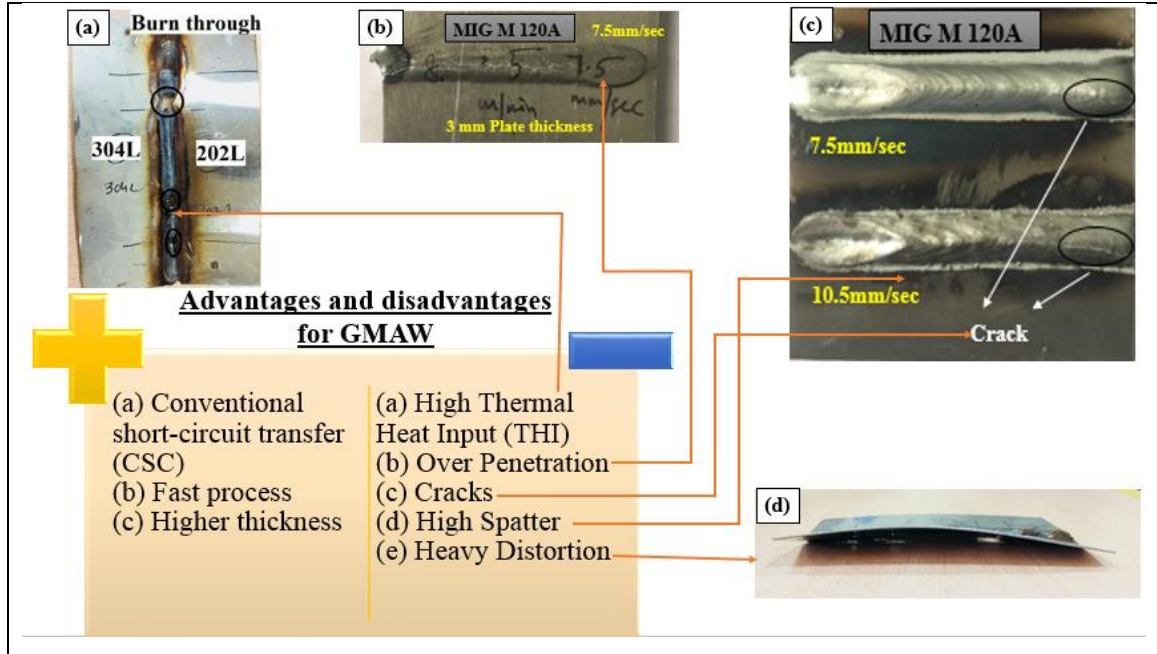


**Fig. 1.1** Advantages and disadvantages for GMAW process

CMT welding is an upgraded technology in conventional GMAW/MIG process based on short-circuiting transfer established by “Fronius of Austria” in 2004 which is different from the CSC given by GMAW [Kumar et al., 2016 and Schierl, 2005]. As the word suggests ‘Cold’ means this is the only fusion welding technique that has a very low ‘Thermal Heat Input’ (THI) [Irizalp et al., 2016] due to very low non-zero current. By integrating an advanced wire feeding mechanism coupled with high-speed digital monitoring, CMT enables a controlled method of material deposition with low THI [Pickin et al., 2011]. The main innovation in CMT is in its wire movement assimilation. The digital process-control imposes the power supply each time when the short circuit occurs and controls the movement of wire's retraction. The liquid metal droplet on the tip of the wire is detached with the assistance of the wire retraction motion at the time of short-circuiting. In CMT welding, 1/4th of the total time will be in a short-circuit phase where the magnitude

of current tends to almost zero. It greatly reduces the cost of welding and energy consumption by 30%-40%, which makes it energy efficient welding process. As opposed to MIG welding, electromagnetic force does not have any influence on the short-circuiting of liquid metal droplet transfer with recorded decrement in the heat input and weld spatter [Schierl, 2005]. Fig. 1.2 shows the comparison between GMAW and CMT welding process. It provides no post-welding operations such as machining, grinding, honing, burnishing, etc. because of the very low spatter or spatter-free weld even in the case when 100% carbon-di-oxide (CO<sub>2</sub>) shielding gas. It provides high gap bridge-ability which is highly appropriate for automation. Fig. 1.3 gives the major difference between CMT and GMAW according to the current and voltage waveform. As seen in the image, at the time of short-circuiting the current and voltage waveform of GMAW is increasing which results in high spatter and high heat input delivered to the welded samples. In CMT, the current waveform is low and constant while the voltage waveform is almost touching zero and constant due to the wire retraction motion of the CMT guided by digital process control (DPC). This helps in minimizing the heat input and spatter-less welding.

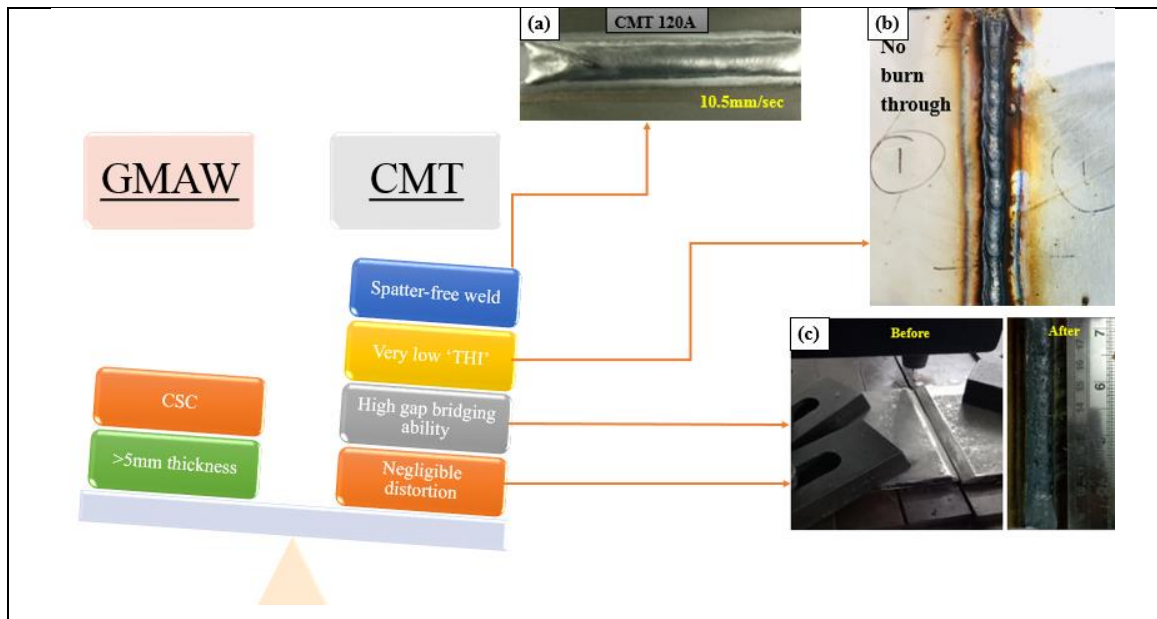


**Fig. 1.2** Comparison between GMAW and CMT welding process



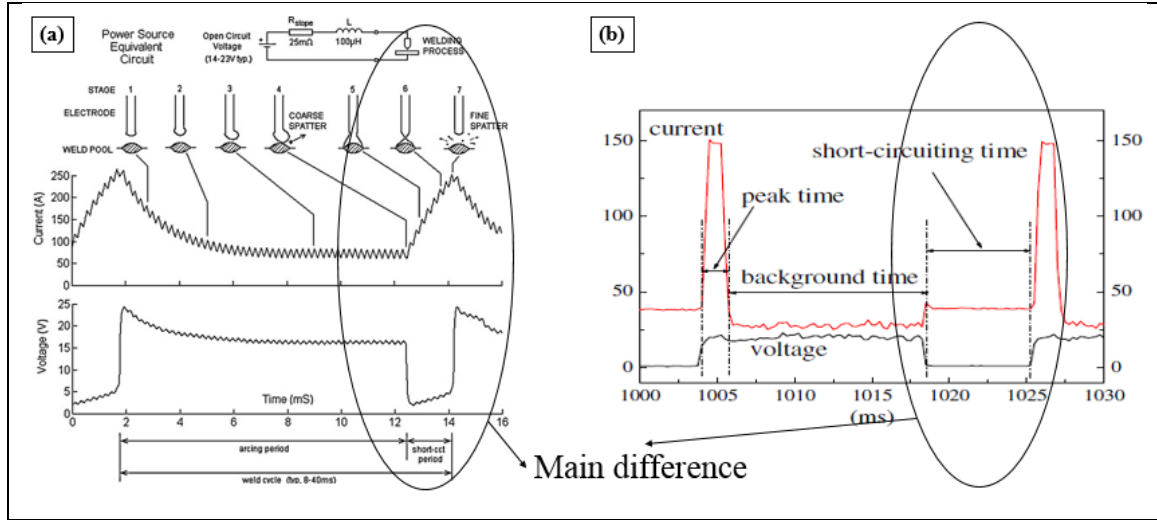


**Fig. 1.3** Current and voltage waveform (a) during GMAW (b) during CMT

In this extensive literature review, CMT welding is used mostly to weld dissimilar materials like “Aluminium to Galvanized Steel” [Cao et al., 2013; Zhou & Lin, 2014; Yang et al., 2013 and Zhang et al., 2013], “Aluminium to Magnesium” [Madhavan et al., 2017; Shang et al., 2012; Cao et al., 2013; Pang et al., 2016 and Jing et al., 2013], “Titanium to other materials” [Cao et al., 2014; Cao et al., 2014 and Sun et al., 2017]. Dissimilar metal joints are used in a variety of engineering applications, including aircraft, shipbuilding, rail transportation, nuclear power plants, coal-fired boilers, and the automotive manufacturing industry etc. [Ghosh et al., 2017 and Chaudhari et al., 2014].

In the present scenario, industries are moving towards a lighter material, which can significantly reduce the cost of transportation or energy consumption during transportation by increasing the efficiency. Aluminum alloys are preferred worldwide in every sector of the industry owing to its low weight without compromising the strength. Transport is among the biggest power-consuming industries, making use of around 19% of the world's power supply. Today, around 96% of the world's transportation structures depend on petroleum engines and products, with worldwide transport systems responsible for almost 40% of the world's petroleum consumption of almost 75 million tons of petroleum per day [Elrefaey and Ross 2015 and Mcauley 2003].

Thin aluminium sheets are used worldwide in every sector of the industry especially in automotive because it is lightweight, durable and recyclability. Car manufacturers are now adopting this trend of rapidly developing thin aluminum alloy sheets, and these manufactured products are already achieving a positive response in the market [Feng et al., 2009 and Fang et al., 2013]. It has been shown that the results which are evidently proving that there is a reduction in measured weight of automobiles for instance cars, buses etc. During transportation, energy consumption is decreased by way of decreasing its total weight of the vehicle, which inevitably improves the engine's effectiveness. There are many different grades of aluminium which are weldable but specially 6000-series alloy is used for body parts of vehicle, exterior and interior body panels, structural and weldable components [Totten and MacKenzie 2003; Mossman and Lippold 2002; Kaufman, 2000 and Mathers, 2002]. Arc welding of aluminum alloy thin sheets possess distinctive difficulties, which can be ascribed to increased coefficient of thermal expansion and conductivity with reference to steel. It is essential to avoid certain issues such as burning and distortion by controlling the heat input of the welds [Feng et al., 2009 and Pickin et al., 2011]. It is difficult to achieve coalescence of thin sheets of aluminium by conventional MIG welding process due to the impediments such as dearth of control, over penetration and excessive spatter during welding process. It constrains its use in the field and as a result, expensive welding techniques were used which inevitably increased the fabrication cost. Lower heat inputs have made short-circuit metal transfer as a desirable method for joining thin sheets of aluminum [Hermans and Den Ouden 1999]. CMT mode of operation provides solution for welding thin sheets since it mitigates problems such as over penetration, spattering, high heat input, distortion etc. that come across MIG welding.

#### 1.1.1 Aluminium Alloys

Aluminium alloys used as a substrate material has evolved with the research that is poured into the topic. This led to a lot of various types of aluminium being available for the use as a substrate material. Such diversity gave rise to the need of a designation system.

An aluminium alloy is designated as AAXXXX. The first digit (XXXX) depicts the major alloying element, which describes the series of the aluminium alloy, for instance, 1000 series, 2000 up to 8000 series. The second digit (XXXX) depicts the modification, if

any, is done to the alloying element. If the second digit is “0” then no modification has been done. The third and last digit (XXXX) are arbitrary number given to help in determining a specific series. In the 1000 series the last two digit describe the percentage of aluminium in the base metal, and no such inference is drawn in any other series. 6000 Series: 6061 and 6082 aluminium alloy plates are precipitation-hardened alloy of aluminium. It has magnesium (Mg) and silicon (Si) as the major contributor as alloying elements. 6061 and 6082 aluminium alloy plate has proved to have one of the widest ranges of alloys which happens to be heat treatable alloy being obtained through artificial aging at a low temperature of approximately 180 °C for 2 hours until it reaches a stable condition. This increases strength to a greater level after solution heat-treating quicker than natural aging.

AA6061-T6 and AA6082-T6 has found fadom amongst researchers owing to its fabulous medium to high strength, considerable improved toughness and great enhancement in resistance of corrosion.

#### 1.1.2 Motivation

In present scenario, new advances in welding methods are replacing the conventional welding methods in the advanced engineering application and industrial purposes. CMT which is an advanced version of MIG welding, is now the used worldwide for better bead aesthetics, negligible spatter generation and most importantly lower heat input. This characteristics has made CMT unique in its applications. Nowadays, even additive manufacturing products are also fabricated using CMT via wire-arc additive manufacturing (WAAM). Fabricating a dissimilar aluminium alloy butt joint with varying thicknesses using CMT is carried out with a full factorial design matrix. Further advances is done to use the ultrasonic probe while welding a dissimilar aluminium alloy butt joint with varying thicknesses.

## 1.2 CMT MECHANISM

CMT offers the meticulous technique of material deposition with low THI by integrating a pioneering wire feed system combined with high-speed digital process control (DPC) [Pickin et al., 2011]. In CMT mechanism, the electrode is moved towards the weld pool

during an arcing period. When the electrode wire tip makes interaction with the molten pool, the arc column is extinguished and the welding current drops to non-zero which helps in avoiding any spatter generation. The consequence of dropping of the current is that the heat input that is given by this process for the short-arc variation is significantly reduced. With the help of this, it is feasible to weld thinner materials with minimum amount of distortion, low dilution rate, low structural stress and low residual stress in the weld area [Cao et al., 2013; Cao et al., 2014; Wang et al., 2008; Lorenzin & Rutili, 2009 and Lin et al., 2013]. The movement of wire is reversed by digital process control with the help of synergic power source which aids droplet detachment during the short-circuiting phase (SCP) [Yang et al., 2013]. The wire motion is reversed and the procedure commences all over again [Gungor et al., 2014]. CMT process decreases the heat-affected-zone (HAZ) because of its little THI to the substrate material which is the noticeable feature of this process. The electrical signal cycle in traditional CMT welding can be defined as the time required to deposit a droplet of molten electrode into the weld pool. It is necessary to examine the analysis of current and voltage waveforms, which provides the duration of different phases of the process in microseconds, for energy distribution at different phases of the droplet transfer process [Sun et al., 2015]. There are three phases to the CMT cycle:

- **Peak Current Phase (PCP):** It is a constant arc voltage (CAV) corresponding to a high pulse of current for a short duration triggering the ignition of the welding arc effortlessly and then melts the electrode wire to form a droplet.
- **Background Current Phase (BCP):** It has corresponded to a lower current phase. As in the peak current phase, the liquid droplet is formed on the wire tip, the current is reduced to non-zero to prevent the globular transfer which helps in avoiding any spatter generation. This phase lasts until short-circuiting occurs.
- **Short-Circuiting Phase (SCP):** This phase corresponds to a zero arc voltage. In this, the arc voltage drops to zero as the wire comes in contact with the weld pool. At the same time, the retractor mechanism provided to the wire feeder by ‘Digital Process Control’ (DPC) which gives the wire a back-drawing force assists in the liquid bridge fracture and transfer of material into the weld pool. The arc is then re-ignited and then the sequence repeats itself all over again. [Feng et al., 2009]

CMT welding cycle demonstration as shown in Fig. 1.4:

- a) Arc initiation: During the arcing period, the filler metal is moved into the weld pool.
- b) Short circuiting current: The arc is extinguished as the filler metal wire dips into the weld pool. The welding current is reduced which results in lower heat input.
- c) Retraction of wire: During the short circuit, the rearward movement of the wire aids droplet detachment. The current from the short circuit is kept low.
- d) Process continues: The motion of the wire is reversed and the mechanism continues all over again.

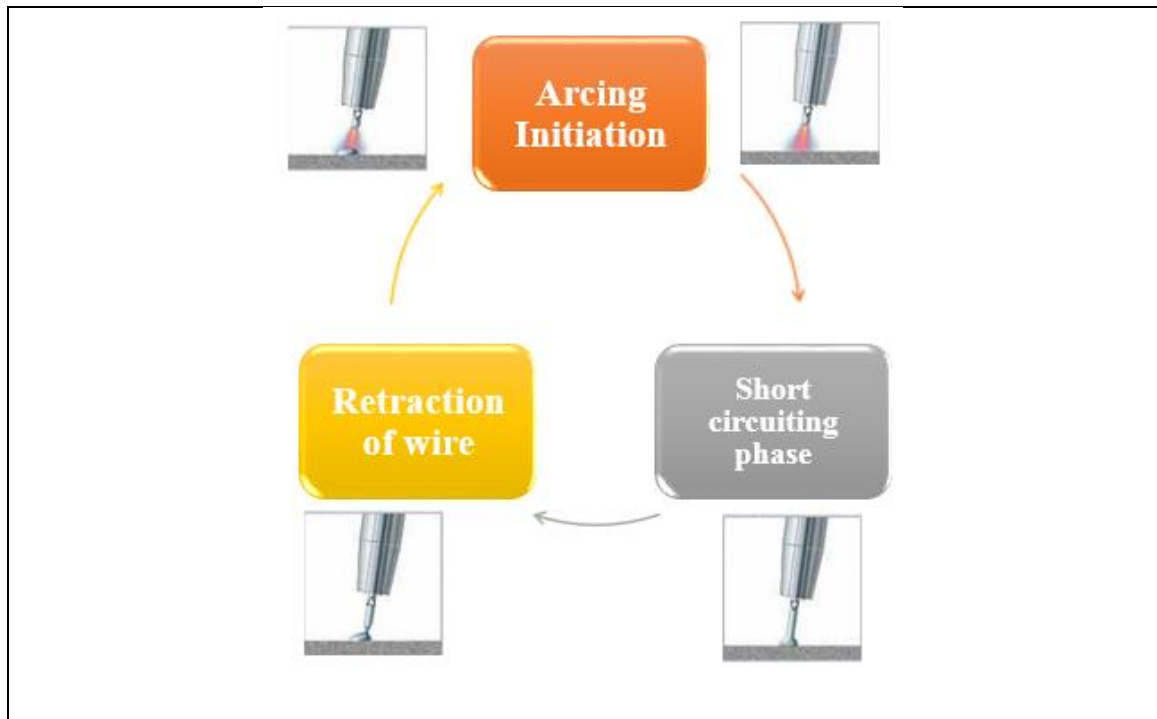


**Fig. 1.4** CMT welding process

### 1.3 OVERVIEW OF THE THESIS

**Chapter 1** includes the introduction of CMT and motivation behind using CMT in place of its parent process GMAW. CMT mechanism of welding and benefits of using CMT over GMAW with its application are also discussed.

**Chapter 2** includes literature review related to CMT and it discusses various outcomes by the researchers in the field of different types of material being joined by using these

processes with research gaps. The research objectives of this research and a flow diagram of experimentation are discussed.

**Chapter 3** includes CMT mechanism, methods and experimentation and information about the developed setup for bead-on-plate, butt joining of dissimilar aluminium alloys using CMT and ultrasonic-assisted CMT (U-CMT). Working principle of CMT welding is discussed in a detailed manner in this section along with information regarding the advancement of using ultrasonic vibrations during welding. Experimental process parameters and procedure are elaborated in this section. Information regarding the tensile test, residual stress, micro-hardness and microstructure has been explained.

**Chapter 4** gives details of the results and discussion on bead-on-plate experimentation. AA6061-T6 is used as a base plate on which the bead-on-plate experiment is performed. Influence of process parameters on dilution, heat input, penetration and residual stress is discussed in detail. Microstructural changes with respect to the process parameters are discussed. Comparison with MIG pulse (MIG P) and MIG manual (MIG M) is included and optimization of bead-on-plate experiments using CCFC in RSM is also in this chapter. Optimal parameters are found out and confirmation test is also carried out for validation.

**Chapter 5** includes results and discussion on CMT butt joints of AA6061-T6 and AA6082-T6 having a dissimilar thickness. Influence of various process parameters on UTS, microhardness, microstructure and residual stress is included in this chapter. Optimization of process parameters used in butt joining is done by RSM-GRA coupled with PCA technique is also included in this chapter. Optimal parameters are found out and confirmation test is also carried out for validation.

**Chapter 6** includes result and discussion on ultrasonic-assisted CMT (U-CMT). Influence of various process parameters on UTS, microhardness, microstructure and residual stress is included in this chapter. Comparison is done without U-CMT butt joints.

**Chapter 7** includes the conclusion drawn from this research work, significant contributions and future scope of the research study.

## **1.4 SUMMARY**

Joining of dissimilar materials or dissimilar alloys possesses several difficulties such as material compatibility, different physical properties, weldability etc. This chapter presented brief overview of joining dissimilar materials or alloys with the existing fusion welding techniques. Advantages and limitations of GMAW process in welding thin sheets is illustrated. Comparison between CMT and GMAW is highlighted with some processed weld images. CMT mechanism of welding and benefits of using CMT over GMAW with its application is also discussed. Motivation behind using CMT in place of its parent process GMAW is illustrated. The organization of the thesis is also presented.

## CHAPTER 2 : LITERATURE REVIEW

---

### 2.1 INTRODUCTION

This chapter presents a literature survey on dissimilar materials joints (different alloys or different metal joints), dissimilar types of joints (lap and butt joints) and dissimilar thickness of joints (variable thickness like both sheets are of different thickness being welded). Literature review is scrutinised from last 15 years of papers published to get a clear picture of the work done in the field of welding using different joining techniques. Based on the literature review the research gap and objectives of the work are identified. Finally, plan of work to fabricate the joints are presented.

### 2.2 CMT WELDING OF DISSIMILAR MATERIALS

#### 2.2.1 Aluminium and Steel

[Zhang et al., \(2009\)](#) used Al-Si alloy wire in welding of the pure aluminium and steel sheet which is coated with zinc and this joint is successfully fabricated by the process of CMT without having any cracks. It is not easy to weld aluminium and steel because of their varying thermo-physical properties. The IMC layer which has the maximum thickness of  $4\mu\text{m}$  at the interface between steel and WM which mainly consists of  $\text{Fe}_2\text{Al}_5$  and  $\text{FeAl}_3$  phase which shows low solid solubility of Fe in Al. Intensity of  $\text{FeAl}_3$  phase is much higher as compared to  $\text{Fe}_2\text{Al}_5$  phase. The tensile test results show that the bonding strength is about 83MPa, equalled nearly to 86% of that of the pure aluminium and fracture all occurred in the HAZ of the Al side. [Jácome et al., \(2009\)](#) uses four different types of Al-filler wire ( $\text{Al}_{99.5}$ ,  $\text{AlSi}_5$ ,  $\text{AlMn}_1$ , and  $\text{AlSi}_3\text{Mn}_1$ ) with addition of Mn and Si, to study the mechanical properties and microstructural characterization. Its major emphasis is on intermetallic phases (IMP). Formation of intermetallic compounds (IMCs) could be significantly controlled with the presence of Si in the filler wire. Upto 1% of Mn in the filler wire improves the overall behavior of joint without influencing the nature of inter-metallic phase (IMP). If process fluctuation remains minimal, then choice of filler material greatly influences the mechanical behavior.  $\text{AlSi}_3\text{Mn}_1$  filler wire gives significant results in terms of mechanical behavior and IMP. [Kang & Kim \(2015\)](#) uses both Al-Si alloy (Al 4043 and



Al 4047) and Al-Mg alloy (Al 5356 and Al 5183) as a filler wire to join Al5052 alloy to hot-dip aluminized (Al coated) steel sheet using CMT. The Si composition of the filler metal primarily influences the thickness of the IMC layer. When using Al-Si (Al 4043 and Al 4047) filler wires, the thickness of the IMC layer was approximately constant along the interface direction, which means it is almost parallel to the x-axis corresponding to IMC thickness of 2 $\mu$ m to 3 $\mu$ m. However, when Al-Mg (Al 5356 and 5183) filler wires were used, the IMC layer thickness was maximum at the center of interface and lowest at the ends (root and toe). The development of the IMC layer could not be regulated with Al-Mg (Al 5356 and 5183) filler wires. As the content of Si in the filler wire increases, the thickness of IMC layer decreases. [Yang et al., \(2013\)](#), discussed the reasons of porosity in welding of aluminium and steel. The development of porosity which is a major welding defect in the weld could be attributed to the  $Al_xO_y$  contains hydrogen, which has distinctive solubility in the solid and liquid Al phase. The solid Al has a less solubility than that of liquid aluminium. So during the solidification process, the unnecessary atomic hydrogen is ejected from the newly formed solid into the surrounding liquid phase. When the hydrogen reaches a critical solubility level in the liquid, the porosity could be produced in the weld [[Ransley, 1948](#)]. Zinc coating on steel surface controls the formation of brittle  $Al_xFe_y$  in the intermetallic layer (IML). Due to the presence of Si in the molten filler wire, a very thin IML was observed at the interface between weld bead and steel. Si particles not only decreases the diffusion of Al through the IML but also dissolves the IML. ‘Scanning Electron Microscope’ (SEM) was used to examine the typical characteristics of the WZ, IML and steel base metal side. The intermetallic layer (IML) has lots of protruding in the aluminium side and its average thickness is less than 5 $\mu$ m which facilitates the achievement of relatively high weld strength which can be improved by appropriate PWHT. [Lin et al., \(2013\)](#) showed that the variation of shear strength of the joint with different thickness of low carbon steel substrate. When joining 0.7 mm thickness of low carbon steel with aluminium with the help of ER4043 filler material, lower shear strength (2.1 kN of applied load) was observed with an interface failure. In contrast with this, higher shear strength (>2.5 kN of applied load) was observed in CMT braze lap joint when thickness of low carbon steel is 1.2mm with a fusion line failure. Similar to this, CMT braze lap joint of AA6061 with high strength DP600, higher shear strength (>2.5 kN) is also observed with

a fusion line failure. [Cao et al., \(2013 A\)](#) uses three different aluminium wires 4043, 4047 and 5356 as filler metal to join 6061 aluminium alloy and galvanized mild steel (Q235) using CMT welding. The joint strength of the weld depends on the thickness of intermetallic (regulated at about 5µm which is less than the critical value of 10 µm) and softening of the aluminium HAZ. Because of the softening phenomenon, failure commenced at the aluminium HAZ rather than the weld-brazed interface. This is proved by experimentation, that the hardness of aluminium HAZ is smaller than that of aluminium base metal. Thus, during loading processes, the shrinkage would develop at the aluminium HAZ, which would further decreases the joint strength. Therefore, minimizing the heat input would narrow the width of the aluminium HAZ, and subsequently improve the joint strength. The wire type was the most influential process parameter with a 48.92% contribution. The welding speed contributed 13.13%, wire feed speed-19.35% and their interaction-23.82%. [Cao et al., \(2013\)](#) states that the microstructure investigation for the materials shows a portion of the Mg<sub>2</sub>Si which helps in strengthening secondary phases that were melted causing them to transform from rod-shaped grains to columnar grains in the HAZ near the FZ. However, in the HAZ far from the FZ, most Mg<sub>2</sub>Si strengthening second phases were melted and precipitated out along the grain boundaries during cooling, which specifies that over-ageing softening phenomena was induced at the HAZ of the aluminium 6061 [[Ma & Den Ouden, 1999](#)].

### 2.2.2 Magnesium and Aluminium alloy

[Shang et al., \(2012\)](#) uses pure Cu as a filler wire, the proper processing parameters for a successful joining of Mg-Al dissimilar metals using CMT are welding current and voltage of 129A and 12.0V respectively, WFS of 95mm/sec, welding speed of 10.83mm/sec. The bonding strength of the welded joint was 34.7MPa. The fracture appeared in a brittle IMC layer of the FZ adjacent to Mg substrate. The ice-sugar pattern morphology, which was indicated by SEM, confirms that the fracture was in brittle mode. SEM image shows that the growth of columnar crystals is along the weld center. Energy Dispersive X-ray (EDX) results showed that the ice-sugar pattern morphology comprises of 34.12% Al, 65.01% Mg and 0.87% Si, which specifies that this position must be composed of α-Mg solid solution, γ(Mg<sub>17</sub>Al<sub>12</sub>) and dispersed Mg<sub>2</sub>Si. Columnar crystals consists of 35.59% Al and 64.41%

Mg, which suggests that this location mainly consists of  $\alpha$ -Mg solid solution and  $\gamma$  ( $\text{Mg}_{17}\text{Al}_{12}$ ) eutectic structure [Jing et al., 2013].

A comparative study concludes that brittle fracture arose in the FZ of Mg side at the highest value of micro-hardness due to a significant quantity of  $\text{Cu}_2\text{Mg}$  'Inter-Metallic Compounds' (IMC) [Shang et al., 2012]. Jing et al., (2013) use ER4043/AlSi5 as a filler wire for butt joint, which had equivalent micro-hardness in both sides of the substrates, about 540MPa (55.06 HV) in Mg side and 350MPa (35.69 HV) in Al side. The micro-hardness increases abruptly and reaches its maximum value of 2380 (242.7 HV) in the FZ of Mg side. The micro-hardness within the WZ exhibits a declining trend from the Mg to Al side with reduction of IMC because Mg and Al in the melting state has a very high mutual solubility, whereas in the solidification state eutectic reaction takes place to form precipitate such as  $\beta(\text{Mg}_2\text{Al}_3)$  and  $\gamma(\text{Mg}_{17}\text{Al}_{12})$  which is hard and brittle. Wang et al., (2008) uses ER4043/AlSi5 as a filler wire for lap joining of aluminium and magnesium, has micro-hardness of 230-240 HM in the FZ of Mg side which is higher than the Mg substrate (60 HM). Filler wire used had the great weld bead aesthetics without any cracks or weld defects. Using CMT which is a super low heat input welding process with the addition of silicon, creates brittle IMC's. Four continuous layers, which consisted like solid solution layer, eutectic structure layer,  $\text{Mg}_{17}\text{Al}_{12}$  layer and  $\text{Mg}_2\text{Al}_3$  layer created by the Mg substrate though the FZ into the WM.

Cao et al., (2013) uses aluminium 4047 as a filler wire, there were considerable amounts of Mg-rich inter-metallic  $\gamma\text{-Al}_{12}\text{Mg}_{17}$  and  $\beta\text{-Al}_3\text{Mg}_2$  in the weld joint which degraded the weld strength. The Mg-rich intermetallic should be minimized to improve the joint. Wang et al., (2016) uses VP-CMT to join AZ31B magnesium and 6061 aluminium alloy with the help of ER4043 filler wire. VP-CMT process constituted of two cycles that are EP-CMT cycles and EN-CMT cycles which are further divided into three phases; SCP, PCP and BCP that are similar to standard CMT process. To accomplish steady welding, the polarity reversal took place at the commencement of the SCP. Current and voltage during the EP-CMT cycle is around 97.3 A and 13.2 V respectively which is much higher than EN-CMT (62.8 A and 8.9 V). Despite of the lower current of EN-CMT cycles as compared to EP-CMT cycles, the material deposition is same because negative electrode is used to generate maximum heat in the arc which directly used to melt the wire. As EN-

CMT has less current and voltage, so the average power of the EN-CMT cycle is almost less than twice as that of the EP-CMT-cycle. There are some beneficial results follows by reducing EP/EN ratio from 4:1 to 1:4,

- The overall IMC thickness was steadily reduced from 190 mm to 95 mm, whereas the compounds produced within the weld like  $Mg_2Al_3$  layer and  $Mg_{17}Al_{12}$  layer were lessened from 80 mm to 10 mm and 105 mm to 80 mm respectively.
- The tensile strength of the Mg-Al dissimilar weld using VP-CMT technique which significantly increases from 16.3 MPa to 37.2 MPa. This increase in tensile strength is almost over 100 %.

In order to enhance the Mg-Al dissimilar welded joint strength, VP-CMT process is superior to standard CMT process because of the inclusion of EN-CMT cycle. More number of EN-CMT cycles results in lesser energy input which helps in minimizing the thickness of IMC that ultimately causes higher welded joint strength. Likewise, the welded joint strength of test sample 5 is 37.2 Mpa using VP-CMT process which is comparatively higher than that using standard CMT process using pure Cu as the filler metal (34.7 MPa) [Shang et al., 2012].

Madhavan et al., (2017) uses Al-5%Si filler metal to weld AZ31B Mg and AA6061 using CMT welding. It is concluded that at highest value of heat input (205 J/mm) the tensile strength shows a maximum value of 360 N/mm<sup>2</sup>. This states that, as the heat input increases the tensile strength also increases due to high travel speeds. Minimum HAZ is created with high travel speeds. FZ thickness is directly proportional to the heat input. As the heat input increases from 175 to 205 J/mm, the thickness of FZ also increases from 3 to 12  $\mu$ m which has a significant effect on the joint strength. The FZ nearby Mg displays a maximum value of micro-hardness due to mainly three reasons; diffusion of alloying elements, the development of IMC and presence of precipitates like  $Mg_2Si$  and  $Al_6Mn$ . At the heat input of 185 J/mm, the coarser dendrites and coarsening of precipitates leads to the reduction in micro-hardness at the FZ. Lower rate of cooling causes the formation of coarser dendrites. This rate of cooling is directly proportional to welding speed; for slower welding speed the rate of cooling is also lower. There is an insignificant rise in micro-hardness at the WZ because of occurrence of alloying elements in solution state. At 205 J/mm heat input, the joints produced has a higher micro-hardness at the FZ along with the

WZ due to increased travel speed which causes solidification of the weld bead at a faster rate.

### 2.2.3 Titanium and other materials

[Cao et al., \(2014\)](#) used to weld titanium TA2 and copper T2 using CMT welding method with the help of ER CuNiAl copper wire as a filler metal. Satisfactory butt joint was effectively obtained at 150-158.34 mm/sec (current at 210-223 A). The micro-hardness in the Cu base metal (95 HV) is relatively higher than that of the Cu HAZ (75 HV) with 9 mm width that indicates the softness phenomenon which appear in Cu HAZ. The micro-hardness of titanium base metal and WM is approximately same which is about 175HV and 170 HV, respectively. However, the brazing interface zone which is also known as IMC reaches a micro-hardness of 500 HV. [Cao et al., \(2014 B\)](#) uses Mg AZ61 wire to weld titanium TA2 and Mg AZ31B using CMT. For Mg-Ti joint and Ti-Mg joint, the higher tensile load of 2.10kN and 1.83kN can be obtained by optimal welding parameter. The micro-hardness of titanium sheet is about 175 HV and Mg WM is about 55 HV. However, the brazing interface layer has the maximum value of micro-hardness of 212 HV. [Sun et al., \(2017\)](#) using hybrid CMT welding-brazing process with ER4043 filler metal used to join pure titanium TA2 to AA6061-T6. The electromotive force will have an effect on the wettability and flow-ability of the filler wire on the surface of Al-Ti unlike metal joints. This joint is highly dependable than that of conventional welding method due to increase in bonding area and a decrease in wetting angle. Without the EMF the micro-hardness declined abruptly from the Al substrate metal to HAZ and then becomes almost constant till the WZ. Conversely, with the application of EMF, the micro-hardness declined steadily from the Al substrate metal to the WZ. In comparison with the conventional welding method, the micro-hardness of the WZ and HAZ increases with the application of EMF. Since the addition of the magnetic field affects the weld structure.

### 2.2.4 Tailor Welded Blanks (TWB)

[Sterjovski et al., \(2014\)](#) used pulsed-tandem GMAW and experiences higher deposition with lower distortion for naval shipbuilding application. It is explained that naval surface ships with considerably less hull distortion reduces hydrodynamic drag, speed and fuel

efficiency. The different kinds of materials and even different thickness of materials can be welded to realize the Tailor Welded Blanks (TWB). This fabrication technique has further delivered a new platform for the deployment of multiple automotive material system (MAMS) [Li-li et al., 2012; Gery et al., 2005; Aslanlar et al., 2007 and Xia et al., 2008]. Moulton and Weckman (2010) used double sided arc welding (DSAW) for TWB applications with thin sheets of aluminium alloys. Beneficial results are found to facilitate aluminium alloy TWBs manufacturing.

#### 2.2.5 Aluminium alloys

Írizalp et al., (2016) investigated the welding parameters by CMT method and mechanical behavior of 2 mm thick AA1050 sheet. Results exhibited highest tensile strength and micro-hardness due to minimum heat input. Liu et al., (2007) worked on AA2024-T3 joints. It is revealed that the stress corrosion cracking at inter granular level when subjected to constant loading condition. In welded specimens, it is observed that on subjection to compressive residual stress, there is a considerable reduction in crack growth rate, whereas when subjected to tensile stress there is an incredible increase in local stress concentration factor, which has often been found as a leading factor to inter-granular stress corrosion cracking (IGSCC) throughout its service life. Shu et al., (2014) investigated residual stress in narrow gap welded joint of aluminium alloy by CMT. Results revealed that the final allocation of residual stress was evaluated based on the distribution of stress along various lines. Homogeneity was discovered in the stress field with stress concentrated on the weld metal and its neighboring zones. Petroyiannis et al., (2005) experimented with AA2024 hydrogen embrittlement induced by corrosion. Removal of oxidized areas mechanically, almost restored ultimate and yield stress to their original values but ductility is not restored. Hydrogen evolution always occurs in the active growth of localized positions and cracks of corrosion. There is an observation of crack propagation of hydrogen embrittlement (HE), which can be resulted by hydrogen absorption into the alloy of aluminium [Lynch, 1988]. Hermans & Den Ouden (1999) worked towards achieving the stability while performing short-circuit GMAW while accompanying the process behavior. It was brought into conclusion that to pursue maximum stability, standard deviation of frequency should be kept minimum for short-circuiting. Moreira et al., (2009) used solid-state welding i.e.

Friction Stir Welding (FSW) to join 6061-T6 and 6082-T6 aluminium alloys. It was able to produce lower yield and ultimate stress, and intermediate properties were shown by the dissimilar joints. Failures occurred close to the weld edge line in the tensile tests where minimum hardness value was perceived. As exhibited by [DuPont and Marder \(1996\)](#), dilution is expressed as the fraction of the parent metal in the subsequent weld metal (WM) and, for a solitary weldment deposit. [Sakthivel et al., \(2016\)](#) performed welding on AA2012 plate which indicates the impact of current (I), voltage (V) and flow rate of shielding gas increase the weld penetration (P), weld width (W), and reduces the height of weld reinforcement (R).

Table 2.1 contains a full analysis of the literature review done on the basis of the welding parameters on CMT machine. This includes cleaning action required before welding and prior taking the microstructure. Welding parameters such as current, voltage, wire feed rate, welding speed and heat input are classified for dissimilar material joints. Table 2.2 gives the major conclusion highlighted by some reseachers for dissimilar material joints on CMT welding machine. Table 2.3 and 2.4 gives the information about the type of joint i.e. butt and lap joint respectively welded with CMT.

**Table 2.1** Welding parameters of CMT welding process

<u>S.No.</u>	<u>Source</u>	<u>SM/BM</u>	<u>FM</u>	<u>Joint configurat ion</u>	<u>SG</u>	<u>Welding Parameters</u>							
						<u>Cleaning action on surface</u>		<u>Machine</u>	<u>I (A)</u>	<u>V (V)</u>	<u>WFR (mm/ sec)</u>	<u>S (mm /sec)</u>	<u>Q (J/m m)</u>
						<u>Prior Welding</u>	<u>Prior Microstructure</u>						
1.	<a href="#">Wang et al., (2008)</a>	Aluminium 1060 (1mm) to Mg AZ31 (1mm)	AlSi5 alloy wire ( $\phi$ 1.2 mm)	Lap joint	-	Emery cloth and acetone	Etching by 2 ml of malic acid and 98 ml H <sub>2</sub> O for 2 seconds.	CMT Welding	50	11.4	8	7.5	-
2.	<a href="#">Zhang et al., (2009)</a>	Aluminium 1060 (1mm) to Zn-coated Steel (0.6mm)	Al-Si alloy wire ( $\phi$ 1.2 mm)	Lap joint	Argon (15dm <sup>3</sup> /min)	Acetone	-	CMT Welding -Brazing	-	-	-	-	-



3.	<a href="#">Jácome et al., (2009)</a>	AW5182-H111 aluminum alloy (1.5 mm) to DX54D steel (1 mm) having Zn coating (14 mm)	Four wires are used: Al <sub>99.5</sub> , AlSi <sub>5</sub> , AlMn <sub>1</sub> , and AlSi <sub>3</sub> Mn <sub>1</sub>	Butt joint	Argon	-	-	CMT welding	70	12	-	10	-
4.	<a href="#">Shang et al., (2012)</a>	AZ31B Mg alloy (3 mm) and AA6061 (3 mm)	Pure copper (HS201) (φ 1.2 mm)	Butt joint with 'V' groove of 40°	-	Oxide layer is removed by stainless steel wire brush, and then acetone is used for removal of the oil.	Mg alloy side-Solution of 1 ml C <sub>2</sub> H <sub>2</sub> O <sub>4</sub> , 1 ml HNO <sub>3</sub> , 1 ml CH <sub>3</sub> COOH and 150 ml H <sub>2</sub> O. Al alloy side-Solution of 2 ml HF, 5 ml HNO <sub>3</sub> and 95 ml distilled H <sub>2</sub> O.	CMT Fronius-5000	114-134	11.1 to 12.4	85 to 98.3	7.5 to 10.8 3	-

5.	Yang et al., (2013)	AA6061-T6 (2 mm) and zinc coated low-carbon steel (1.2 mm)	ER 4043 ( $\phi$ 1.2 mm)	Lap joint with overlap distance of 15mm	Pure Argon (16 L/min)	Acetone	polished and etched	CMT Fronius-5000	-	-	0.073 or 0.078	0.00 83 or 0.00 67	-
6.	Cao et al., (2013)	Mg AZ31B (1 mm) and AA6061-T6 (1mm)	Aluminium 4047 ( $\phi$ 1.6mm )	Lap shear joint with overlap distance of 10mm	Pure Argon (15 L/min)	Acetone is used for degreasing and polishing is done using abrasive cloth	Mg side- Etched by 5 g picric + 10 ml distilled H <sub>2</sub> O + 50 ml ethanol + 5 g CH <sub>3</sub> COOH Al side- Nital	CMT Fronius-3200	-	10	30 to 50	5.0 to 8.8	-
7.	Cao et al., (2013 A)	AA6061-T6 (1.0 mm) to Galvanized mild steel (Q235) (1mm)	Aluminium wires 4043, 4047, 5356 ( $\phi$ 1.2mm)	Lap shear joint with an overlap distance of 10mm	Pure Argon (15L/ min)	Polished	Al side- Dix-Keller's reagent Steel side- Nital reagent	CMT Welding -Brazing CMT 3200		10 to 16	66.66 to 100	6 to 13	50-450 Optimal (100-200)

8.	<a href="#">Jing et al., (2013)</a>	AZ31B magnesium alloy (3 mm) to AA6061 (3 mm)	ER4043 ( $\phi$ 1.2 mm)	Butt joint with 'V' groove of 50°	Argon	Stainless steel wire brush for oxide removal, and the oil is removed with acetone.	Mg alloy side-Solution of $C_2H_2O_4$ , $HNO_3$ , $CH_3COOH$ (1 ml each) and 150 ml distilled $H_2O$ . Al alloy side-Solution of 2 ml $HF$ , 5 ml $HNO_3$ and 95 ml distilled $H_2O$ .	CMT Fronius-5000	77	12.3	4.3	8.33	-
9.	<a href="#">Lin et al., (2013)</a>	AA6061 (2 mm) to low carbon steel (0.7 mm and 1.2mm)	ER4043 ( $\phi$ 1.2 mm)	Lap joint with an overlap of 8 mm or 15 mm	-	-	-	CMT braze-welding	70	11.1	-	11.67	-

10.	<a href="#">Gungor et al., (2014)</a>	5083-H111 and 6082-T651 aluminium alloys (6 mm)	ER5183 ( $\phi$ 1.2 mm)	Butt joint with 'V' groove of 60°	Argon	-	-	Pulsed robotic CMT	189 to 199	18.5 to 20.5	180 to 186.67	6.67	-
11.	<a href="#">Cao et al., (2014)</a>	Pure titanium TA2 (3 mm) and pure copper T2 (3 mm)	ERCuNi Al copper wire ( $\phi$ 1.2 mm)	Butt joint	Argon (17 L/min)	Degreased by acetone and polished by abrasive cloth first	Ti sheet- HF 5% + HNO <sub>3</sub> 35% for 10-20 min, then wiped and rinsed with ethanol and tap water. Cu sheet- ethanol and tap water.	Welding -Brazing CMT TPS-3200	158 to 223	14.7 to 20.3	116.67 to 158.34	6	680-754

12.	Cao et al., (2014 A)	Pure titanium TA2 (1 mm) to Pure copper T2 (1 mm) [JI (top Cu-bottom Ti, JII (top Ti-bottom Cu)]	ERCuNi Al copper wire ( $\phi$ 1.2mm)	Lap shear joint with an overlap distance of 10mm	Argon (15L/min)	stainless steel wire brush and acetone	-	Welding -Brazing CMT TPS-3200	JI-112-136 JII-136-170	JI-11-12.6 JII-12.6-15.8	JI-83.34 to 100 JII-100 to 125	6	-
13.	Cao et al., (2014 B)	Pure titanium TA2 (1 mm) to Mg AZ31B (1 mm) JI- Mg-Ti JII- Ti-Mg	Mg AZ61 wire ( $\phi$ 1.2 mm)	Lap shear joint with an overlap distance of 10 mm	-	degreased by acetone and polished by abrasive cloth first.	5 g picric acid +10 ml distilled H <sub>2</sub> O +50 ml ethanol +5 g CH <sub>3</sub> COOH for 30 s at room temperature	CMT welding-brazing	-	13	83.34	7.14	-

14.	<a href="#">Kang &amp; Kim, (2015)</a>	Al 5052 alloy (1 mm) to hot-dip aluminized (Al-coated) steel sheet (1.2 mm)	Al 4043, Al 4047, Al 5356 and Al 5183 ( $\phi$ 1.2 mm)	Lap fillet joint with an overlap distance of 30 mm.	Argon (15 L/min)	-	-	CMT Braze-welding Fronius CMT 3200	76	12.3	70 to 80	8.33	-
15.	<a href="#">Elrefaey and Ross (2015)</a>	2-mm-thick 5182-O and 6082-T4 aluminum alloy sheets	ER5356 and ER4043	Butt joint	Argon (15 L/min)	Cleaned with acetone and steel brush to remove the oxide layer	Etched with Barker's reagent (5 ml HBF <sub>4</sub> (48%) in 200 ml water)	CMT machine	55-104	13.9-16.7	2.9-6.2	10-20	65-98
16.	<a href="#">Wang et al., (2016)</a>	Mg alloy AZ31B (2 mm) and Al alloy 6061 (2 mm)	ER4043 ( $\phi$ 1.2 mm)	Butt joint with 'V' groove of 90°	-	-	Polished and etched by 5g Picric + 20 ml CH <sub>3</sub> COOH + 20 ml distilled H <sub>2</sub> O + 100 ml ethanol	Fronius CMT Advance d 4000R	0 to 150	0 to 25	70	11.66	-

17.	<a href="#">Sun et al., (2017)</a>	Pure titanium TA2 (1 mm) to AA6061-T6 (2 mm).	ER4043 ( $\phi$ 1.2 mm)	Lap joint with an overlap distance of 10mm	Argon (15 L/min)	stainless steel wire brushing and then degreased using acetone	-	CMT welding-brazing Fronius TPS 4000	Coil Current-0.5-1.5	-	88.3	10	-
18.	<a href="#">Silvayeh et al., (2017)</a>	AA EN AW 6014 T4 (1.15 mm) to galvanized dual-phase steel HCT 450X+ZE 75/75 (0.8 mm)	Six different aluminium-based filler wires ( $\phi$ 1.20 mm)	Butt joint	Argon (12 L/min)	-	Epoxy resin, grinding with sand papers and polishing with diamond suspensions	Fronius CMT Advance d 4000	66 to 74	7.9 to 9.3	56.66 to 78.33	6.67	78-95
19.	<a href="#">Madhavan et al., (2017)</a>	AA6061-T6 (2 mm) to AZ31B Magnesium alloy (3 mm)	Al-5 %Si ( $\phi$ 1.2 mm)	Lap joint with an overlap distance of 10 mm	Pure Argon (18 L/min)	Wire brush and cleaned with acetone	Solution of 70 ml Picral + 10 ml H <sub>2</sub> O <sub>2</sub> + 10 ml Glacial Acetic acid	CMT	70 to 100	12.2 to 12.9		3.91 to 5.083	175 to 205

20.	<a href="#">Li et al., (2019)</a>	AA6061-T6 (6 mm) to 7N01-T4 (6 mm)	ER4043 ( $\phi$ 1.2 mm)	Y-Butt joint geometry of groove of 90° with a 2-mm blunt edge.	Pure argon (15 L/min)	-	Etchant consisting of 1.5 ml HCl, 1 ml HF, 2.5 ml HNO <sub>3</sub> , and 45 ml H <sub>2</sub> O	CMT Advanced 4000R (CMT+P)	-	-	125	5	445 to 557
SM/BM = Substrate material/ Base material; FM = Filler material; SG = Shielding gas; I = Current; V = Voltage; WFR = Wire feed rate; S = Welding speed; Q = Heat input; JI = Joint I; JII = Joint II; AA = Aluminium alloy													



**Table 2.2** Major conclusions on dissimilar materials using CMT

<u>S. No.</u>	<u>Source</u>	<u>SM1</u>	<u>SM2</u>	<u>FM</u>	<u>Key Findings</u>
1.	<a href="#">Wang et al., (2008)</a>	Aluminium 1060 (1 mm)	Mg AZ31 (1 mm)	AlSi5 alloy wire ( $\phi$ 1.2 mm)	<ul style="list-style-type: none"> <li>No obvious weld defect can be observed in welding of AZ31 Mg alloy and 1060 Al alloy by super low heat input welding process with the help of AlSi5 alloy wire.</li> <li><math>Mg_{17}Al_{12}</math> and <math>Mg_2Al_3</math> are the two majorly consisting brittle IMC's which significantly deteriorates the joint strength. Fracture morphology showed mixed mode fracture- the typical cleavage and intergranular fracture.</li> <li>The micro-hardness in the FZ near Mg side was about 230–240 HM higher than the WZ 120 HM and the Mg substrate 60 HM due to hard and brittle IMC's.</li> </ul>
2.	<a href="#">Zhang et al., (2009)</a>	Pure aluminium 1060 (1 mm)	Zn-coated Steel (0.6 mm)	Al-Si alloy wire ( $\phi$ 1.2 mm)	<ul style="list-style-type: none"> <li>It is possible to join pure aluminium and steel sheet which is coated with zinc layer without having any cracks by the CMT process in a lap-joint.</li> <li>The IML which has its thickness under 5 <math>\mu m</math>, consists of <math>Fe_2Al_5</math> and <math>FeAl_3</math> phase at the interface between steel and WM.</li> </ul>
3.	<a href="#">Jácome et al., (2009)</a>	AW5182-H111 aluminium alloy (1.5 mm)	DX54D steel (1 mm) with Zn coating (14 mm)	Four wires: $Al_{99.5}$ , AlSi5, $AlMn_1$ , and $AlSi_3Mn_1$	<ul style="list-style-type: none"> <li>Upto 1% of Mn in the filler wire improves the overall behavior of joint without influencing the nature of inter-metallic phase (IMP)</li> <li>Formation of intermetallic compounds (IMCs) could be significantly controlled with the presence of Si in the filler wire.</li> </ul>

4.	<a href="#">Shang et al., (2012)</a>	6061 Al alloy (3 mm)	AZ31B Mg alloy (3 mm)	Pure copper (HS201) ( $\phi$ 1.2 mm)	<ul style="list-style-type: none"> <li>• Optimum processing parameters are, current of 129A, voltage of 12.0V, WFS of 95mm/sec, welding speed of 10.83mm/sec for successful joining of Mg/Al dissimilar metals by CMT.</li> <li>• The fracture occurred in the FZ of Mg side at the highest value of micro-hardness. The brittle fracture occurred due to continued distribution of a large amount of <math>\text{Cu}_2\text{Mg}</math> IMC.</li> <li>• The tensile strength of the joint was 34.7 MPa.</li> </ul>
5.	<a href="#">Yang et al., (2013)</a>	AA6061-T6 (2 mm)	Zinc coated low-carbon steel (1.2 mm)	ER 4043 ( $\phi$ 1.2 mm)	<ul style="list-style-type: none"> <li>• The erratic zinc vapour's formed can lead to the unstable welding process.</li> <li>• Zinc coating on the steel surface controls the formation of brittle <math>\text{Al}_x\text{Fe}_y</math> in the IML.</li> <li>• Weld strength can be improved by appropriate PWHT.</li> </ul>
6.	<a href="#">Cao et al., (2013)</a>	AA6061-T6 (1 mm)	Mg AZ31B (1 mm)	Aluminium 4047 ( $\phi$ 1.6 mm )	<ul style="list-style-type: none"> <li>• There were significant amounts of Mg-rich intermetallic <math>\gamma</math>- <math>\text{Al}_{12}\text{Mg}_{17}</math> and <math>\beta</math>- <math>\text{Al}_3\text{Mg}_2</math> in the weld joint which degraded the weld strength.</li> <li>• The Mg-rich intermetallic should be minimized to improve the joint strength.</li> </ul>
7.	<a href="#">Cao et al., (2013 A)</a>	AA6061-T6 (1.0 mm)	Galvanized mild steel (Q235) (1 mm)	Aluminium wires 4043, 4047, 5356 ( $\phi$ 1.2 mm)	<ul style="list-style-type: none"> <li>• The welded joint strength depends on the thickness of IMC and softening of the aluminium HAZ.</li> <li>• In CMT welding, different wire types used were the most governing process parameter with a contribution of about 48.92%. The other parameters like weld speed contributed 13.13%, WFS-19.35% and their interaction- 23.82%.</li> </ul>

8.	Jing et al., (2013)	AA6061 (3 mm)	AZ31B magnesium alloy (3 mm)	ER4043 ( $\phi$ 1.2 mm)	<ul style="list-style-type: none"> <li>With the reduction of IMC, the hardness decreases from Mg side to Al side in the weld.</li> <li>The brittle fracture on the Mg side joint is due to these IMC's- <math>Mg_2Si</math>, <math>Mg_2Al_3</math> and <math>Mg_{17}Al_{12}</math> in the FZ.</li> </ul>
9.	Lin et al., (2013)	AA6061 (2 mm)	low carbon steel (0.7 mm and 1.2 mm)	ER4043 ( $\phi$ 1.2 mm)	<ul style="list-style-type: none"> <li>Lower shear strength was observed when aluminium was brazed with low carbon steel of 0.7mm thickness with an interface failure position.</li> <li>Higher shear strength was observed in CMT brazed lap joint of AA6061 and low carbon steel of 1.2 mm thickness with a fusion line failure. Similar to this, CMT braze lap joint of AA6061 with high strength DP600, higher shear strength is observed with a fusion line failure.</li> </ul>
10.	Gungor et al., (2014)	5083-H111 aluminium alloy (6 mm)	6082-T651 aluminium alloy (6 mm)	ER5183 ( $\phi$ 1.2 mm)	<ul style="list-style-type: none"> <li>Welding of AA5083 and AA6082 has 65% efficiency, whereas that of 6082 with itself has 62%.</li> <li>There were no defects detected by radiography and microscopy in the WZ, while there were rare void effects by SEM analysis.</li> <li>CMT which has extremely low thermal heat input with higher melting coefficient of wire as compared with the pulsed MIG process provided high welding speed of 400 mm/min and insignificant distortion on welded plates.</li> </ul>
11.	Cao et al., (2014)	Pure titanium TA2 (3 mm)	Pure copper T2 (3 mm)	ERCuNiAl copper wire ( $\phi$ 1.2 mm)	<ul style="list-style-type: none"> <li>Satisfactory butt joint was successfully obtained at 150-158.34mm/sec (current=210-223A)</li> <li>The IMC layer thickness was 117–129<math>\mu</math>m in middle groove surface, and 80–100<math>\mu</math>m in root groove surface.</li> </ul>

12.	<a href="#">Cao et al., (2014 A)</a>	Pure titanium TA2 (1 mm)	Pure copper T2 (1 mm)	ERCuNiAl copper wire ( $\phi$ 1.2 mm)	<ul style="list-style-type: none"> <li>Satisfactory welded joint could be obtained with low heat input CMT welding process, for both the Joint I (top Cu sheet–bottom Ti sheet) and Joint II (top Ti sheet–bottom Cu sheet) with key features like desired welding appearance and good wettability and spreadability of filler metal on the surface of both alloys.</li> <li>A layer of IMCs, i.e. <math>Ti_2Cu</math>, <math>TiCu</math> and <math>AlCu_2Ti</math> presented in titanium-weld interface whereas <math>\alpha</math>-Cu solid solution and Ti–Cu–Al–Ni–Fe multi-phase presented in the WM. But fracture takes place at Cu-HAZ in both the Joints I and II.</li> <li>Tensile shear strength for joint I reaches to a value of 197.5N/mm whereas for joint II it reaches a value of 205.8N/mm, which is comparable with CMT lap welded Cu-T2 to Cu-T2 with a tensile strength of 194 N/mm.</li> </ul>
13.	<a href="#">Cao et al., (2014 B)</a>	Pure titanium TA2 (1 mm)	Mg AZ31B (1 mm)	Mg AZ61 wire ( $\phi$ 1.2 mm)	<ul style="list-style-type: none"> <li>Al and Zn elements in the Mg base metal with the use of Mg wire are crucial in joining successfully Mg and Ti base metals.</li> <li>Higher tensile load of 2.10kN and 1.83kN can be attained by optimal welding parameters for Mg-Ti joint and Ti-Mg joint respectively.</li> </ul>
14.	<a href="#">Kang &amp; Kim, (2015)</a>	Al 5052 alloy (1 mm)	Hot-dip aluminized (Al-coated) steel sheet (1.2 mm)	Al 4043, Al 4047, Al 5356 and Al 5183 ( $\phi$ 1.2 mm)	<ul style="list-style-type: none"> <li>In the braze welding of aluminized steel and Al 5052, wettability was not affected by kinds of filler metal used. Moreover, the galvanized steel using Al 5052 filler wire braze welded joint showed better wettability than the aluminized steel using Al 5052 joint filler wire.</li> <li>Silicon composition in the filler metal primarily influences the IMC layer thickness. Minimum the thickness of IMC layer, the better will be the joint strength of the weld.</li> </ul>

					<ul style="list-style-type: none"> <li>• In a tensile shear test, the joint strength was equal to that of the heat-affected zone of the Al 5052 alloy for the Al5052/aluminized steel/Al-Mg (Al 5356 and 5183) filler cases.</li> <li>• In a ductile shear test, the joint strength was equivalent to that of the HAZ of the Al 5052 alloy for the Al5052/aluminized steel/Al-Mg (Al 5356 and 5183) filler cases.</li> <li>• In Salt spray corrosion test, duration of salt spray influences the joint strength. As the duration of salt spray increases the joint strength decreases.</li> </ul>
15.	<a href="#">Elrefaey and Ross (2015)</a>	5182-O aluminum alloy (2 mm)	6082-T4 aluminum alloy (2 mm)	ER5356 and ER4043	<ul style="list-style-type: none"> <li>• Use of ER5356 filler metal in welding 5182 alloy sheet is better than ER4043 since it produces a weld metal with low Mg and Si content.</li> <li>• The corresponding joints are characterized by low hardness, high ductility, and high strength. However, for the 6082 alloy, both filler metals are compatible.</li> <li>• The HAZ microstructure showed fine precipitates of second phases and coarsening of the Mg<sub>2</sub>Al<sub>3</sub> precipitates in the aluminum matrix for 5182 sheets, whereas HAZ of 6082 showed no change compared to the BM.</li> </ul>
16.	<a href="#">Wang et al., (2016)</a>	AA6061 (2 mm thick)	Mg alloy AZ31B (2 mm)	ER4043 (φ 1.2 mm)	<ul style="list-style-type: none"> <li>➤ VP-CMT process was composed of EP-CMT cycles and EN-CMT cycles. The mean power of the EP-CMT cycles was more than twice as that of the EN-CMT cycles.</li> <li>➤ With decreasing EP/EN ratio from 4:1 to 1:4,</li> <li>• the thickness of the whole IMC layer was gradually reduced from 190mm to 95mm, and the Mg<sub>2</sub>Al<sub>3</sub> layer and Mg<sub>17</sub>Al<sub>12</sub> layer were reduced from 80 mm to 10 mm and from 105 mm to 80 mm, respectively.</li> <li>• The tensile strength improved ominously by over 100%.</li> </ul>

					<ul style="list-style-type: none"> <li>➤ With the inclusion of EN-CMT cycles, VP-CMT process is superior to the standard CMT welding process to weld Mg/Al dissimilar alloys.</li> <li>➤ The number of EN-CMT-cycles result in the higher joint strength due to the lower energy input which corresponds to thinner IMC layer.</li> </ul>
17.	<a href="#">Sun et al., (2017)</a>	AA6061-T6 (2 mm).	Pure titanium TA2 (1 mm)	ER4043 (φ 1.2 mm)	<ul style="list-style-type: none"> <li>• The EMF can influence the flowability and wettability of the filler metal on the surface of Al/Ti dissimilar metal joints. This joint is more dependable than that of conventional welding technique due to increase in bonding area and a decrease in wetting angle.</li> <li>• With the aided of EMF, the microhardness of HAZ is increased. The maximum tensile shear strength reaches up to 4.105kN, increasing by 93.4% compared to the conventional welding process.</li> </ul>
18.	<a href="#">Silvayeh et al., (2017)</a>	AA EN AW 6014 T4 (1.15 mm)	Galvanized dual-phase steel HCT 450X+ZE 75/75 (0.8 mm)	Six different aluminium-based filler wires (φ 1.20 mm)	<ul style="list-style-type: none"> <li>• Higher silicon content filler materials e.g., Al-3Si-1Mn which consist of 3% Si and 1% Mn, reduces IMC layer thickness by more than half as compared to high magnesium content fillers.</li> <li>• Scandium is the material which is known to lessen cracking of the weld seam and it also prevents cracking of the IMC layer (Al-4Mg-0.6Sc).</li> <li>• The CMT Braze+ torch is more favourable than the Robacta500 torch for minimization of the thickness of IMC layer, placing the torch closer to the work-piece tends to enhance the surface quality of the weld seam.</li> </ul>

19.	<a href="#">Madhavan et al., (2017)</a>	AA6061-T6 (2 mm)	AZ31B Magnesium alloy (3 mm)	Al-5 %Si ( $\phi$ 1.2 mm)	<ul style="list-style-type: none"> <li>The maximum tensile strength of 360 N/mm was attained at a heat input of 205 J/mm which is higher of the other heat input. At higher heat inputs, tensile strength increased due to high welding speeds which resulted in minimal HAZ.</li> <li>The thickness of the FZ increase from 3 to 12 <math>\mu</math>m with linearly increasing the heat input which shows that FZ is directly proportional to heat input. The thickness of FZ had a substantial consequence on the joint strength.</li> </ul>
20.	<a href="#">Li et al., (2018)</a>	AA6061-T6 (6 mm)	7N01-T4 (6 mm)	ER4043 ( $\phi$ 1.2 mm)	<ul style="list-style-type: none"> <li>Heat input increases during the CMT+P welding process with decrease in the CMT/P ratio which induces grain growth in WM. Equiaxed grains are formed in the HAZ on 6061 side whereas strip shape grains are observed in HAZ on 7N01 side which is retained after rolling.</li> <li>Due to silicon impurities, trend of micro-hardness on the 7N01 side were opposite of those on the 6061 side.</li> <li>Maximum tensile strength of the welded joint is about 60% of the strength of the 6061 substrate and it is observed that the HAZ on the 6061 side is the weakest part of the weld joint due to thermal cycling where fracture takes place in all the samples.</li> </ul>
IMC- Intermetallic compounds; FZ- Fusion Zone; WZ- Weld Zone; IML- Intermetallic layer; WFS- Wire feed speed; PWHT- Post Weld Heat Treatment; VP-CMT- Variable Polarity CMT; EP-CMT- Electrode Positive-CMT; EN-CMT- Electrode Negative-CMT; EP/EN- Electrode positive to Electrode negative ratio; EMF- External magnetic field; HAZ- Heat affected zone; CMT+P- CMT with pulse mode; CMT/P ratio- Ratio of number of CMT stages to P stages in one CMT+P cycle; WM- weld metal; AA- Aluminium alloy.					

**Table 2.3** Experimental results for butt joint using CMT welding process

<u>S.</u> <u>No</u>  :	<u>Source</u>	<u>SM 1</u>	<u>SM 2</u>	<u>Filler</u> <u>metal</u>	<u>Experimental results for butt joint</u>										<u>Fracture</u>
					<u><sup>a</sup>IMC</u>			<u>Thickness</u>  <u>of IMC</u> <u>(μm)</u>	<u><sup>b</sup>Micro-Hardness (HV)</u>					<u>TS</u> <u>(MPa)/</u>	
					<u>FZ 1</u>	<u>WZ</u>	<u>FZ 2</u>		<u>BM</u> <u>1</u>	<u>FZ</u> <u>1</u>	<u>WZ</u>	<u>FZ</u> <u>2</u>	<u>BM</u> <u>2</u>	<u>TL</u> <u>(kN)</u>	
1.	<a href="#">Jácome et al., (2009)</a>	AW518 2-H111 AA (1.5 mm)	DX54D steel (1 mm) Zn coating (14 mm)	Al <sub>99.5</sub> , AlSi <sub>5</sub> , AlMn <sub>1</sub> , and AlSi <sub>3</sub> Mn <sub>1</sub>	-	-	-	<4 μm	-	-	-	-	-	300 Mpa	Depends on the type of wire
2.	<a href="#">Shang et al., (2012)</a>	AA6061 (3 mm)	AZ31B Mg alloy (3 mm)	Pure copper (HS201) (φ 1.2 mm)	AlCu, CuAl <sub>2</sub> , Cu <sub>9</sub> Al <sub>4</sub>	Cu based solid solution like Al <sub>2</sub> CuMg, AlCuMg, Al <sub>5</sub> Cu <sub>6</sub> Mg <sub>2</sub> and Al <sub>7</sub> Cu <sub>3</sub> Mg <sub>6</sub>	Cu <sub>2</sub> Mg and Al–Cu–Mg ternary eutectic structure	-	35-40	260	115 - 140	362	50-55	34.7	FZ of Mg side



3.	<a href="#">Jing et al., (2013)</a>	AA6061 (3 mm)	AZ31B magnesium alloy (3 mm)	ER4043 ( $\phi$ 1.2 mm)	-	-	$\beta(\text{Mg}_2\text{Al}_3)$ , $\gamma(\text{Mg}_{17}\text{Al}_{12})$ and $\text{Mg}_2\text{Si}$	-	35	100	115	242	55	<20	FZ of Mg side
4.	<a href="#">Gungor et al., (2014)</a>	AA5083-H111 (6 mm)	AA6082-T651 (6 mm)	ER5183 ( $\phi$ 1.2 mm)	-	-	-	-	77	82	80	79	82	230	HAZ of 6082 base metal side
5.	<a href="#">Cao et al., (2014)</a>	Pure titanium TA2 (3 mm)	Pure copper T2 (3 mm)	ERCuNiAl copper wire ( $\phi$ 1.2 mm)	$\text{Ti}_2\text{Cu}$ , $\text{TiCu}$ and $\text{AlCu}_2\text{Ti}$	Cu–Al–Ti–Fe–Ni multiphase	$\alpha$ -Cu solid solutions	117–129 $\mu\text{m}$ in middle groove surface, and 80–100 $\mu\text{m}$ in root groove surface.	175	500	170	95	110	5.10 kN	II- Cu interface and Cu-HAZ III- Cu-HAZ III- Ti interface and Cu-HAZ

6.	Elrefaey and Ross (2015)	5182-O (2 mm)	6082-T4 (2 mm)	ER5356	Al <sub>3</sub> Mg <sub>2</sub>	Al <sub>3</sub> Mg <sub>2</sub> , Al <sub>3</sub> Fe and AlMg <sub>2</sub> Mn	Mg <sub>2</sub> Si	-	69	75	60	82	75	Max. 275	Within the weld
				ER4043					69	77	100	82	75		5182 BM
7.	Wang et al., (2016)	AA6061 (2 mm)	Mg alloy AZ31B (2 mm)	ER4043 (φ 1.2 mm)	-	Mg <sub>2</sub> Al <sub>3</sub> layer, Mg <sub>17</sub> Al <sub>12</sub> layer, and Mg <sub>17</sub> Al <sub>12</sub> + α-Mg solid solution eutectic layer	-	For EP/EN=1: 4-95 μm	-	-	125	310	55-60	37.2	IMC's layer
8.	Silvayeh et al., (2017)	AA EN AW 6014 T4 (1.15 mm)	Galvanized dual-phase steel HCT	Six different aluminium-based filler wires (φ	-	Al <sub>3</sub> Fe	Al <sub>5</sub> Fe <sub>2</sub>	Mg rich filler- >8. Scandium-containing fillers- 5-6 μm.	-	-	-	-	-	-	-

			450X+Z E 75/ 75 (0.8 mm)	1.20 mm)				Al-3Si- 1Mn filler alloy- <4 µm.							
9.	Li et al., (2018)	AA606 1-T6 (6 mm)	7N01- T4 (6 mm)	ER4043 (φ 1.2 mm)	α-Al phas es	α-Al phase, Al <sub>9</sub> Si phase, and a Fe <sub>0.9</sub> Si <sub>0.3</sub> phase	α-Al phases	-	85	70	75	115	120	194- 206	HAZ's on the AA6061- T6 side for all samples
<sup>a</sup> IMC- Intermetallic compounds; FZ1- Fusion Zone of substrate material 1; FZ2- Fusion Zone of substrate material 2; WZ- Weld zone; <sup>b</sup> BM1- Base metal or substrate material 1; BM2- Base metal or substrate material 2; TS - Tensile strength (MPa); TL - Tensile Load (kN); JI - Joint I; JII - Joint II; JIII - Joint III															

**Table 2.4** Experimental results for lap joint using CMT welding process

<u>S. No</u>	<u>Source</u>	<u>Substrate Material</u> <u>1</u>	<u>Substrate Material</u> <u>2</u>	<u>Filler metal</u>	<u>Experimental results for lap joint</u>									
					<u><sup>a</sup>IMC</u>		<u>Thickness of IMC</u> <u>(<math>\mu</math>m)</u>	<u><sup>b</sup>Micro-Hardness (HV/HM)</u>					<u>TS</u> <u>(MPa)/(N/mm)/TL</u> <u>(kN)/</u>	<u>Fracture</u>
					<u>WZ</u>	<u>Interface</u>		<u>BM</u> <u>1</u>	<u>FZ</u> <u>1</u>	<u>WZ</u>	<u>FZ</u> <u>2</u>	<u>BM</u> <u>2</u>		
1.	Wang et al., (2008)	Aluminium 1060 (1 mm)	Mg AZ31 (1 mm)	AlSi5 alloy wire ( $\phi$ 1.2 mm)	Mg <sub>2</sub> Al <sub>3</sub>	Mg <sub>17</sub> Al <sub>12</sub>	-	-	-	120	230 - 240	60	-	The typical cleavage and inter-granular fracture.
2.	Zhang et al., (2009)	Pure aluminium 1060 (1 mm)	Zn-coated Steel (0.6 mm)	Al-Si alloy wire ( $\phi$ 1.2 mm)	Fe <sub>2</sub> Al <sub>5</sub> and FeAl <sub>3</sub>	-	4	-	-	-	-	-	83MPa	-
3.	Yang et al., (2013)	AA6061-T6 (2 mm)	Zinc coated low-carbon steel (1.2 mm)	ER 4043 ( $\phi$ 1.2 mm)	FeAl <sub>3</sub> and Fe <sub>2</sub> Al <sub>5</sub>	-	<5	-	-	-	-	-	3.5-4kN	Mode I: HAZ close to the weld region Mode II: At the interface of both materials.

4.	<a href="#">Cao et al., (2013)</a>	AA6061-T6 (1 mm)	Mg AZ31B (1 mm)	Aluminum 4047 (φ 1.6 mm)	β-Al <sub>3</sub> Mg <sub>2</sub> , γ-Al <sub>12</sub> Mg <sub>17</sub> , and Mg <sub>2</sub> Si		-	-	-	125	360	85	-	At the γ-Al <sub>12</sub> Mg <sub>17</sub> , Mg rich IMZ
5.	<a href="#">Cao et al., (2013 A)</a>	AA6061-T6 (1 mm)	Galvanized mild steel (Q235) (1 mm)	Aluminum wires 4043, 4047, 5356 (φ 1.2 mm)	α-Al solid solution and Al-Si second phase.	Galvanized steel brazing interface: γ-Fe solid solutions, Fe <sub>3</sub> Al, FeAl <sub>2</sub> , FeAl <sub>3</sub> , Fe <sub>2</sub> Al <sub>5</sub> intermetallics, α-Al + Si eutectic compounds	5	-	-	-	-	-	-	-
6.	<a href="#">Lin et al., (2013)</a>	AA6061 (2 mm)	low carbon steel (0.7 mm)	ER4043 (φ 1.2 mm)	-	-	-	81.1	61	60.3	-	-	For 0.7 mm-kN	For 0.7 mm-interface

			mm and 1.2 mm)										For 1.2 mm>2.5 kN	For 1.2 mm-fusion line
7.	Cao et al., (2014 A)	Pure titanium TA2 (1 mm)	Pure copper T2 (1 mm)	ERCuNi Al copper wire ( $\phi$ 1.2 mm)	$\alpha$ -Cu solid solution and Ti-Cu-Al-Ni-Fe multi-phase	Ti <sub>2</sub> Cu, TiCu and AlCu <sub>2</sub> Ti	140-160	-	-	-	-	-	JI-197.5 N/mm. JII- 205.8 N/mm	Cu HAZ for both Joint I (top Cu sheet–bottom Ti sheet) and Joint II (top Ti sheet–bottom Cu sheet)
8.	Cao et al., (2014 B)	Pure titanium TA2 (1 mm)	Mg AZ31B (1 mm)	Mg AZ61 wire ( $\phi$ 1.2 mm)	$\alpha$ -Mg solid solution	Ti <sub>3</sub> Al, Mg <sub>17</sub> Al <sub>12</sub> and small Mg <sub>0.97</sub> Zn <sub>0.03</sub> phases	-	175	210	60	65	55	JI-2.10 kN JII-1.83 kN	-
9.	Kang & Kim, (2015)	Al 5052 alloy (1 mm)	Hot-dip aluminized (Al-coated)	Al 4043, Al 4047, Al 5356	Fe <sub>2</sub> Al <sub>5</sub> and FeAl <sub>3</sub>	Fe <sub>x</sub> (AlSi) <sub>y</sub>	For 4XXX filler wire- 3-4	-	-	-	-	-	Maximum for aluminized steel	HAZ for AlMg (Al 5356 and Al 5183) filler wires.

			steel sheet (1.2 mm)	and Al 5183 (φ 1.2 mm)			For 5XXX filler wire- 15- 22						with 5183 filler wire- 193 N/mm	WM for AlSi (Al 4043 and Al 4047) filler wires.
10.	Sun et al., (2017)	AA6061- T6 (2 mm).	Pure titanium TA2 (1 mm)	ER4043 (φ 1.2 mm)	Ti <sub>3</sub> Al, TiAl and TiAl <sub>3</sub> ,	TiAl <sub>3</sub> and Ti(Al, Si) <sub>3</sub>	Without EMF- 10	93	55	62	-	-	2.123 kN	Interface
							With EMF- 5	90	75	70	-	-	Maximu m 4.105 kN	Ti base metal
11.	Madha van et al., (2017)	AA6061- T6 (2mm)	AZ31B Magnesi um alloy (3mm)	Al-5 %Si (φ 1.2 mm)	Mg <sub>2</sub> Si, γ- Al <sub>12</sub> Mg <sub>1 7 and β- Al<sub>3</sub>Mg<sub>2</sub></sub>	Mg <sub>2</sub> Si and Al <sub>6</sub> Mn	3-12 With increase in heat input	65	95	110	200	80	Maximu m 360 N/mm at heat input 205 J/mm	-

<sup>a</sup>IMC- Intermetallic compounds; WZ- Weld zone;

<sup>b</sup> BM1- Base metal or substrate material 1; BM2- Base metal or substrate material 2; FZ1- Fusion Zone of substrate material 1; FZ2- Fusion Zone of substrate material 2; WZ- Weld zone; TS - Tensile strength (MPa); TL - Tensile Load (kN); JI - Joint I; JII - Joint II.

## 2.3 COMPARISON WITH OTHER WELDING TECHNIQUES

### 2.3.1 MIG Welding-Brazing

[Milani et al., \(2016\)](#) considered three different types of filler wires (AlSi<sub>3</sub>Mn, AlSi<sub>5</sub>, and AlSi<sub>12</sub> with  $\phi=1.2$  mm) for joining of AA5754 to galvanized steel (EX280) claiming the highest tensile strength of 188 Mpa with AlSi<sub>3</sub>Mn filler wire. [Pinto et al., \(2006\)](#) indicated that the porosity of the MIG-P was greater than that of the CMT weld. The heat-affected zone of the MIG weld is greater than the CMT and the laser hybrid welds. The residual stresses in the CMT weld are slightly lower compared to the MIG weld, especially on the bottom side of the weld. This can be attributed to the lower heat input in CMT process.

### 2.3.2 TIG Welding-Brazing

[Lin et al., \(2010\)](#) worked on butt welding-brazing of Al alloy and stainless steel with the help of Al-Cu6 filler wire and non-corrosive flux. It is found that the average thickness of IML is in the range of 3-5  $\mu\text{m}$  with 644.7 HV of micro-hardness. Weld bead and steel matrix has 104.5 HV and 200 HV of micro-hardness respectively. Tensile strength of the joint is found to be 172.5 MPa with fracture at IMC layer. [Dong et al., \(2012\)](#) investigated tensile strength and microstructure of the resultant joint by using different filler wire comprising of Si, Cu and Zn. Highest tensile strength is achieved is 136 MPa by Al12%Si and further controls the thickness of IML to about 2  $\mu\text{m}$ . It is concluded that the increase in Si content in the weld results in increase in tensile strength and decrease in thickness of IMC. This is because Si content into the weld could suppress the diffusion of Fe from the steel base plate into the weld.

### 2.3.3 LASER + MIG Welding-Brazing

[Qin et al., \(2014\)](#) investigated mechanical and microstructural properties of the brazed-fusion welded joint. Maximum tensile strength is achieved is 247.3 MPa with a fracture occurring at fusion zone. [Xue et al., \(2018\)](#) found maximum tensile strength of 200 MPa and 180 MPa for with and without reinforcement respectively.



## 2.4 SHIELDING GAS

Shielding gas is used to protect the arc column from outside impurities which helps in minimizing the weld defects. The significant properties of shielding gases are:

- Thermal conductivity
- Heat transfer properties
- Density relative to air
- Ease with which they undergo ionization

It majorly influences the arc stability, metal transfer mode, weld bead shape, molten droplet detachment, etc. [Praveen et al., 2005]. For visual checking of the weld, the effect of shielding gas is noticeable by the welder especially when welding non-ferrous metals. When sufficient shielding gas is being used and is protecting the weld adequately, then weld bead has a clean appearance and is spatter free. If insufficient shielding gas is used, there is a tendency for the weld bead to have surface porosity and ripples are disrupted [Little, 1994]. Fig. 2.1 shows the demonstration of weld bead samples with and without shielding gas.

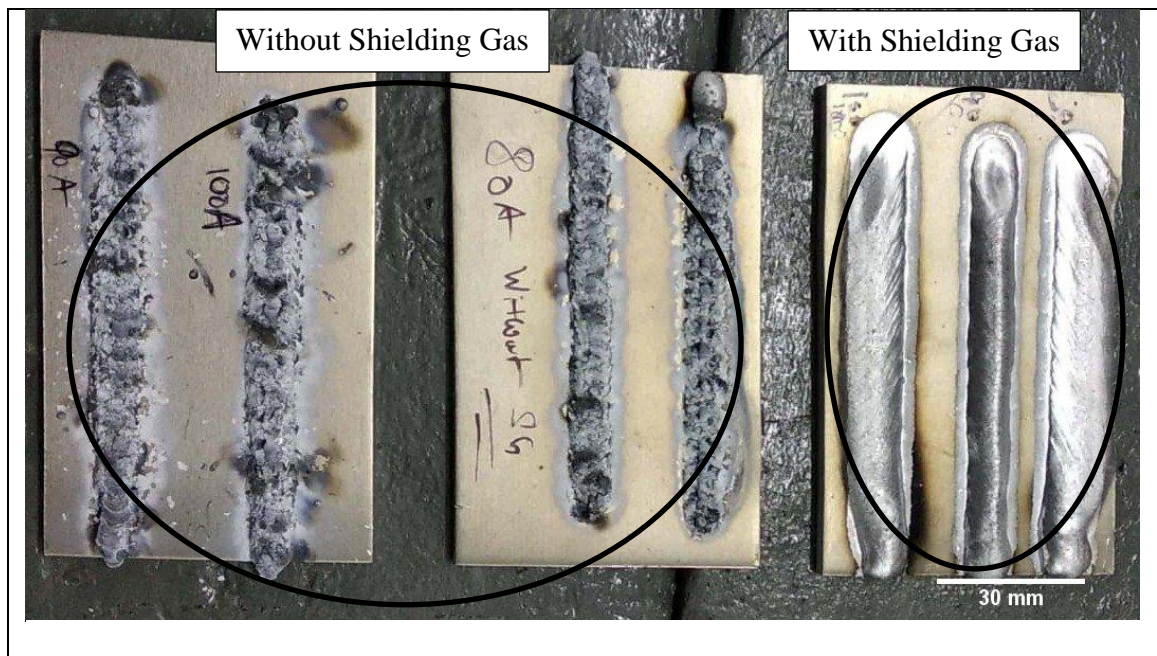


**Fig. 2.1** Demonstration of weld bead with and without shielding gas

Clean and proper weld bead aesthetics and a shiny outer surface having spatter-less weld could be seen with shielding gas. High oxidation weld bead (ER4043 wire), high amount of surface porosity and poor weld aesthetics are exhibited without shielding gas. Shielding gases can be used as pure like argon, helium, oxygen and carbon dioxide, or as a combination of these gases in dissimilar proportion.

#### 2.4.1 Argon

Argon is the principal inert gas used to join non-ferrous metals like Al, Mg etc [Lindberb, 1998]. Pure argon gases are used mostly as a shielding gas. It is denser than air so lower flow rates are sufficient to protect the arc column. Lower voltage is often used because of its lower electrical resistance, so it is good to use with short-circuiting welding and for thin sheets welding. Majority of the researchers worked on CMT have preferred argon gas over helium credited to its low thermal conductivity (16.94 mW/m K) which provides deeper finger-like penetration profile. It is denser than air (density 1.7818 g/dm<sup>3</sup>) results in lower flow rates. Lastly, it has low ionization potential (15.7 eV) facilitates better arc starting/stability which improves the quality of weld by lowering chances of spatter.

- Argon with Helium: Helium, when blended with argon offers a more liquid weld pool when contrasted with when just helium is utilized which eventually enhances and produces a flatter weld bead. In the greater part of the cases, a blend of 75 % argon and 25 % helium is recommended; great outcomes have been acquired with helium contents of 15 to 30 %.
- Argon with CO<sub>2</sub> and O<sub>2</sub>: Mixtures of these gases are generally used for the welding of mild steel. O<sub>2</sub> can be used up to 10 % because above that it will yield porosity in the weld bead.

#### 2.4.2 Helium

Helium is lighter or less dense gas than air so larger flow rates are required. It is an inert gas, which doesn't react with the molten metals as every inert gas has their outer electrons subshell completely full and is stable. Its 'thermal conductivity' is higher as contrasted to argon. Due to higher 'Ionization Potential' it generates a hotter arc at a higher voltage, provides wider and deeper bead [Little, 1994]; this is an advantage for aluminium

(Al), magnesium (Mg), and copper (Cu) alloys. Combination of both argon (5-10%) and CO<sub>2</sub> (2-5 %) with helium which is called as a "tri-mix" blends are used for stainless steel welding. Utilized for thicker welds in aluminum and other non-ferrous metals. In correlation with argon, helium offers more energy-rich but a less stable arc. Helium is utilized as a protecting gas in laser welding for CO<sub>2</sub> lasers. Helium costs more than argon and needs higher rate of flow, so it may not be an economical choice for higher volume production [Dawes, 1992]. Pure helium is not used for steel because it offers erratic arc and encourages spatter. Fig. 2.2 shows the comparison of argon and helium based on there characteristics.

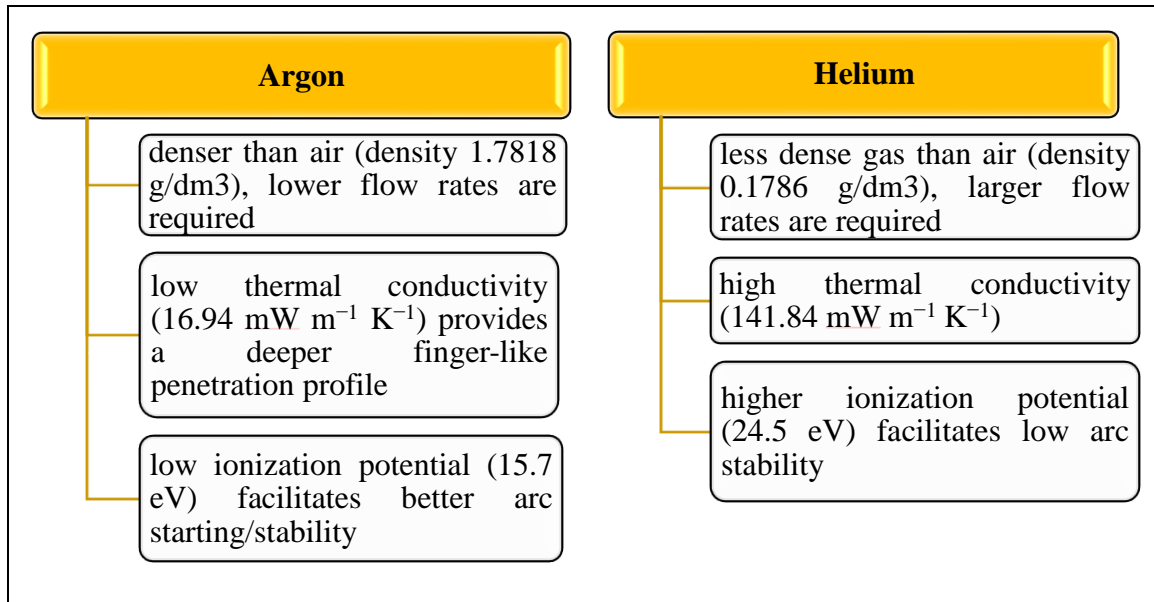


**Fig. 2.2** Comparison between Argon and Helium as shielding gas

#### 2.4.3 Carbon-di-oxide

Carbon dioxide (CO<sub>2</sub>) is used for fusion of ferrous metals because of its inexpensiveness, providing deep penetration but the major disadvantage is that it adversely affects the steadiness of the arc and increases the tendency to spatter. Using CO<sub>2</sub> for welding application, should only be used when it is completely dry or free from all the moisture content. Since moisture content in CO<sub>2</sub> liberates hydrogen which creates porosity in the metal that is being welded. Heat generated in the arc column results in the

development of a low amount of oxygen in the metal, which reduces the nominal test strength of the metal. When the oxygen molecule is released from CO<sub>2</sub>, the gas that is formed in the outer shielding portion of the shielding gas is carbon mono-oxide (CO) which is a toxic gas [Little, 1994]. CO<sub>2</sub> in a lower concentration of approximately 1-2% is generally used with a combination of Argon to reduce the surface tension of the molten metal.

Argon having many characteristics over helium and carbon-di-oxide such as lower arc energy, penetration and spatter and higher arc stability.

## **2.5 RESEARCH GAP**

- Researchers have not explored in the field of dissimilar alloy joining with different thickness using CMT process.
- Although some of the authors have considered the variety of work-piece material (substrate), filler metal, shielding gases at different flow rates, etc., but not all the welding parameters and their interactions are together analyzed.
- Limited advancements in CMT welding.

## **2.6 RESEARCH OBJECTIVES**

From the literature survey the research gaps are identified. Accordingly, the following objectives are formulated:

- To study the effects of various process parameters (i.e. voltage, current, wire feed rate, welding speed and flow rate of shielding gas) on weld bead geometry and strength of the processed joints.
- To determine the optimal parameters for welding of dissimilar aluminium alloy joints using Cold Metal Transfer process via Response Surface Methodology (RSM).
- To characterize the joints by metallographic study such as Field Emission Scanning Electron Microscope (FESEM) and Optical Microscope (OM).
- To study of mechanical properties of welded metals such as micro-hardness, tensile behavior and residual stresses.
- To perform comparative analysis between CMT and MIG welding.

## 2.7 FLOW CHART FOR PRESENT WORK

Flow chart gives the summarized version of the detailed work. Fig. 2.3 shows the flow chart of the present work which includes step by step procedure or methodology carried out during this work.

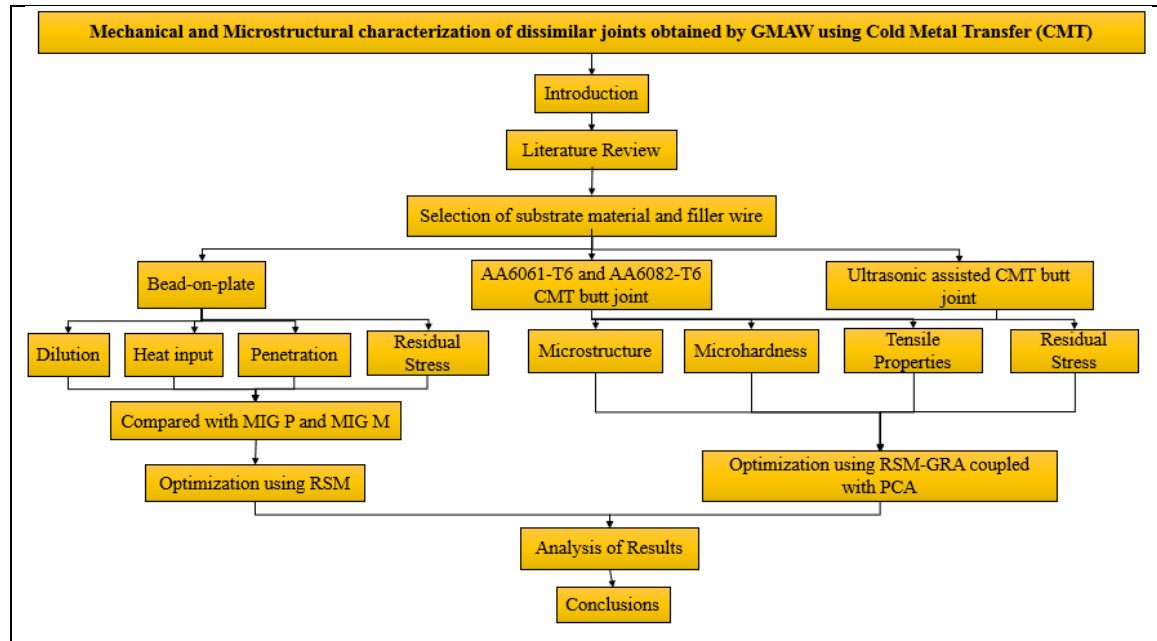


**Fig. 2.3** Flow chart of present research work

This research is primarily emphasizing on CMT welding's such as CMT process used during bead on plate, butt welding of different alloys of aluminium, microstructural behaviour, mechanical properties, optimization in pursuit for optimal process parameters and application of ultrasonic vibrations in CMT butt joints.

## 2.8 SUMMARY

This chapter presents a detailed review for joining dissimilar materials or alloys on the basis of welding parameters and types of joint such as butt and lap joint on CMT welding machine. Major conclusions are highlighted for joining of dissimilar materials on CMT welding machine. For aluminium alloys the major conclusions are, the optimum welding parameters depends on the type of substrate chosen, type of filler metals, environmental

conditions and shielding gases. Current less than 100 A, for lower thickness material, welding speed ranges from 4 to 10 mm/sec and flow rate of shielding gases ranges from 15 to 20 L/min with argon. In CMT welding, different wire types used were the most governing process parameter. Mechanical properties deteriorate due to softened zone in HAZ. The microhardness exhibits inversely proportional relationship with the grain size of various zones. Post weld heat treatment (PWHT) shows positive results in context of mechanical properties. For aluminium and steel the major conclusions are, current in range of 50 to 75 A, voltage in 10 to 15 V, welding speed in 6 to 10 mm/sec, wire feed rate in 50 to 100 mm/sec with filler wire size of 1.2mm and flow rate of shielding gases in 15 L/min with argon. Zinc coating on the steel surface controls the formation of brittle  $Al_xFe_y$  in the IML. Silicon (Si) composition in the filler metal primarily influences the IMC layer thickness. Higher Si content filler wire reduces IMC layer thickness by more than half as compared to high magnesium content fillers. Minimum the thickness of IMC layer, the better will be the joint strength of the weld. For aluminium and magnesium the major conclusions are current in range of 70 to 150 A, voltage in 10 to 13 V, welding speed in 4 to 10 mm/sec, wire feed rate in 70 to 100 mm/sec with filler wire size of 1.2 mm and flow rate of shielding gases in 15 to 18 L/min with argon. The fracture occurred in the fusion zone of Mg side at the highest value of micro-hardness. There were significant amounts of Mg-rich intermetallic  $\gamma-Al_{12}Mg_{17}$  and  $\beta-Al_3Mg_2$  in the weld joint which degraded the weld strength. The Mg-rich intermetallic should be minimized to improve the joint. Fusion zone is directly proportional to heat input. The thickness of fusion zone had a substantial consequence on the joint strength. For titanium and other materials the major conclusions are current in range of 150 to 220 A, voltage in 14 to 20 V, welding speed in 6 to 8 mm/sec, wire feed rate in 80 to 150 mm/sec with filler wire size of 1.2 mm and flow rate of shielding gases in 15 to 17 L/min with argon. Comparison with other welding techniques are also discussed such as MIG, TIG and LASER welding on joining of thin sheets. Types of shielding gases with their detailed comparison are also presented. Research gap and research objectives are formulated. Flow chart is also presented for the existing work.



## CHAPTER 3 : EXPERIMENTAL SETUP & PROCEDURE

---

### 3.1 MATERIAL SELECTION

#### 3.1.1 Substrate / Base Material

Aluminium alloys of grade AA6082-T6 and AA6061-T6 were chosen of thickness 2 mm and 3.18 mm respectively for joining with the help of CMT welding machine. These sheets have proved to have one of the widest ranges of alloys which happens to be heat treatable alloy being attained through artificial aging at a low temperature of nearly 180 °C for 2 hours until it reaches a stable condition. This increases strength to a greater level after solution heat-treating quicker than natural aging with considerable improved toughness and great enhancement in resistance of corrosion. Aluminium alloys, specifically 6082-T6 and 6061-T6 are high strength Al-Mg (0.636 & 0.840)-Si(1.06 & 0.665) alloys that contain manganese (0.745 & 0.0676) to increase ductility and toughness used in trucks, canoes, railroad cars, furniture, pipelines etc. The raw images of the substrate material is displayed in the Fig. 3.1.

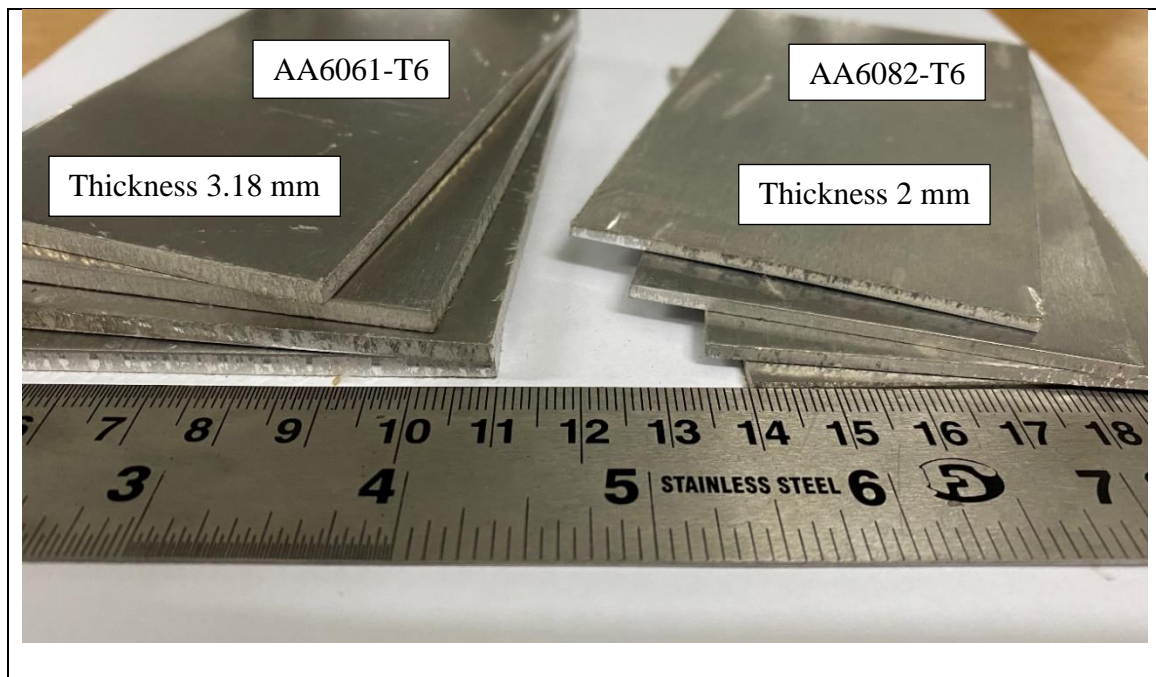


**Fig. 3.1** Substrate material as purchased

Table 3.1 displays the chemical compositions (wt. %). of substrate materials obtained by chemical spectroscopy as per ASTM E 1251:2011. Microstructure of substrate material is shown in Fig. 3.2 which clearly shows the grain boundaries/structure (elongated grains). Mechanical properties of substrate material is tested as per ASTM and presented in Table 3.2. Stress vs strain curve of substrate materials are shown in Fig. 3.3.

<b>Table 3.1</b> Chemical compositions (wt%) obtained by chemical spectroscopy of substrate materials as per ASTM standards									
Elements	Al	Cu	Zn	Si	Mg	Fe	Mn	Cr	Ti
AA6082-T6	Bal.	<0.003	0.0045	1.06	0.636	0.189	0.745	0.009	0.0184
AA6061-T6	Bal.	0.153	0.0226	0.66	0.840	0.253	0.068	0.178	0.0225

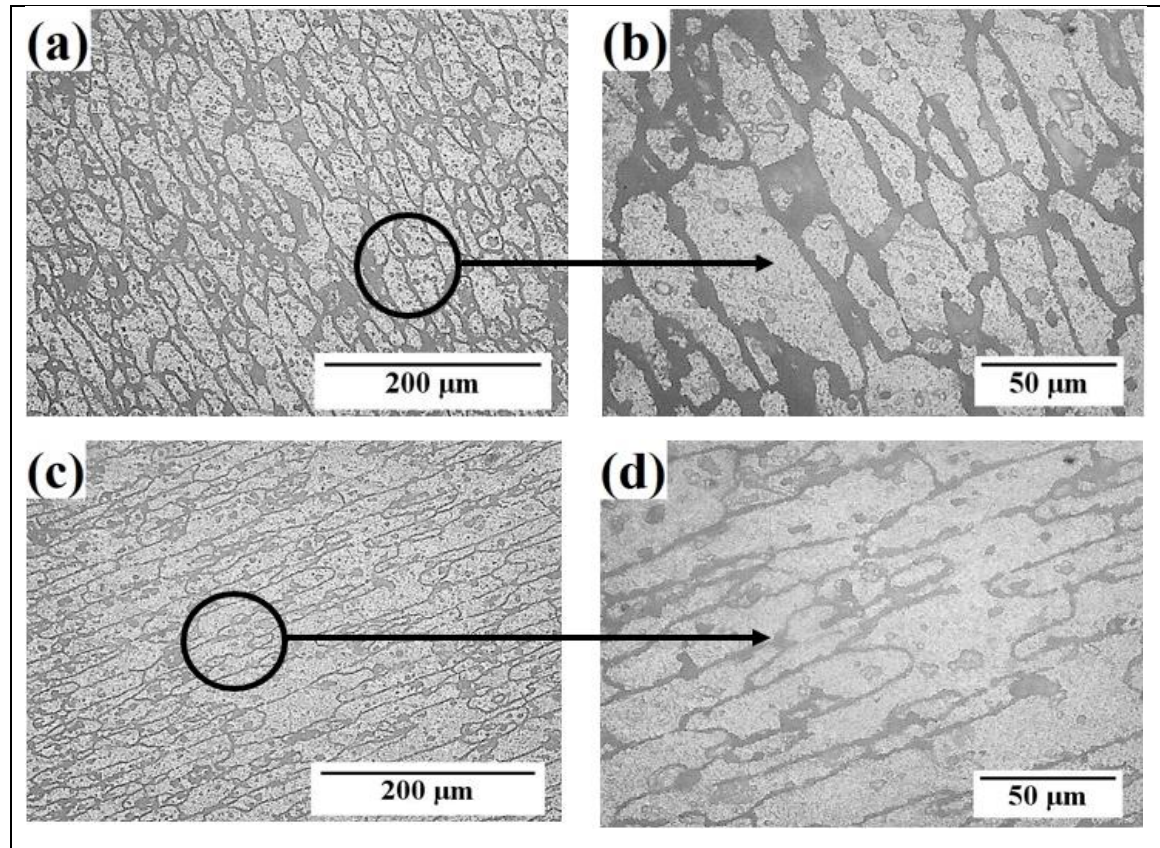


**Fig. 3.2** Microstructural images by optical microscope (a) AA6061-T6 (b) Magnified view of AA6061-T6 (c) AA6082-T6 (d) Magnified view of AA6082-T6



<b>Table 3.2</b> Mechanical properties of substrate material					
Properties	$\sigma_{0.2}$ (MPa)	$\sigma_{UTS}$ (MPa)	$\delta$ (%)	HV <sub>0.3N</sub>	Y (GPa)
AA6082-T6	269	304	20.1	109±9	90±7
AA6061-T6	247	284	24.9	116±9	97±4

$\sigma_{0.2}$  – Tensile strength (TS) at 0.2% offset;  $\sigma_{UTS}$  – Ultimate tensile strength (UTS);  $\delta$  – Elongation; HV<sub>0.3N</sub> – Vicker’s microhardness at 300 grams load; Y – Young’s modulus.

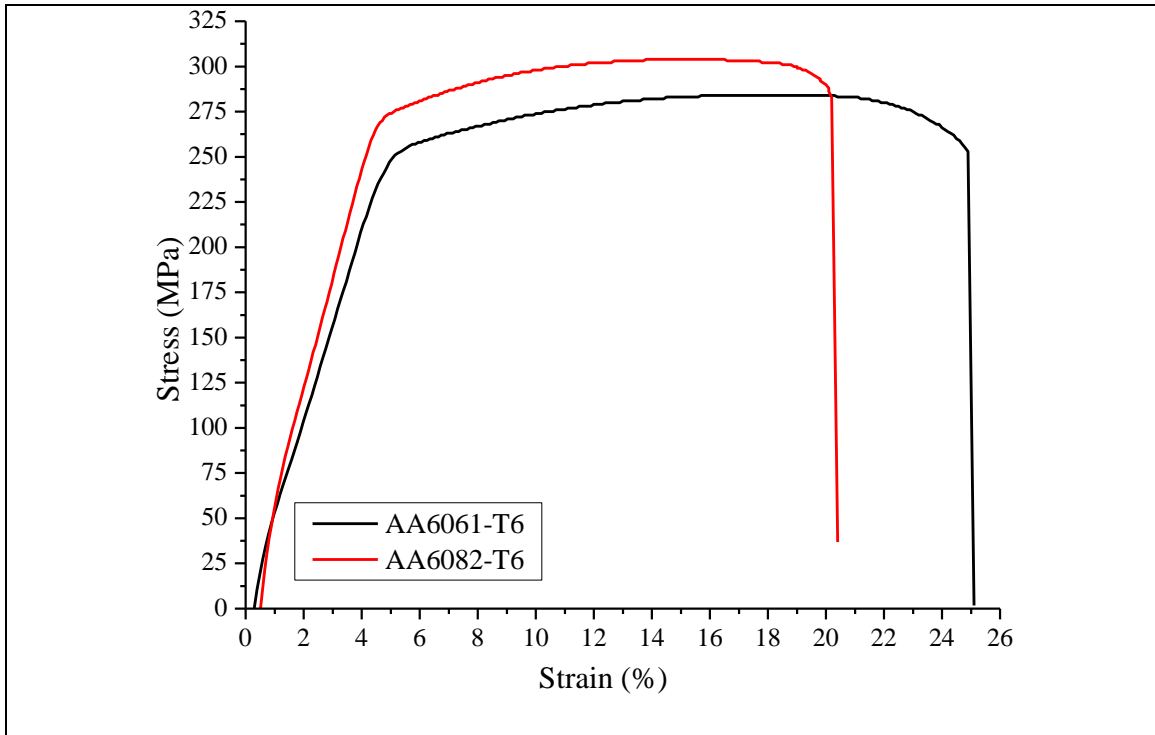


**Fig. 3.3** Stress vs strain curve of substrate material

XRD plots for parent materials are presented, which constitutes its primary elements at various intensity as shown in Fig. 3.4. FESEM images are displayed in Fig. 3.5 showing grain equiaxed grains in AA6061-T6 and elongated grains in AA6082-T6 along the rolling direction.

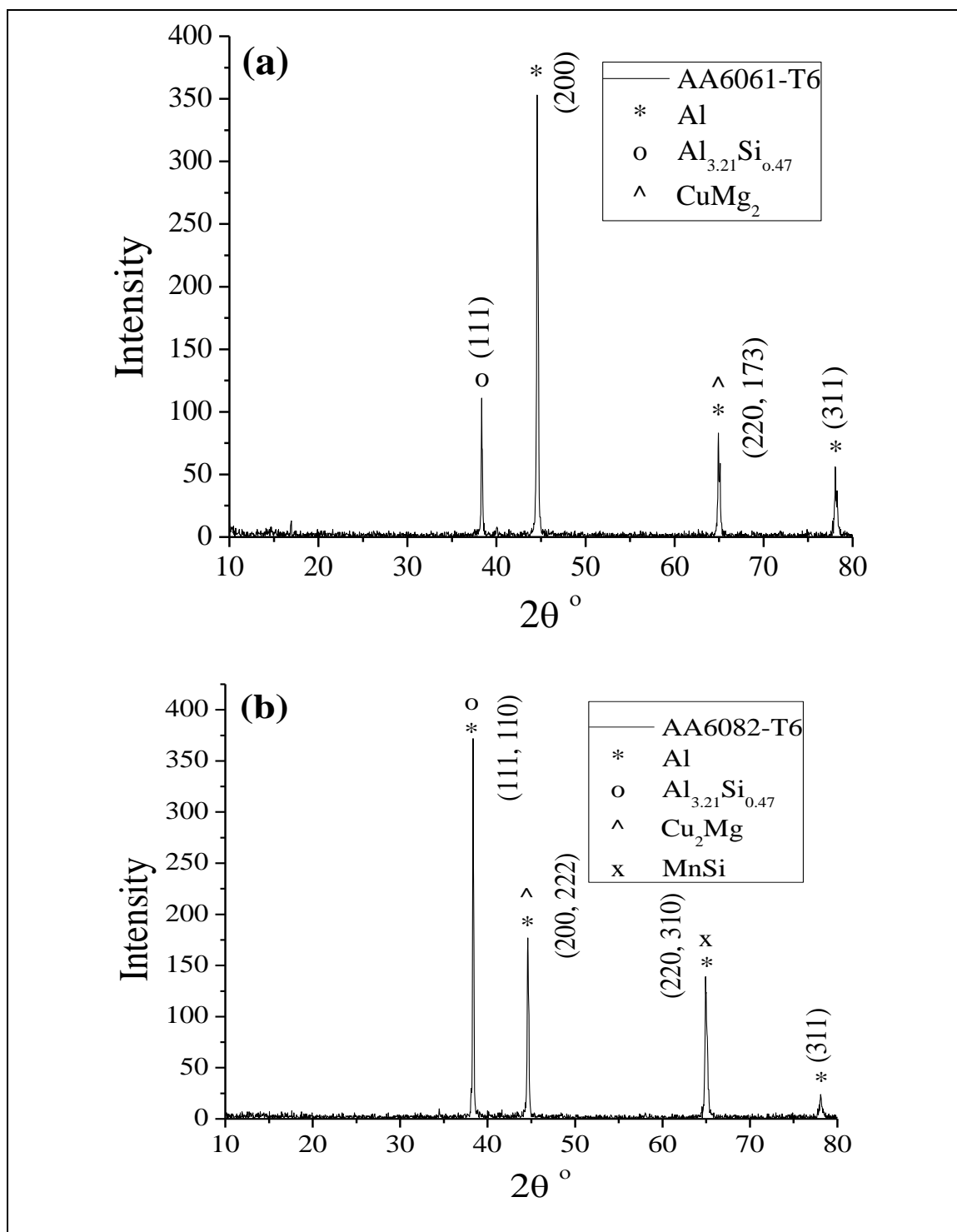


**Fig. 3.4** XRD plots (a) AA6061-T6 (b) AA6082-T6

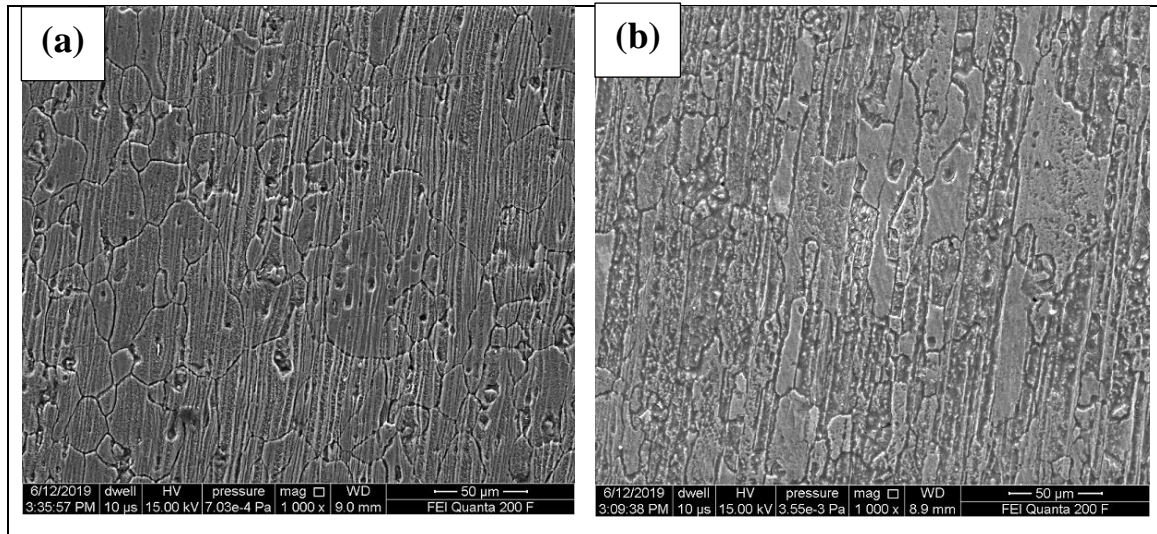


**Fig. 3.5** FESEM images (a) AA6061-T6 (b) AA6082-T6

### 3.1.2 Filler Material

ER4043 (Al-Si5%) having 1.2 mm diameter filler wire is used for this welding process. This filler wire is readily compatible with 6XXX aluminium alloys as reported in the literature survey and extensive trial tests. Table 3.3 shows the chemical compositions (wt. %). of filler material obtained by chemical spectroscopy as per ASTM E 1251:2011. The silicon particles are uniformly distributed in the aluminium wire which is clearly seen in the enlarged view at different magnification as black spots in Fig. 3.6. Microhardness of filler wire is 75 HV as measured experimentally by the vicker's microhardness machine.

<b>Table 3.3</b> Chemical composition (wt.%) of filler wire as per ASTM standards									
Material	Al	Cu	Zn	Si	Mg	Fe	Mn	Cr	Ti
ER4043	Bal.	0.3	0.10	5.6	0.05	0.8	0.05	0.05	0.02

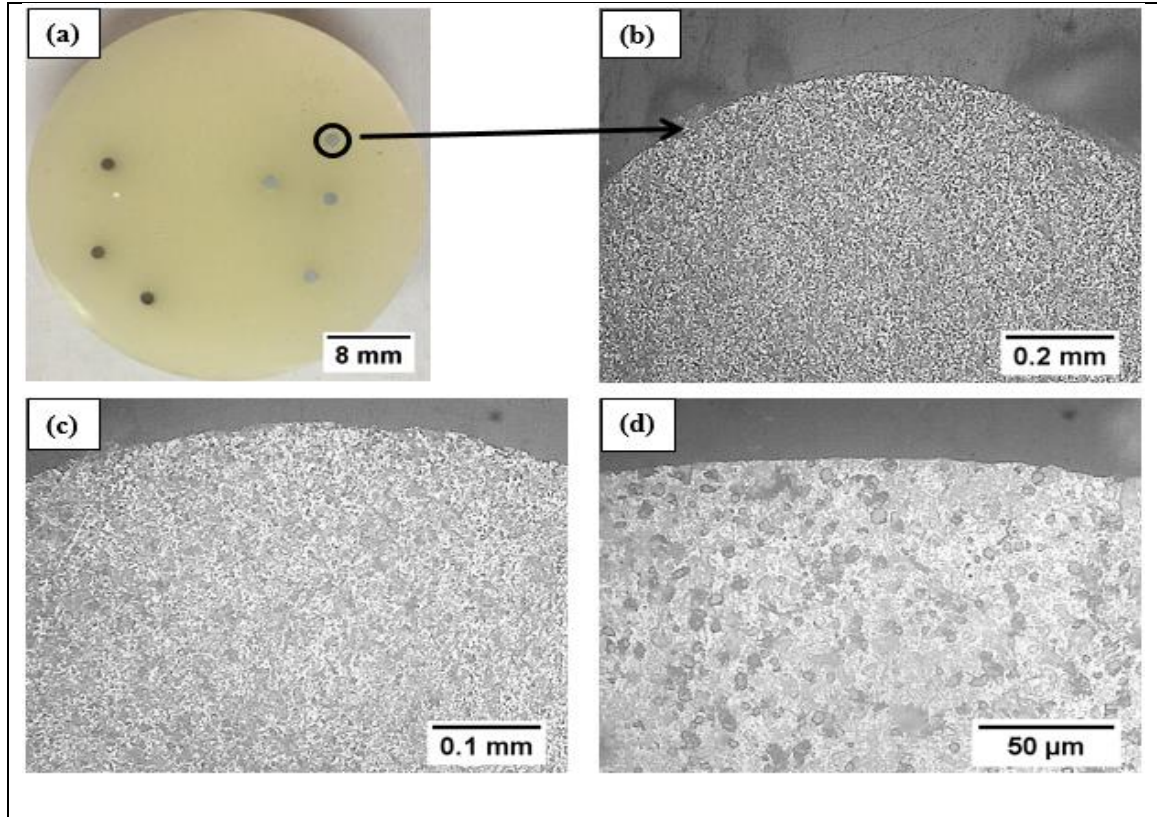


**Fig. 3.6** (a) Cold mounting of Filler wire (b) Microstructure at 0.2mm (c) Microstructure at 0.1mm (d) Microstructure at 50 μm of filler wire

## 3.2 SAMPLE PREPARATION

### 3.2.1 Macrostructure Characterization

Macrostructure depicts the geometry or dimensions of the weld bead. These dimensions are important to be measured to understand the insight view of the bead geometry that helps in the overall cost of the welding. Specimens were prepared by taking out the 15 x 15 mm square piece from the weld bead. Then the cross-sectional surface of the weld bead was polished with the help of the emery paper of grade 100, 320, 400, 600, 800, 1000, 1200, 1500, 1800, 2000 and 2500. Only dry polishing is needed to explore the macrostructure of the weld bead. Macrostructure reveals the bead geometry as shown in Fig. 3.7 which includes weld reinforcement (WR), weld penetration (WP), weld width (WW) and contact angle (CA).

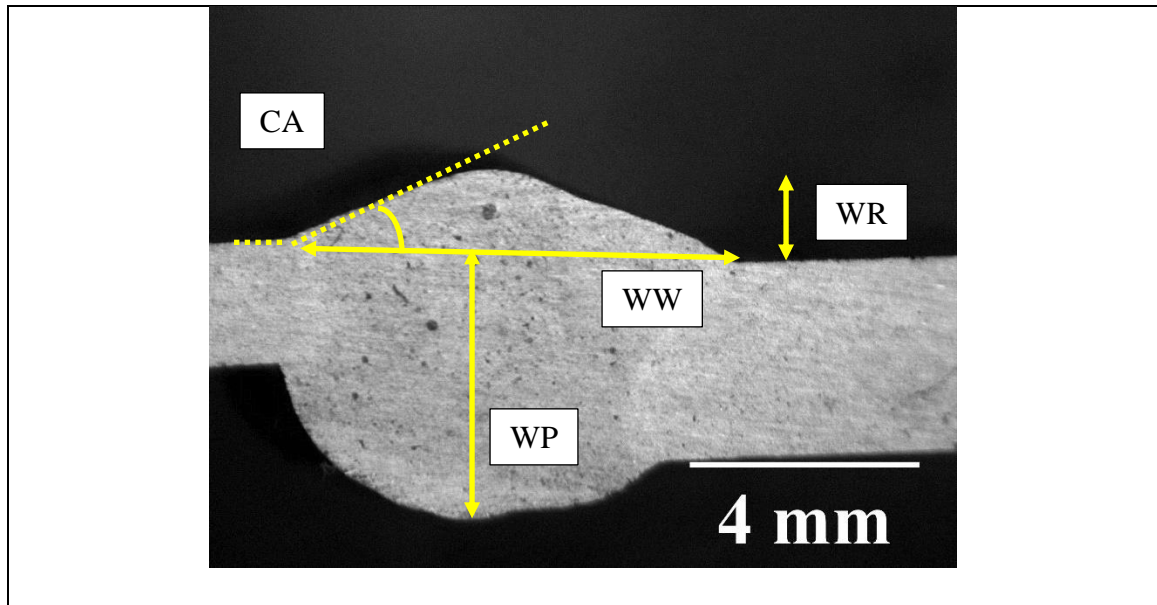


**Fig. 3.7** Macrostructure specimen of the weld bead

### 3.2.2 Microstructure Characterization

Microstructure characterization reveals the information about the grain structure, grain boundaries, grain size etc. The optical microscope is used as the main instrument to characterise the metal's internal grain structure. Samples were prepared by taking out the 15 x 15 mm square piece from the weld bead. The cross-sectional phase was mounted in a bakelite powder with using a hot mounting press at 135°C for 20 minutes. Then these samples were allowed to cool in the mounting press for 15-20 minutes. Now the cross-sectional surface of the weld bead undergoes dry polishing with the help of the emery paper of grade 100, 320, 400, 600, 800, 1000, 1200, 1500, 1800, 2000 and 2500. Then velvet emery paper was used for wet polishing with the help of alumina powder. After dry and wet polishing, the samples were dried using a hot air blower. Keller's reagent (1ml HF, 1.5 ml HCl, 2.5 ml HNO<sub>3</sub> and 95 ml of water for 20 second) was used for the AA6061-T6 and AA6082-T6 for revealing the microstructure. After etching with keller's reagent, the samples were allowed to dry using a hot air blower and seen under an optical microscope. Fig. 3.8 shows the step by step sample preparation for microstructure characterization.





**Fig. 3.8** Steps of sample preparation for microstructure characterization

### 3.2.3 Microhardness

Microhardness is a mechanical property which gives the indication of hardness of material at micron level. It is resistant to indentation. The surface was prepared for microhardness testing by following steps:

- The hardness specimen initially dry polishing was implemented via different grade of emery papers (180, 320, 400, 600, 800, 1000, 1200, 1500, 2000 and 2500)
- Then wet polishing is carried out via velvet cloth using different grades (I, II & III) of alumina powder.

Surface was polished so that, the indenter's diagonal is easily seen for accurate measurement as seen in the Fig. 3.9.

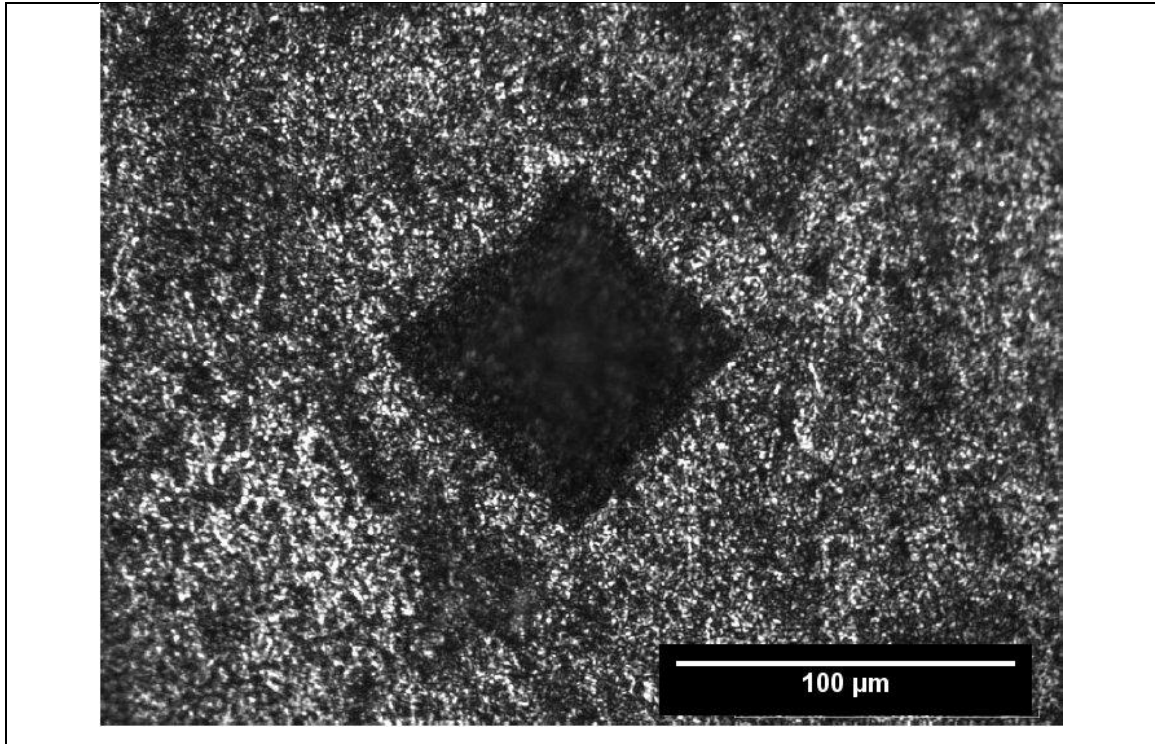


**Fig. 3.9** Microhardness indentation on aluminium sample

#### 3.2.4 Tensile Testing

The strength of the material undergoing a basic lengthening operation is determined by tensile testing. The key use of the testing machine is to produce the curve of stress-strain and the curve of load vs displacement. The tensile test is used to determine the mechanical properties of the material under tested. The conclusion of tensile tests can be used for engineering applications in the selection of materials. Tensile properties are commonly involved in material specifications to assure quality. Specimens were cut by wire-EDM (Electrical Discharge Machine) as per the ASTM E8 standard as presented in Fig. 3.10. In this work, a single sheet size is 100 mm x 60 mm which is to be butt weld with the same size of the sheet for different thickness. After the welding, the total fabricated sample is 100 mm x 120 mm in size with 120 mm for cross-sectional side. Due to this, a sub-size tensile specimen (100 mm length of tensile specimen) is preferred over the full-size tensile specimen (200 mm).

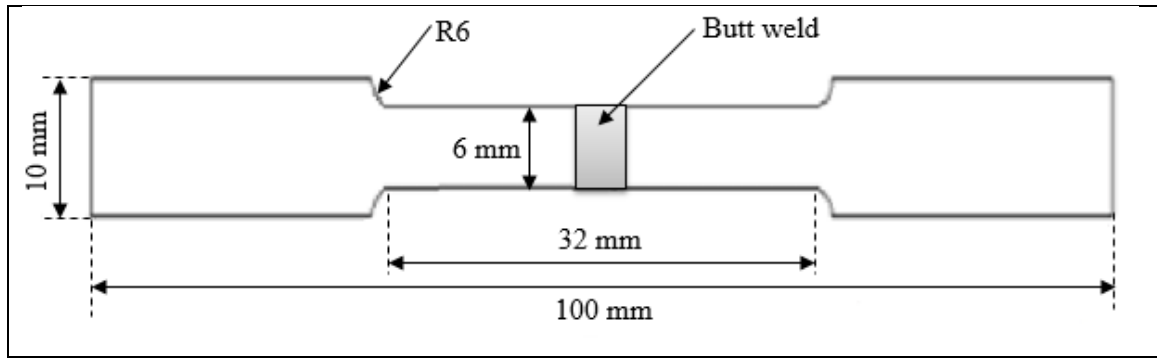


**Fig. 3.10** Tensile Specimen as per ASTM E8

### 3.2.5 Residual Stress

Specimens for residual stress measurement were cut using a wire EDM machine of size 10 mm x 10 mm. Then the crosssectional surface is dry polished using a waterproof emery paper (180, 320, 400, 600, 800, 1000, 1200, 1500, 2000 and 2500) of different grades.

## 3.3 EXPERIMENTAL MACHINES

### 3.3.1 CMT Machine

CMT machine is an advanced version of GMAW machine. TPS400i CMT machine (Fig. 3.11) is used in this research work and its technical specification is presented in Table 3.4. The overall time of CMT welding would be  $1/4^{\text{th}}$  in a short-circuit phase where the maximum current tends to almost zero. It greatly reduces the cost of welding and energy consumption by 30%-40%. This is achieved by the combination of high-speed digital process control (DPC) and wire buffer [Pickin et al., 2011]. When short-circuit happens in the short-circuiting phase, DPC immediately gives signal to the wire buffer to retract the filler wire with the help of synergic power source which automatically reduces the amount of current during this phase. This reduction in current helps in low thermal heat input (THI), negligible spatter, minimal distortion, low dilution etc. [Cao et al., 2013; Cao et al., 2014; Wang et al., 2008; Lorenzin & Rutili 2009 and Lin et al., 2013].



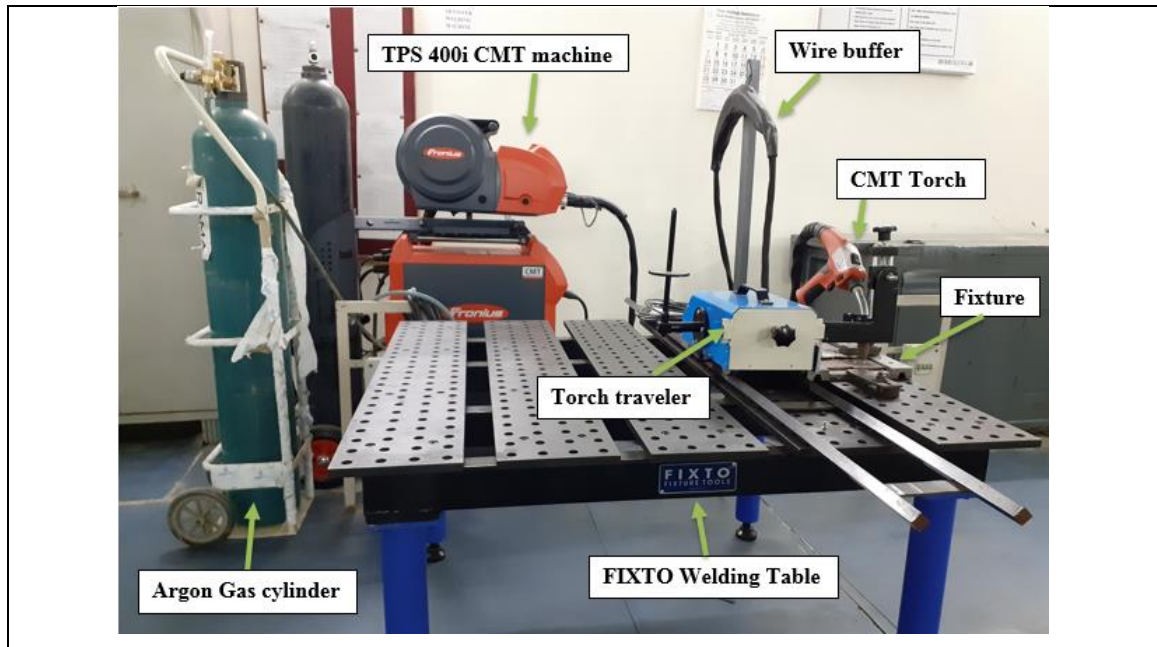


**Fig. 3.11** TPS400i CMT machine

<b>Table 3.4</b> Specification of CMT machine		
Specifications	Units	Range
Maximum / minimum welding current	A / A	400 / 3
Welding current / Duty cycle [10 min/40°C]	A / %	400 / 40
Welding current / Duty cycle [10 min/40°C]	A / %	360 / 60
Welding current / Duty cycle [10 min/40°C]	A / %	320 / 100
Operating voltage	V	14, 2-34, 0
Open circuit voltage (OCV)	V	73
Mains frequency	Hz	50-60
Mains voltage	V	3 x 400
Mains fuse	A	35
Dimension / b	mm	300
Dimension / l	mm	706
Weight	kg	36, 45
Degree of protection	-	IP23

Direct current electrode positive (DCEP) is implemented in this CMT machine where welding torch which consists of wire electrode is coupled with the positive terminal of CMT power source and the base metal (BM) is coupled with the negative terminal, it is also recognized as direct current reverse polarity (DCRP). DCEP/DCRP is implemented because the electrons flowing from the negative terminal (workpiece) to the positive terminal (electrode wire) in the arc column helps in the uniform deposition. As the distance from the electrode to the base metal is much closer (i.e. CTWD), so larger number of metal ions are mixed into the plasma arc column. These positive ions attracted to the base metal, which strikes the same in a much hotter condition. This results in more heat liberation in the BM compared with wire electrode tip helps to increase penetration. Direct current electrode negative (DCEN) results in thicker welds with an unstable arc and frequent arc outages. In CMT welding of synergic lines, voltage (V), current (I) and wire feed speed (WFS) are inter-related to each other i.e. by changing one of the above parameters the rest two also changes. Arc length correction (ALC) is the factor, which corrects the arc length (i.e. allows even more precise control of heat input). It ranges from “-10% to +10%”. The negative range is applied when shorter arc length is needed that gives narrow weld bead with higher penetration by reducing the voltage. The positive range is applied when longer arc length is needed that gives wider weld bead with lower penetration by increasing the voltage. Zero is for neutral arc length (i.e. without any change in the correction factor). Pulse dynamic correction (PDC) is for correcting the pulse energy during pulsed arc welding or modulating the frequency of pulses per second. It ranges from “-10% to +10%”. The negative range is for lower droplet detachment force/energy that reduces the arc length by keeping the stickout distance same. It reduces the pulse time and current that increase the frequency of pulses per second. This increases the penetration by forming a narrow weld bead. The positive range is for increased droplet detachment force/energy that increases the arc length by keeping constant stickout distance. It increases the pulses time and current that reduces the frequency of pulses per second. This decreases the amount of penetration by providing wider weld bead. Zero is for neutral droplet detachment force.

### 3.3.2 Tensile Testing Machine

The material used for engagement in engineering applications are advised on the basis of their mechanical properties such as tensile strength, percentage elongation etc. Such properties are induced by tensile testing. The tensile properties are always documented for a new material as they help in stabilising the new material against the available options in the market. The tensile strength of a material is governed by various attributes, some of the prominent attributes are listed below.

- **Molecular structure:** Intermolecular forces are directly dependent on the molecular structure hence even a slightest change in the molecular arrangement will affect the outcome of tensile strength.
- **Temperature:** With the rise in temperature, tensile strength of the metal increases up to a point beyond which the properties start depreciating.
- **Composition:** Different composition leads to different arrangement of molecular structure and there is difference in the level of molecular binding hence effecting the ultimate tensile strength (UTS) of the material.

The tensile strength of the material can only be quantified by the performance of testing on the material. Tensile testing of a material is done by subjecting the material on Universal Testing Machine (UTM) as shown in Fig. 3.12 (Tinius Olsen H50KS) and its technical specification is presented in Table 3.5. The specimen for the same is prepared according to the standard specified in ASTM-E8, to procure the sample help of wire EDM was taken. The dimension of the sample for tensile testing can be seen in Fig. 3.10 which was prepared when produced look like dog bone in shape. At room temperature, the tensile tests performed on the processed samples are tested at a constant cross-head speed of 1 mm/min.

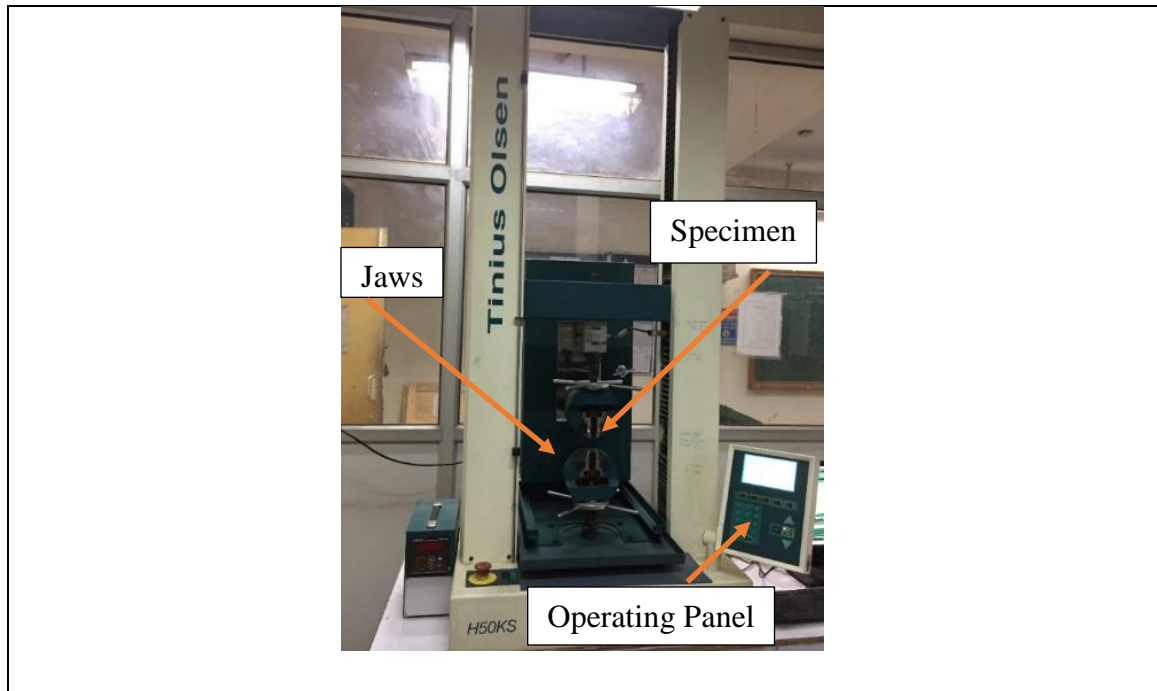


**Fig. 3.12** Tensile machine (Model: Tinius Olsen H50KS)

<b>Table 3.5</b> Specification of Tensile Testing Machine		
Capacity	kN/Kg	50/5000
Clearance between columns	mm	405
Load cells	-	Rapid change, low profile Z type load cells with digital encoding for automatic recognition.
Maximum crosshead travel	mm	1100
Testing speed range	mm/min	0.001-500
Capacity at maximum speed	kN	25
Maximum speed at capacity	mm/min	250
Jog speed	mm/min	0.001-500
Return speed	mm/min	0.001-500
Dimensions (H x W x D)	mm	1613 x 720 x 500
Weight	Kg	140

### 3.3.3 Microhardness Machine

Microhardness Testing is a technique used to determine hardness or resistance to penetration of the material under study. Microhardness is tested when test samples are very small or thin, or whether small regions in a welded sample need to be measured. The microhardness analysis is done on an Struers Duramin-40 as shown in Fig. 3.13 and its technical specification is presented in Table 3.6.

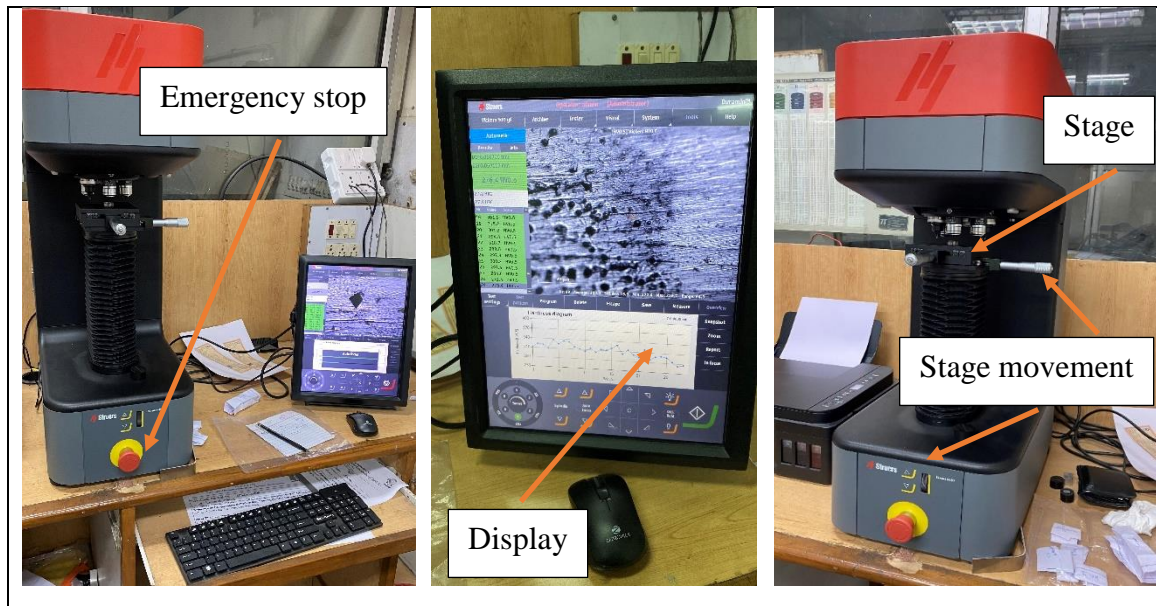


**Fig. 3.13** Microhardness testing machine (Struers Duramin-40)

A Vickers diamond indenter is pressed into the surface of the material with a penetrator and a light load (300 grams) during the microhardness test. When a load is applied on the material it penetrates on indentation causing permanent deformation on the surface if the material in the shape of the indenter. The test is performed under controlled condition by monitoring pressure for a given time segment (20 seconds of dwell time), for a diamond indenter that is square in shape. The resulting diagonal due to indentation on the material surface is measured and with the help of formula to calculate the Vickers hardness value.

<b>Table 3.6</b> Specification of Microhardness testing machine (Struers Duramin-40)	
Model	Duramin-40 M1
Loads and Applications	
Load Range (Main Loads)	10 gf – 10 kgf
Vickers Capability	Yes
Knoop Capabiblity	Yes
Brinell Capability	Yes
Stages and Turrets	
XY-stage	Manual
XY-stage or anvil size (mm)	90 x 90
XY-stage stroke, max (mm)	25 x 25
Vertical capacity	172
Throat depth (mm)	170
Motorized Z-axis	Yes
Motorized turret	Yes
Turret positions	6
Anti-collision protection	Yes
Machine weight	101 kg
Camera and Optics	
Evaluation camera resolution	18 MP
Auto illumination	Yes
Stage illumination	Yes
Laser or LED guider	Yes
Interfaces and Connectivity	
Operation	Embedded Windows 10 PC with 15 inch touch screen.
Communication Ports	HDMI, VGA, RJ45, WLAN, USB, RS232
Wifi	Yes
Bluetooth	Optional

### 3.3.4 Optical Microscopy

Optical microscopy is done on olympus GX41 compact inverted metallurgical microscope as shown in Fig. 3.14 and its technical specification is presented in Table 3.7. The inverted metallographic microscope GX41 is suitable for fast and reliable characterization of specimens and for determining whether metallurgical properties comply with production requirements. Portability is facilitated by its compact and lightweight body. Mobility and Ergonomics, Ergonomic Eyepoint Adjustment and Excellent Image Quality and Excellent Resolution with Brightfield and Polarized Illumination are three special characteristics.

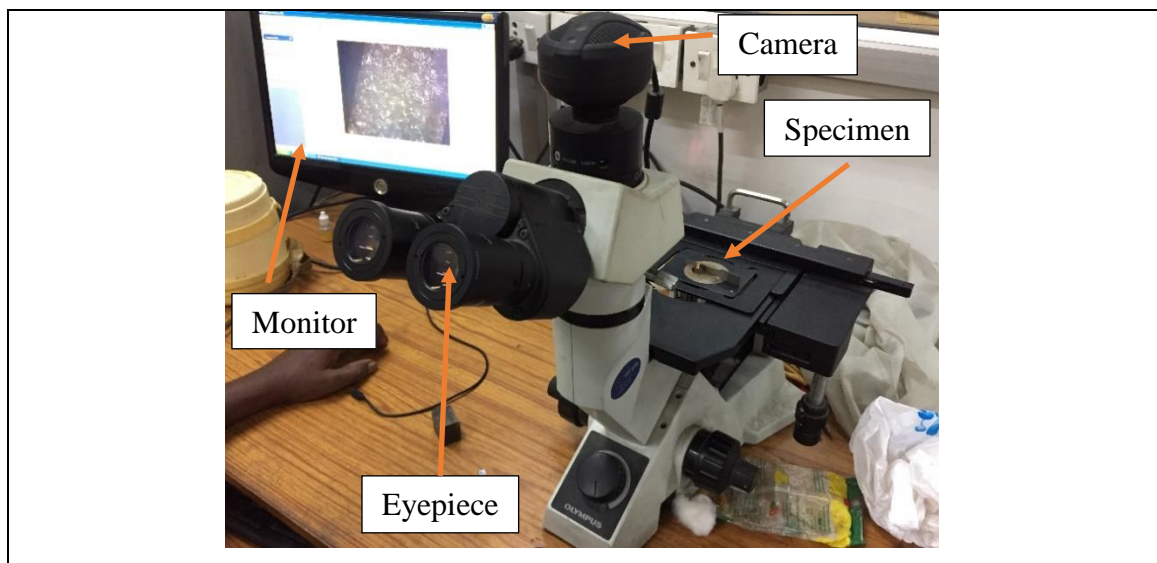


**Fig. 3.14** Olympus GX41 compact inverted metallurgical microscope

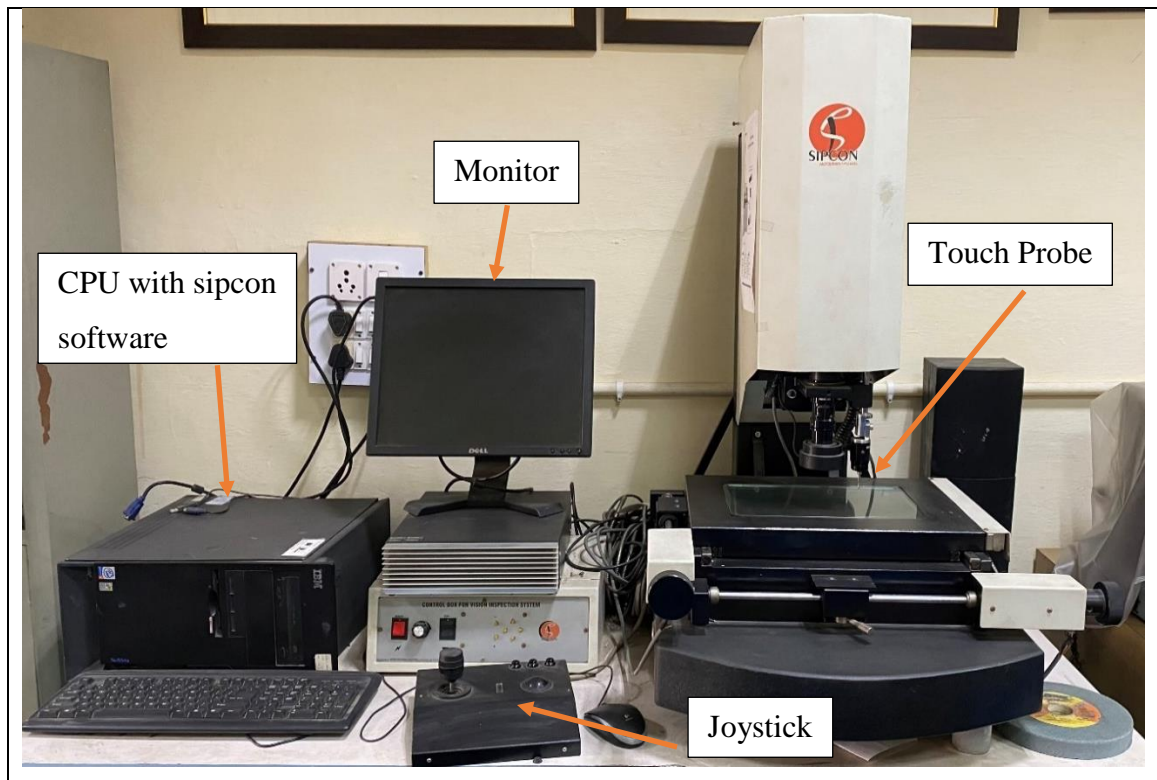
A compact body means mobility and ergonomics. Compact body can be mounted in a small space and is also portable, satisfying the requirements either in the laboratory or alongside the manufacturing line for on-the-spot inspection. A Tilting Binocular Observation Tube provides an ergonomic Eyepoint Adjustment that helps the user to use the GX41 either while standing or seated and offers a comfortable working atmosphere. For Brightfield and Polarized Illumination, Superior Image Quality and Excellent Resolution provide clear, bright observation at any magnification. This is due to infinity-corrected UIS2 optics, which allow high-clarity observation with excellent images filling the entire field of view (F.N.22). On both bright-field and clear polarising observations, objective magnifications range from 5x to 100x.

Table 3.7 Specifications of Optical Microscope			
Optical System			UIS2 Optical System (Infinity-corrected)
Microscope Frame	Observation Method		BF/KPO*
	Reflected/Transmitted		Reflected
	Illuminator		-
	Illumination System	Reflected light	30W Halogen or Fiber Light Guide(Light source:100 W)
		Transmitted light	-
	Focus	Motorized/Manual	Manual Revolving Nosepiece Up/Down Movement (Stage Stationary Type)
		Stroke	9 mm
		Resolution/Fine adjustment sensitivity	Fine Stroke per Rotation 0.2 mm
	Revolving Nosepiece	Motorized type	-
		Manual type	Quadruple for BF
Stage	Stroke		120(X)x78(Y) mm
Observation Tube	Standard Field (Field number 18)	Inverted Image	Tilting Binocular Observation Tube
	Standard Field (Field number 20)	Inverted Image	Binocular/Trinocular/Tilting Binocular Observation Tube
	Wide Field (Field number 22)	Inverted Image	Binocular/Trinocular/Tilting Binocular Observation Tube
		Erect Image	-
Dimensions			236(W) x 624(D) x 407(H) mm
Weight			10 kg (in Standard Combination)



### 3.3.5 Vision Inspection Machine

Vision inspection machine is done with the help of sipcon multi sensor CNC inspection system as shown in Fig. 3.15 and its technical specification is presented in Table 3.8. It has some unique features like superior performance and robust construction, longer service life with low maintenance, low power consumption and CNC inspection system. It has 3 measuring technologies in one i.e. vision, touch probe and laser. Vision offers highest through put in flat non-contact measurement, most accurate microscopic parts measurements and quick to capture even the smallest details. Touch probe gives the best solution for 3-D measurements, perfect solution for non-pliable parts and application includes 3-D measurements of metal processed parts like apertures, included angle etc. Laser gives highest accuracy in depth measurements, best for surface contouring and surface scanning and lastly its application include complex contouring of moulds and measurements of soft and flexible components.



**Fig. 3.15** Sipcon multi sensor CNC inspection system

<b>Table 3.8</b> Specification of Vision Inspection Machine	
Model No.	SVI-5300-CNC-VT
Software	QC-5300-VED-CNC/MSU-25D-CNC
Measuring range	200 x 150 x 100 mm
Resolution	0.005/0.001/0.0005 mm
Linear Accuracy	(3+L/200) micron
Repeatability	+/- (0.002 mm)
Vision	1/3" High Resolution CCD Camera
Magnification	Optical Magnification 0.7x – 4.5x
Video Edge Detection	Standard
Optional Hardware	PC P4 + 17" TFT Monitor
Illumination Surface	Fibre Optic/LED
Illumination Contour	Halogen Lamp/LED
Operation	Manual with quick release knob & CNC
Base Platform and Column	Granite
Platform Load Capacity	30 Kg
Power Supply	220 – 240V, 50/60 Hz
Motion control through joystick	Standard
Programmable light control	Optional
Autofocus	Optional
Touch	Renishaw TP-8

### 3.3.6 Field Emission Gun Scanning Electron Microscope

Field Emission Scanning electron microscopy (FESEM) is done with the help of electron-optical column as shown in Fig. 3.16 and its technical specification is presented in Table 3.9. The electron beam, or electron probe, that is employed to pursue the image should be as small as possible, typically it is kept around 10 nm. The electron probe diameter is directly influencing the resolution of the image obtained by FESEM process. The process by which the electron probe covers the whole specimen is known as raster scanning. During the scanning the accelerated electrons are bombarded on the specimen, on interaction with the specimen they are scattered. The scattering phenomena is observed as elastic and inelastic in nature of electron interaction.



**Fig. 3.16** Field Emission Gun Scanning Electron Microscope (FEG-SEM) (Model: FEI QUANTA 3D FEG)

The image formed after the scanning can be of differing brightness in response to the electron bombardment. Secondary electrons and backscattered electrons are responsible for the differing brightness, which can be easily differentiated according to their kinetic energy and the latter having greater energy. Images generated using the secondary electron are showing only the surface structure and nothing regarding the

underlying structure is known only topographical contrast is displayed. Backscattered electron images on the other hand has depth, providing information under the topography of the specimen, as the information is generated by the signals coming from half the penetration depth. They are known to show contrast in the images on the basis of the chemical composition of the specimen (Egerton, 2005).

<b>Table 3.9</b> Specification of FESEM machine	
Electron optics	High-resolution FESEM column optimized for high brightness/high current
Ion optics	Magnum ion column with Ga liquid metal ion source with a lifetime of 1500 hours
Electron beam resolution	- 1.2 nm @ 30 kV @ high vacuum mode - 1.5 nm @ 30 kV @ ESEM mode - 1.5 nm @ 3 kV @ low vacuum mode
Ion beam resolution	10 nm @ 30 kV @ 1pA
Accelerating voltage	200V to 30 kV for electron beam imaging and 5 to 30kV for ion beam imaging
Detectors	Everhardt-Thornley SED, Low-vacuum SED, Gaseous SED, IR-CCD, EDS detector and Gaseous BSED
Specimen stage	4-axis motorized eucentric goniometer stage X = 50 mm, Y = 50 mm, T = -15 +75°(manual), Z = 50 mm (25 mm motorized), rotation = 360° continuous

### 3.3.7 X-Ray Diffraction

Diffraction patterns are observed due to scattering of light by a recurring array with long range order thus generating an interference constructive in nature. Such constructive interference is observed only on some specific angles. The analysis of the XRD driven data is done to spot trends which correspond to the directionality in the crystal structure, which is further analysed by the miller indices of the peaks in diffraction pattern. The wavelength

used for the X-ray and the distance between the atoms is almost similar. A diffraction pattern is observed when X-rays are scattered on interacting with the atoms, this pattern helps us with the information regarding the atomic arrangement in the crystal. Bruker D8 advanced machine is used for XRD spectrum as shown in Fig. 3.17 and its technical specification is presented in Table 3.10.



**Fig. 3.17** X-Ray diffraction (Model: BRUKER D8 ADVANCED)

Diffraction peaks observed on the XRD are associated with the plans of atoms. Diffraction peaks formed are related to the planes of atoms, which assist in analysing of the atomic structure and microstructure. Now the determination the position of the diffraction peaks is done with the help of Bragg's law ( $n\lambda = 2 d_{hkl} \sin\theta$ ).  $d_{hkl}$  is the distance between the crystal (parallel) planes of atom.  $\theta$  is the angle between the beam which is incident and the normal to the lattice where reflection has taken place.  $\lambda$  is the wavelength and  $n$  is the order of reflection (an integer). Bragg's law helps in identification of the angle at which diffraction peaks are observed due to constructive interference formed by the scattered X-ray from the crystal planes of atoms. The intensity of the diffraction peaks and their position are dependent on the crystal structure, i.e. the arrangement of atoms in periodic array in the entire crystal.

<b>Table 3.10</b> Specification of XRD machine	
X-ray	
Source	2.2 kW Cu anode long fine focus ceramic X-ray tube
Running Condition	40 kV and 40 mA
X-ray Beam Shaping Optics	
Beam [Cu-K <sub>α1</sub> ]	Collimated, compressed and frequency filtered by a Göbel mirror and V-Groove
Collimated beam dimensions	0.3 mm by 11 mm
Göbel mirror	60 mm multilayer X-ray mirror on a high precision parabolic surface
Goniometer	
Maximum and minimum measurement circle diameter	250 mm & 100 mm
Smallest angular step size	0.0001°
Reproducibility	+/- 0.0001°
Maximum rotational speed	1500 °/min
Angular range (Theta)	-5° to 40°
Angular range (2Theta)	-10° to 60°
Reflectometry Sample Stage	
Samples size	200 mm in diameter and 50 mm thick
Detector	
Maximum count rate	2 x 10 <sup>6</sup> s <sup>-1</sup> (although it should not be exposed to in excess of 5 x 10 <sup>5</sup> s <sup>-1</sup> for periods longer than about 1 second)
Detector electronics count rate	3 x 10 <sup>7</sup> s <sup>-1</sup>

### 3.3.8 Residual Stress Measurement Machine

Pulstec  $\mu$ -X360n Full 2D High-Resolution x-ray Diffraction (HR-XRD) machine is used for measurement of residual stresses at various position of the weldment as shown in Fig. 3.18 and its technical specification is presented in Table 3.11.



**Fig. 3.18** Pulstec  $\mu$ -X360n Full 2D High-Resolution X-ray Diffraction (HR-XRD) machine

Device specification contains a standard Cr x-ray tube (30 kV and 1mA) with a collimator size of  $\phi$  1 mm and measurement conditions. It is based on  $\text{Cos}\alpha$  method, which acquire a full Debye-Scherrer ring (reveals grain orientation (texture) & grain coarsening, etc); by a single short duration x-ray exposure from a 2-D detector [Kumar et al., 2018]. It is a faster process because it does not require sample tilts at multiple angles as compared to traditional  $\sin^2\psi$  technique. In this method, x-ray exposure is upto 1  $\mu\text{m}$  into the material and measure the fundamental atomic plane spacing and difference in spacing as a result of processing. This measured lattice spacing is collected by Debye ring with a single measurement using a 2D detector.

<b>Table 3.11</b> Specification of Residual stress machine	
X-ray tube	30 kV & 1 mA (Safety & Ecology)
Collimator size	φ 1 mm (φ 0.04 inch)
X-ray detector	Full 2 D (visual analysis)
Precision mech.	Not necessary
2D Full data of Debye-Scherrer ring	Max. 500 points
Cos $\alpha$ line Data	Max. 125 points
Permissible range	±5 mm (easy setting)
Measurement time	90 sec.
Portable	Air cooling, Goniometer not required
Sensor unit weight	4 kg (8.8 lbs) (Z height stage)
Power supply unit weight	6 kg (13.2 lbs)

### 3.4 OPTIMIZATION OF CMT PROCESS PARAMETERS

Nowadays, design of experiments (DOE), computational techniques and optimization techniques are primarily used to obtain mathematical relationship in finding the optimal parameters and verify the results using simulation software. The DOE is a systematic procedure to investigate the relationship between factors affecting a process and to determine the response of that process.

#### 3.4.1 Response Surface Methodology

Response surface methodology (RSM) is mostly used for the modeling and analysis of several independent variables influence a dependent variable and is to optimize the response [Montgomery, 2017]. Central composite design (CCD) is used to find the significance of the model for the DOE. CCD under RSM is accomplished by using Design Expert (DE).



In the response surface design analysis the independent variables like  $x_1, x_2, \dots, x_n$  influence a dependent variable  $Y$  or response, and the aim is to optimize the response. The bead geometry and mechanical properties of bead-on-plate and CMT butt joints respectively depend upon various factors like travel speed / welding speed (mm/sec), current (A) and shielding gas flow rate (L/min), CTWD, stick-out distance, filler wire material, welding torch angle, type of shielding gases, diameter of filler wire, etc. The response function representing the weld geometry is expressed as shown in equation 3.1 as there are only two independent variables are choosen.

$$Y = \varphi (A, B) \quad (3.1)$$

Where  $Y$  represents the responses,  $\varphi$  is the response function and  $A$  and  $B$  are the input variables like current and welding speed respectively. The relationship between responses and independent variables is achieved by incorporating them into the general polynomial equation of second order as shown in equation 3.2.

$$Y = b_0 + b_1x_1 + b_2x_2 + b_{12}x_1x_2 + b_{11}x_1^2 + b_{22}x_2^2 \quad (3.2)$$

Where  $Y$  represents the responses,  $b_0$  is an intercept,  $b_1$  and  $b_2$  represents the coefficient values for linear effects,  $b_{12}$  represents the coefficient values for interaction effects,  $b_{11}$  and  $b_{22}$  are the coefficient values for quadratic effects,  $x_1$  and  $x_2$  are the coded levels for independent variables like current (A) and welding speed (B).

In CMT butt joints, three independent variables are choosen such as current, welding speed, and shielding gas flow rate. So, the response function representing the CMT butt joints is expressed as shown in equation 3.3.

$$Y = \varphi (A, B, C) \quad (3.3)$$

Where  $Y$  represents the responses,  $\varphi$  is the response function and  $A, B$  and  $C$  are the input variables like current, welding speed and shielding gas flow rate respectively. The

relationship between responses and independent variables is achieved by incorporating them into the general polynomial equation of second order as shown in equation 3.4.

$$Y = b_0 + b_1x_1 + b_2x_2 + b_3x_3 + b_{12}x_1x_2 + b_{23}x_2x_3 + b_{31}x_3x_1 + b_{11}x_1^2 + b_{22}x_2^2 + b_{33}x_3^2 \quad (3.4)$$

Where Y represents the responses,  $b_0$  is an intercept,  $b_1, b_2$  and  $b_3$  represents the coefficient values for linear effects.  $b_{12}, b_{23}$  and  $b_{31}$  represents the coefficient values for interaction effects.  $b_{11}, b_{22}$  and  $b_{33}$  are the coefficient values for quadratic effects,  $x_1, x_2$  and  $x_3$  are the coded levels for independent variables like current (A), welding speed (B) and shielding gas flow rate (C).

### 3.4.2 Grey Relation Analysis (GRA)

In 1982 Ju-Long began the GRA based on the theory of grey systems [Ju-Long, 1982]. This technique is useful for effectively shedding light on the complex interrelationships between the multi-response variables into a single GRG [Wang, 1996].

*Step 1: Normalizing:* Due to the avoidance of various units and to decrease the uncertainty, the data is first to be normalized. As the variance of one information differs from other data, it is essentially required. From the original value, an appropriate value is extracted to render the array between 0 and 1 [Haq et al., 2008]. It is, in general, a way to transform the original data to a comparable data. Smaller-the-better features are intended to scale it into an appropriate range for normalization if the response is to be reduced and vice versa through the following formulas.

$$X^*_{i^*}(k) = \frac{\max xi(k) - xi(k)}{\max xi(k) - \min xi(k)} \quad (3.5)$$

$$X^*_{i^*}(k) = \frac{xi(k) - \min xi(k)}{\max xi(k) - \min xi(k)} \quad (3.6)$$

Where,  $i = 1, 2, \dots, m$ ;  $k = 1, 2, \dots, n$ ; the number of experimental data is 'm' and the number of responses is 'n'.  $xi(k)$  signifies the original sequence,  $Xi^*(k)$  signifies the order after preprocessing or normalizing the experimental data,  $\max xi(k)$  constitutes the largest  $xi(k)$  value,  $\min xi(k)$  constitutes the smallest  $xi(k)$  value and 'x' is the anticipated value

[Tosun and Pihtili, 2010]. Equation 3.5 stands for smaller-the-better whereas larger-the-better is obtained by equation 3.6.

**Step-2: Deviation Sequence:** After completing the normalizing process, the next step is to compute the deviation sequence ' $\Delta_{oi}$ ' (i.e. in the array of 0 to 1), which is obtained using the following formula (equation 3.7) from the normalized values.

$$\Delta_{oi} = || X_o(k) - X_i(k) || \quad (3.7)$$

where  $X_o(k)$  is the maximum value in the normalized column (i.e. 1) for a specific response and  $X_i(k)$  denotes the original sequence of that specific response.

**Step-3: Grey relation coefficient (GRC):** After normalizing and deviation sequence, the major step in GRA analysis is finding the GRC as per equation 3.8.

$$\xi_i(k) = \frac{\Delta_{min} + (\xi * \Delta_{max})}{\Delta_{oi}(k) + (\xi * \Delta_{max})} \quad (3.8)$$

where  $\Delta_{oi}(k)$  is the deviation sequence which is obtained using equation 3.7;  $\Delta_{min}$  (i.e. 0) and  $\Delta_{max}$  (i.e. 1) is the minimum and maximum value of the deviation sequence at a specific response respectively;  $\xi$  is in the range of 0 to 1, it is an identification or distinguishing coefficient which is usually taken as 0.5 for GRA analysis.

**Step-4: Grey relation grade (GRG) with rank:** Now grey relation grade (GRG),  $[\gamma_i(k)]$  is determined which is the average value of the GRC of all the response for a specific process parameter and is calculated with the help of equation 3.9. The highest value of GRG corresponds to 1<sup>st</sup> rank while lowest GRG value corresponds to the last rank.

$$\gamma_i(k) = \frac{1}{n} \sum_{k=1}^n \xi_i(k) \quad (3.9)$$

where GRG  $[\gamma_i(k)]$  indicates the degree of association between the values of the output response and the organization of likeness.

*Step 5: Optimal level of process parameters:* From equation 3.9, the highest value of GRG with rank 1 is considered to be the optimal GRG which indicates the optimal level of process parameters that gives better product quality.

*Step 6: ANOVA table for GRG:* The next step is to use the ANOVA table for GRG to find out the significant parameters influencing the multi-response at a 95 % confidence level. Significant parameter is identified by checking the p-value on the ANOVA table. If the p-value is less than 0.05 the process parameter is significant and vice versa.

*Step 7: Confirmation runs:* Confirmation runs are needed for reliability checks and also for the level of GRG improvements. With the optimal process parameters, minimum of 3 experiments were performed and their results were analyzed and compared with the predicted confirmation run at optimal level which is calculated by equation 3.10.

$$\gamma_t = \gamma_m + \sum_{i=1}^o (\gamma_o - \gamma_m) \quad (3.10)$$

where  $\gamma_t$  is the GRG value predicted confirmation run at an optimal level;  $\gamma_m$  is the total mean GRG and  $\gamma_o$  is the GRG value of a specific process parameter at an optimal level.

### 3.4.3 Principal Component Analysis (PCA)

A multivariate statistical analysis method was first introduced by [Pearson \(1901\)](#) and further developed by [Hotelling \(1933\)](#), which is also known as the dimensionality reduction technique. It begins with a multi-response array with 'n' investigations with 'm' characteristics. After the estimation of the normalized value  $X_i^*(k)$  from equation 5 or 6 and deviation sequence  $\Delta_{oi}$  from equation 7, response parameters are retrieved to evaluate the criterion weights. The equation below is used for calculating the correlation coefficient [\[Saha and Mondal, 2017\]](#). Response variable ( $R_{ji}$ ) is obtained by equation 3.11.

$$R_{jl} = \left[ \frac{COV(Xi(j), Xi(l))}{\sigma Xi(j) * \sigma Xi(l)} \right] \quad (3.11)$$

where  $COV(xi(j), xi(l))$  is the covariance of response variables  $j$  and  $l$  obtained by equation 3.12, whereas  $xi(j)$  is the normalized values of an individual response,  $\sigma Xi(j)$  and  $\sigma Xi(l)$  are the standard deviation (SD) of response variables  $j$  and  $l$ .

$$COV(x, y) = \frac{1}{n-1} \sum_{k=1}^n (xi - \bar{x})(yi - \bar{y}) \quad (3.12)$$

After that, the following are eigenvalues and corresponding eigenvectors from equation 3.13.

$$(R - \lambda_x I_m) V_{ik} = 0 \quad (3.13)$$

where  $\lambda_x$  is the eigenvalues,  $\sum_{x=1}^n \lambda_x = n$ ,  $x = 1, 2, \dots, n$ , and  $V_{ik} [a_{k1}, a_{k2}, \dots, a_{k(m-1)}, a_{km}]^T$  are the eigenvectors corresponding to eigenvalue  $\lambda_x$ . Equation 3.14 corresponds to the principal components.

$$Y_{mk} = \sum_{i=1}^n X_m(i) V_{ik} \quad (3.14)$$

where  $Y_{m1}, \dots, Y_{mk}$  are known as the first principal component (PC1) and so on to the 'k' principal component. The principal components are adjusted for variance in descending order, and consequently,  $Y_{m1}$  (PC1) represents the most variance in the data. Thus, the weights of the response parameters are calculated by simply squaring the most variance date i.e. PC1.

#### 3.4.4 GRA-PCA Hybrid Technique

Grey relation analysis (GRA) technique is used worldwide for solving the multiple attribute decision making (MADM) problems in an efficient way. With principal component analysis (PCA) coupled with GRA, it gives much more accurate and precise results in

solving MADM problems compared to other optimization technique. In hybrid GRA-PCA technique, first, the response parameters are distinguished in terms of smaller-the-better and larger-the-better using equations 3.5 and 3.6 respectively. Then unlike units were transformed into normalized values. The GRC  $[\xi_i(k)]$ , was calculated using equation 3.8 in the next step. Because as the weights of the individual responses are different, PCA is implemented using equations 3.11 – 3.14 to determine the exact weights of the specific response parameter of the existing system. By using the actual response weights that are determined from PCA, GRG  $[\gamma_i(k)]$  of each experiment is determined using equation 3.9. Of all the experiments, the highest GRG-PCA value gives us the most optimized set of process parameters.

### 3.4.5 Process Parameters

Current (I): Current is also sub-divided into peak current and base current which is also known as background current.

- Peak Current: It considerably influences different types of metal transfer mode (such as globular, spray, pulse, etc.), penetration, and detachment of molten metal droplet and tapering of an electrode.
- Base Current: This significantly influences molten metal droplet detachment, transferred metal temperature, fluidity, weld pool width, weld bead wetting, and drop size.

Current influences weld bead in addition to penetration. As the current rises, the weld bead width becomes larger and contains deeper penetration. Whereas if current decreases, the weld bead width becomes smaller and having shallower penetration [Little, 1994].

Voltage (V): Constant arc voltage power supply is used widely. In this, as the arc length (voltage) shortens a small amount; there is a large increase in the welding current that automatically increases the burn off rate of the electrode. In this, the operator adjusts the arc voltage to the desired level, and the machine then maintains the level over a wide range of amperage settings [Little, 1994].

Welding speed / Travel speed (S): The speed at which the nozzle moves above the welding plate. It greatly influences penetration and metal transfer mode.

Wire size: Wire size that is generally used in CMT is 1.2 mm in diameter as per literature survey. It helps in influencing penetration or the quantity of deposition. Increase in wire size leads to shallower penetration and faster deposit rate, while a decrease in wire size leads to deeper penetration and slower deposit rate.

Filler wire type: Few researchers has considered “type of wire” as a parameter in fusion welding, which considerably influences mechanical and metallurgical properties with decrease in intermetallic layer (IML) thickness and minimal intermetallic phases/compounds (IMP/IMC).

Wire feed rate (WFR): Rate at which the wire that comes out of the wire spool and pushes through the nozzle. It influences deposit rate and weld bead shape. Increase in wire feed rate leads to larger bead and faster deposit rate, while a decrease in wire feed rate leads to smaller bead and slower deposit rate [Little, 1994].

Shielding gases flow rate: A flow rate that is too low does not offer sufficient weld shielding, whereas excessively high flow rates can interfere with the arc's stability. The four modes of metal transfer in GMAW have different shielding gas flow requirements. Short-circuiting and pulsed spray modes require about 10 L/min (20 ft<sup>3</sup>/hr) flow rate which is generally suitable [Zhang et al., 2013; Liang, et al., 2017], while for globular transfer 15 L/min (30 ft<sup>3</sup>/hr) is preferred. Rate of flow in the spray transfer variation is around 20-25 L/min (40–50 ft<sup>3</sup>/hr) which is higher among the rest since it consist of greater value of heat input and thus bigger weld pool [Cary, 1988].

From the above discussion on welding parameters as per literature suvey and preliminary trials work, the key parameters are like current, shielding gas flow rate and welding speed, which majorly influences the weld bead. Apart from these, choice of filler

wire, size of filler fire, shielding gas, type of joint and cleaning action done before welding are also important in context of wettability, spreadability and joint strength.

#### 3.4.6 The limits of the process parameter and design matrix

By varying one of the parameters while keeping the others constant, a significant number of preliminary trial runs were performed to determine the upper and lower limits of CMT process parameters. Typical defects such as improper penetration, cracks, lack of fusion, and undercuts were observed during trial periods. Feasible upper and lower limits of each factor were chosen in such a way that the processed composite should be free from any visible defects. In this study, central composite face centered design (CCFCD) is used to determine the significance of the model for the design of experiment (DOE). CCD under RSM is executed by using Design Expert (DE) software, which helps to give the optimal results with a high precision from minimum number of trials. Alpha value equals to 1 is desirable as it ensures axial point position within the factorial part region. It is termed as face-centered design (FCD) and provides three distinct levels for the variables which are to be included in the matrix of experimental design. Total number of experiments designed by CCD is calculated from the equation 3.15.

$$N = k^2 + 2k + n \quad (3.15)$$

Where "N" stands for the total number of experiments, "k" denotes the number of factors studied and "n" is for number of replicates [Elemery, 2019]. For bead-on-plate experiment, there are two factors (process parameters) so the minimum number of experiments as per CCFCD is 13 including the 5 replicates. Similarly, for CMT butt joint experiments there are three factors so the minimum number of experiments as per CCFCD is 20 including the 5 replicates. The upper limit and lower limit of each factor were coded as +1 and -1 respectively [Lakshminarayanan and Balasubramanian, 2009].

Adequate numbers of sample experiments were performed in this research work to determine the parameter ranges in which effective, failure-free welding occurs. The selected process parameters & their levels are presented in Table 3.12 and 3.13 for bead-



on-plate and CMT butt joint respectively. Design matrix are presented in Table 3.14 and Table 3.15 for bead-on-plate and CMT butt joint respectively.

<b>Table 3.12</b> Process parameters for bead-on-plate experiments for CMT, MIG P and MIG M with their levels					
Welding Process Parameters	Units	Symbols	Levels		
			-1	0	1
Current	A	I	80	100	120
Welding speed	mm/sec	TS	7.5	10.5	13.5

<b>Table 3.13</b> Design of experiments for CMT butt joints					
Welding process Parameters	Units	Symbols	Levels		
			-1	0	1
Current	A	I	80	90	100
Welding speed	mm/sec	TS	5	7	9
Flow rate	L/min	Q	14	16	18

## 3.5 EXPERIMENTAL PROCEDURE

### 3.5.1 Bead-on-Plate

CMT welding machine (TPS400i) by Fronius is used for performing the experiments, as per the design of experiment (DOE) given in Table 3.14 for CMT, MIG P (MIG Pulse) and MIG M (MIG Manual). Schematic diagram of fixture containing AA6061-T6 plate of dimension 100 mm x 60 mm x 3.18 mm is shown in Fig. 3.19. Before welding, each plate was cleansed with acetone ( $(\text{CH}_3)_2\text{CO}$ ). In order to eliminate the surface films and various other impurities, metal surface was subsequently cleaned with steel wire brush. After cleaning the surface, sample was fastened in a fixture as displayed in Fig. 3.19, with torch angle placed at 90 °, CTWD is 10 mm, stick-out is 5 mm and pure argon (99.99 % purity) as a shielding gas at flow rate of 15 L/min are kept constant. The standard bead-on-plate procedure was used to lay the weld beads on AA6061-T6 plates by using a wire of Ø1.2 mm of ER4043 (AlSi5 %). Current, voltage and wire feed rate (WFR) are the dependent parameters in CMT and MIG P. Changing the value of one parameter contributes to change in the other owing to synergic lines. The current and welding speed are chosen among the

different welding parameters for experiments because the geometry of the bead is highly influenced as per literature survey and extensive amount of experimental trials.

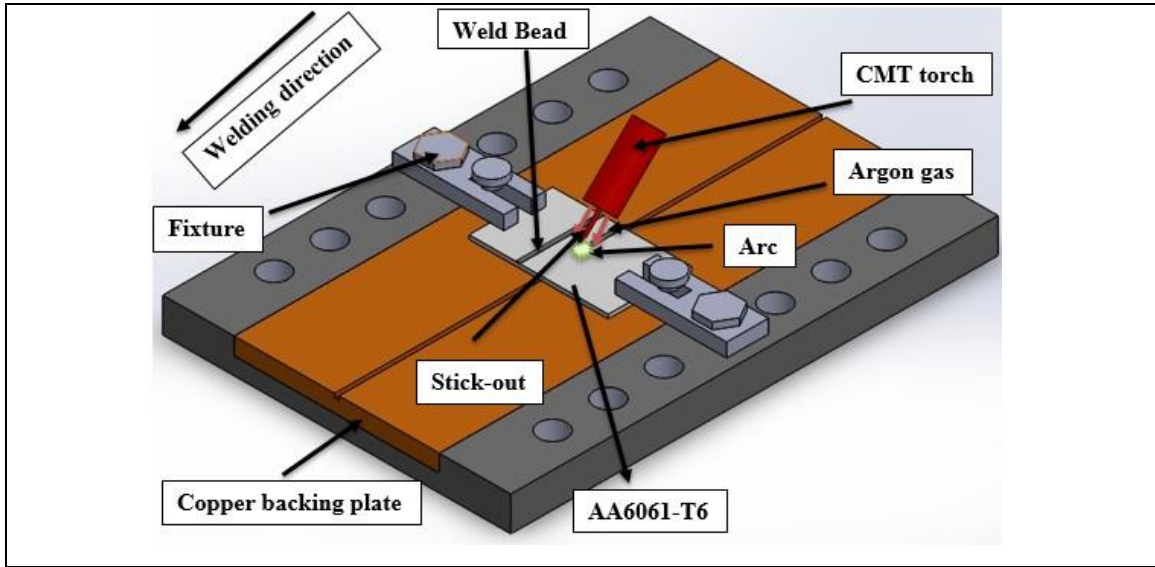


**Fig. 3.19** Fixture setup for bead-on-plate experiments

<b>Table 3.14</b> Central composite design matrix for bead-on-plate experiment			
Std	Run	A:Current A	B:Welding Speed mm/sec
1	11	-1	-1
2	13	1	-1
3	2	-1	1
4	3	1	1
5	7	-1	0
6	1	1	0
7	8	0	-1
8	5	0	1
9	6	0	0
10	4	0	0
11	10	0	0
12	12	0	0
13	9	0	0

### 3.5.2 CMT Butt Joint

Aluminium alloys of grade AA6082-T6 and AA6061-T6 were chosen of thickness 2mm and 3.18 mm respectively for joining with the help of CMT welding machine TPS400i developed by Fronius is operated for performing the experiments. Single side butt joint with a negligible gap between the sheets having the bevel angle of 90° and dimension of 100mm x 60mm was fabricated. Before welding, a plastic covering on each sample is removed which protects the substrate material from the environment. Each sample was cleaned with acetone and wire brush made of steel to remove the oxide film and other unwanted impurities from the welded surface. After preparing the surface, the samples were fastened in the fixture, as shown in the schematic diagram in Fig. 3.20.

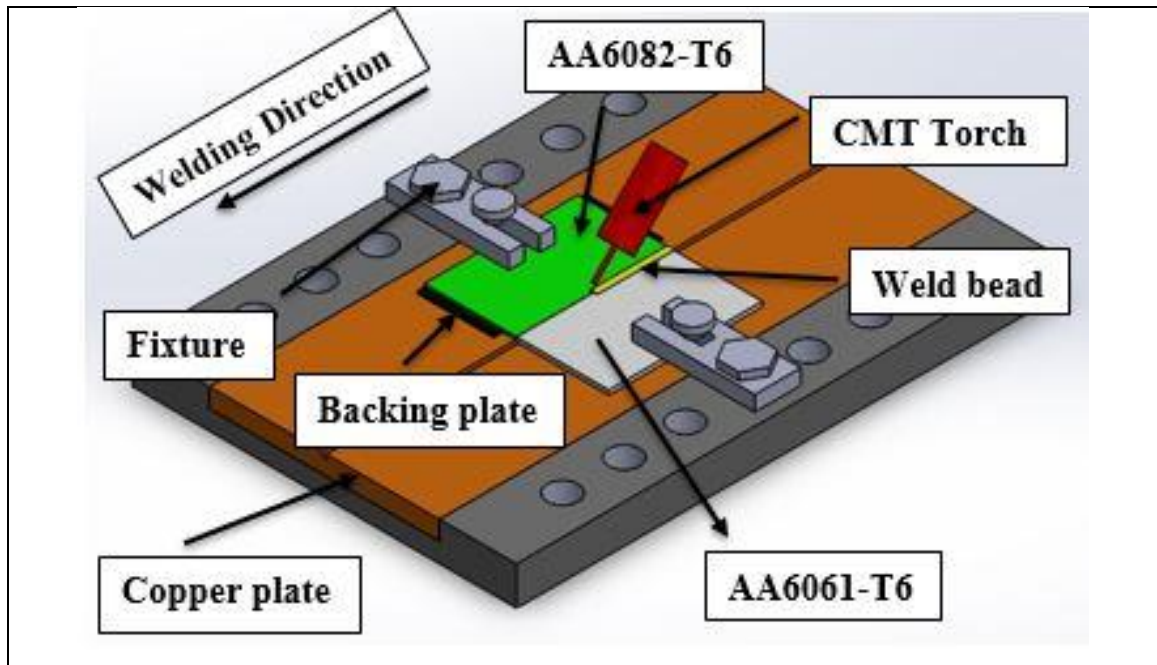
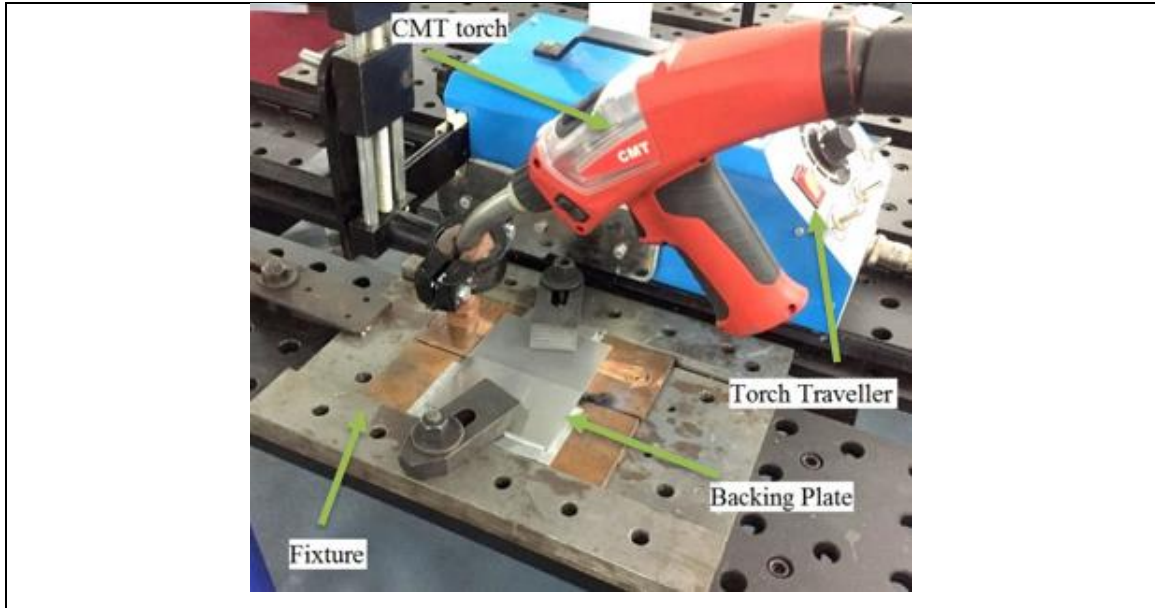


**Fig. 3.20** Fixture setup for CMT butt joints







The argon gas (Ar) with 99.99% purity was used as a shielding gas at 15 L/min of flow rate was turned on to provide the arc stability. Experimental setup is presented in the Fig. 3.21 and the experiments as per the DOE given in Table 3.15 for CMT butt joints. Table 3.16 shows the experimental table with increasing heat input as per CCFC matrix with the weld bead images.









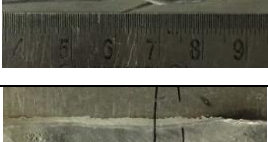


**Fig. 3.21** Experimental setup for CMT butt joints

<b>Table 3.15</b> Central composite design matrix for CMT butt joints				
Std	Run	Process Parameters		
		Current A	Welding Speed mm/sec	Gas flow rate L/min
3	17	-1	1	-1
7	18	-1	1	1
12	3	0	1	0
4	6	1	1	-1
8	4	1	1	1
9	2	-1	0	0
13	13	0	0	-1
17	5	0	0	0
19	7	0	0	0
18	8	0	0	0
15	11	0	0	0
20	12	0	0	0
16	16	0	0	0

14	1	0	0	1
10	15	1	0	0
1	9	-1	-1	-1
5	19	-1	-1	1
11	10	0	-1	0
2	14	1	-1	-1
6	20	1	-1	1

<b>Table 3.16</b> Experimental table with increasing heat input as per CCFC matrix					
S.No.	Current (A)	Welding Speed (mm/sec)	Flow Rate (L/min)	Heat Input (J/mm)	Bead profile
1	80	9	14	163	
2	80	9	18	168	
3	90	9	16	183	
4	100	9	14	195	
5	100	9	18	198	
6	80	7	16	204	

7	90	7	14	220	
8	90	7	16	227	
9	90	7	18	243	
10	100	7	16	245	
11	80	5	14	311	
12	80	5	18	323	
13	90	5	16	347	
14	100	5	14	352	
15	100	5	18	369	

### 3.5.3 Ultrasonic Assisted CMT (U-CMT) Butt Joint

U-CMT butt joints were fabricated for the comparison purpose with CMT butt joints. Selected samples of CMT butt joints were compared with U-CMT butt joints as shown in Table 3.17. Ultrasonic generator box was used to generate the vibrations at constant frequency with varying amplitude. Ultrasonic probe touches the workpiece material to transfer the vibrations created by the generator box to the workpiece as displayed in Fig. 3.22.

<b>Table 3.17</b> Experimental welding parameters for different welding process and weld geometry							
S.No.	Current (A)	Welding Speed (I) (mm/sec)	Process	Reinforcement height (mm)	Weld width (mm)	Penetration depth (mm)	Contact angle (°)
S-1	80	7	CMT	1.108	8.13	4.594	29.745
S-2	80	7	U-CMT	1.068	8.5	4.759	25.991
S-3	90	5	CMT	1.181	13.21	4.496	14.281
S-4	90	5	U-CMT	0.736	13.74	4.705	9.728
S-5	90	7	CMT	1.433	9.91	4.170	17.819
S-6	90	7	U-CMT	0.614	10.99	4.95	11.634
S-7	90	9	CMT	1.499	8.26	4.105	40.764
S-8	90	9	U-CMT	1.186	9.11	4.745	27.553
S-9	100	7	CMT	1.042	10.67	4.596	28.435
S-10	100	7	U-CMT	-1.023	13.74	4.755	336.371
Current Type				: Direct current electrode positive (DCEP)			
Flow rate of shielding gas				: 16 L/min (Constant)			
CTWD				: 10 mm (Constant)			
Ultrasonic frequency				: 20 kHz (Constant)			
Ultrasonic vibrational amplitude				: 66 $\mu$ m (Constant)			



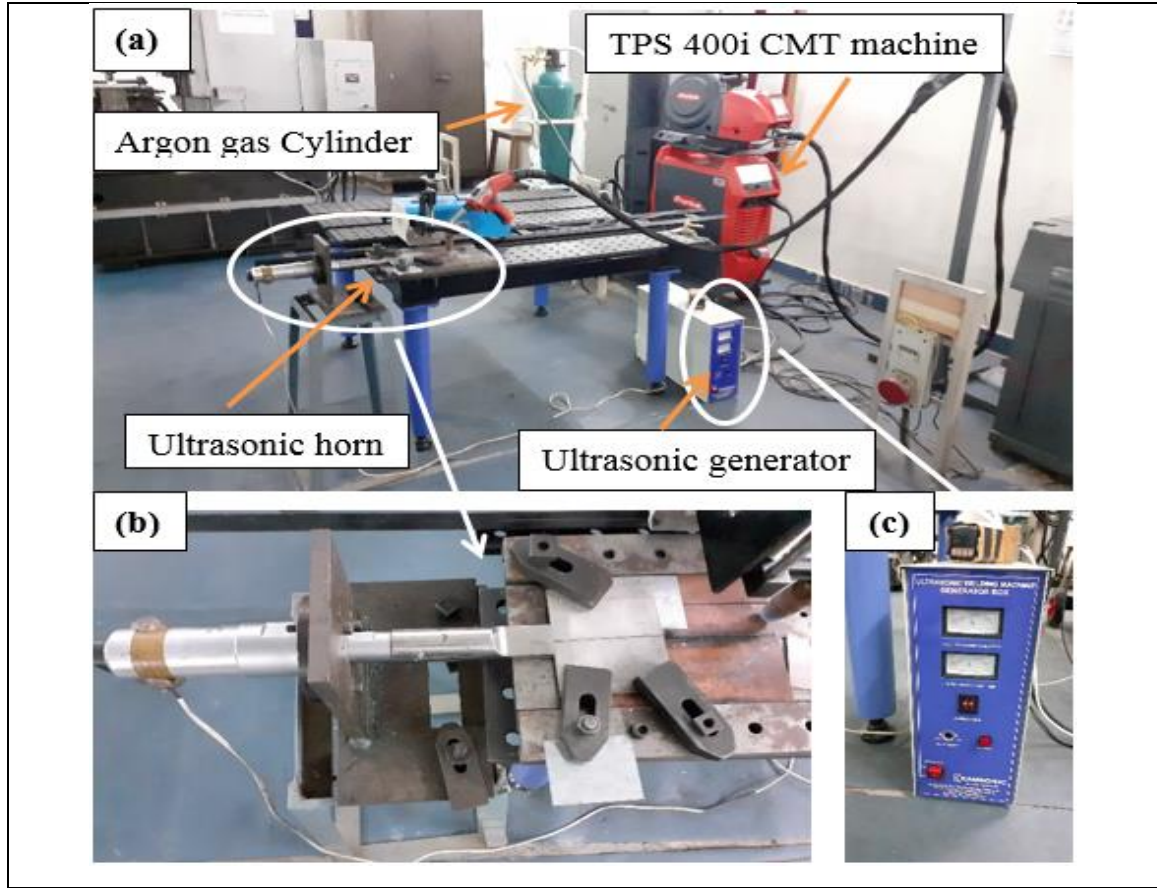


**Fig. 3.22** (a) Ultrasonic setup (b) Ultrasonic Probe (c) Generator

### 3.6 TEMPERATURE PROFILE

A thermocouple of type 'K' was used to determine the temperature and a thermostat is used to digitalize the measured thermocouple temperature of the bottom surface of the weld bead as presented in Fig. 3.23. Fluke Ti400 infrared fusion technology camera was also used to sense the temperature of the weld bead, which gives the approximately similar temperature readings a range of  $\pm 5^{\circ}\text{C}$ . [Lanc et al., \(2018\)](#) used infrared thermography technique to determine the emissivity of AA6082. The investigations exhibited that the emissivity decreases with decrease in temperature and increases with surface roughness in the ranges from 0.09 to 0.24. The emissivity of both the aluminum materials was used in this experiment is 0.07. The maximum temperature was observed at the weld bead ( $1200^{\circ}\text{C}$ ) followed by HAZ ( $550^{\circ}\text{C}$ - $650^{\circ}\text{C}$ ) and BM ( $150^{\circ}\text{C}$ - $300^{\circ}\text{C}$ ). These data was checked with the help of K type thermocouple and it exhibited more or less the similar values. Fig. 3.24



shows the thermal imaging camera images taken at various points of S-10 welded sample. Six horizontal lines (Line 0 to Line 5) from top to bottom are marked on the thermal image of welded sample and the temperature profile is shown in Fig. 3.24 and 3.25 respectively. Temperature decreases as moved from weld zone to the base metal on either side.

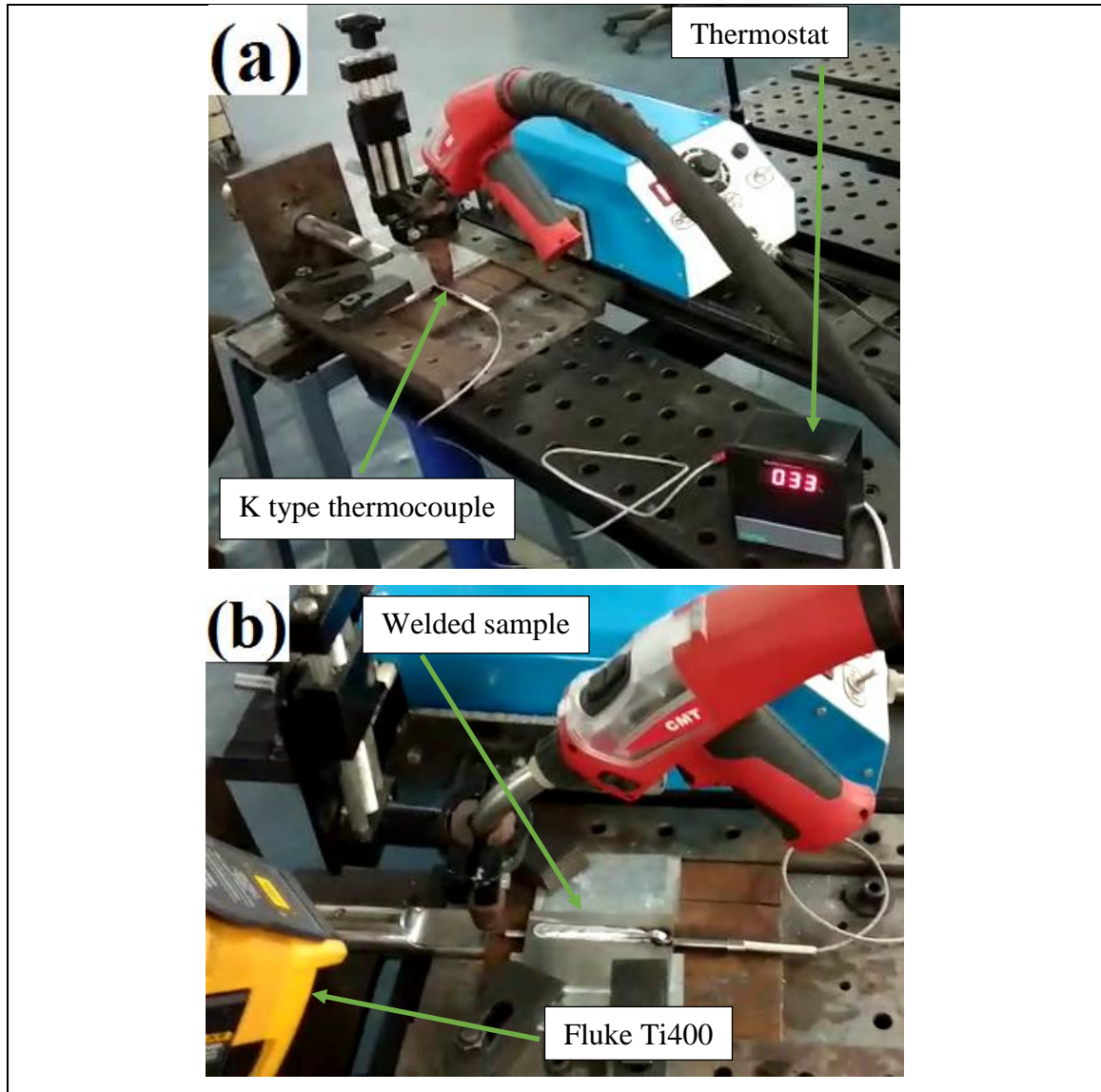


**Fig. 3.23** Temperature setup (a) K-type thermocouple and thermostat method (b) Thermal imaging camera method.

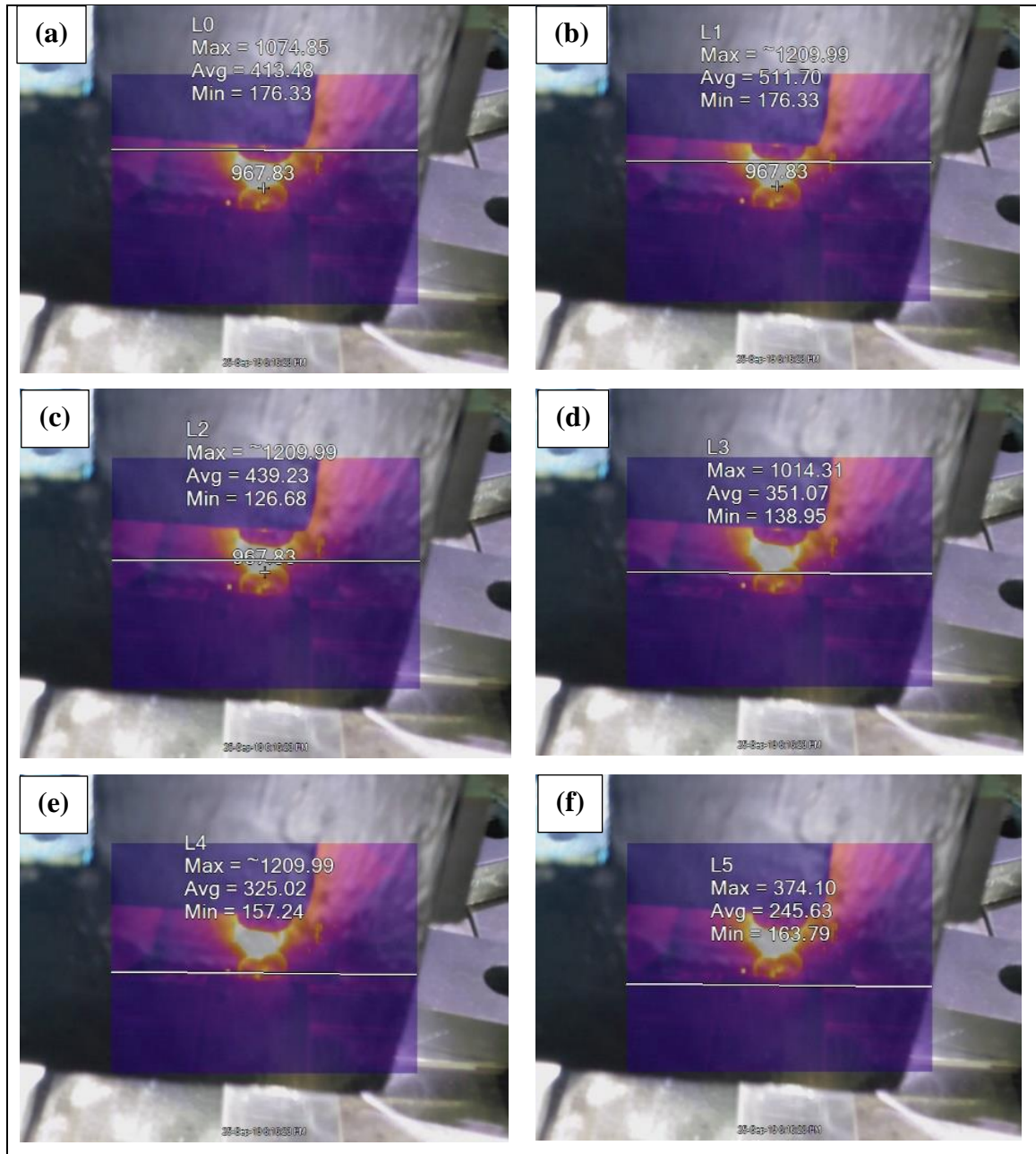


**Fig. 3.24** Thermal imaging camera images of welded S-10 sample at various points (a) Line 0 (b) Line 1 (c) Line 2 (d) Line 3 (e) Line 4 (f) Line 5

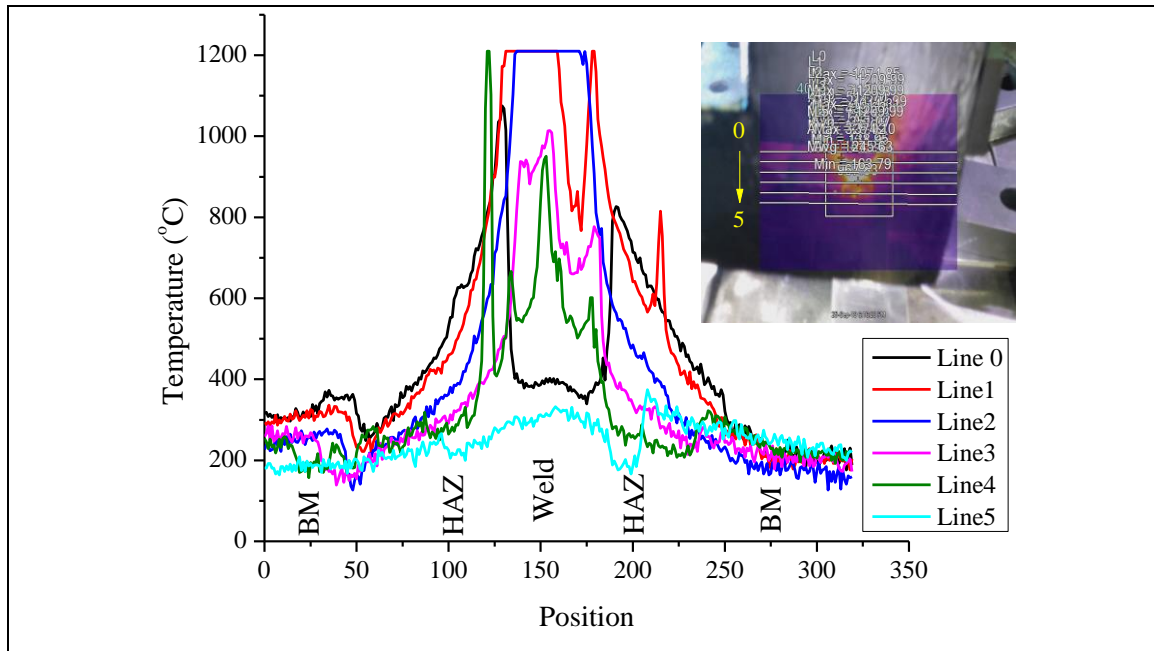


**Fig. 3.25** Temperature profile of welded sample at variable lines marked on the image

### 3.7 SUMMARY

This chapter presented materials selection of substrate and filler material. AA6061-T6 and AA6082-T6 as substrate material and ER4043 (Al-Si5%) as filler wire was chosen based on compatibility. Various characterization of substrate and filler material were presented. Sample preparation for various test such as macrostructure and microstructural characterization, microhardness, tensile and residual test were described step by step. Various machines involved in the experimentation were discussed in detail. Mechanical properties procedure for tensile, microhardness and residual stress were also discussed. The process of metallurgical characterization of microstructure, phase analysis, elemental composition using OM, FESEM and XRD were illustrated. The specimen for all the test were as per ASTM standards. Experimental procedure for bead-on-plate, CMT butt welding and U-CMT butt joining was illustrated and explained briefly. Optimization for bead-on-plate was done by CCFCD under RSM. For CMT butt joints, optimal parameters were found by GRA-PCA hybrid technique which is compared further by CCFCD under RSM. Lastly, temperature profile was obtained using K-type thermocouple and thermal imaging camera.

## CHAPTER 4 : RESULTS AND DISCUSSION ON BEAD-ON-PLATE

---

### 4.1 INTRODUCTION

Bead on plate analysis gives the overall picture of the weld bead geometry, which consists of weld reinforcement (R), weld penetration (P), weld width (W) and the contact angle ( $\theta$ ) as shown in Fig. 4.1. Weld bead dimensions is important to be measured to understand the insight view of the bead geometry that helps in the overall cost of the welding. Good and economical weld joint needs deeper penetration for higher tensile strength; lower HAZ, weld width and weld reinforcement for lesser consumption of filler wire [Greyjevo and Metodo 2009]. In this, the shaded portion “A” is the reinforcement area and “B” is the penetrated area. Dilution is the ratio of molten base metal (BM) area to the area of the total fusion zone (FZ). It can also be expressed as the ratio of the penetrated area (B) to the area of total weld metal (A+B) as shown in equation 4.1. The absolute importance of dilution is that the final weld metal's chemical composition is totally distinct from the substrate and filler components, creating a fresh intermediate alloy between the two [Hunt et al., 1994; Sun et al., 2019 and Saha et al., 2019]. Dilution enhances the mechanical properties of the weld bead by introducing a suitable filler material to the BM. Results showed that all bead dimensions are increasing by raising the current and reducing the welding speed. Weld reinforcement form factor (WRFF) is the ratio of bead width (W) to reinforcement height (R) and calculated by equation 4.2. Weld penetration shape factor (WPSF) is the ratio of bead width (W) to penetration (P) which is calculated by equation 4.3. Heat input is a very important term in the context to the material thickness and is calculated using equation 4.4 [Cook & Eassa, (1985)]. Thermal heat input has a substantial influence on the weld zone (WM) properties [Irizalp et al., (2016)] and it has huge consequence for the cooling rate of the WM. It is a comparative measure of the transfer of energy per unit weld length. For a more economical method, the heat input of the same joint needs to be reduced, resulting in stronger weld [Mandez & Eagar, (2001)].

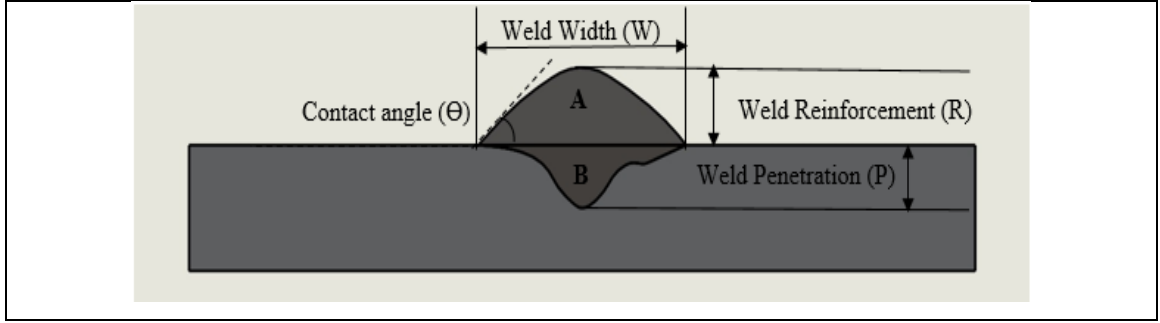


**Fig. 4.1** Weld Bead geometry

$$\text{Dilution (D)} = \frac{\text{Area B}}{\text{Area A} + \text{Area B}} \times 100 \quad (4.1)$$

$$\text{WRFF} = \frac{W}{R} \quad (4.2)$$

$$\text{WPSF} = \frac{W}{P} \quad (4.3)$$

$$\text{Heat Input (Q)} = \eta \frac{VI}{S} \quad (4.4)$$

Where Q, V, I, S,  $\eta$  are heat input (J/mm), voltage (V), current (A), welding speed (mm/sec) and efficiency (%) respectively. The thermal efficiency for welding is approximately 80 % [Quintino et al., 2013 and Joseph et al., 2003]. Fig. 4.2 shows the schematic diagram in 3-D of the weld bead dimensions.

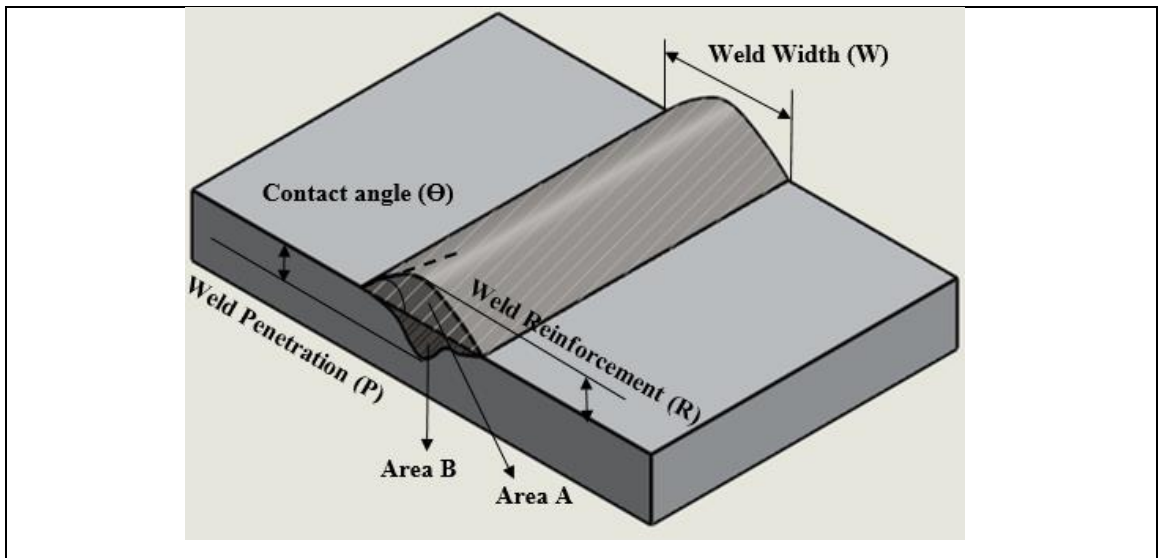


**Fig. 4.2** Schematic diagram (3-D) of weld bead dimensions



## 4.2 OPTIMIZATION OF PROCESS PARAMETERS

### 4.2.1 Introduction

Currently, DOE, computational techniques and optimization techniques are mostly used to identify the optimum parameters and validate the outcomes using simulation tools in order to achieve a mathematical relationship. CCD is used to define the importance of the model for DOE. Using Design Expert (DE) or minitab software, CCD under RSM is achieved. It is observed by [Adak et al., \(2015\)](#) that GMAW is an extremely complex, multi-variable system in which the factors influencing the welding performance are not explicitly recognized. The development of a model to make predictions of the geometry of the welding beads has therefore proved to be essential. Numerous investigators attempt to explore the impacts of distinct welding parameters on bead profile. Most of the mathematical models and empirical relations on bead-on-plate are developed for Metal Inert Gas (MIG) [[Adak et al., 2015](#) and [Lee and Rhee 2000](#)], Submerged Arc Welding (SAW) [[Gunaraj and Murugan 2002](#), [Chandel et al., 1997](#)] and Tungsten Inert Gas (TIG) [[Jou 2003](#)]. There are limited number of papers of bead-on-plate from CMT process and its comparison with its parent techniques (MIG P and MIG M). Most of the research work is published for GMAW (MIG) and SAW on bead geometry and bead-on-plate. Taguchi design method was used to optimize welding parameters such as current, voltage and travel speed in order to achieve the highest penetration depth on mild steel in MIG welding by [Sapakal and Telsang \(2012\)](#). For TIG and MIG welding processes, GRA method is applied to analyze the process parameter's influence on the bead hardness of material AISI 1020 [[Patel and Chaudhary, 2013](#)]. [Balasubramanian \(2016\)](#) used statistical design to forecast the optimum weld pool profile of pulsed current TIG welding of titanium alloy. The models established is used to obtain the required weld bead sizes readily. [Haragopal et al., \(2011\)](#) introduces the taguchi technique for designing process parameters to optimize the mechanical characteristics of MIG aluminium welded alloy (Al-65032). [Utkarsh et al., \(2014\)](#) demonstrates the impact of voltage (V), current (I), flow rate of gas and welding speed (S) on tensile strength of st-37 low alloy steel material on MIG welding. The tests use L9 orthogonal array, and the findings showed that current and voltage have an important impact on UTS. [Khanna and Maheshwari \(2018\)](#) developed a mathematical model in MIG welding of SS409M for predicting the weld bead dimensions. Central

composite rotatable design (CCRD) method is being used to create model, which is found to be a powerful tool [Sharma and Maheshwari 2019]. Gunaraj and Murugan (1999) created regression equations to forecast bead characteristics, heat-affected zone (HAZ) attributes, and model adequacy was confirmed by ANOVA method using CCRD. Their research discovered the beneficial impact of heat input (HI) and wire feed rate (WFR), but welding speed has an adverse impact on all features of the bead and HAZ. Results showed that all bead sizes are increasing by raising the current and reducing the welding speed.

The bead-on-plate is processed using CMT, MIG P and MIG M to get the insight view of the weld bead as per DOE displayed in Table 3.12. The processed bead-on-plate should be exempt from weld defects such as undercuts, lack of fusion, improper penetration, cracks etc. The input process parameters (current and welding speed) greatly influences the weld bead dimensions and its integrity. Multi- responses (penetration, dilution and heat input) taken for this work are essential because they not only influence the dimensions of the bead but also provide insight into the metallurgical features. The weld bead dimensions between CMT, MIG P and MIG M welding techniques are to be compared and mathematical modelling is carried out using RSM to discover ideal welding parameters to achieve improved welding quality, enhanced productivity and minimal welding costs. The Central composite face centered design (CCFCD) is used to determine the significance of the model for the DOE. Thus the effects of process parameters on the weld bead and the contribution of each parameter on the output responses (penetration, dilution and heat input) can be analyzed through ANOVA. Consequences of welding process parameters and various different welding techniques on the weld bead is also carried out. Quadratic model equations are established to get the model significant and lack of fit to be insignificant. The percentage contribution of each process parameter is established. Model reliability is checked and confirmatory runs are done for the justification.

#### 4.2.2 Experimental results for Bead-on-Plate

The experiments are conducted as per DOE using the CCFCD for finding out the optimum input process parameters. Total of 13 experiments were carried out for each of welding technique (CMT, MIG P and MIG M). Input process parameters are current and welding

speed while the output parameters are penetration, dilution and heat input. Table 4.1, 4.2 and 4.3 presents the design matrix of experiments and corresponding results for CMT, MIG P and MIG M respectively.

<b>Table 4.1</b> Experimental results for CMT						
Std	Run	A:Current	B:Welding Speed	Penetration	Dilution	Heat Input
		A	mm/sec	mm	%	J/mm
1	11	80	7.5	2.46	30.67	105.81
2	13	120	7.5	3.58	55.67	185.6
3	2	80	13.5	0.361	12.45	58.79
4	3	120	13.5	1.81	39.34	103.11
5	7	80	10.5	0.98	20.34	75.58
6	1	120	10.5	2.32	45.67	132.57
7	8	100	7.5	3.11	48.73	148.27
8	5	100	13.5	1.095	30.69	82.37
9	6	100	10.5	1.7	38.51	107.5
10	4	100	10.5	1.67	38.16	105.9
11	10	100	10.5	1.678	38.2	106.1
12	12	100	10.5	1.65	38.05	105.2
13	9	100	10.5	1.685	38.09	105.6

<b>Table 4.2</b> Experimental results for MIG P						
Std	Run	A:Current	B:Welding Speed	Penetration	Dilution	Heat input
		A	mm/sec	mm	%	J/mm
1	2	80	7.5	1.755	35.19	158.72
2	7	120	7.5	3.67	65.17	249.45
3	12	80	13.5	0.37	16.04	90.18
4	11	120	13.5	1.965	52.09	137.14
5	1	80	10.5	1.05	19.41	113.37
6	5	120	10.5	3.01	55.25	180.11
7	8	100	7.5	3.315	58.15	203.73
8	9	100	13.5	1.68	45.28	113.19
9	6	100	10.5	2.73	48.3	145.65
10	10	100	10.5	2.705	47.3	145.52
11	3	100	10.5	2.639	46.4	144.32
12	4	100	10.5	2.647	46.8	144.92
13	13	100	10.5	2.641	46.5	144.42



<b>Table 4.3</b> Experimental results for MIG M						
Std	Run	A:Current	B:Welding Speed	Penetration	Dilution	Heat Input
		A	mm/sec	mm	%	J/mm
1	5	80	7.5	1.86	37.45	164.13
2	3	120	7.5	3.78	69.78	271.64
3	8	80	13.5	0.38	19.78	91.074
4	4	120	13.5	2.65	56.67	149.47
5	13	80	10.5	1.11	25.56	115.81
6	11	120	10.5	3.31	62.34	194.74
7	10	100	7.5	3.41	63.13	219.73
8	2	100	13.5	1.98	49.34	122.07
9	12	100	10.5	2.942	56.17	158.1
10	9	100	10.5	2.92	55.67	156.95
11	1	100	10.5	2.93	55.93	157.95
12	7	100	10.5	2.823	54.57	155.05
13	6	100	10.5	2.925	55.87	157.9

#### 4.2.3 Mathematical Model Equation

Experimental results obtained are scrutinized using the statistical analysis system's response surface regression procedure.

##### 4.2.3.1 Model Equations of Penetration

The values of the coefficient were governed using equation 2 and multi-response mathematical model for penetration in CMT, MIG P and MIG M are represented by the equations 4.5, 4.6 and 4.7 respectively in terms of coded variables.

$$P_{CMT} = +7.42998 + 0.037069*A - 1.43166*B + 0.001371*A*B - 0.000094*A^2 + 0.046080*B^2 \quad (4.5)$$

$$P_{MIG P} = -17.21718 + 0.360290*A + 0.183299*B - 0.001333*A*B - 0.001504*A^2 - 0.014879*B^2 \quad (4.6)$$

$$P_{MIG M} = -15.54579 + 0.345782*A - 0.065335*B + 0.001458*A*B - 0.001539*A^2 - 0.014521*B^2 \quad (4.7)$$

The final model for penetration in terms of actual variables are represented by equations 4.8, 4.9 and 4.10 for CMT, MIG P and MIG M welding process.

$$P_{CMT} = +7.42998 + 0.037069 * \text{Current} - 1.43166 * \text{Welding Speed} + 0.001371 * \text{Current} * \text{Welding Speed} - 0.000094 * \text{Current}^2 + 0.046080 * \text{Welding Speed}^2 \quad (4.8)$$

$$P_{MIG P} = -17.21718 + 0.360290 * \text{Current} + 0.183299 * \text{Welding Speed} - 0.001333 * \text{Current} * \text{Welding Speed} - 0.001504 * \text{Current}^2 - 0.014879 * \text{Welding Speed}^2 \quad (4.9)$$

$$P_{MIG M} = -15.54579 + 0.345782 * \text{Current} - 0.065335 * \text{Welding Speed} + 0.001458 * \text{Current} * \text{Welding Speed} - 0.001539 * \text{Current}^2 - 0.014521 * \text{Welding Speed}^2 \quad (4.10)$$

#### 4.2.3.2 Model Equations of Dilution

Following the same modeling operation as follows for penetration, the following equation was achieved in terms of the actual factor for dilution and heat input respectively as the final empirical model. The final model for dilution in terms of actual variables are represented by equations 4.11, 4.12 and 4.13 for CMT, MIG P and MIG M welding process.

$$D_{CMT} = -98.30578 + 3.15461 * \text{Current} - 7.24980 * \text{Welding Speed} + 0.007875 * \text{Current} * \text{Welding Speed} - 0.012969 * \text{Current}^2 + 0.168602 * \text{Welding Speed}^2 \quad (4.11)$$

$$D_{MIG P} = -168.73967 + 5.41516 * \text{Current} - 16.05127 * \text{Welding Speed} + 0.025292 * \text{Current} * \text{Welding Speed} - 0.024159 * \text{Current}^2 + 0.524598 * \text{Welding Speed}^2 \quad (4.12)$$

$$D_{MIG M} = -247.20559 + 6.19745 * \text{Current} - 7.31088 * \text{Welding Speed} + 0.019000 * \text{Current} * \text{Welding Speed} - 0.027568 * \text{Current}^2 + 0.139751 * \text{Welding Speed}^2 \quad (4.13)$$

#### 4.2.2.3 Model Equations of Heat Input

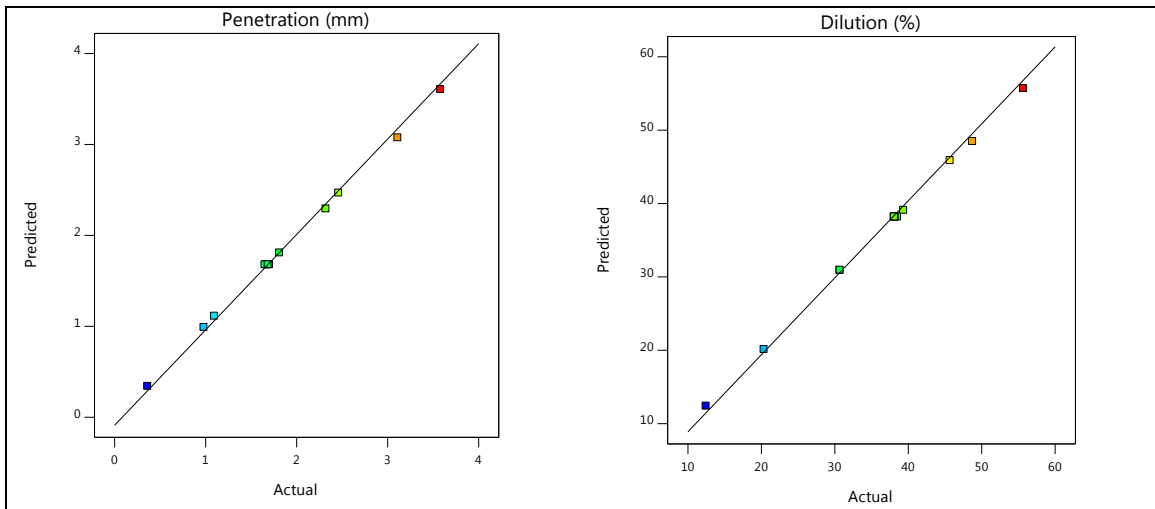
The final model for heat input in terms of actual variables are represented by equations 4.14, 4.15 and 4.16 for CMT, MIG P and MIG M welding process.

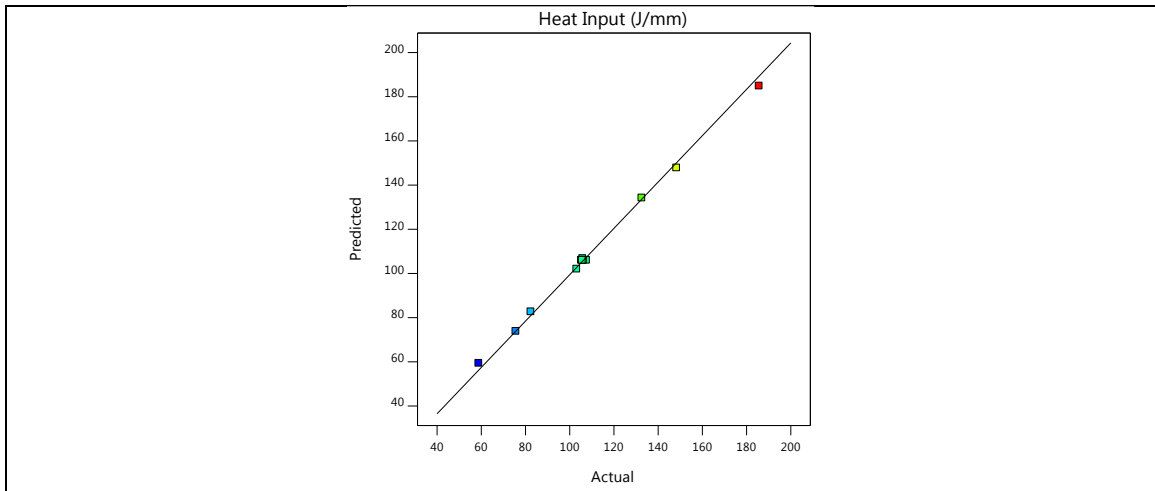
$$\mathbf{H}_{\text{CMT}} = -22.37259 + 4.05529 * \text{Current} - 17.67516 * \text{Welding Speed} - 0.147792 * \text{Current} * \text{Welding Speed} - 0.004972 * \text{Current}^2 + 1.02849 * \text{Welding Speed}^2 \quad (4.14)$$

$$\mathbf{H}_{\text{MIG P}} = +126.78052 + 3.06016 * \text{Current} - 26.79208 * \text{Welding Speed} - 0.182375 * \text{Current} * \text{Welding Speed} + 0.002792 * \text{Current}^2 + 1.42630 * \text{Welding Speed}^2 \quad (4.15)$$

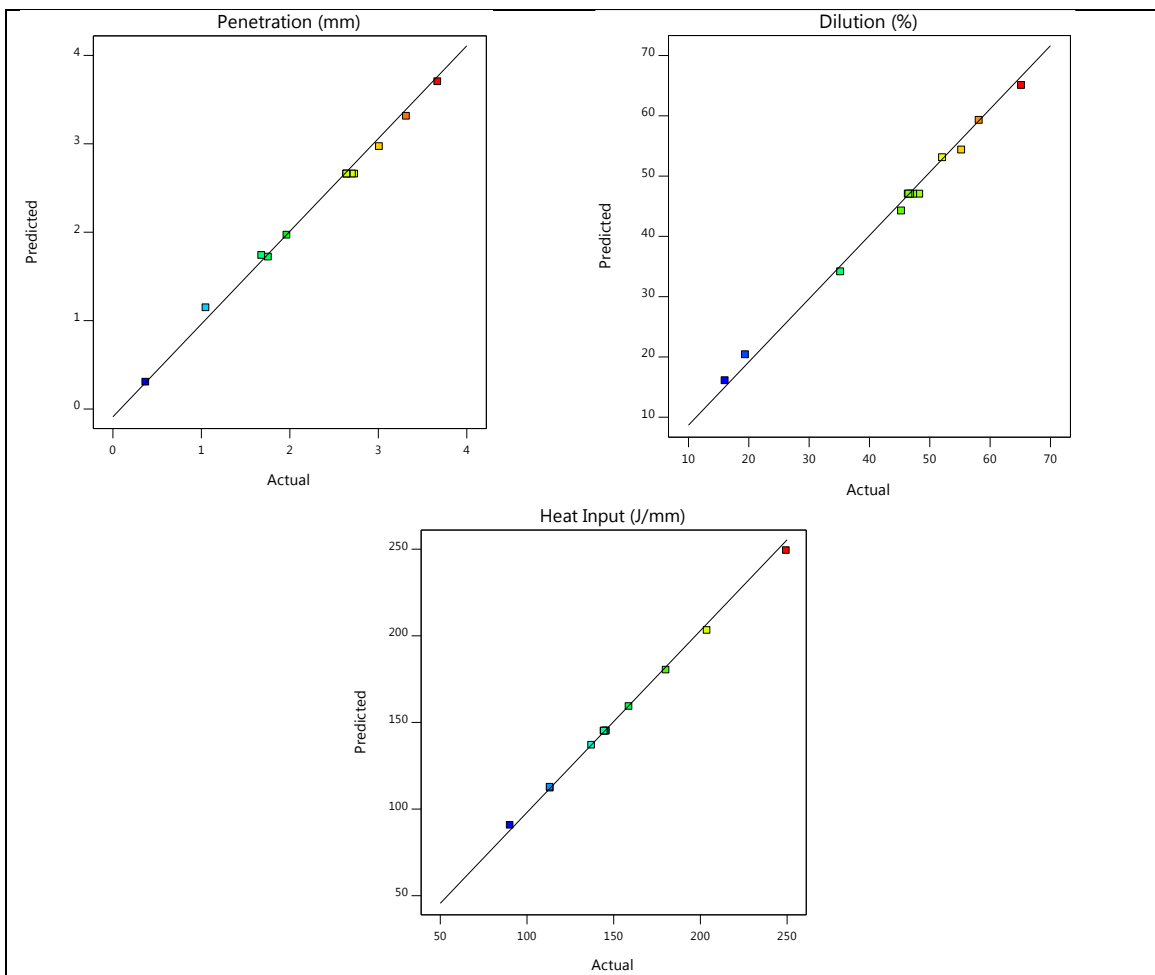
$$\mathbf{H}_{\text{MIG M}} = +30.87741 + 5.12397 * \text{Current} - 27.90260 * \text{Welding Speed} - 0.204642 * \text{Current} * \text{Welding Speed} - 0.004675 * \text{Current}^2 + 1.52835 * \text{Welding Speed}^2 \quad (4.16)$$

Fig. 4.3, 4.4 and 4.5 shows the predicted vs actual response for CMT, MIG P and MIG M respectively, which almost coincides with each other and concludes that the model is significant.





**Fig. 4.3** Predicted vs Actual graphs for CMT



**Fig. 4.4** Predicted vs Actual graphs for MIG P

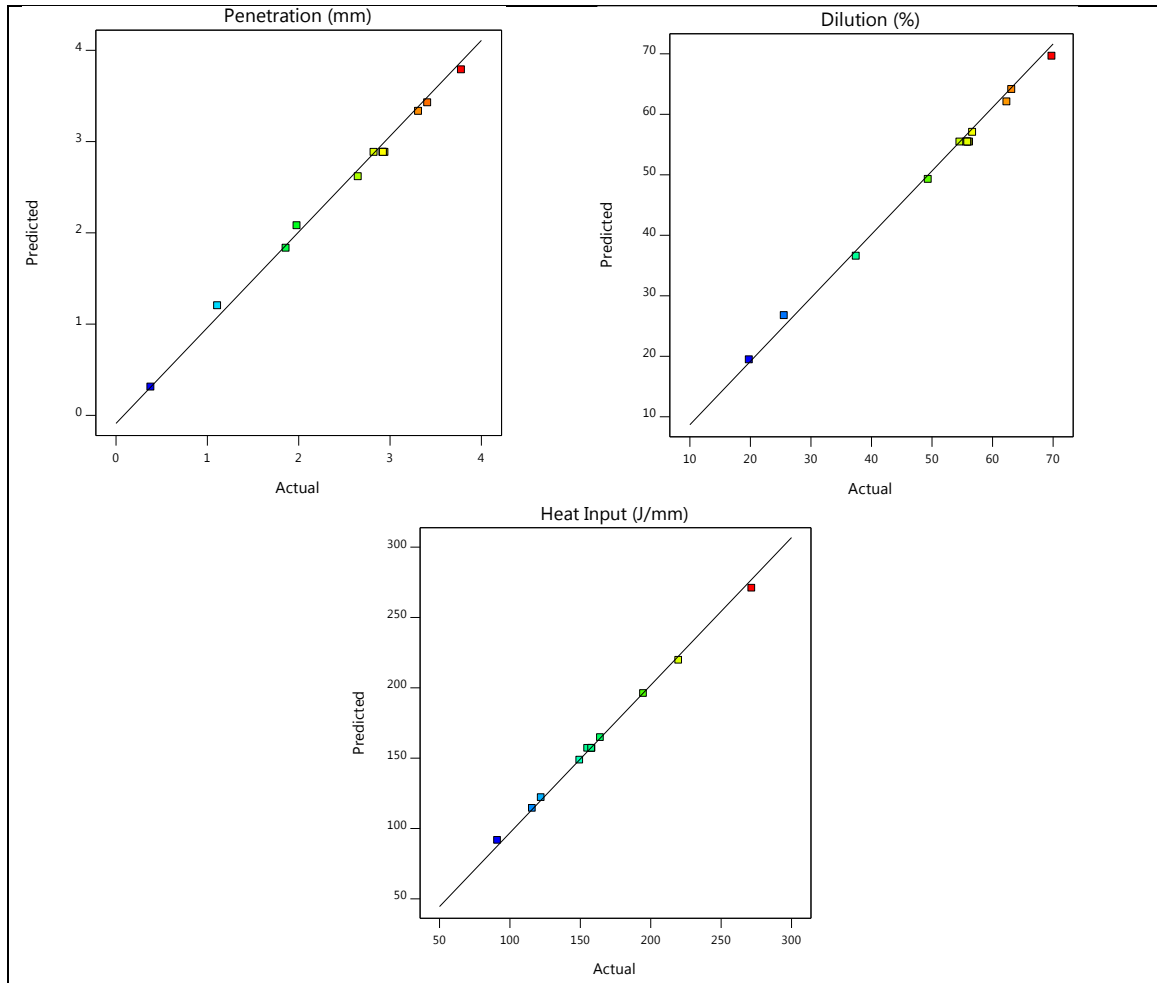


**Fig. 4.5** Predicted vs Actual graphs for MIG M

#### 4.2.4 Checking the adequacy of the model for penetration, dilution and heat input

The ANOVA technique was used to check the adequacy of the model. Table 4.4, 4.5 and 4.6 shows the analysis of variance (ANOVA) for penetration in CMT, MIG P and MIG M respectively. Table 4.7, 4.8 and 4.9 for dilution and Table 4.10, 4.11 and 4.12 for heat input, it shows sum of squares (SS), degree of freedom (DOF), mean square (MS) which is expressed as the ratio of SS and DOF, F-value, P-value and percentage contribution. F-value is the ratio of variation between the factors to the variation within the factors. P-value signifies the probability, which should be less than 0.05. Contribution is the percentage influence of the independent factors that affect the responses. By altering the value of factor which has the highest percentage contribution will majorly change the response output.

This signifies the sensitivity of that factor. ANOVA tables of CMT, MIG P and MIG M concludes that the model is significant with more than 99% of contribution because of higher F-values. Model terms are significant when P-values are less than 0.05. ANOVA tables depicts that all the model terms (A, B, AB, A<sup>2</sup> and B<sup>2</sup>) are considerable with less than 0.05 P-value. Values above 0.1 specify that the model terms are not significant. All ANOVA tables shows the full quadratic model for penetration, dilution and heat input with distinctive welding techniques because all model terms including interactions between input parameters (AB) are significant.

<b>Table 4.4</b> ANOVA table of full quadratic model for Penetration in CMT							
Source	SS	DOF	MS=(SS/DOF)	F-value	P-value	Contrib. (%)	Remarks
Model	8.87	5	1.77	2518.86	< 0.0001	99.94	significant
A-Current	2.55	1	2.55	3617.76	< 0.0001	28.89	
B-Welding Speed	5.77	1	5.77	8196.97	< 0.0001	65.38	
AB-Current*Welding Speed	0.0271	1	0.0271	38.44	0.0004	0.31	
A*A	0.0039	1	0.0039	5.60	0.0499	0.04	
B*B	0.4750	1	0.4750	674.82	< 0.0001	5.38	
Residual	0.0049	7	0.0007			0.06	
Lack of Fit (LOF)	0.0036	3	0.0012	3.46	0.1309		not significant
Pure Error	0.0014	4	0.0003				
Cor Total	8.87	12					
SD		0.0265		R*R			0.9994
Mean		1.85		Adjusted- R*R			0.9990
C.V. %		1.43		Predicted- R*R			0.9958
				Adequate Precision			181.1008

Lack of fit is not significant as shown in the ANOVA tables, as its P-value is more than 0.1. For penetration, welding speed is a more dominant (65.38%) as compared to current (28.89%) in CMT but in MIG P and MIG M, current is more dominant (51.00% and 63.90%) as compared to welding speed (38.02% and 25.52%) because of higher F-values and lower P-values (<0.0001). For dilution, current is the major influencing parameter for

all the three process with more than 64% contribution whereas for heat input, welding/travel speed is the dominant factor with more than 50% contribution for all the three welding technique. For all the response parameter, the value of predicted  $R^2$  is reasonably in agreement with the Adjusted  $R^2$ ; i.e. the distinction is less than 0.2. Closeness in the values of predicted  $R^2$  and adjusted  $R^2$  determines the maximum number of points falls within the regression line. The major difference between predicted  $R^2$  and adjusted  $R^2$  is that the predicted  $R^2$  assumes that the variation in the dependent variable is explained by each single variable. The adjusted  $R^2$  only informs the independent variables that actually influence the dependent variable, which explains the percentage of variation.

<b>Table 4.5</b> ANOVA table of full quadratic model for Penetration in MIG P							
Source	SS	DOF	MS=(SS/DOF)	F-value	P-value	Contrib. (%)	Remarks
Model	10.16	5	2.03	493.68	< 0.0001	99.72	significant
A-Current	4.99	1	4.99	1211.80	< 0.0001	51.00	
B-Welding Speed	3.72	1	3.72	904.19	< 0.0001	38.02	
AB-Current*Welding Speed	0.0256	1	0.0256	6.22	0.0413	0.26	
A*A	0.9990	1	0.9990	242.75	< 0.0001	10.21	
B*B	0.0495	1	0.0495	12.04	0.0104	0.51	
Residual	0.0288	7	0.0041			0.28	
Lack of Fit (LOF)	0.0217	3	0.0072	4.06	0.1048		Not significant
Pure Error	0.0071	4	0.0018				
Cor Total	10.19	12					
SD	0.0642		R*R				0.9972
Mean	2.32		Adjusted- R*R				0.9952
C.V. %	2.76		Predicted- R*R				0.9790
			Adequate Precision				77.9768

Adequate Precision measures the desirable signal-to-noise ratio (S / N), which is higher than 4 as shown in the ANOVA table. The developed models was found to be significant at a confidence level of 95%. It is desirable to have a ratio of more than 4 which shows a suitable signal [Goyal et al., 2015].

<b>Table 4.6</b> ANOVA table of full quadratic model for Penetration in MIG M							
Source	SS	DOF	MS=(SS/ DOF)	F-value	P-value	Contrib. (%)	Remarks
Model	11.03	5	2.21	404.08	< 0.0001	99.65	significant
A-Current	6.81	1	6.81	1246.08	< 0.0001	63.90	
B-Welding Speed	2.72	1	2.72	498.09	< 0.0001	25.52	
AB- Current*Welding Speed	0.0306	1	0.0306	5.61	0.0498	0.29	
A*A	1.05	1	1.05	191.70	< 0.0001	9.85	
B*B	0.0472	1	0.0472	8.64	0.0217	0.44	
Residual	0.0382	7	0.0055			0.35	
Lack of Fit (LOF)	0.0289	3	0.0096	4.15	0.1015		not significant
Pure Error	0.0093	4	0.0023				
Cor Total	11.07	12					
SD		0.0739		R*R			0.9965
Mean		2.54		Adjusted- R*R			0.9941
C.V. %		2.91		Predicted- R*R			0.9783
				Adequate Precision			69.2480

<b>Table 4.7</b> ANOVA table of full quadratic model for Dilution in CMT							
Source	SS	DOF	MS=(SS/ DOF)	F-value	P-value	Contrib. (%)	Remarks
Model	1530.67	5	306.13	4723.33	< 0.0001	99.97	significant
A-Current	993.82	1	993.82	15333.63	< 0.0001	64.69	
B-Welding Speed	460.95	1	460.95	7112.00	< 0.0001	30.00	
AB- Current*Welding Speed	0.8930	1	0.8930	13.78	0.0075	0.06	
A*A	74.33	1	74.33	1146.77	< 0.0001	4.84	
B*B	6.36	1	6.36	98.12	< 0.0001	0.41	
Residual	0.4537	7	0.0648			0.03	
Lack of Fit (LOF)	0.3214	3	0.1071	3.24	0.1429		not significant
Pure Error	0.1323	4	0.0331				



Cor Total	1531.13	12					
SD		0.2546		R*R			0.9997
Mean		36.51		Adjusted- R*R			0.9995
C.V. %		0.6974		Predicted- R*R			0.9977
				Adequate Precision			250.1793

<b>Table 4.8</b> ANOVA table of full quadratic model for Dilution in MIG P							
Source	SS	DOF	MS=(SS/DOF)	F-value	P-value	Contrib. (%)	Remarks
Model	2339.21	5	467.84	381.01	< 0.0001	99.63	significant
A-Current	1729.58	1	1729.58	1408.58	< 0.0001	72.15	
B-Welding Speed	339.00	1	339.00	276.08	< 0.0001	14.14	
AB-Current*Welding Speed	9.21	1	9.21	7.50	0.0290	0.38	
A*A	257.92	1	257.92	210.05	< 0.0001	10.76	
B*B	61.57	1	61.57	50.14	0.0002	2.57	
Residual	8.60	7	1.23			0.37	
Lack of Fit (LOF)	6.18	3	2.06	3.42	0.1330		not significant
Pure Error	2.41	4	0.6030				
Cor Total	2347.81	12					
SD		1.11		R*R			0.9963
Mean		44.76		Adjusted- R*R			0.9937
C.V. %		2.48		Predicted- R*R			0.9717
				Adequate Precision			65.0763

<b>Table 4.9</b> ANOVA table of full quadratic model for Dilution in MIG M							
Source	SS	DOF	MS=(SS/DOF)	F-value	P-value	Contrib. (%)	Remarks
Model	2572.78	5	514.56	680.33	< 0.0001	99.79	significant
A-Current	1872.67	1	1872.67	2475.99	< 0.0001	73.46	
B-Welding Speed	331.08	1	331.08	437.75	< 0.0001	12.99	
AB-Current*Welding Speed	5.20	1	5.20	6.87	0.0343	0.20	

A*A	335.85	1	335.85	444.05	< 0.0001	13.17	
B*B	4.37	1	4.37	5.78	0.0472	0.17	
Residual	5.29	7	0.7563			0.21	
Lack of Fit (LOF)	3.73	3	1.24	3.18	0.1464		not significant
Pure Error	1.56	4	0.3909				
Cor Total	2578.07	12					
SD	0.8697		R*R			0.9979	
Mean	50.94		Adjusted- R*R			0.9965	
C.V. %	1.71		Predicted- R*R			0.9861	
			Adequate Precision			84.9488	

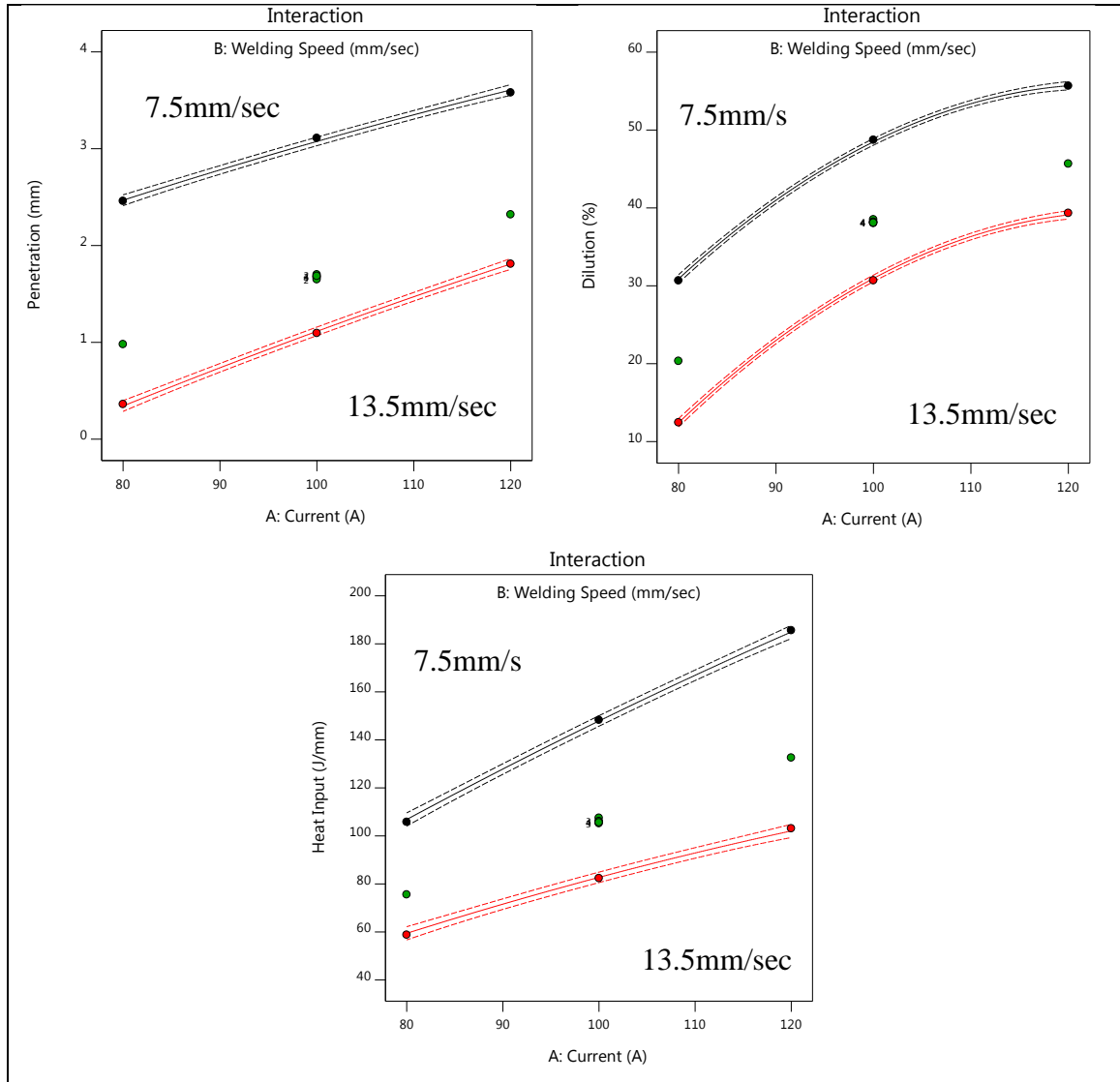
<b>Table 4.10</b> ANOVA table of full quadratic model for Heat Input in CMT							
Source	SS	DOF	MS=(SS/ DOF)	F-value	P-value	Contrib. (%)	Remarks
Model	12389.19	5	2477.84	1440.55	< 0.0001	99.90	significant
A-Current	5466.20	1	5466.20	3177.90	< 0.0001	44.11	
B-Welding Speed	6364.18	1	6364.18	3699.96	< 0.0001	51.36	
AB- Current*Welding Speed	314.53	1	314.53	182.86	< 0.0001	2.54	
A*A	10.92	1	10.92	6.35	0.0398	0.09	
B*B	236.64	1	236.64	137.58	< 0.0001	1.91	
Residual	12.04	7	1.72			0.10	
Lack of Fit (LOF)	8.99	3	3.00	3.93	0.1098		not significant
Pure Error	3.05	4	0.7630				
Cor Total	12401.23	12					
SD			1.31	R*R		0.9990	
Mean			109.42	Adjusted- R*R		0.9983	
C.V. %			1.20	Predicted- R*R		0.9923	
				Adequate Precision		140.8571	

<b>Table 4.11</b> ANOVA table of full quadratic model for Heat Input in MIG P							
Source	SS	DOF	MS=(SS/ DOF)	F-value	P-value	Contrib. (%)	Remarks
Model	20291.33	5	4058.27	6680.84	< 0.0001	99.98	significant

A-Current	6965.27	1	6965.27	11466.44	< 0.0001	34.52	
B-Welding Speed	12275.42	1	12275.42	20208.18	< 0.0001	60.84	
AB- Current*Welding Speed	478.95	1	478.95	788.47	< 0.0001	2.37	
A*A	3.44	1	3.44	5.67	0.0488	0.02	
B*B	455.11	1	455.11	749.22	< 0.0001	2.26	
Residual	4.25	7	0.6074			0.02	
Lack of Fit (LOF)	2.76	3	0.9199	2.47	0.2018		not significant
Pure Error	1.49	4	0.3731				
Cor Total	20295.58	12					
SD		0.7794		R*R			0.9998
Mean		151.59		Adjusted- R*R			0.9996
C.V. %		0.5141		Predicted- R*R			0.9987
				Adequate Precision			299.5455

<b>Table 4.12</b> ANOVA table of full quadratic model for Heat Input in MIG M							
Source	SS	DOF	MS=(SS/ DOF)	F-value	P-value	Contrib. (%)	Remarks
Model	25450.12	5	5090.02	2981.95	< 0.0001	99.95	significant
A-Current	9990.78	1	9990.78	5853.02	< 0.0001	39.30	
B-Welding Speed	14297.03	1	14297.03	8375.81	< 0.0001	56.24	
AB- Current*Welding Speed	603.05	1	603.05	353.29	< 0.0001	2.37	
A*A	9.66	1	9.66	5.66	0.0490	0.04	
B*B	522.56	1	522.56	306.14	< 0.0001	2.06	
Residual	11.95	7	1.71			0.05	
Lack of Fit (LOF)	5.40	3	1.80	1.10	0.4462		not significant
Pure Error	6.55	4	1.64				
Cor Total	25462.07	12					
SD		1.31		R*R			0.9995
Mean		162.66		Adjusted- R*R			0.9992
C.V. %		0.8032		Predicted- R*R			0.9975
				Adequate Precision			201.9403

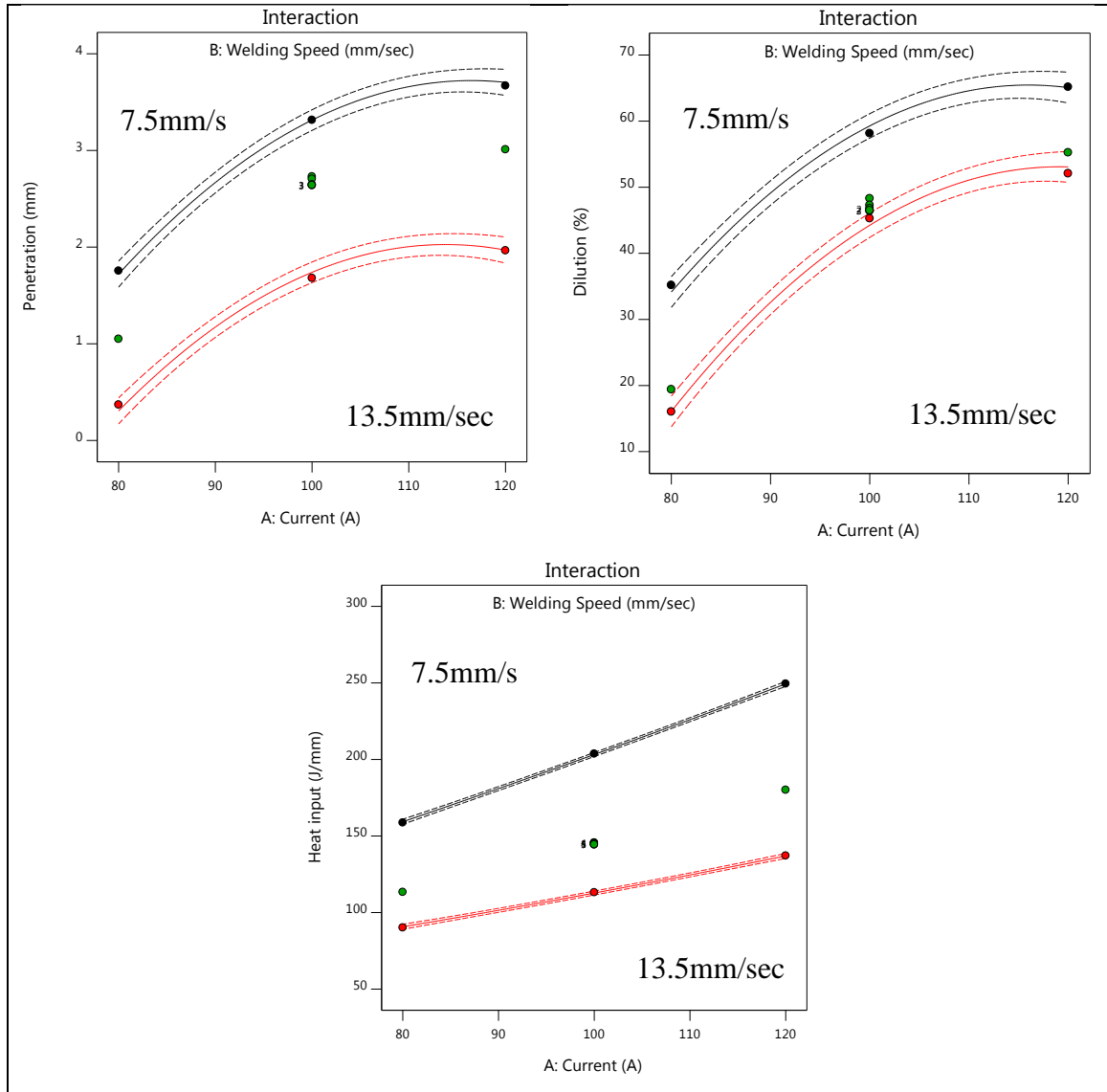
It can be noticed from Fig. 4.6, 4.7 and 4.8 that the confidence interval (95%) is very near to the average value in CMT as compared with MIG P and MIG M. The black curve indicates the welding speed of 7.5 mm/sec whereas the red curve indicated the welding speed of 13.5 mm/sec.



**Fig. 4.6** Interaction curve of input and output parameters for CMT

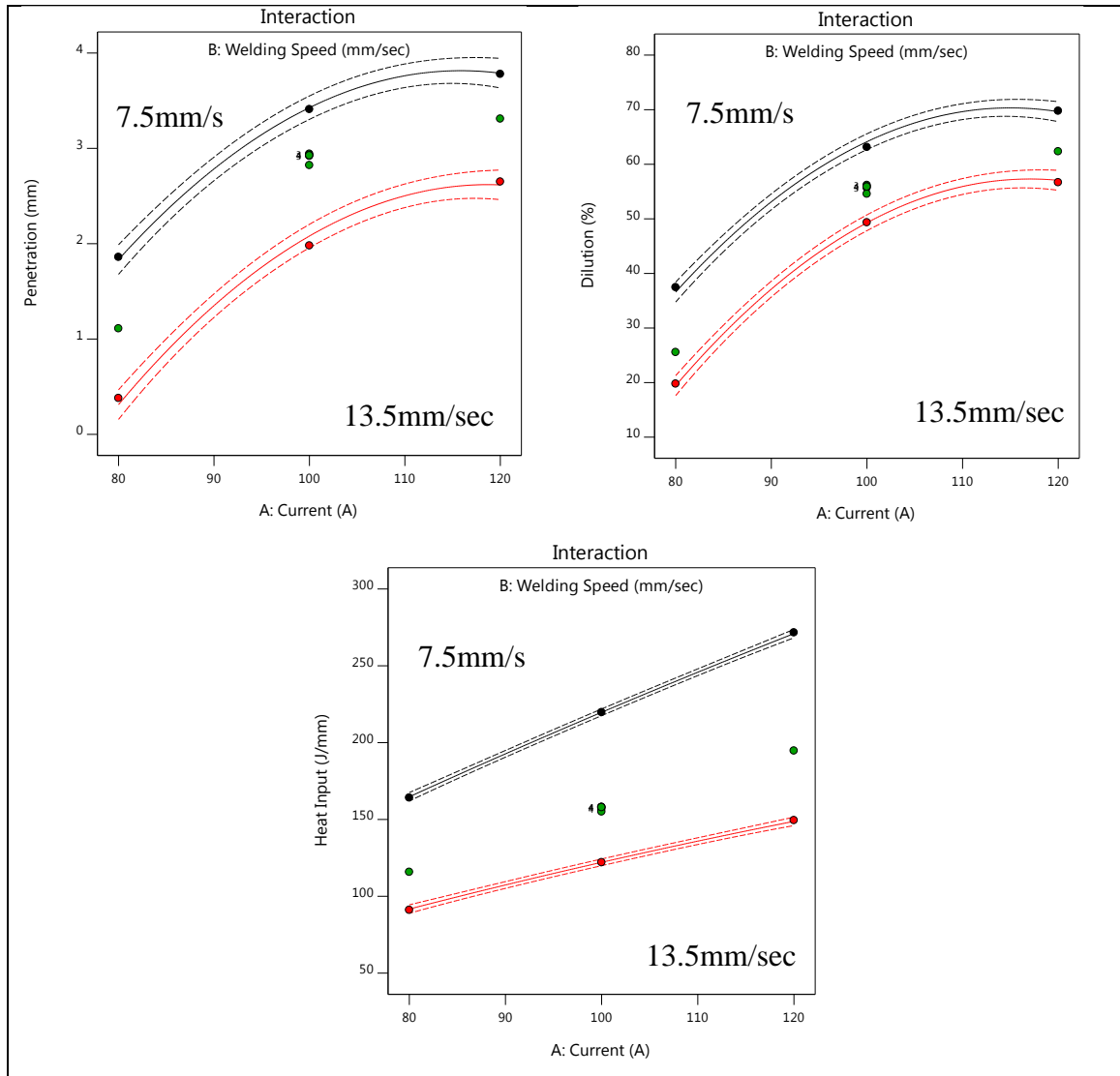
For the current factor settings, 95 % of the confidence intervals produced from comparable autonomous experiments will contain the real average result. From this, it can be stated that CMT is achieving similar amount of penetration as compared with MIG P and MIG M by almost reducing the heat input to 50 % which is helps in energy saving. Dilution is a

key factor in these responses, as higher percentage of dilution means deeper penetration and lower reinforcement height. Dilution should be in the range of 35-45 % as discussed by various researchers and scientists in MIG welding. CMT is achieving the dilution in the satisfactory range by almost saving on 50 % energy.



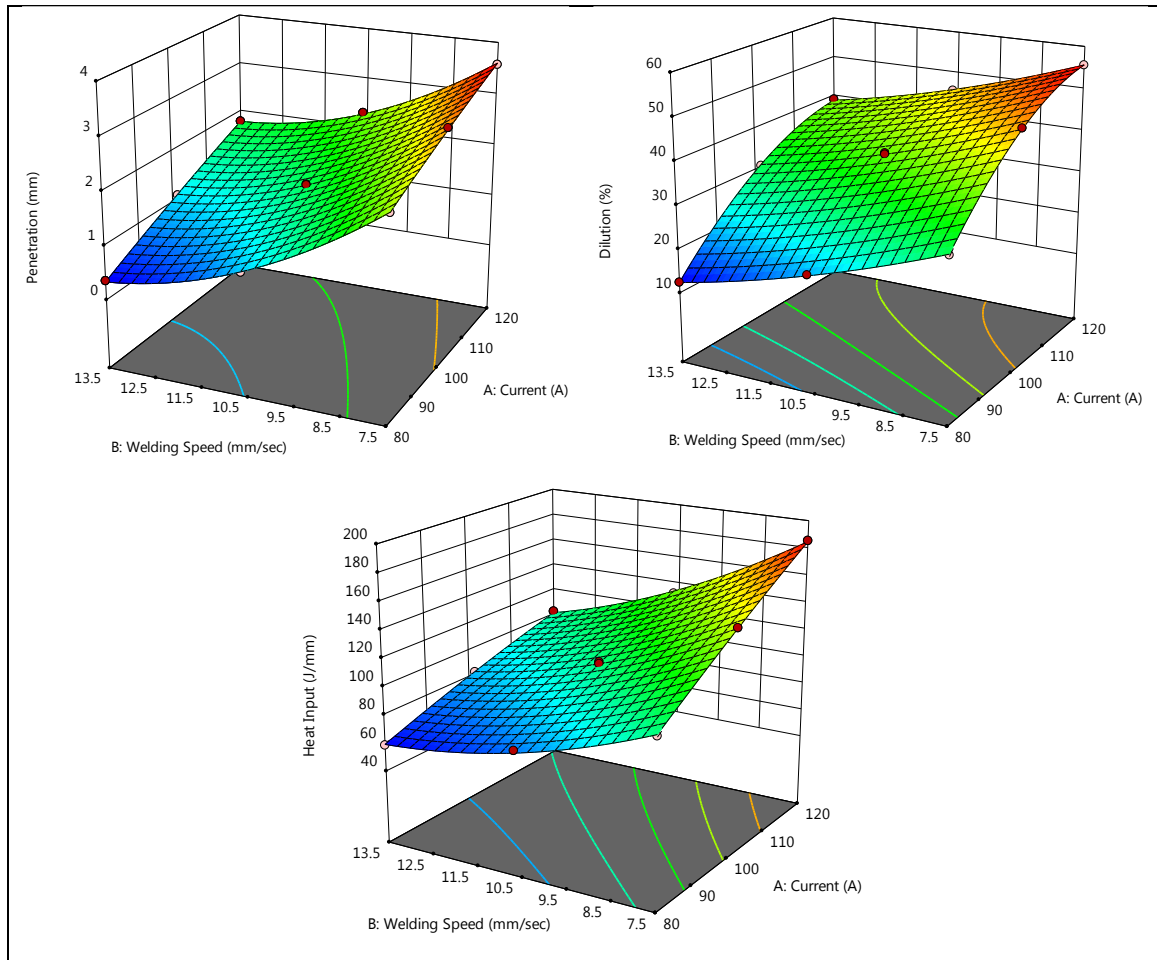
**Fig. 4.7** Interaction curve of input and output parameters for MIG P

Too high dilution results in creating holes (burn through) during welding of thin plates (2-3 mm) whereas too low dilution results in insufficient joining of the plates. Lower dilution (<5 %) is achieved by CMT for cladding purpose as claimed by the Fronius itself.

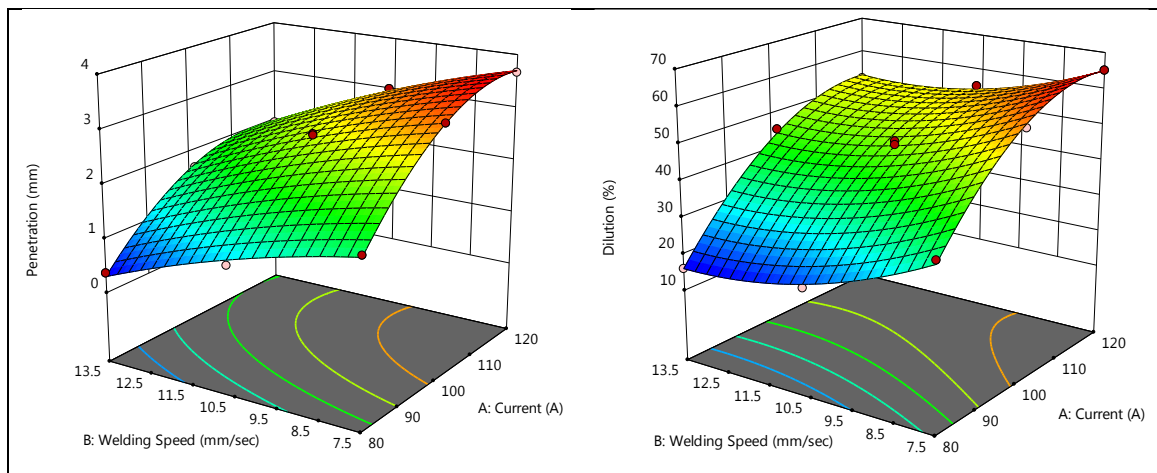


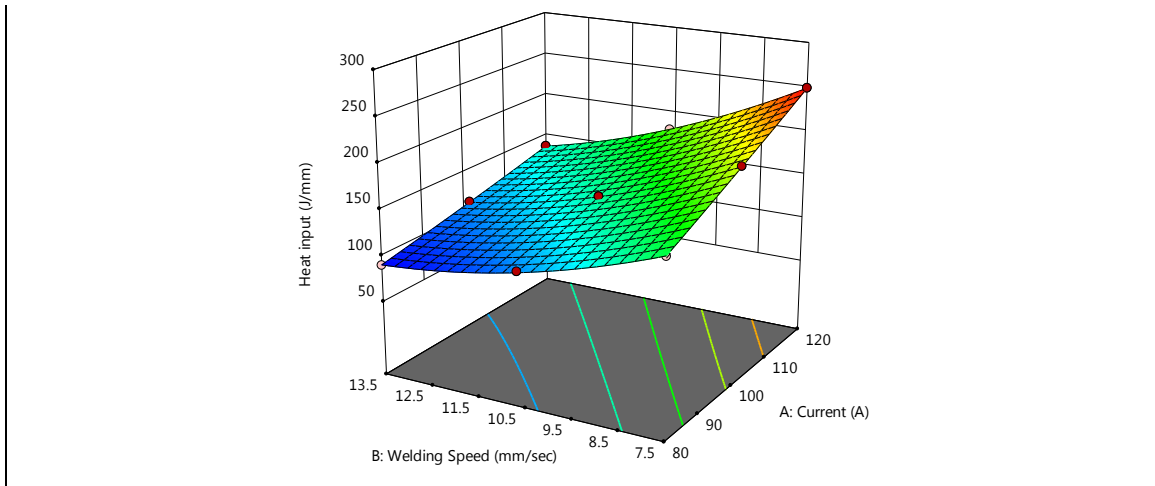
**Fig. 4.8** Interaction curve of input and output parameters for MIG M

Fig. 4.9, 4.10 and 4.11 shows the 3-D surface plot of interaction between input and output parameters for CMT, MIG P and MIG M.



**Fig. 4.9** 3-D surface plot of interaction between input and output parameters for CMT





**Fig. 4.10** 3-D surface plot of interaction between input and output parameters for MIG P

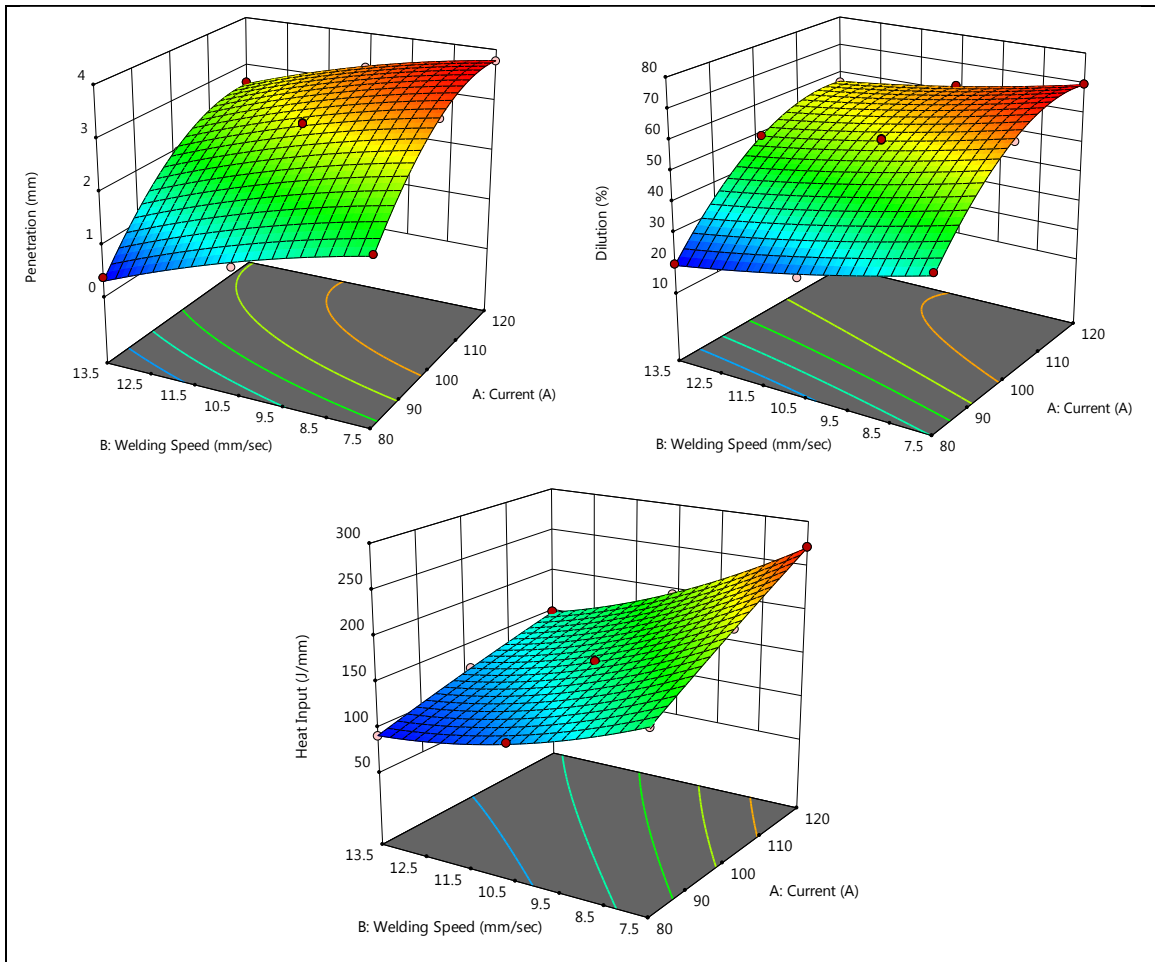


**Fig. 4.11** 3-D surface plot of interaction between input and output parameters for MIG M



With the assistance of the model equations, percentage error is calculated from actual and predicted values as shown in Table 4.13, 4.14 and 4.15 for CMT, MIG P and MIG M respectively. The average % error is minimum for CMT as compared to MIG P and MIG M, which states high repeatability of weld geometry in CMT.

<b>Table 4.13</b> Model reliability for CMT											
S.no	I (A)	S (mm/ sec)	Penetration (mm)		% error	Dilution (%)		% error	Heat Input (J/mm)		% error
			Actual	Pred.		Actual	Pred.		Actual	Pred.	
1	80	7.5	2.460	2.471	-0.449	30.67	30.897	-0.739	105.81	106.843	-0.977
2	80	10.5	0.980	0.993	-1.370	20.34	20.142	0.974	75.58	73.886	2.241
3	80	13.5	0.361	0.345	4.363	12.35	12.422	-0.582	58.79	59.442	-1.109
4	100	7.5	3.110	3.080	0.975	48.73	48.482	0.509	148.27	147.881	0.262
5	100	10.5	1.670	1.684	-0.857	38.16	38.199	-0.103	105.90	106.057	-0.148
6	100	13.5	1.095	1.118	-2.137	30.69	30.952	-0.853	82.37	82.745	-0.455
7	120	7.5	3.580	3.613	-0.925	55.67	55.692	-0.039	185.60	184.941	0.355
8	120	10.5	2.320	2.300	0.862	45.67	45.882	-0.464	132.57	134.249	-1.267
9	120	13.5	1.810	1.816	-0.351	39.34	39.107	0.593	103.11	102.070	1.009
Average %error					0.012			-0.078			-0.010

<b>Table 4.14</b> Model reliability for MIG P											
S.no	I (A)	S (mm/ sec)	Penetration (mm)		% error	Dilution (%)		% error	Heat Input (J/mm)		% error
			Actual	Pred.		Actual	Pred.		Actual	Pred.	
1	80	7.5	1.755	1.718	2.084	35.19	34.155	2.942	158.72	159.326	-0.382
2	80	10.5	1.05	1.145	-9.041	19.41	20.399	-5.097	113.37	112.200	1.032
3	80	13.5	0.37	0.304	17.941	16.04	16.087	-0.291	88.18	90.747	-2.911
4	100	7.5	3.315	3.310	0.155	58.15	59.279	-1.942	203.73	203.224	0.248
5	100	10.5	2.705	2.656	1.797	47.3	47.042	0.546	145.52	145.156	0.250
6	100	13.5	1.68	1.735	-3.280	45.28	44.246	2.283	113.19	112.760	0.380
7	120	7.5	3.67	3.698	-0.766	65.17	65.077	0.143	252.16	249.356	1.112
8	120	10.5	3.01	2.965	1.506	55.25	54.356	1.617	180.11	180.345	-0.130
9	120	13.5	1.965	1.963	0.081	52.09	53.079	-1.898	140.09	137.007	2.201
Average %error					1.164			-0.189			0.200

<b>Table 4.15</b> Model reliability for MIG M											
S.no	I (A)	S (mm/ sec)	Penetration (mm)		% error	Dilution (%)		% error	Heat Input (J/mm)		% error
			Actual	Pred.		Actual	Pred.		Actual	Pred.	
1	80	7.5	1.86	1.835	1.336	37.45	36.585	2.311	164.13	164.790	-0.402
2	80	10.5	1.11	1.205	-8.552	25.56	26.759	-4.689	115.81	114.499	1.132
3	80	13.5	0.38	0.313	17.543	19.78	19.448	1.679	91.074	91.718	-0.707
4	100	7.5	3.41	3.429	-0.560	63.13	64.139	-1.598	219.73	219.743	-0.006
5	100	10.5	2.92	2.886	1.152	55.67	55.453	0.390	156.95	157.174	-0.142
6	100	13.5	1.98	2.082	-5.163	49.34	49.282	0.117	122.07	122.114	-0.036
7	120	7.5	3.78	3.792	-0.313	69.78	69.639	0.203	271.64	270.956	0.252
8	120	10.5	3.31	3.337	-0.803	62.34	62.093	0.397	194.74	196.108	-0.703
9	120	13.5	2.65	2.620	1.135	56.67	57.062	-0.692	149.47	148.770	0.468
Average %error					0.642			-0.209			-0.016

#### 4.2.5 Process Parameter Optimization

RSM's desirability function optimization was used for multi-response optimization. Target was set using the optimization process to obtain optimal process parameter values to maximize penetration and dilution while minimizing the heat input at the same time. Penetration and dilution is maximized to get higher depth and fusion by using filler wire, which increases the mechanical properties of the joint. Whereas heat input is minimized for energy conservation. Table 4.16 summarizes the criteria used in the optimization method.

<b>Table 4.16</b> Criteria of optimal parameters								
			CMT		MIG P		MIG M	
Factors	Units	Goal	Min. limit	Max. limit	Min. limit	Max. limit	Min. limit	Max. limit
Current	A	In range	80	120	80	120	80	120
Welding Speed	mm/sec	In range	7.5	13.5	7.5	13.5	7.5	13.5
Penetration	mm	Maximum	0.361	3.58	0.37	3.67	0.38	3.78
Dilution	%	Maximum	12.45	55.67	16.04	65.17	19.78	69.78
Heat Input	J/mm	Minimum	58.79	185.6	90.18	249.45	91.074	271.64

In this current and welding speed are in range as per DOE whereas the output response is denoted as maximum or minimum. For best output, penetration and dilution is maximized keeping the heat input at minimum level which states that with minimum amount of heat input, maximum output can be achieved. The optimal solutions are stated in Table 4.17 in order of decreasing desirability level. The optimal values of current and welding speeds are 92.518 A and 7.50 mm/sec respectively for CMT process with 61.11 % desirability. These optimal parameters creates a response for the values of minimum heat input (132.999 J/mm) and maximum dilution (43.118 %) and penetration (2.857 mm), which gives an aesthetic weld bead with higher joint efficiency. The optimal values of current and welding speeds are 109.418 A and 10.873 mm/sec respectively for MIG P with 68.80 % desirability. These optimal parameters creates an optimal response of 2.852 mm, 52.120 % and 155.372 J/mm for penetration, dilution and heat input respectively. For MIG M, 110.847 A and 11.527 mm/sec are the optimal parameters that gives 3.051 mm, 59.606 % and 161.381 J/mm response values for penetration, dilution and heat input with 72.60 % desirability as shown in Fig. 4.12.

<b>Table 4.17</b> Optimization result for optimal parameters							
CMT							
Number	Current	Welding Speed	Penetration	Dilution	Heat Input	Desirability	
1	92.518	7.500	2.857	43.118	132.999	0.611	Selected
2	92.318	7.500	2.851	42.955	132.593	0.611	
3	92.742	7.500	2.864	43.300	133.452	0.611	
4	92.956	7.500	2.870	43.472	133.885	0.611	
5	91.893	7.500	2.838	42.604	131.729	0.611	
6	120.000	10.954	2.167	44.663	128.203	0.574	
MIG P							
1	109.418	10.873	2.852	52.120	155.372	0.688	Selected
MIG M							
1	110.847	11.527	3.051	59.606	161.381	0.726	Selected

It is observed that, optimal process parameters for CMT is lower as compared to MIG P and MIG M. With lesser amount of current and welding speed, CMT achieves a good depth of penetration, which is almost similar to MIG P and MIG M with low THI.

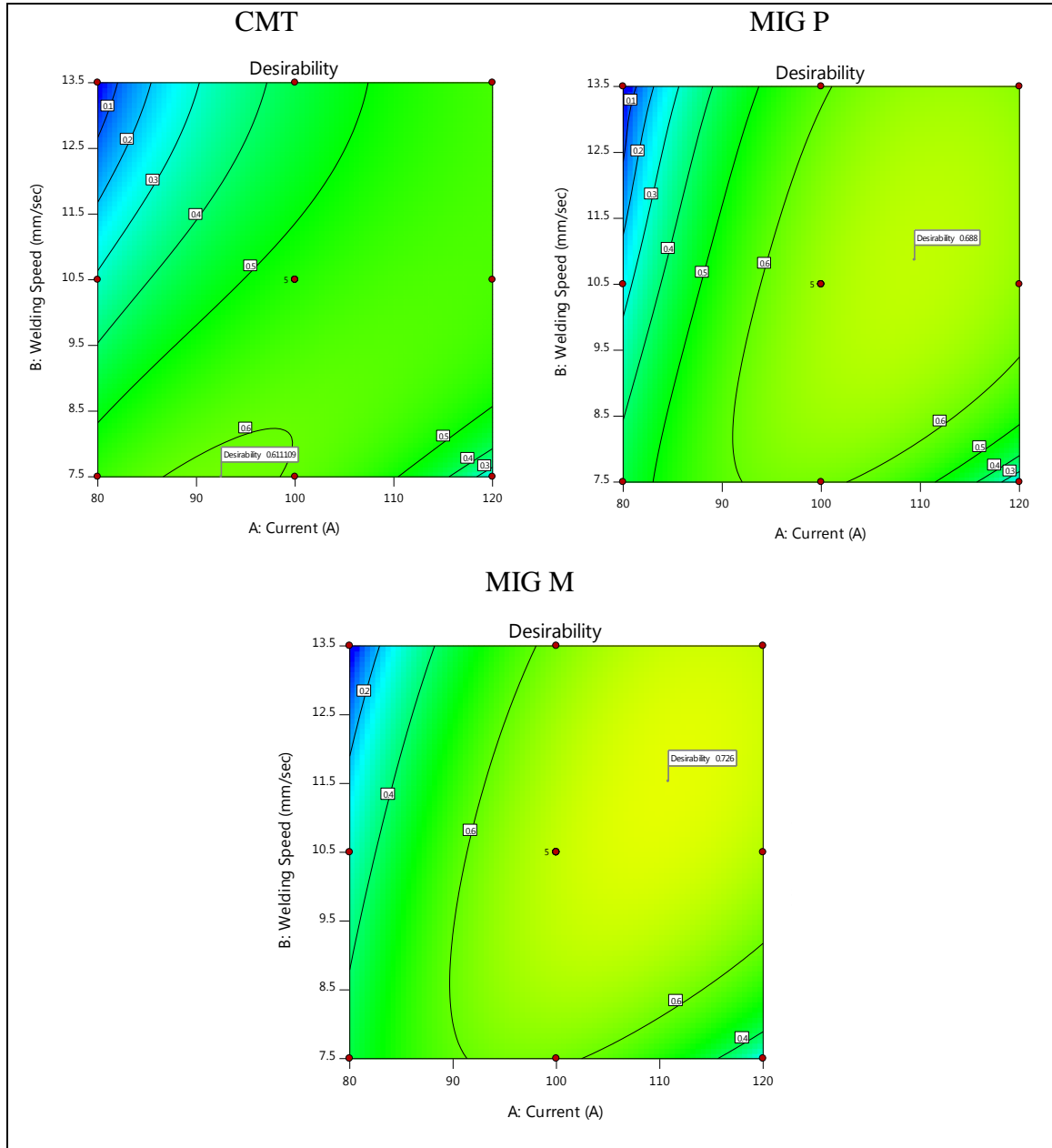


**Fig. 4.12** Desirability curve of CMT, MIG P and MIG M

#### 4.2.6 Confirmation Test

Confirmation test is the additional trials done at the single combination of optimal parameters. The average of a response's confirmation test is compared to the prediction interval from the model. The model is confirmed if the average observation from the confirmation experiment falls within the prediction interval of the confirmation node. In order to validate the model three confirmatory runs were performed for each of the welding process (CMT, MIG P and MIG M) and then the mean value is taken as depicted in Table 4.18. Using design expert software's point prediction capability, the results were predicted at a 95 % confidence level. Predicted values of penetration, dilution and heat input were calculated from model equations.

<b>Table 4.18</b> Confirmation test				
CMT (I=92.5A and S=7.5mm/sec)				
	Experimental data mean	Predicted values	Standard Deviation	% error
Penetration	2.84267	2.85683	0.026532	-0.49812
Dilution	43.216	43.1148	0.254584	0.234173
Heat Input	132.484	132.991	1.31151	-0.38269
MIG P (I=109.4A and S=10.9mm/sec)				
	Experimental data mean	Predicted values	Standard Deviation	% error
Penetration	2.87067	2.86962	0.06415	0.036577
Dilution	52.69	52.1274	1.1081	1.067755
Heat Input	156.85	156.082	0.77939	0.48964
MIG M (I=110.8A and S=11.5mm/sec)				
	Experimental data mean	Predicted values	Standard Deviation	% error
Penetration	3.073	3.0535	0.0739013	0.634559
Dilution	59.9833	59.6047	0.869673	0.631176
Heat Input	161.965	161.465	1.3065	0.308709

### 4.3 MACROSTRUCTURE OF WELD BEAD

Macrostructure in the cross-sectional direction of the weldment clearly shows the amount of pores that are present in the weld, depth of penetration, reinforcement, HAZ and BM. Fig. 4.13, 4.14 and 4.15 shows the macro-images of cross-section of CMT, MIG pulse synergic and MIG manual weld bead respectively.

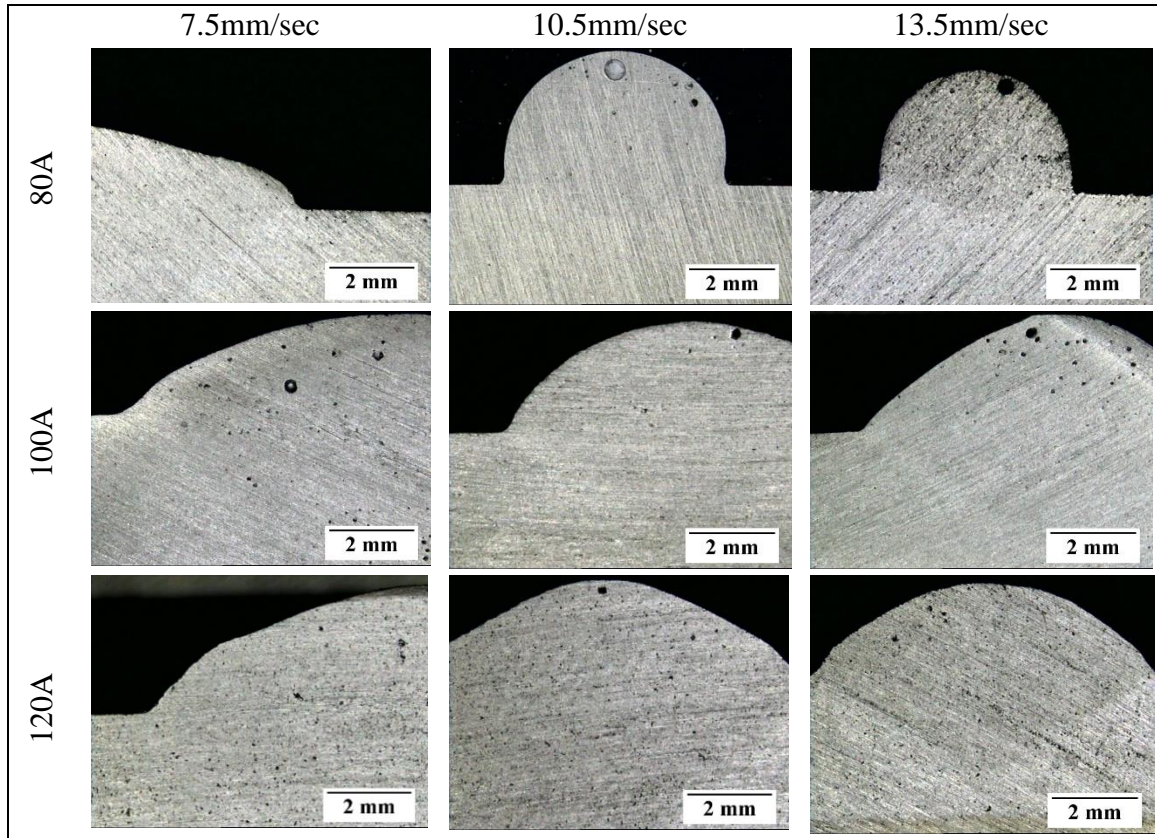


**Fig. 4.13** Macro-images of CMT weld bead

It can be seen that MIG P and MIG M is having high number of pores, which is formed due to gases entrapment when bead undergoes fusion. At such high heat inputs in MIG M and MIG P, aluminium alloys are susceptible to solubility of gases, majorly hydrogen which creates porosity. In contrast to heat input, alloying element is also responsible for hydrogen solubility. Mg element in aluminium alloys has high hydrogen affinity because the interactions between the Mg atoms and hydrogen atoms are stronger than those between aluminium and hydrogen [Anyalebechi, 1995]. Different welding zones are also visible after polishing and etching of the samples. Welding process parameters has

variable effect on the weld bead, as current increases while keeping welding speed constant all the weld geometry increases due to high amount of high input. As welding speed increases while keeping current constant, penetration, weld width and dilution is decreased due to low heat input. Fig. 4.16 (B & C), shows the crack formation on the plates of MIG P and MIG M. When heat input is 249.45 J/mm (120 A, 7.5 mm/sec) for MIG P and 271.64 J/mm (120 A, 7.5 mm/sec) & 194.74 (120 A, 10.5 mm/sec) for MIG M, cracks are seen on the surface of the bead with high amount of deposition. This elevated heat input and rapid cooling of the molten pool produces high amount of tensile residual stresses, which leads to formation of cracks on the surface of the bead.

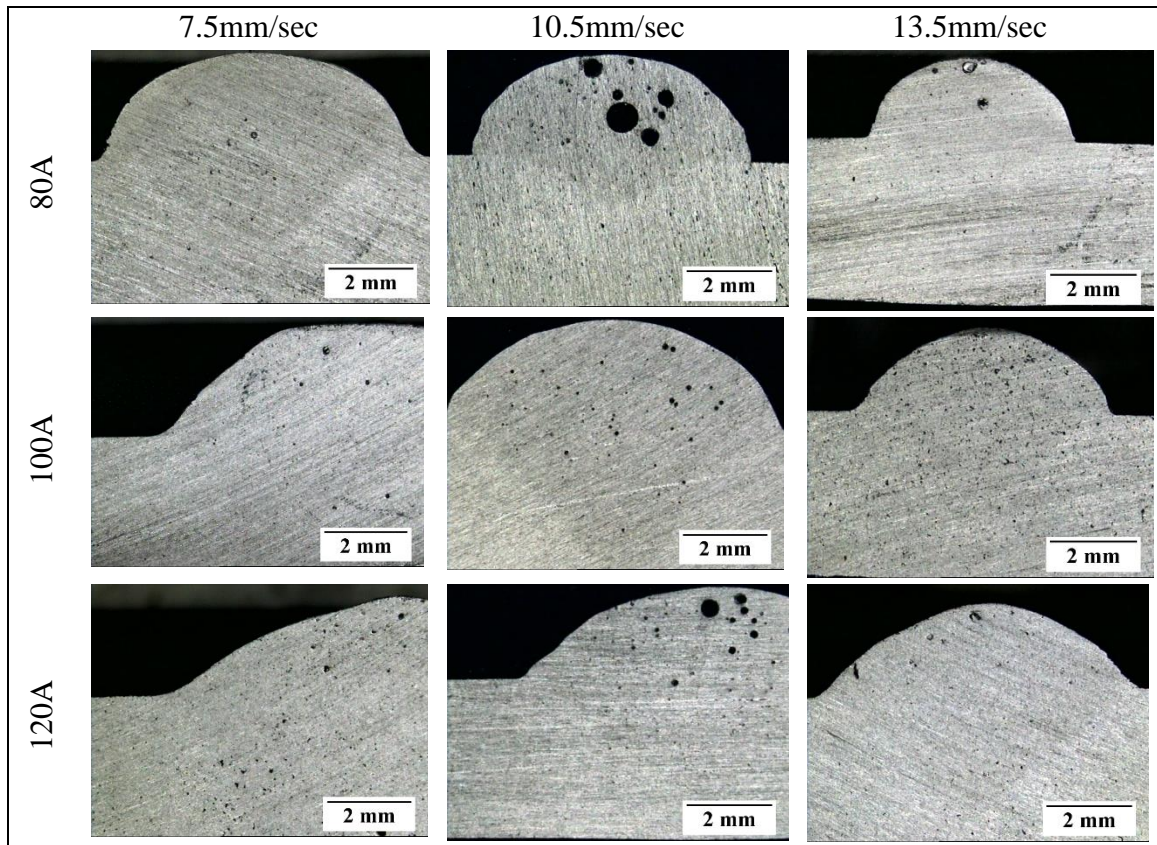


**Fig. 4.14** Macro-images of MIG P weld bead

CMT is a welding process of low heat input is able to produce beads free from cracks with the same process parameters as shown in Fig. 4.16 (A). It is noticed that the oxide layer deposition (aluminium oxide) i.e. white layer adjacent to the weld bead, is having more thickness in MIG P and MIG M as compared to CMT. Black soot, which is highly shown



in MIG P and MIG M plates of 120 A, is magnesium oxide, which is formed by vaporized magnesium due to arc's heat.

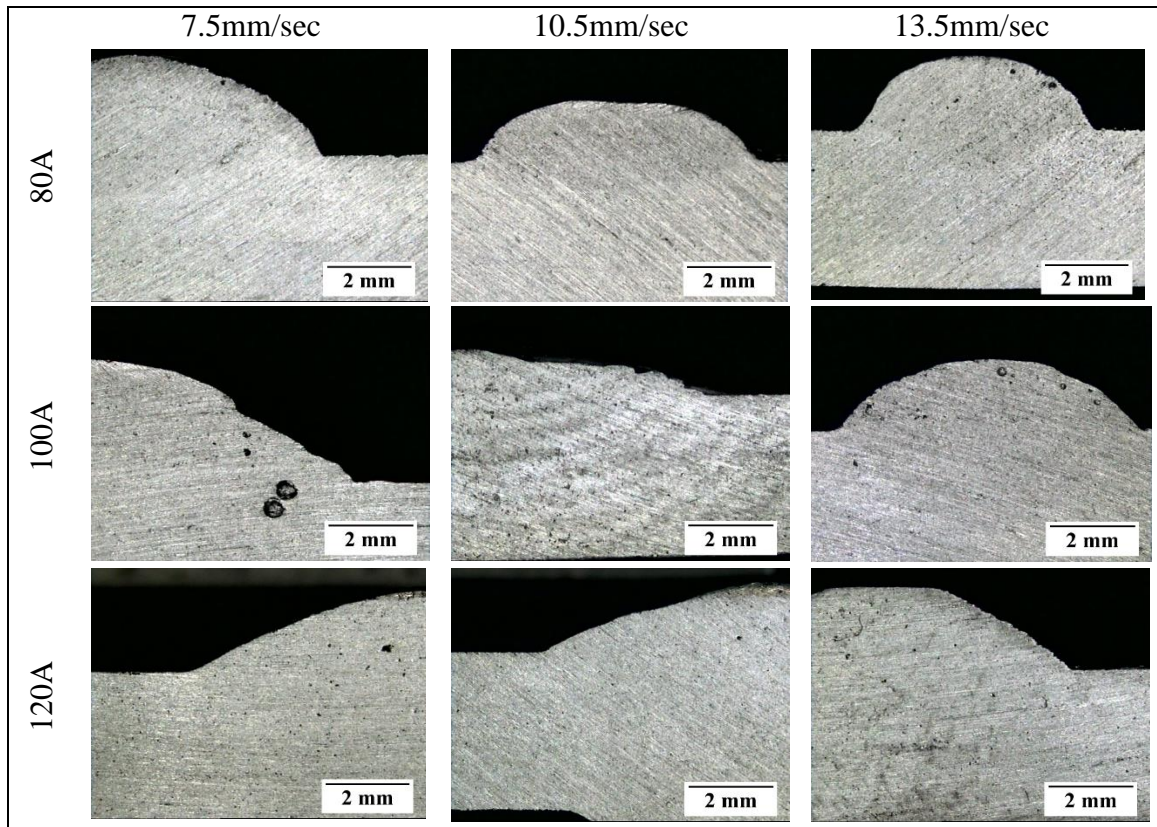


**Fig. 4.15** Macro-images of MIG M weld bead

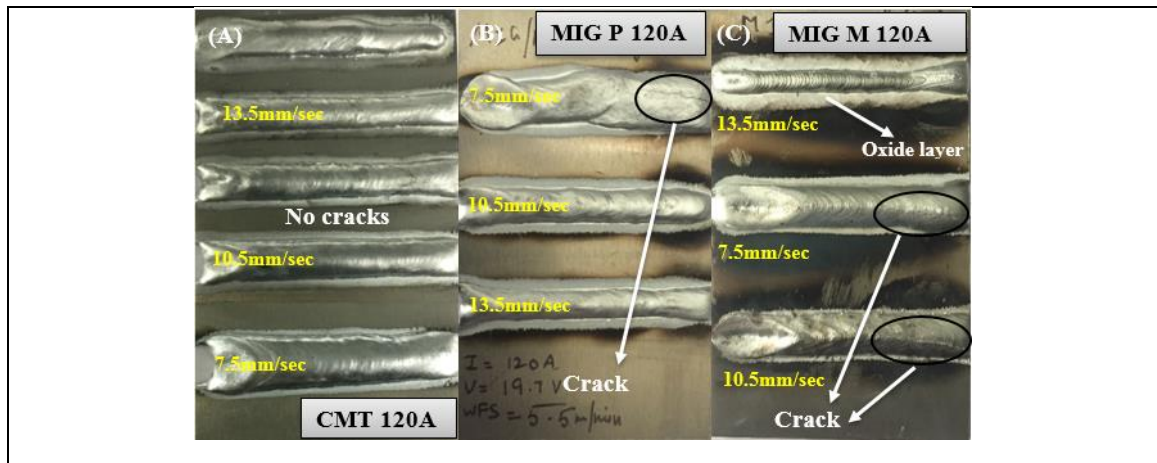


**Fig. 4.16** (A) No crack on CMT 120 A; Crack formation on bead on plate (B) MIG P (120 A) (C) MIG M (120 A)



#### 4.3.1 Consequence of welding parameters on bead dimensions

Process parameters i.e. current and welding speed have major effect on the weld bead geometry, mechanical properties and its microstructural analysis. It is clearly shown in the Fig. 4.17 that with increase in welding speed (7.5 mm/sec to 13.5 mm/sec) at constant current (80 A) for a specific welding technique (CMT), the penetration is reduced to almost 50% of the initial value owing to its minimal heat input. It is also shown that weld width is decreasing with rise in the welding speed while reinforcement height is having less change as compared to weld width owing to its minimal heat input. Fig. 4.18 shows the increase in penetration with increasing current (80 A to 120 A) by keeping welding speed (13.5 mm) constant. For the interval of 80 A to 100 A, penetration increases drastically and then increases gradually with rise in current owing to increase in heat input. The width of the weld increases gradually due to the rise in heat input.

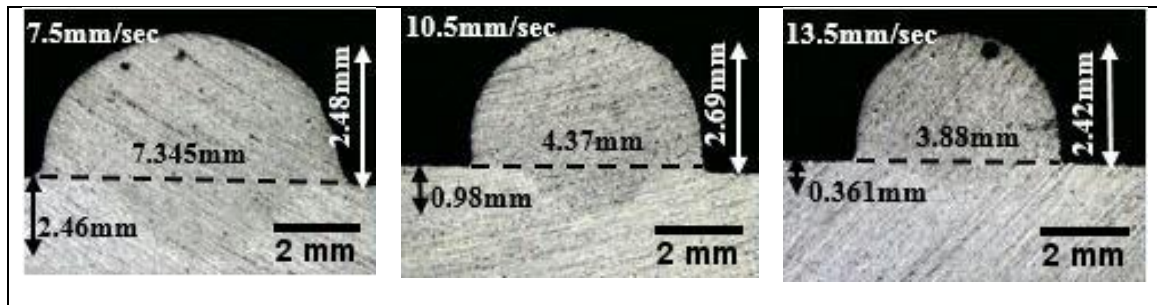


**Fig. 4.17** Variation in macro-images of bead geometry for variable welding speeds (7.5mm/sec, 10.5mm/sec and 13.5mm/sec) at constant current of 80A for CMT process

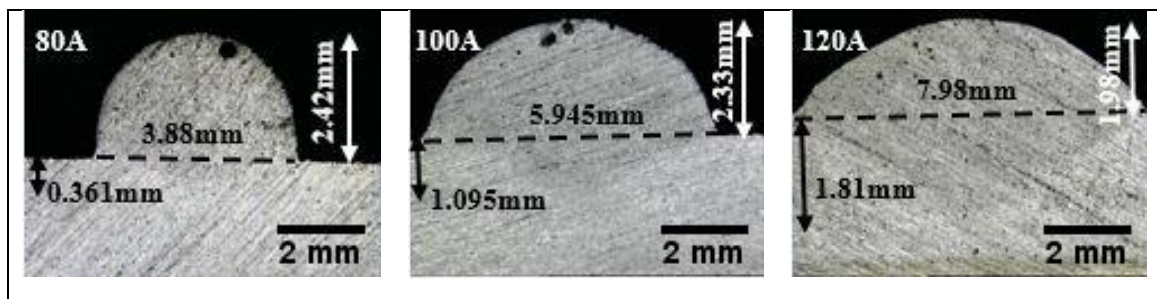


**Fig. 4.18** Variation in macro-images of bead geometry for variable current (80A, 100A and 120A) at constant welding speed of 13.5mm/sec for CMT process

#### 4.3.2 Consequence of different welding techniques on bead dimensions

CMT, MIG P and MIG M are the three welding techniques employed in this work. The major difference between the three is the mode of droplet transfer and the heat input produced during welding. It can be seen from Fig. 4.19 that CMT is producing lower penetration as compared to MIG P and MIG M at 100A current and 13.5 mm.sec of welding speed, but the bead profile is aesthetic for CMT. From higher current (120 A) and lower welding speed (7.5 mm/sec), CMT (3.58 mm) produces nearly the same penetration depth compared to MIG P (3.67 mm) and MIG M (3.78 mm) from nearly 35 % and 46 % lower heat input compared to MIG P and MIG M respectively.

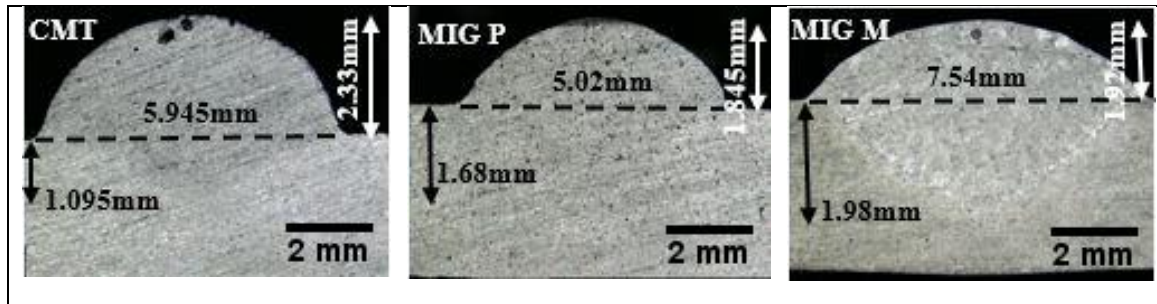


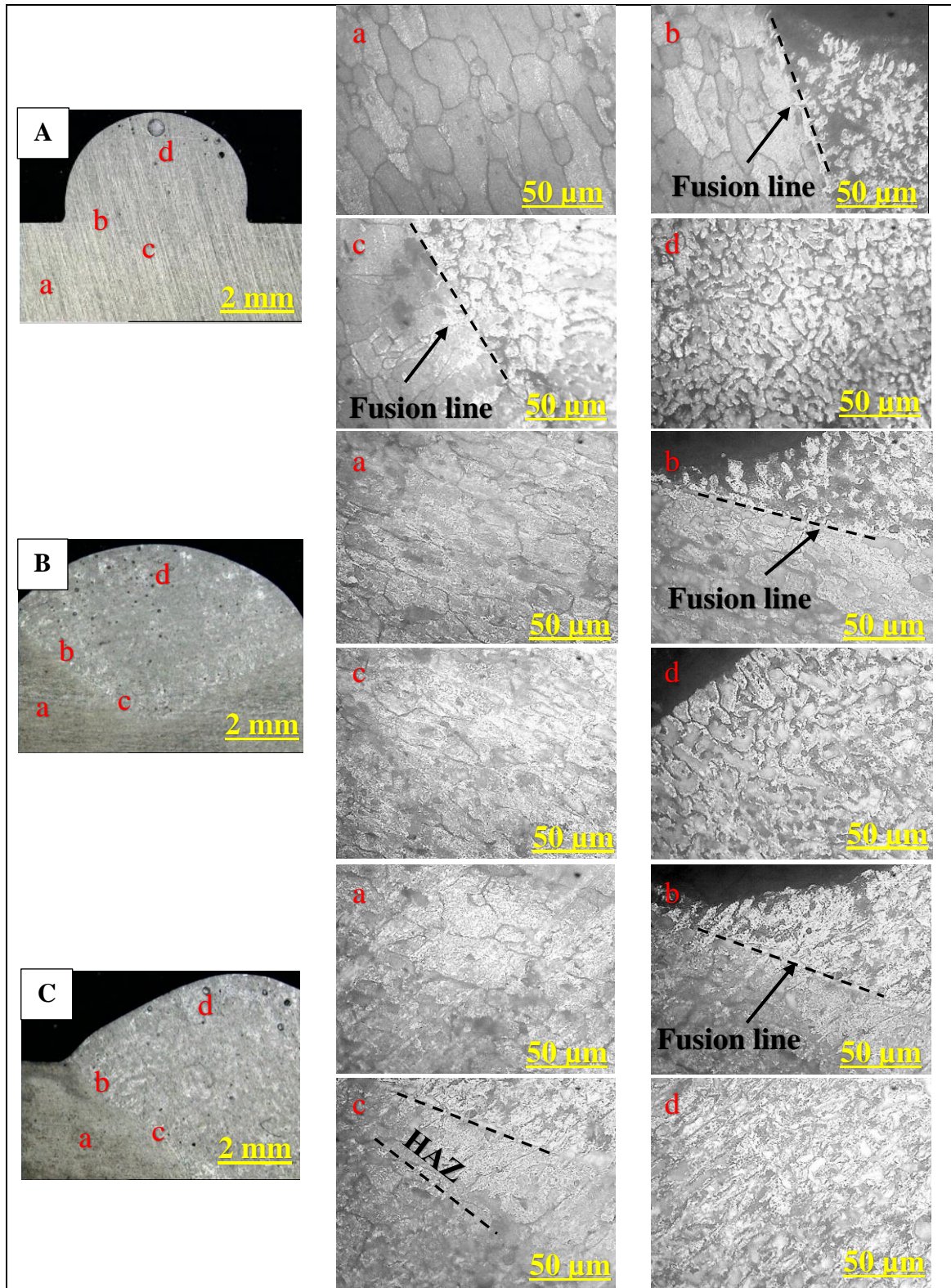
**Fig. 4.19** Variation in macro-images of bead geometry for different welding techniques (CMT, MIGP and MIG M) at constant current (100A) and welding speed (13.5mm/sec)

#### 4.4 MICROSTRUCTURAL ANALYSIS

Olympus GX41 compact inverted metallurgical microscope is used for microstructural images. Fig. 4.20, 4.21 and 4.22 shows the microstructural images from optical microscope for CMT, MIG P and MIG M respectively. Three samples were taken for examining the microstructure from each welding processes. Microstructure is taken at the (a) BM, (b & c) FZ and (d) WM. Image (b) clearly shows the fusion line where AA6061-T6 substrate material and ER4043 filler metal fuses. It can be clearly noticed from Fig. 4.20 (b), 4.21 (b) and 4.22 (b) the difference in the microstructure of parent metal and weld zone, which is separated by fusion line (shown in black dashes). Grain boundaries and grain structure is clearly shown in Fig. 4.20 (a), 4.21 (a) and 4.22 (a) which is representing parent metal. At higher current (i.e. 120 A) values it is noticed that high amount of black spot is seen in the parent metal and bead region, which is due to high heat input. It causes non-uniformity

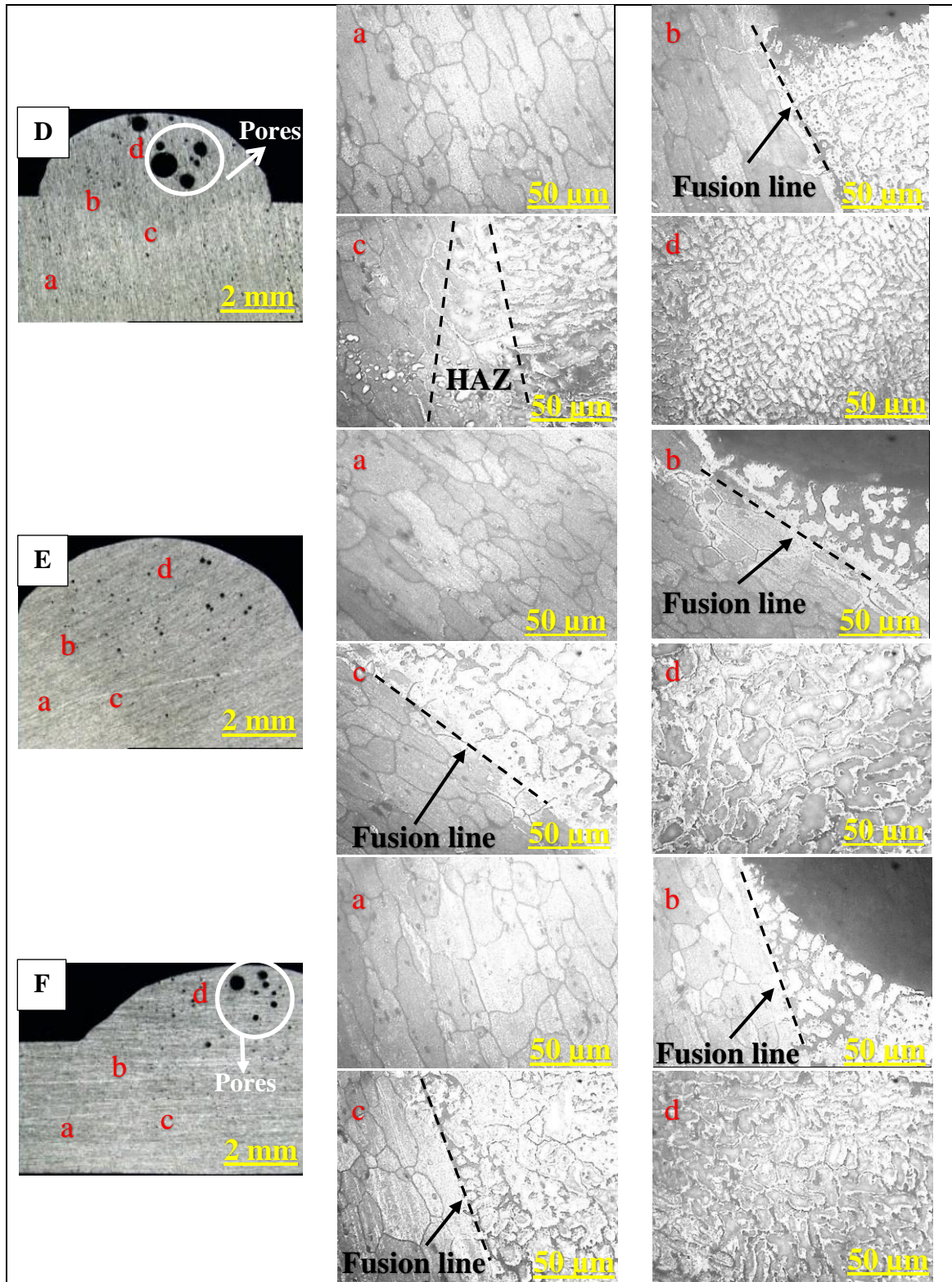
in cooling rate, which results in high amount of brittle compounds ( $\text{Mg}_2\text{Si}$ ) that is seen as the black spots.  $\text{Mg}_2\text{Si}$  dissolves in FZ of the weld bead and results in large precipitation and coarsening of grains [Ahmad and Bakar 2011, Maisonnnette et al., 2011]. These black spots deteriorates the mechanical properties and surface profile of the bead. It is more in MIG M process as compared to CMT and MIG P. High amount of pores are present in MIG P (Fig. 4.21) and MIG M (Fig. 4.22) as compared to CMT (Fig. 4.20), which weakens the joint, and results in reduced tensile strength. CMT is showing better microstructures as compared to MIG M and MIG P owing to its spatter free welds even at high current inputs and better bead aesthetics. FESEM help us examine the morphology and microstructure. Fig. 4.23 shows the FESEM images of fusion zone of CMT at 100 A current with 10.5 mm/sec of welding speed. Fig. 4.23 (b) shows large precipitates of dissolved  $\text{Mg}_2\text{Si}$  in FZ. FESEM clearly shows the difference among the grain structure that is formed due to non-uniformity in temperature. This is majorly seen in the weld bead and fusion zone where high heat input is experienced. The samples were subjected to X-ray diffraction for the identification of the formation of intermetallic phases. As the parent material and filler material majorly constituting aluminum and silicon so primary peaks depicts the same as the major elements as shown in Fig. 4.24, which is confirmed by EDX plots. XRD plots shows lesser amount of intermetallic in CMT as compared to MIG P and MIG M owing to its low heat input. XRD plot of CMT depicts only  $\text{Mg}_2\text{Si}$  and  $\text{Al}_{12}\text{Mg}_{17}$  binary phases, which exists at lower temperature of 580 °C and 450 °C respectively.  $\text{Fe}_2\text{Si}$  binary phase is formed in both MIG P and MIG M, which exists at a temperature of about 1100 °C – 1200 °C due to their high thermal heat input. More amount of intermetallic phases causes lower mechanical properties which results in strength degradation.





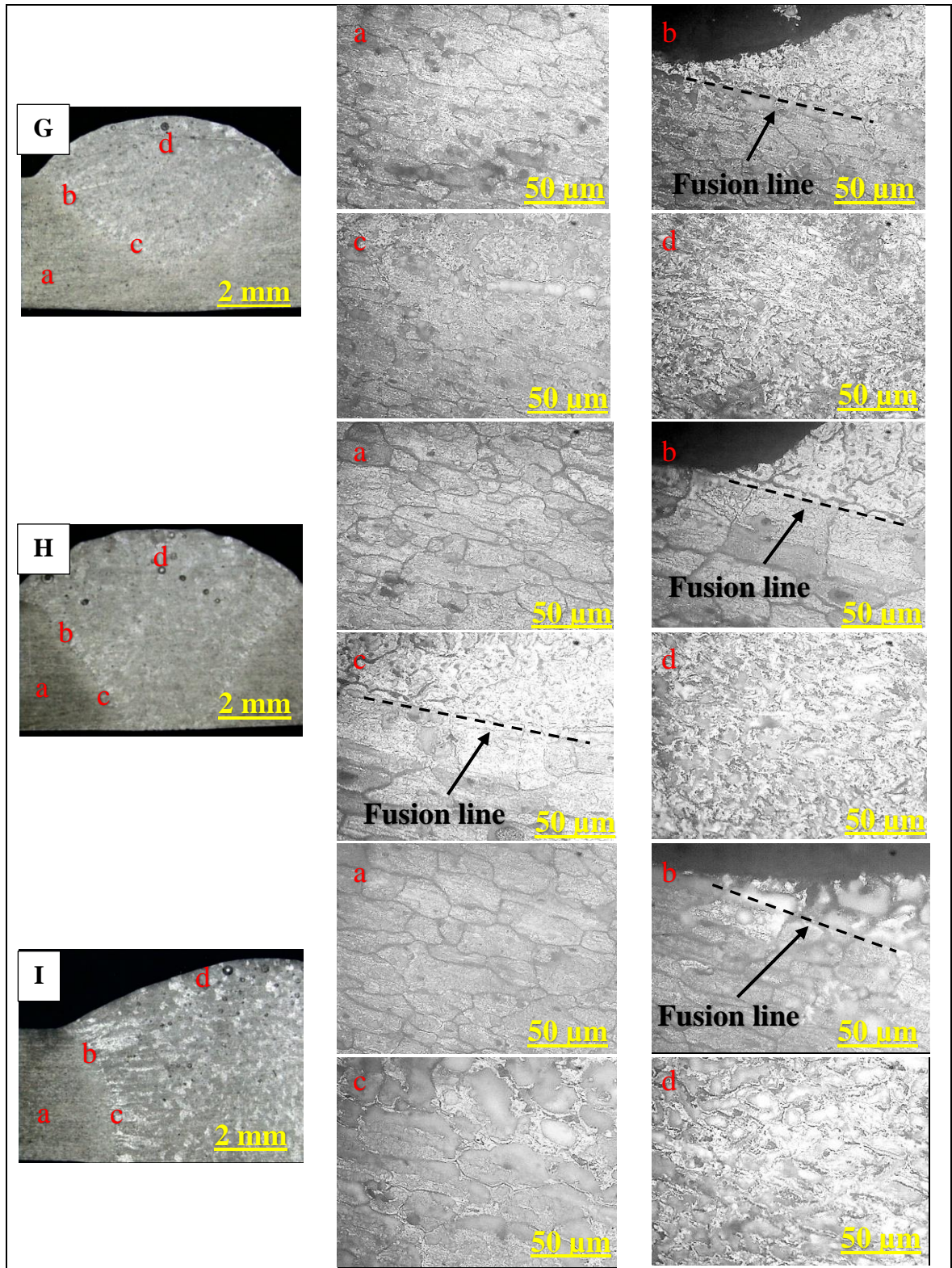
**Fig. 4.20** Vision inspection image A, B and C of CMT 80 A, 100 A and 120 A respectively at 10.5 mm/sec. Optical microscope image (a) BM (b & c) FZ (d) WZ



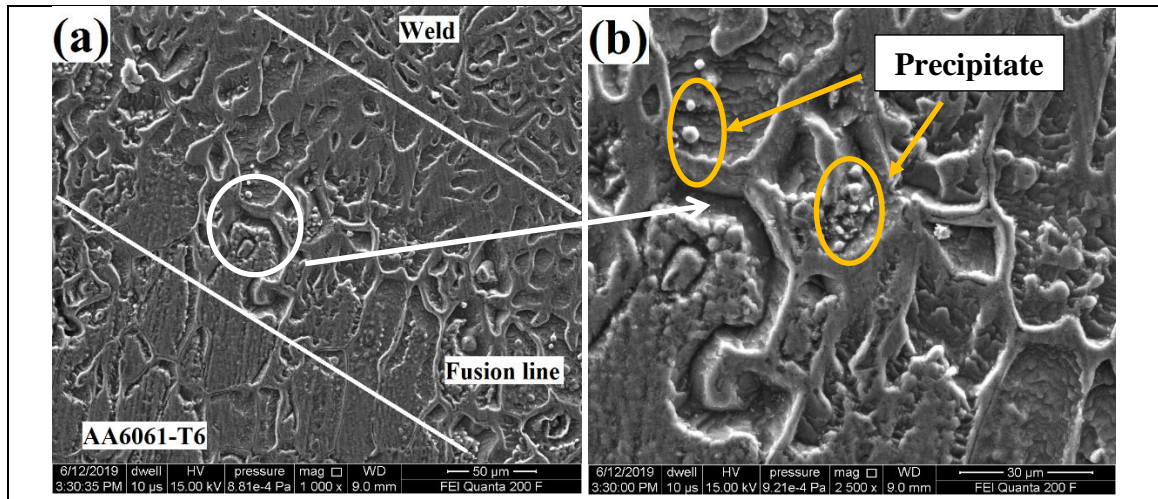


**Fig. 4.21** Vision inspection image D, E and F of MIG P for 80 A, 100 A and 120 A respectively at 10.5 mm/sec. Optical microscope image (a) BM (b & c) FZ (d) WZ

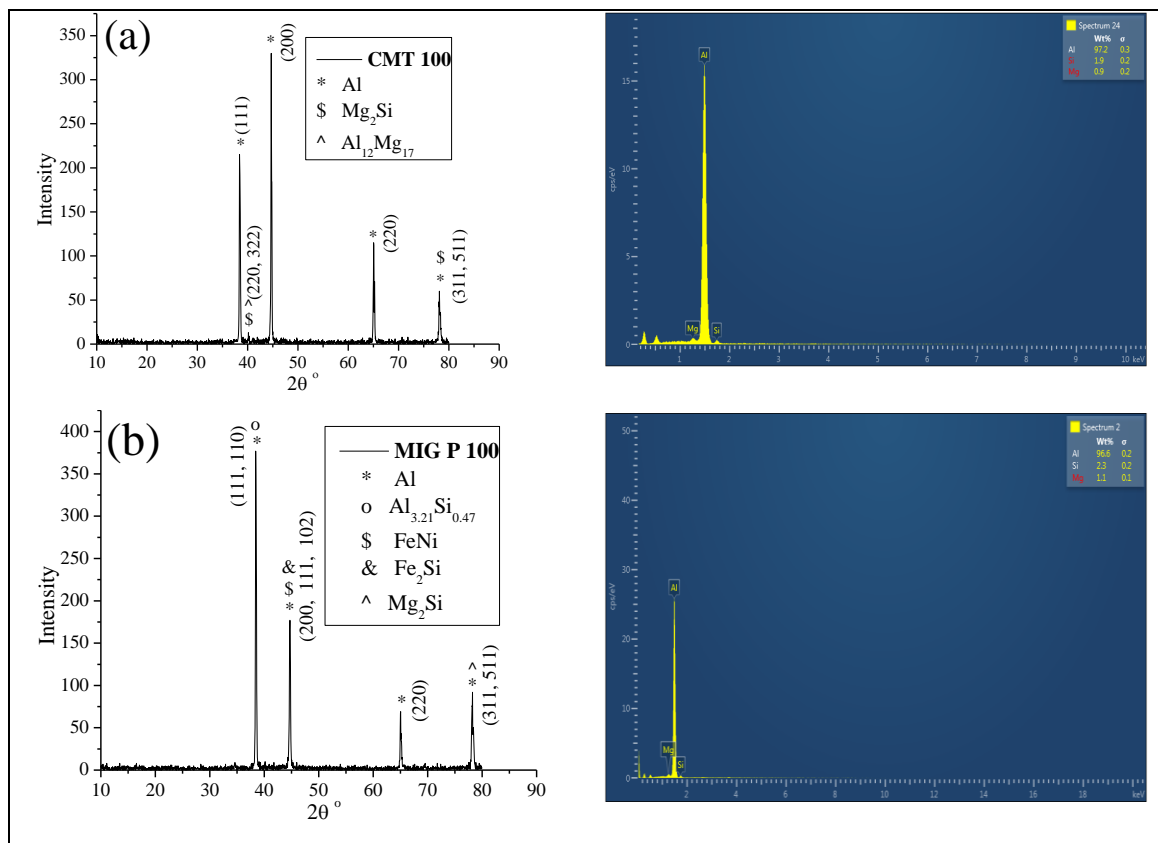




**Fig. 4.22** Vision inspection image G, H and I of MIG M for 80 A, 100 A and 120 A respectively at 10.5 mm/sec. Optical microscope image (a) BM (b & c) FZ (d) WZ



**Fig. 4.23** FESEM images of fusion zone of CMT 100 A at (a) 50 μm scale and (b) 30 μm scale



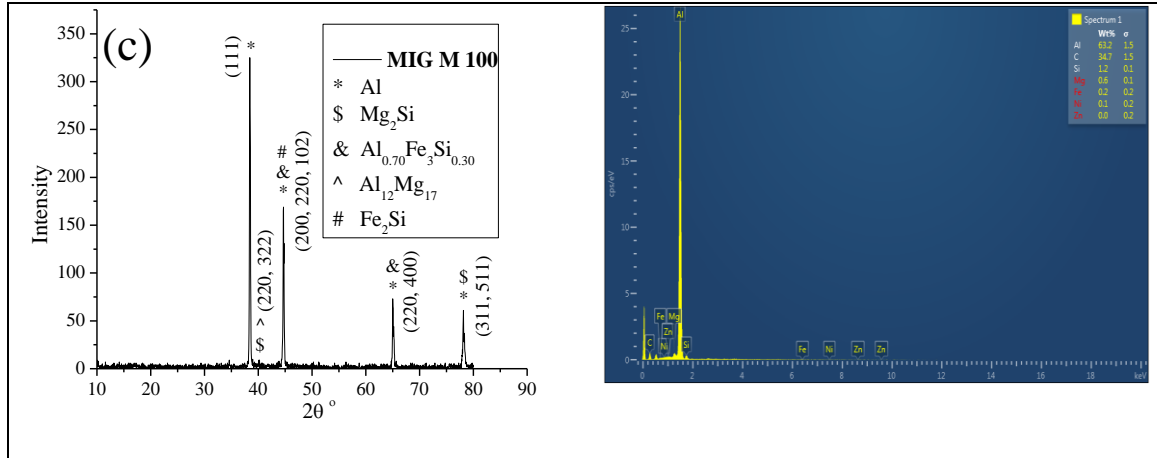


**Fig. 4.24** XRD and EDX plots for (a) CMT-100, (b) MIG P-100 and (c) MIG M-100.

## 4.5 EFFECT BY PROCESS PARAMETERS

### 4.5.1 Effect on dilution (D) and heat input (H)

Dilution (D) and heat input (H) are directly proportional to each other, as heat input on the substrate material increases, more volume being melted, causing increase in dilution and vice versa. As mentioned above, dilution is the fraction of penetration area (B) to the area of total weld metal (A+B) as shown in equation 4.1. It is the factor, which is influenced by primary dimensions of the weld bead. Fig. 4.25 shows the heat input curve and Fig. 4.26 shows the dilution curve between CMT, MIG P and MIG M respectively w.r.t. welding speed (S). Heat input is calculated with the help of equation 4.4. It is an important response in terms of influencing various factors like plate deformation, thickness of HAZ, arc stability, etc. With increase in welding speed causes less dilution, which can be attributed to the lower heat input with increased weld speed. From Fig. 4.26, dilution (D) experiences a decreasing trend with increase in the value of welding speed (S) for all the processes, because as S increases 7.5-13.5 mm/sec, heat input on the weld decreased as shown in Fig. 4.25, and less amount of substrate material melted thereby decreasing the penetration area as shown by macro-images. Similarly, by lowering down the value of S, heat input on the substrate material increases and more amount of substrate material melted which cause deeper penetration resulting in high percentage of dilution. As current increases from 80 A to 120 A, Dilution increases for all the welding processes. Higher current produces high



heat input (as shown in Fig. 4.25) causes melting of substrate material for deeper penetration resulting in increment in percentage of dilution.

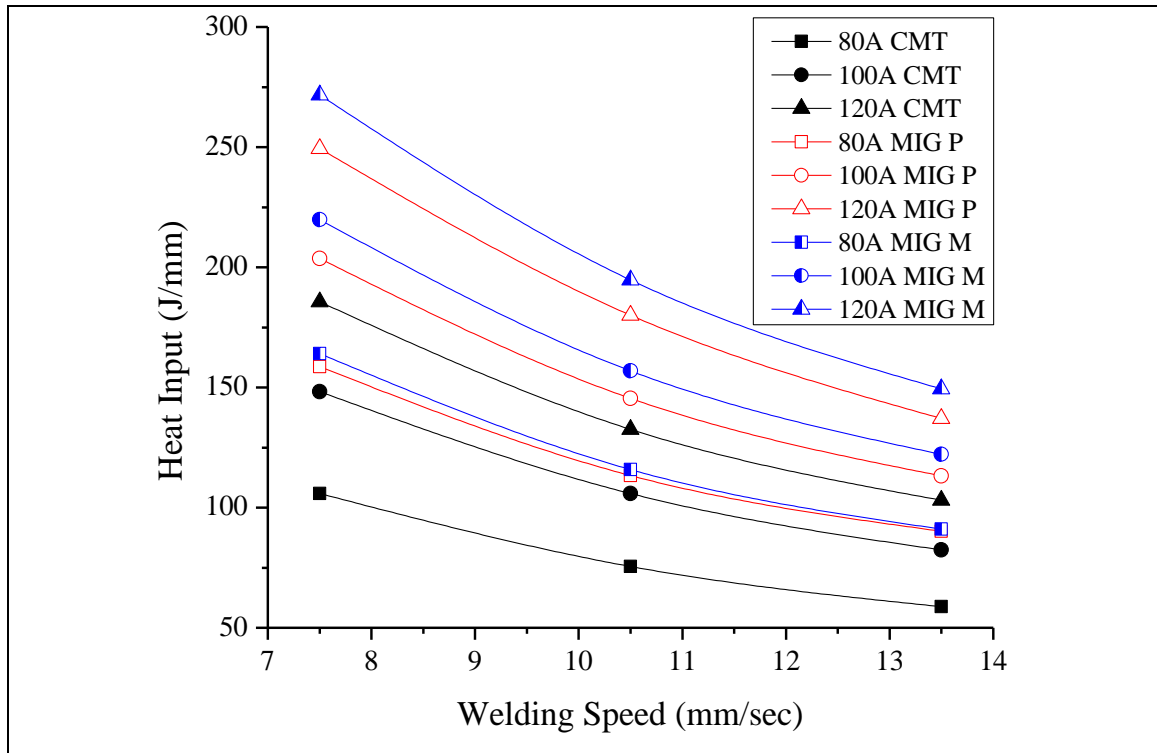


**Fig. 4.25** Comparison of heat input (J/mm) between CMT, MIG P and MIG M

It can be seen from Fig. 4.26, as current increases from 80 A to 100 A, D increases to about 40 % for CMT, 50 % for MIG P and 60 % for MIG M in comparison to 10 % for CMT, 12 % for MIG P and 16 % for MIG M when current is increased from 100 A to 120 A w.r.t welding speed. So, for a current period of 80-100 A, D is showing higher values as compared with current period of 100-120 A because heat input for current period 80-100 A is more as compared with 100-120 A as shown in Fig. 4.25. Fig. 4.27, clearly depicts that the trend for dilution w.r.t heat input. This graph shows, as the current increases from 80-100A for all the processes, there is significant change in the dilution due to variable change in heat input. Comparatively, CMT is having less amount of dilution and heat input on various process parameters from MIG P and MIG M. It is a much stable process in terms of dilution and heat input, as it is not showing any variable change in the output. Lower amount of dilution and heat input is needed for fabricating a good joint, which is having high strength by minimizing the HAZ.

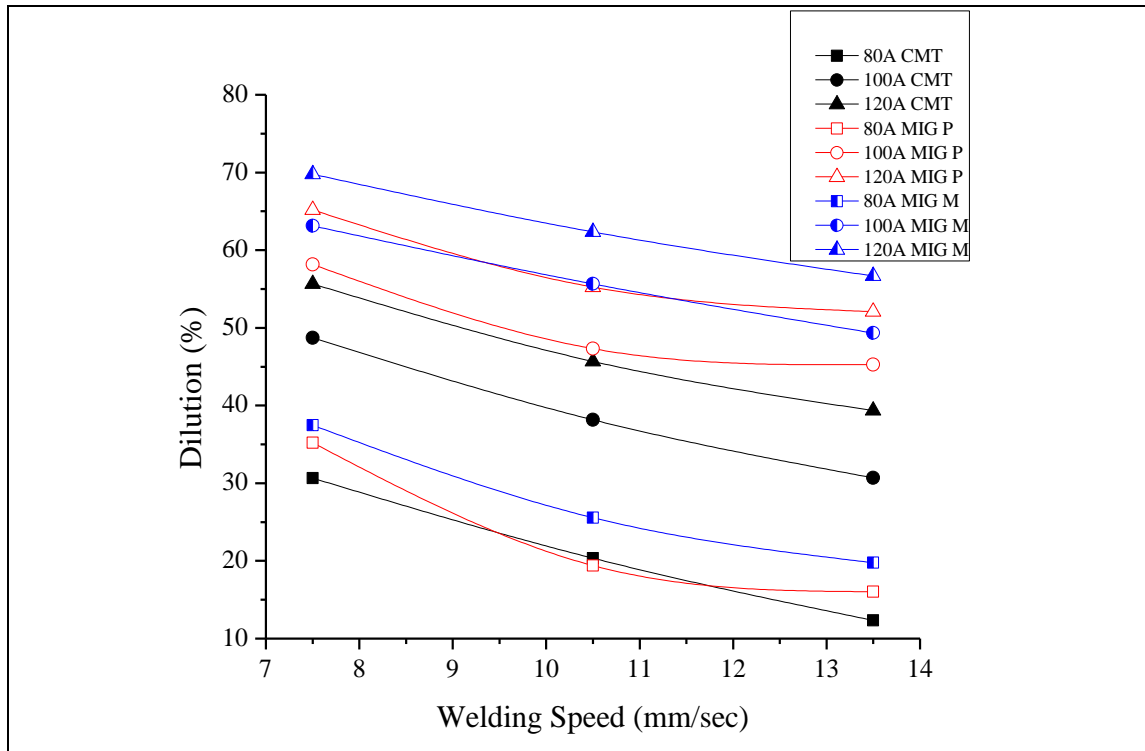


**Fig. 4.26** Comparison of dilution (%) between CMT, MIG P and MIG M

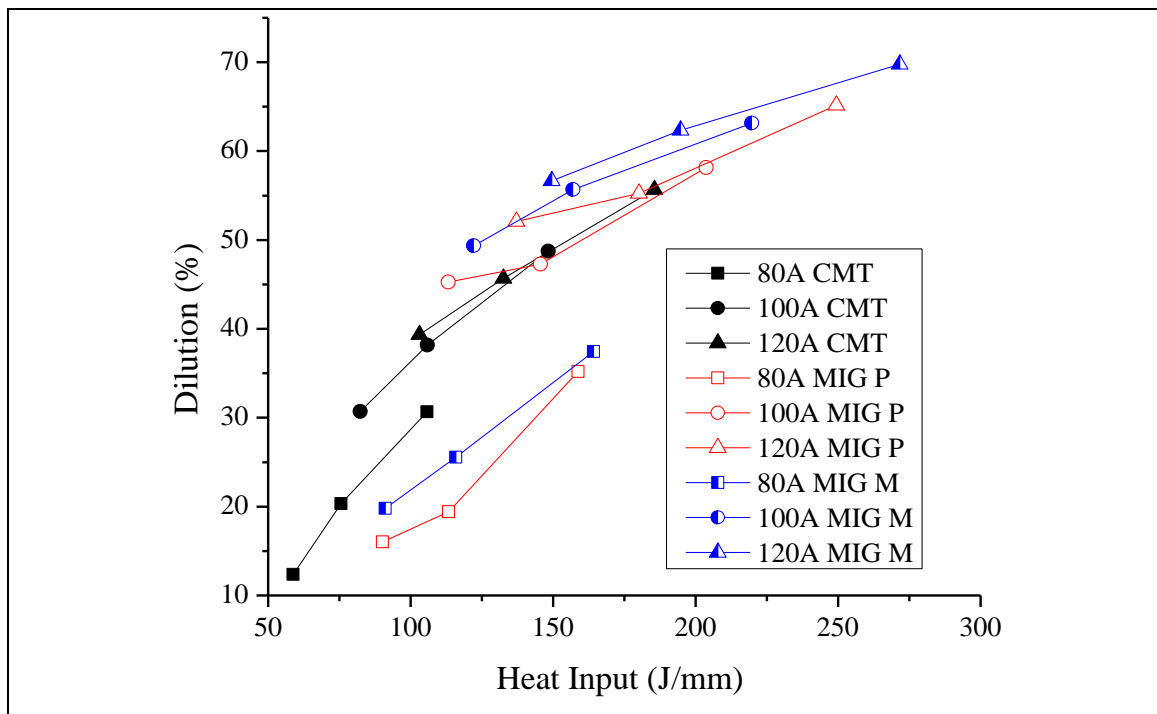


**Fig. 4.27** Dilution (%) vs heat input (J/mm) between CMT, MIG P and MIG M

#### 4.5.2 Effect on penetration

Penetration is an important factor for having a good joint efficiency, deeper penetration results in higher joint efficiency due to filler material fusing into the substrate material. Deeper penetration with higher tensile strength is required for a good quality joint provided its HAZ, weld reinforcement and width are lower to reduce weld metal consumption are vital requirement for all types of welding [Greyjevo and Metodo 2009]. It is usually noted that, as is obvious in Fig. 4.28, penetration is positively influenced by an increase in current and a decrease in welding speed. CMT process exhibits steeper decrement of 60 %, 45 % and 35 % in 80 A, 100 A and 120 A respectively as welding speed increases from 7.5 to 10.5 mm/sec. In comparison to MIG P and MIG M, it is 40 %, 16 % and 14 % in 80 A, 100 A and 120 A respectively. MIG P and MIG M shows deeper penetration of about 45 % in comparison to only 20 % in CMT when current increases from 80 to 100 A for speed of 7.5 mm/sec owing to high amount of heat input at higher current and lower welding speed.

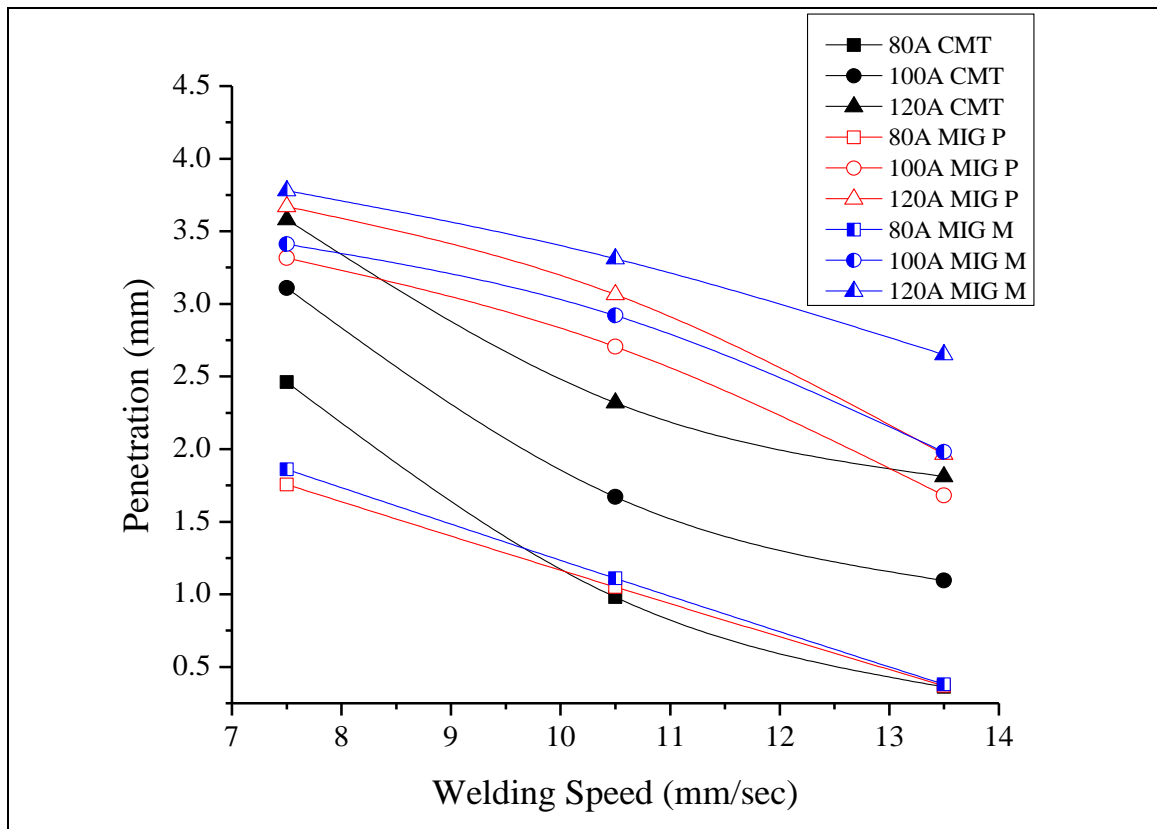


**Fig. 4.28** Comparison of penetration (mm) between CMT, MIG P and MIG M

Wire feed rate (WFR) too plays an imperative role in increasing the penetration. With increase in WFR, current increases, which helps in raising the heat input for a weld duration, leading in high amount of melting of substrate material. In CMT, the oscillatory movement of the wire helps in controlling the penetration by maintaining the arc length. With higher WFR in CMT, the current increases which helps in more droplet detachments, results in higher penetration. It is observed from Fig. 4.29, CMT is achieving similar amount of penetration as compared to MIG P and MIG M with lesser amount of heat input, which ultimately results in saving of energy.

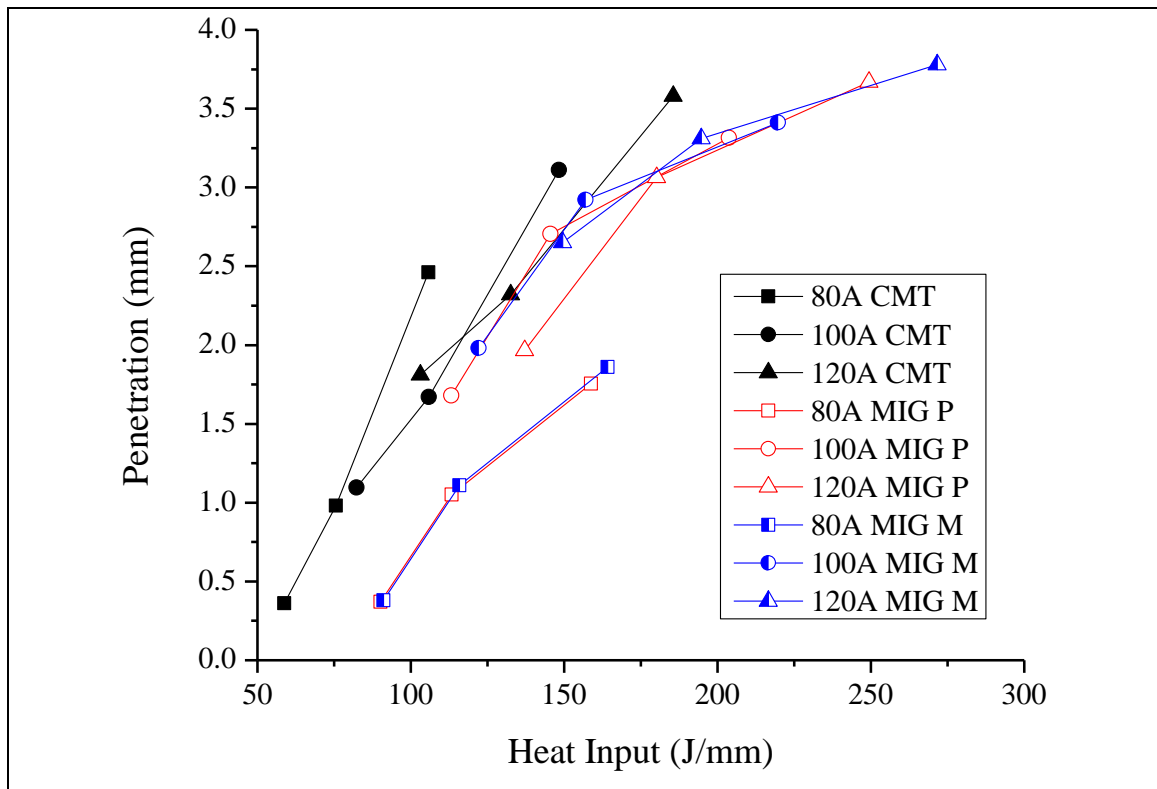


**Fig. 4.29** Penetration (mm) vs heat input (J/mm) between CMT, MIG P and MIG M

#### 4.5.3 Effect of residual stress

Residual stress magnitude depends on several factors such as deposited weld bead size, weld sequence, total deposited weld metal volume, weld geometry, deposited weld metal and adjacent BM strength, and cooling rate. As shown in the Fig. 4.30, CMT shows less residual stress compared to MIG P and MIG M. Due to high heat input and cooling rate, FZ has higher compressive stress for all the fusion welding process (CMT, MIG P and

MIG M) compared to the weld bead. CMT is showing 6-12 % and 21-29 % decrement at the beads compared with MIG P and MIG M respectively. At FZ, CMT is experiencing, 11-14 % and 17-25 % decrement as compared with MIG P and MIG M respectively [Pinto et al., 2006]. Weld bead and fusion zone has compressive stress, which has a positive impact on the tensile and fatigue strength. The top and bottom surfaces of the weld joint experiences a greater cooling rate during welding than the middle part of the weld and HAZ. This creates differential expansion and contraction by welding in the plate's thickness. Metal contraction near the surface begins even if the middle portion of the material is still in solidus form. This contributes to the growth of the residual compressive stress at the middle of the weld bead. Therefore, compressive residual stresses are deliberately caused to improve the fatigue behavior of mechanical parts, while attempts are made to decrease residual tensile stresses using multiple methods such as post-weld heat treatment, shot peening, spot heating, etc. As tensile residual stress, causes crack nucleation and further crack propagation under tensile load condition, which results in tensile failure etc. As the current level increases and the welding speed decreases, residual stress increases, resulting in the crack propagation and base plate distortion.

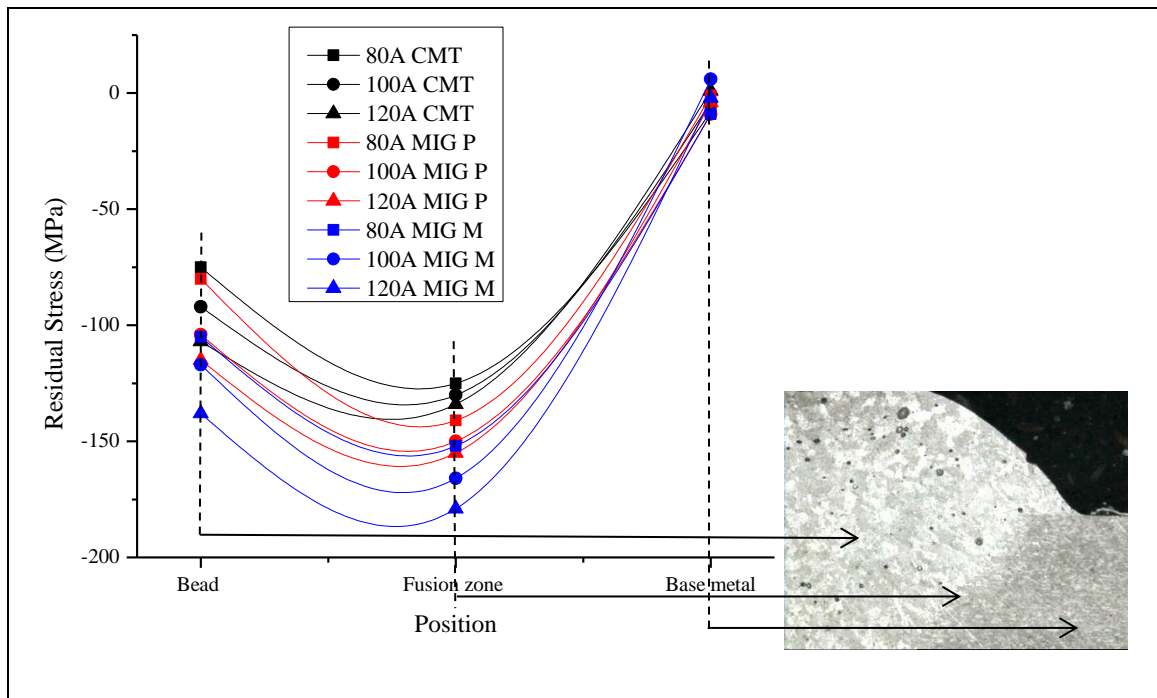


**Fig. 4.30** Residual stresses induced on different position of the specimen

Fig. 4.31 shows the residual stress profile with respect to alpha angle for CMT, MIG P and MIG M welding process at different positions for 100 A and 10.5 mm/sec process parameters.

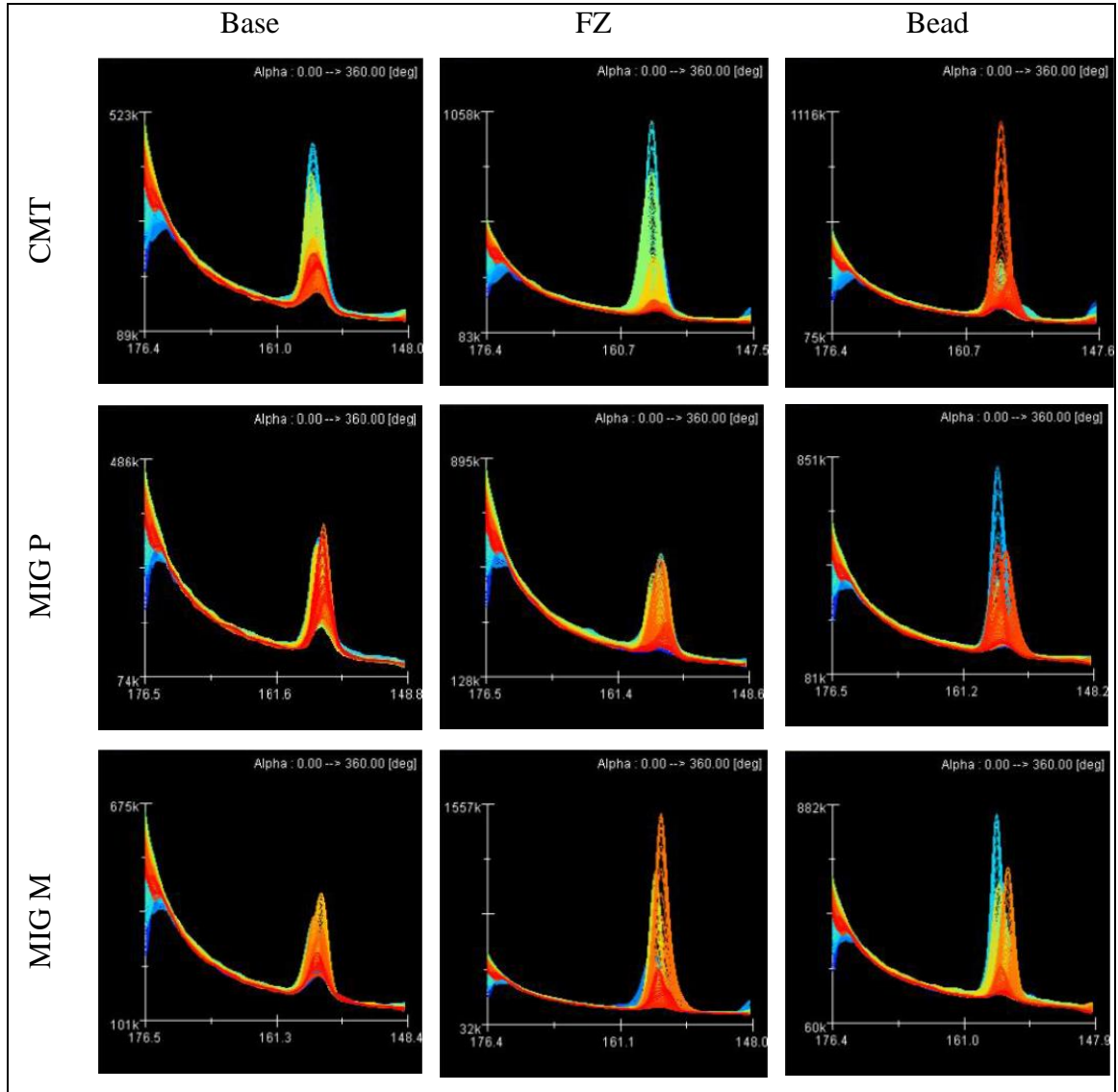


**Fig. 4.31** Residual stress profile vs alpha angle for CMT, MIG P and MIG M at different positions for 100A and 10.5mm/sec process parameters

The residual stress peaks for all the samples are in between 155 ° to 160 °. Red shade peaks are seen in fusion zone and weld bead, which indicated higher concentration of residual stresses. Blue shade peaks means negligible amount of residual stresses. From these

residual profile peaks, FWHM is measured at different position of the weld bead by the machine. Thicker the residual peaks, higher will be the value of FWHM that results in finer grain structure (i.e. higher micro-hardness) as shown in Fig. 4.32. It is seen that, FWHM and micro-hardness are linearly related and directly proportional to each other. As shown in Fig. 4.32, weld bead is having low hardness w.r.t BM and FZ. Compared to MIG P and MIG M, CMT has higher hardness values. It shows a 17.5 % increase in FZ compared to BM. CMT shows an increase in FZ hardness of 5 % compared to MIG P and MIG M. Microhardness at weld bead for MIG welding is in the range of 45-65 HV [Ishak et al., 2015]. Obtained microhardness values for CMT are higher than MIG welding. The variation in micro-hardness only depends on the zone of the weld bead. The material usually loses its original strength during solidification in the FZ owing to the strain hardening effect. Formation of brittle intermetallic compounds (IMC) in the FZ stimulates an increase in micro-hardness in the case of aluminum alloys.

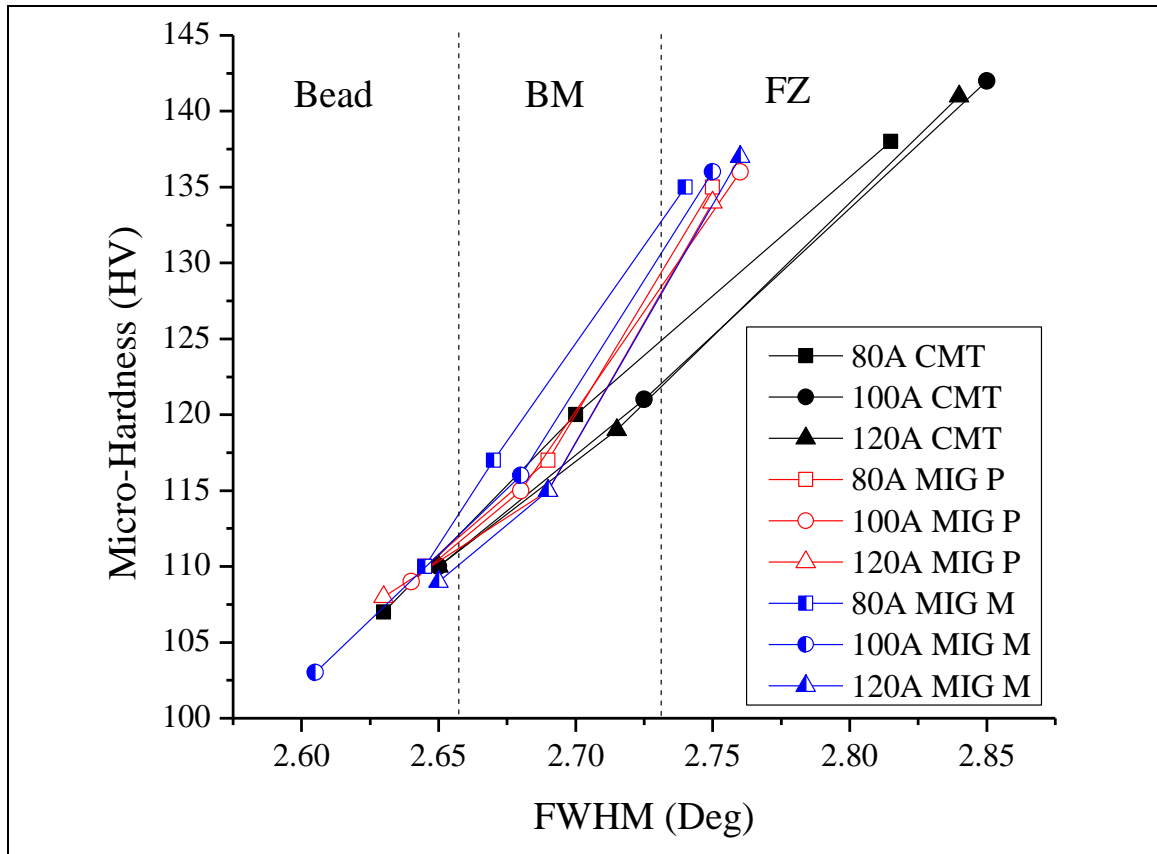


**Fig. 4.32** Microhardness vs FWHM

## 4.6 SUMMARY

This chapter includes weld bead geometry fabricated from the three different welding process such as CMT, MIG P and MIG M. Optimization of bead-on-plate experiment is carried out by CCFED under RSM having three responses such as penetration, dilution and heat input. Quadratic equations, predicted vs actual graphs, interaction curves and 3-D surface plots are illustrated for all the responses for each welding process. Model reliability illustrates that CMT is having minimum error as compared to other welding process. Macro images of weld bead for all the combinations as per the design is presented for all the welding process. Consequences of welding process parameters and different welding process is explained briefly on weld dimensions. Microstructural analysis at various positions such as BM, FZ and WM is explained in detail for each welding process. Effect on penetration, dilution and heat input is monitored on various welding process parameters. Effect of residual stress at various positions is discussed.



## CHAPTER 5 : RESULTS AND DISCUSSION ON CMT BUTT JOINTS

### 5.1 INTRODUCTION

Butt joining of AA6061-T6 and AA6082-T6 with ER4043 wire is carried out at different heat inputs as shown in Fig. 5.1. It can be seen that as the amount of heat input is increased, the weld bead geometry changes and more amount of filler wire gets deposited in the weld bead. This results in dimensional changes as shown in Fig. 5.2. The bead geometry includes weld width (W), weld penetration (P), weld reinforcement (R) and the contact angle (C).

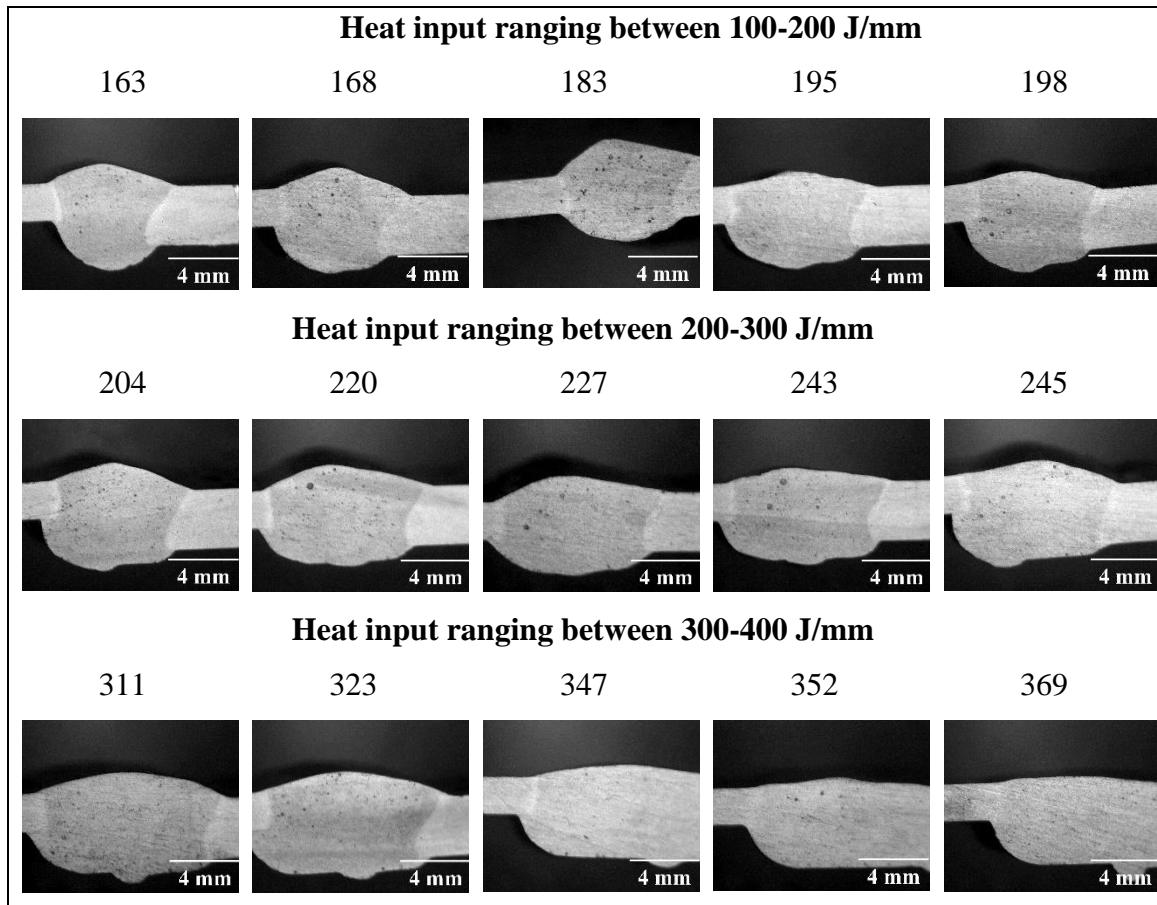


**Fig. 5.1** Macro-images of the weld bead at various ranges of heat input

Fig. 5.2 clearly shows that the weld width and depth of penetration are increased as the heat input is increased, whereas the height of reinforcement and contact angle is decreased with increase in heat input. Due to the high deposition rate of filler wire and softening behavior of aluminium materials at high heat input, the weld width and depth of penetration are increased which further reduces the height of reinforcement and contact angle.

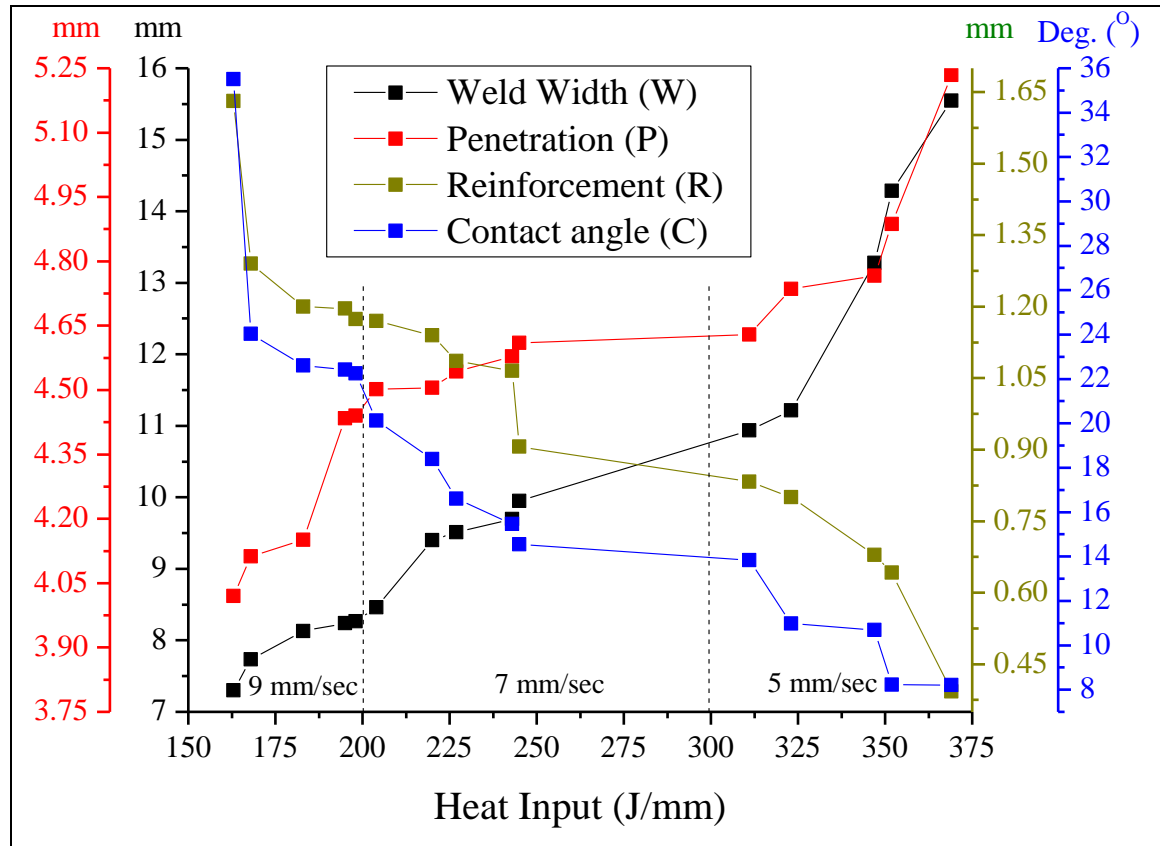


Fig. 5.2 Weld bead geometry as per heat input

## 5.2 OPTIMIZATION OF PARAMETERS FOR WELDED JOINTS

### 5.2.1 Introduction

Several optimizations and modelling approaches have been employed in finding the best CMT welding parameters. Various authors reported that RSM incorporated with GRA paired with PCA i.e. hybrid model gives superior results with higher accuracy. GRA is used to transform multiple output responses having unlike units, into a single output response by allocating GRG to a distinct process parameter [Paulraj 2018, Greyjevo and

Metodo 2009]. Avinash et al., (2019) use the GRA optimization technique on the multiple welding process parameters in Pulse TIG welding for successful welding of AISI 304 and Monel 400 materials. Magudeenswaran et al., (2014) used Taguchi optimization technique for finding out the optimal process parameters for the development of duplex steel sound weld joints. Optimum welding process parameters are 1 mm, 130 mm/min, 140 A and 12 V for electrode gap, travel speed, current and voltage respectively. To obtain optimum parameters, Shanmugarajan et al., (2016) used the GRA optimization method based on Taguchi, taking into account the welding responses like HAZ width, weld bead width and penetration depth of the weld. Using the GRA multi-objective approach, the best optimal results were obtained. Kanakavalli et al., (2020) reported that Taguchi and GRA approach is an effective method of finding the optimized welding parameters for MIG welding of AISI 1010 & AISI 1018 dissimilar joints. Similarly, Kumar and Singh (2019) used GRA based Taguchi approach to optimize the process parameters for MIG welding of AISI 1018 Mild Steel. Results have shown that it is a quick, simple and powerful approach for optimization of process parameters. Majumder et al., (2017) applied PCA-GRA in RSM (hybrid model) for optimizing the surface finish and cutting time of Inconel 800 during wire EDM. It was concluded that this hybrid model was successful and can be used for a wide variety of selection criteria. Kuo et al., (2008) used a GRA based Taguchi approach to optimize the multi-response problem and compared it with Data Envelopment Analysis (DEA). He demonstrated that GRA outperformed DEA in solving problems with multiple attribute decision making (MADM). GRA approach is very simple and fast and can easily be applied to the problems having more than two response for optimization calculations. Sivaraman and Paulraj (2017) applied Taguchi GRA to optimize multi-response welding parameters on MIG Welding of AA2219-T87. The results using GRA were current, voltage and welding speed of order 32 A, 25 V and 185 mm/sec respectively. Based on the outcomes of the ANOVA table of GRA, it was observed that the current having contribution of 82 % had a considerable effect on the response followed by the travel speed and the voltage with contribution of about 15 % and 3 % respectively. Sankar et al., (2018) analyzed the weld parameters by GRA on MIG welding of high-strength stainless steel determined that welding current had a major effect on the fusing process. Current, voltage

and flow rate of gas are 130 A, 27 V and 17 L/min respectively with a 0.8 mm electrode wire diameter are optimum parameters.

Several researchers have inferred that the hybrid (GRA coupled with PCA) model is easy and more reliable for getting accurate and precise results. In this chapter, RSM-GRA model paired with PCA is applied for finding out the optimal process parameters of AA6082-T6 and AA6061-T6 CMT butt joints having different thickness. Table 5.1 presents the experimental results as per CCFCFCD for CMT butt welds.

<b>Table 5.1</b> Experimental design matrix as per CCFCFCD using RSM along with results									
		Process Parameters				Experimental results			
Std	Run	I (A)	TS (mm/sec)	Q (L/min)	HI (J/mm)	UTS (MPa)	Elong. (%)	MH (HV)	RS (MPa)
3	17	80	9	14	163	196	10.6	59.5	-101
7	18	80	9	18	168	203	11.8	63.9	-103
12	3	90	9	16	183	186	9.9	62.8	-112
4	6	100	9	14	195	191	10.1	62.9	-119
8	4	100	9	18	198	187	10.6	65.1	-116
9	2	80	7	16	204	189	10	59.2	-115
13	13	90	7	14	220	190	10	57.3	-135
17	5	90	7	16	227	188	9.8	60.1	-130
19	7	90	7	16	227	184	9.6	59.1	-133
18	8	90	7	16	227	188	9.9	58.9	-131
15	11	90	7	16	227	186	9.7	57.8	-134
20	12	90	7	16	227	190	10.1	60	-129
16	16	90	7	16	227	185	9.7	59.6	-132
14	1	90	7	18	243	190	10.6	59.3	-143
10	15	100	7	16	245	191	10.4	62.5	-140
1	9	80	5	14	311	193	10.7	62.7	-115
5	19	80	5	18	323	190	11.1	63.7	-128
11	10	90	5	16	347	195	11.4	64.6	-133
2	14	100	5	14	352	228	12.5	68.9	-154
6	20	100	5	18	369	210	12.2	67.9	-157
I = Current; TS = Welding speed; Q = Gas flow rate; HI = Heat input; UTS = Ultimate tensile strength; Elong. = Elongation; MH = Micro-hardness; RS = Residual stress									

### 5.2.2 Mathematical Model Equations

Mathematical models for UTS, elongation, microhardness and residual stress have been developed with current (I), welding speed (TS) and flow rate of shielding gas (Q) as the input independent variables or process parameters. The final model equation in terms of actual process parameters is represented in equation 5.1 – 5.4. It is a quadratic equation obtained via CCD in RSM.

$$\text{UTS} = 408.573 - 1.324 * I + 11.555 * \text{TS} - 25.343 * Q - 0.475 * I * \text{TS} - 0.163 * I * Q + 0.750 * \text{TS} * Q + 0.042 * I * I + 1.182 * \text{TS} * \text{TS} + 1.057 * Q * Q \quad (5.1)$$

$$\text{Elongation} = 37.892 - 0.134 * I - 0.987 * \text{TS} - 2.424 * Q - 0.029 * I * \text{TS} - 0.009 * I * Q + 0.050 * \text{TS} * Q + 0.003 * I * I + 0.181 * \text{TS} * \text{TS} + 0.093 * Q * Q \quad (5.2)$$

$$\text{Micro-hardness} = 125.009 - 2.007 * I - 16.261 * \text{TS} + 9.021 * Q - 0.036 * I * \text{TS} - 0.026 * I * Q + 0.206 * \text{TS} * Q + 0.016 * I * I + 1.110 * \text{TS} * \text{TS} - 0.240 * Q * Q \quad (5.3)$$

$$\text{Residual Stress} = 352.281 - 12.786 * I - 56.399 * \text{TS} + 41.239 * Q + 0.231 * I * \text{TS} + 0.094 * I * Q + 0.531 * \text{TS} * Q + 0.047 * I * I + 2.420 * \text{TS} * \text{TS} - 1.705 * Q * Q \quad (5.4)$$

### 5.2.3 Checking the adequacy of the model

#### 5.2.3.1 Ultimate Tensile Strength (UTS)

UTS testing is carried out to understand the joint efficiency/strength, fracture analysis and ductility. Table 5.2 displays the ANOVA table for UTS which clearly illustrates that the model is significant having 97.442 % contribution. It is shown that all the process parameters and their interactions are significant which can be seen from their p-value (< 0.05). Lack of fit is not significant or insignificant because of its p-value exceeding 0.1. For UTS, the interaction of current and welding speed (AB) is the most dominant with 48.746 % as compared to other process parameters and their interaction. This states that minor changes in current and welding speed will majorly affect the UTS. The flow rate of shielding gas has the least contribution (2.188 %) which shows that the change in gas flow rate will affect the UTS negligibly. The closer the values of predicted  $R^2$  (0.851) and

adjusted  $R^2$  (0.946) concludes that within a regression line, the maximum number of point falls. The gap should not be exceeding to 0.2 between the predicted  $R^2$  and the adjusted  $R^2$ . Signal to noise (S/N) ratio is measured by adequate precision (23.785) which should be greater than 4 for suitable signal [Goyal et al., 2015].

<b>Table 5.2</b> ANOVA table for response 1: UTS							
Source	SS	df	Mean	F-value	p-value	Contribution	Remarks
Model	1958.855	9	217.651	38.087	0.000	97.442	significant
A-Current	129.600	1	129.600	22.679	0.001	8.750	
B-Welding speed	280.900	1	280.900	49.155	0.000	18.965	
C-Flow rate	32.400	1	32.400	5.670	0.039	2.188	
AB	722.000	1	722.000	126.344	0.000	48.746	
AC	84.500	1	84.500	14.787	0.003	5.705	
BC	72.000	1	72.000	12.599	0.005	4.861	
$A\hat{A}^2$	49.142	1	49.142	8.599	0.015	3.318	
$B\hat{A}^2$	61.455	1	61.455	10.754	0.008	4.149	
$C\hat{A}^2$	49.142	1	49.142	8.599	0.015	3.318	
Residual	57.145	10	5.715			2.558	
Lack of Fit	32.312	5	6.462	1.301	0.390		not significant
Pure Error	24.833	5	4.967				
Cor Total	2016.000	19					
Std. Dev.	2.391			$R\hat{A}^2$			0.972
Mean	193.000			Adjusted $R\hat{A}^2$			0.946
C.V. %	1.239			Predicted $R\hat{A}^2$			0.851
				Adeq Precision			23.785

Fig. 5.3 shows the important graphs of UTS obtained through design expert software during optimization. Fig. 5.3 (a) shows the interaction curve between current (A) and welding speed (B) while keeping the third process parameter which is flow rate (C) as constant (16 L/min).

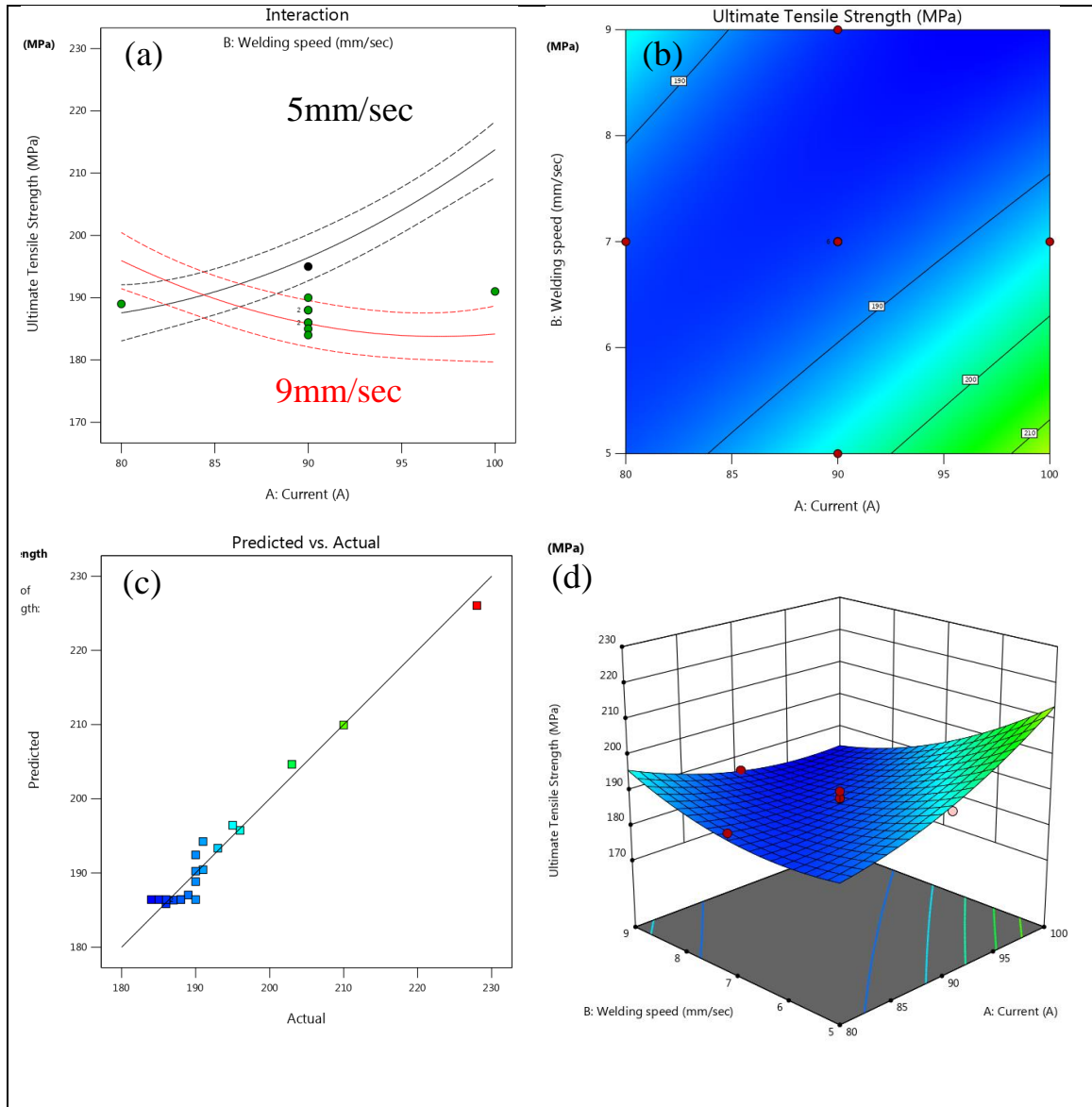


**Fig. 5.3** UTS graphs (a) Interaction curve (b) Contour graph (c) Predicted vs actual (d) 3-D surface plot

As it is discussed above and seen from ANOVA table that the percentage contribution is negligible, so it is kept constant and mainly focused on the major process parameters that affect UTS. So the interaction curve shows the steeper upgrade when working on higher currents (100 A) and lower welding speed (5 mm/sec) results in higher value of UTS. The black colour and red colour curve shows the lower welding speed (5 mm/sec) and higher welding speed (9 mm/sec) respectively and the curve indicates that it is a quadratic model.

The contour, predicted vs actual and 3-D surface plots majorly indicate that the majority of the UTS values falls in the range of 185 - 200 MPa which is good for a fusion welded joint and results in higher joint efficiency.

#### 5.2.3.2 Elongation

Percentage elongation indicates the ductility of the material. The higher the percentage elongation the more ductile is the material. Ductility in welded plates generally allows the redistribution of loads before fracture. Higher ductility also ensures minimum amount of intermetallic compound formation. Table 5.3 shows the ANOVA table of elongation which clearly shows that the model is significant having 97.437 % contribution. Similarly, as in the UTS, the welding speed is the most important process parameters as compared to the others with 28.360 % contribution.

<b>Table 5.3</b> ANOVA table for response 2: Elongation							
Source	SS	Df	Mean	F-value	p-value	Contribution	Remarks
Model	13.530	9.000	1.503	38.015	0.000	97.437	significant
A-Current	0.256	1.000	0.256	6.474	0.029	3.024	
B-Welding speed	2.401	1.000	2.401	60.715	0.000	28.360	
C-Flow rate	0.576	1.000	0.576	14.566	0.003	6.804	
AB	2.645	1.000	2.645	66.885	0.000	31.243	
AC	0.245	1.000	0.245	6.195	0.032	2.894	
BC	0.320	1.000	0.320	8.092	0.017	3.780	
A <sup>2</sup>	0.205	1.000	0.205	5.172	0.046	2.416	
B <sup>2</sup>	1.436	1.000	1.436	36.323	0.000	16.967	
C <sup>2</sup>	0.382	1.000	0.382	9.661	0.011	4.513	
Residual	0.395	10.000	0.040			2.563	
Lack of Fit	0.235	5.000	0.047	1.472	0.341		not significant
Pure Error	0.160	5.000	0.032				
Cor Total	13.926	19.000					
Std. Dev.	0.199			R <sup>2</sup>			0.972
Mean	10.535			Adjusted R <sup>2</sup>			0.946
C.V. %	1.888			Predicted R <sup>2</sup>			0.868
				Adeq Precision			19.402



The interaction of current and welding speed (AB) also has the highest contribution value of 31.243 % which signifies that the effect of shielding gas flow rate is negligible on elongation (%). ANOVA table clearly shows that all the process parameters and their interactions are significant and lack of fit is not significant. Predicted  $R^2$  (0.868) and adjusted  $R^2$  (0.946) value is close which gives good accuracy. Higher adequate precision (19.402) is experienced which results in a higher S/N ratio. Fig. 5.4 shows the major graphs of elongation i.e. interaction curve, contour, predicted vs actual and 3-D surface plots.

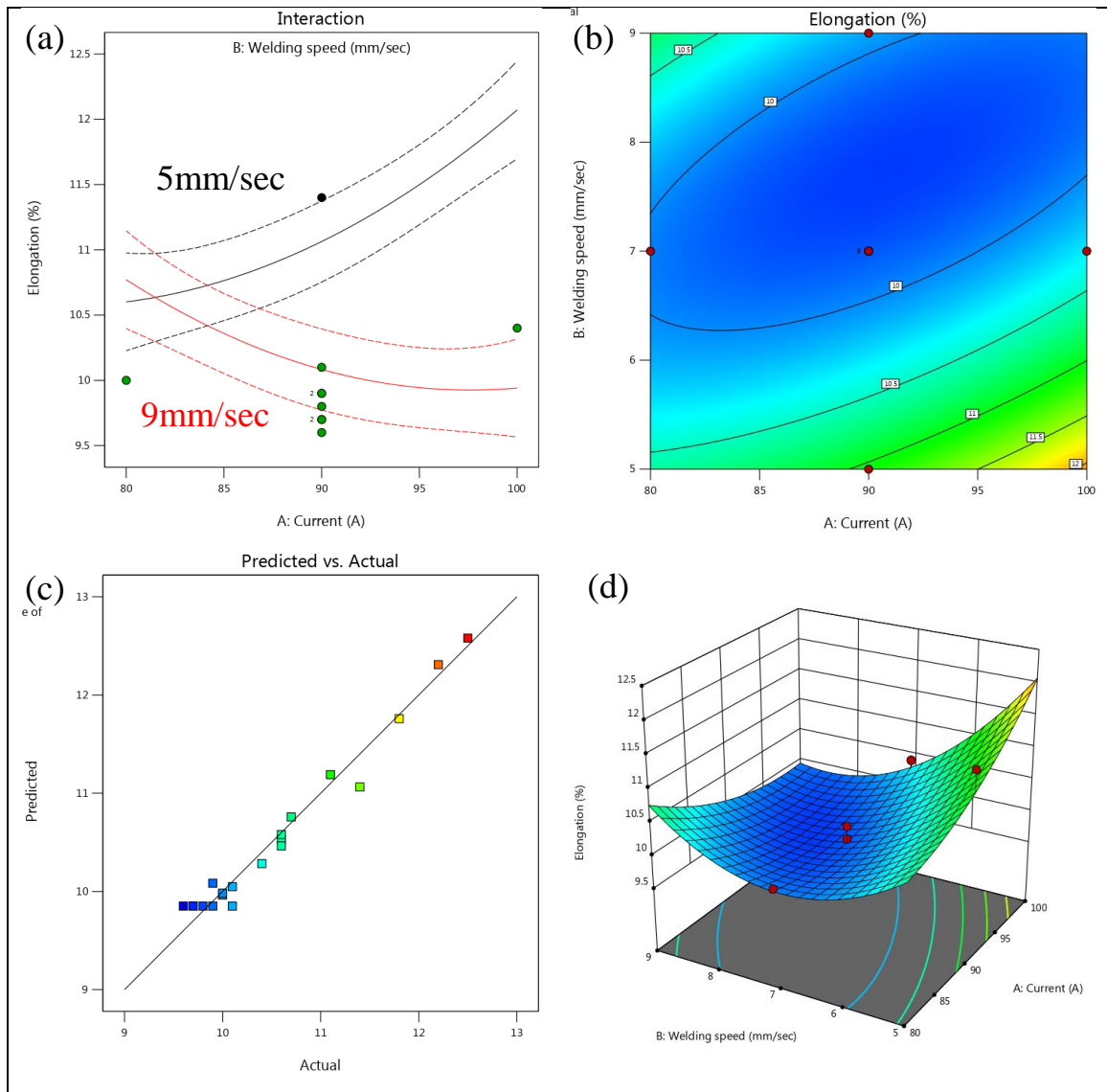


**Fig. 5.4** Elongation graphs (a) Interaction curve (b) Contour graph (c) Predicted vs actual (d) 3-D surface plot

Fig. 5.4 (a) shows that at lower welding speeds (5 mm/sec), increasing the current will increase the percentage elongation while at higher speeds (9 mm/sec) the percentage elongation reduces with increase in the current values. Contour graph and 3-D surface plot shows a significant colour change and a steep pointed end at 100 A current and 5 mm/sec of welding speed which signifies a higher percentage elongation. Predicted vs actual graph shows a uniform distribution of the points which fall on regression line.

### 5.2.3.3 Microhardness (HV)

Table 5.4 shows the ANOVA table having 98.043 % significant model. Here, the current is the dominant (24.814 %) process parameter as compared to other process parameters and also their interactions.

<b>Table 5.4</b> ANOVA table for response 3: Microhardness							
Source	SS	df	Mean	F-value	p-value	Contribution	Remarks
Model	194.779	9.000	21.642	50.106	0.000	98.043	significant
A-Current	33.489	1.000	33.489	77.534	0.000	24.814	
B-Welding speed	18.496	1.000	18.496	42.822	0.000	13.705	
C-Flow rate	7.396	1.000	7.396	17.123	0.002	5.480	
AB	4.205	1.000	4.205	9.735	0.011	3.116	
AC	2.205	1.000	2.205	5.105	0.047	1.634	
BC	5.445	1.000	5.445	12.606	0.005	4.035	
$A\hat{A}^2$	6.960	1.000	6.960	16.114	0.002	5.157	
$B\hat{A}^2$	54.235	1.000	54.235	125.564	0.000	40.186	
$C\hat{A}^2$	2.530	1.000	2.530	5.857	0.036	1.874	
Residual	4.319	10.000	0.432			1.957	
Lack of Fit	0.664	5.000	0.133	0.182	0.958		not significant
Pure Error	3.655	5.000	0.731				
Cor Total	199.098	19.000					
Std. Dev.	0.657			$R\hat{A}^2$			0.978
Mean	61.790			Adjusted $R\hat{A}^2$			0.959
C.V. %	1.064			Predicted $R\hat{A}^2$			0.950
				Adeq Precision			24.309

Current plays a vital role in enhancing or degrading the microhardness. Moreover, it's the combination of current and welding speed which can be stated as heat input has the major significance on microhardness. The gas flow rate has a minor influence on the microhardness. Here adjusted  $R^2$  and predicted  $R^2$  is having an approximately same value which gives higher accurate results. Fig. 5.5 (a) shows the interaction curve which is different from the other two previous responses.

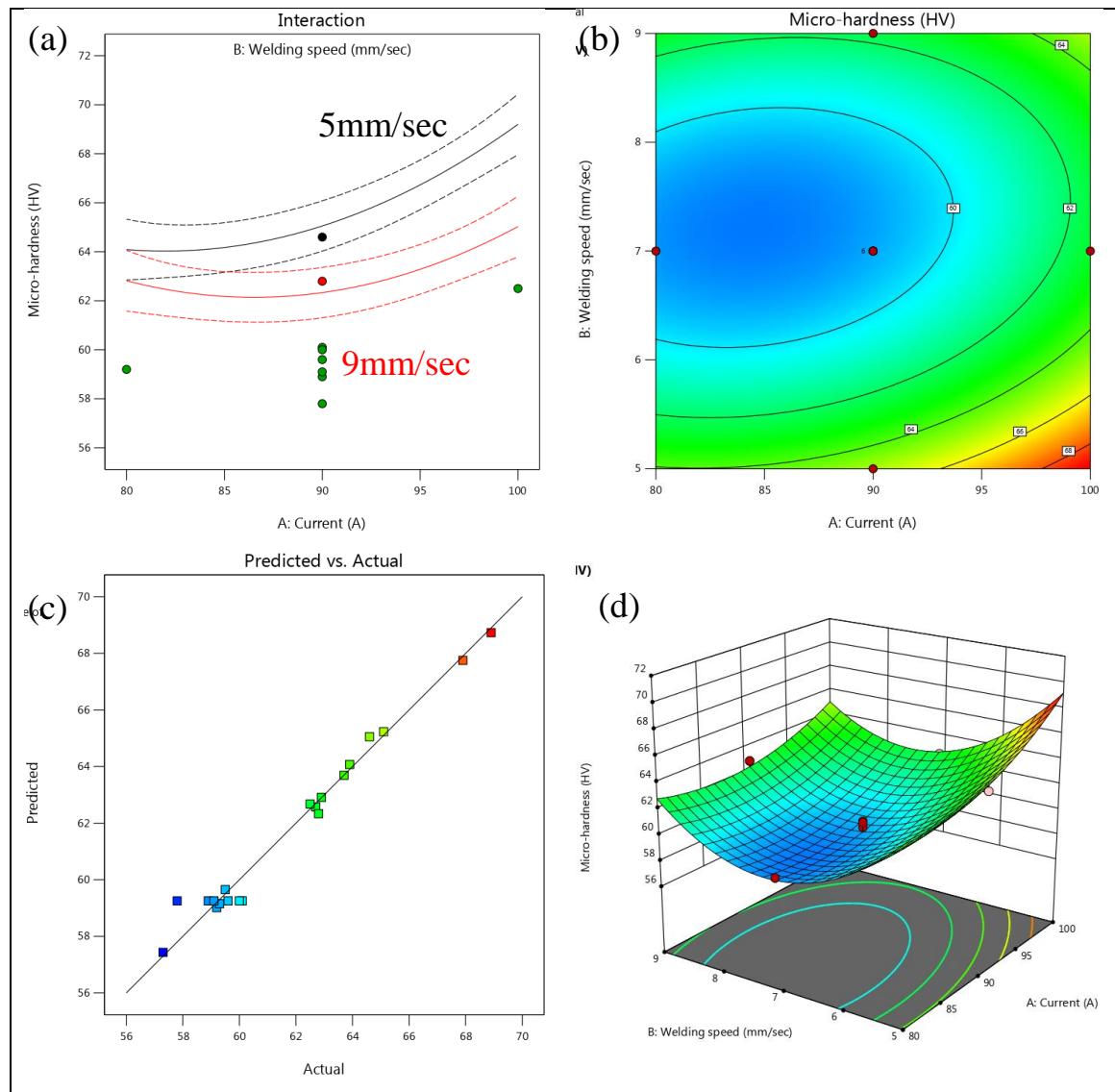


**Fig. 5.5** Microhardness graphs (a) Interaction curve (b) Contour graph (c) Predicted vs actual (d) 3-D surface plot

In this the lower (5 mm/sec) and higher (9 mm/sec) values of welding speeds both shows an increase in the microhardness. Approximately 5 to 7 % increase in microhardness is experienced when working in lower welding speeds as compared to higher welding speeds. Fig. 5.5 (b) shows a contour graph which easily illustrates the significance of colour band bounded with an elliptical curves. These colours are also seen in other two graphs i.e. predicted vs actual and 3-D surface plots. The blue colour and the red colour shows the lower and higher microhardness values respectively.

#### 5.2.3.4 Residual Stress (MPa)

Residual stress is the stresses that endure within a material in the dearth of exterior forces or thermal gradients after manufacturing and material processing. Table 5.5 shows the ANOVA table having the model significance of 98.860 %.

<b>Table 5.5</b> ANOVA table for response 4: Residual stress							
Source	SS	df	Mean	F-value	p-value	Contribution	Remarks
Model	4170.566	9.000	463.396	86.723	0.000	98.860	significant
A-Current	1537.600	1.000	1537.600	287.756	0.000	37.308	
B-Welding speed	1849.600	1.000	1849.600	346.146	0.000	44.878	
C-Flow rate	52.900	1.000	52.900	9.900	0.010	1.284	
AB	171.125	1.000	171.125	32.025	0.000	4.152	
AC	28.125	1.000	28.125	5.263	0.045	0.682	
BC	36.125	1.000	36.125	6.761	0.026	0.877	
A <sup>2</sup>	60.278	1.000	60.278	11.281	0.007	1.463	
B <sup>2</sup>	257.778	1.000	257.778	48.242	0.000	6.255	
C <sup>2</sup>	127.841	1.000	127.841	23.925	0.001	3.102	
Residual	53.434	10.000	5.343			1.140	
Lack of Fit	35.934	5.000	7.187	2.053	0.224		not significant
Pure Error	17.500	5.000	3.500				
Cor Total	4224.000	19.000					
Std. Dev.	2.312			R <sup>2</sup>			0.987
Mean	-128.000			Adjusted R <sup>2</sup>			0.976
C.V. %	1.806			Predicted R <sup>2</sup>			0.918
				Adeq Precision			34.628

Welding speed is the dominant factor with 44.878 % while the contribution of current is also very high at 37.308 %. Similarly, to the other responses, the flow rate of shielding gas is having a negligible amount of contribution. Fig. 5.6 shows the model graphs of residual stress. In the interaction curve, it can be seen that higher welding speeds (9 mm/sec) with lower current values (80 A) is preferable for lower residual stresses.

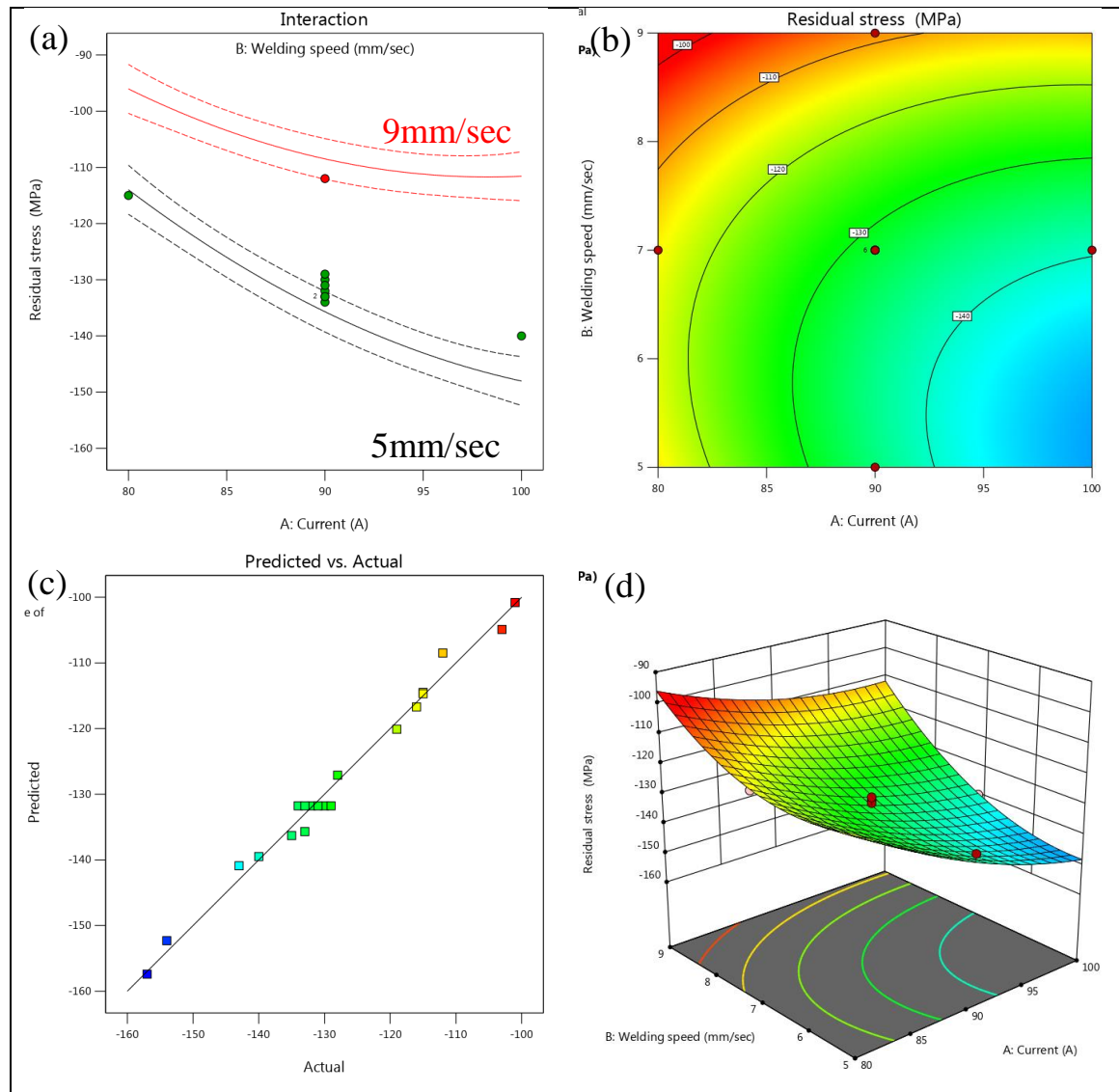


**Fig. 5.6** Residual graphs (a) Interaction curve (b) Contour graph (c) Predicted vs actual (d) 3-D surface plot

As the welding speed reduces from 9 mm/sec to 5 mm/sec the residual stress increases significantly. Approximately 21 % and 36 % increase in residual stress is seen when

welding speed is reduced from 9 mm/sec to 5 mm/sec at 80 A and 100 A current values respectively. Contour and 3-D surface plots shows the similar situation, with a steeper end having red colour which shows lesser residual stress. Predicted vs actual graph shows the uniformity of points fall under the regression line. Finding the optimal process parameters is most important in this type of situation where the first 3 responses (UTS, elongation and microhardness) shows a similar trend with higher currents (100 A) and lower welding speed (5 mm/sec), while the 4<sup>th</sup> response (residual stress) shows the opposite trend with lower currents (80 A) and higher welding speeds (9 mm/sec). For getting accurate optimal parameters with this situation, GRA coupled with PCA is used in this experiment. Fig. 5.7 shows the model reliability of all the responses, which gives the percentage error from actual and predicted values.

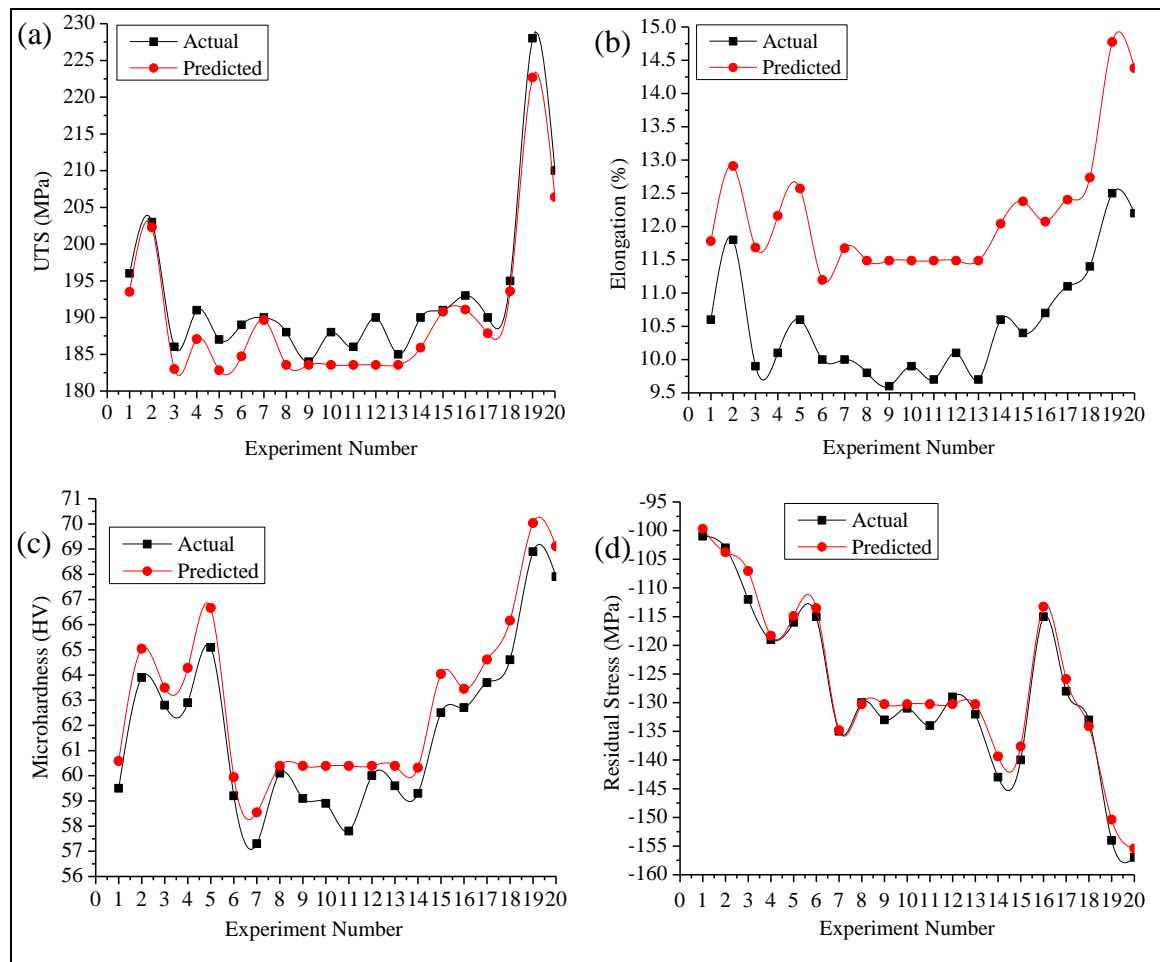


**Fig. 5.7** Model reliability (a) UTS (b) Elongation (c) Microhardness (d) Residual stress

The experimental values obtained and the predicted values generated from the model is having a low percentage of error which results in high repeatability and accuracy due to a significant model. Using CCFCD of RSM, the optimal process parameters are 80 A, 9 mm/sec, 18 L/min for current (I), welding speed (TS) and flow rate (Q) respectively. It has the desirability of 65.99 % at optimal process parameters which the response parameter of 204.64 MPa, 11.75 %, 64.07 HV and -104.90 MPa for UTS, elongation, microhardness and residual stress respectively as shown in Fig. 5.8. I1-TS3-Q3 is the initial optimal process parameter obtained via CCFCD of RSM. These parameters are of experiment 2<sup>nd</sup> of the design matrix. Now GRA-PCA technique is used to obtain the optimal process parameter for enhancing the optimality by obtaining the original weights of the responses.

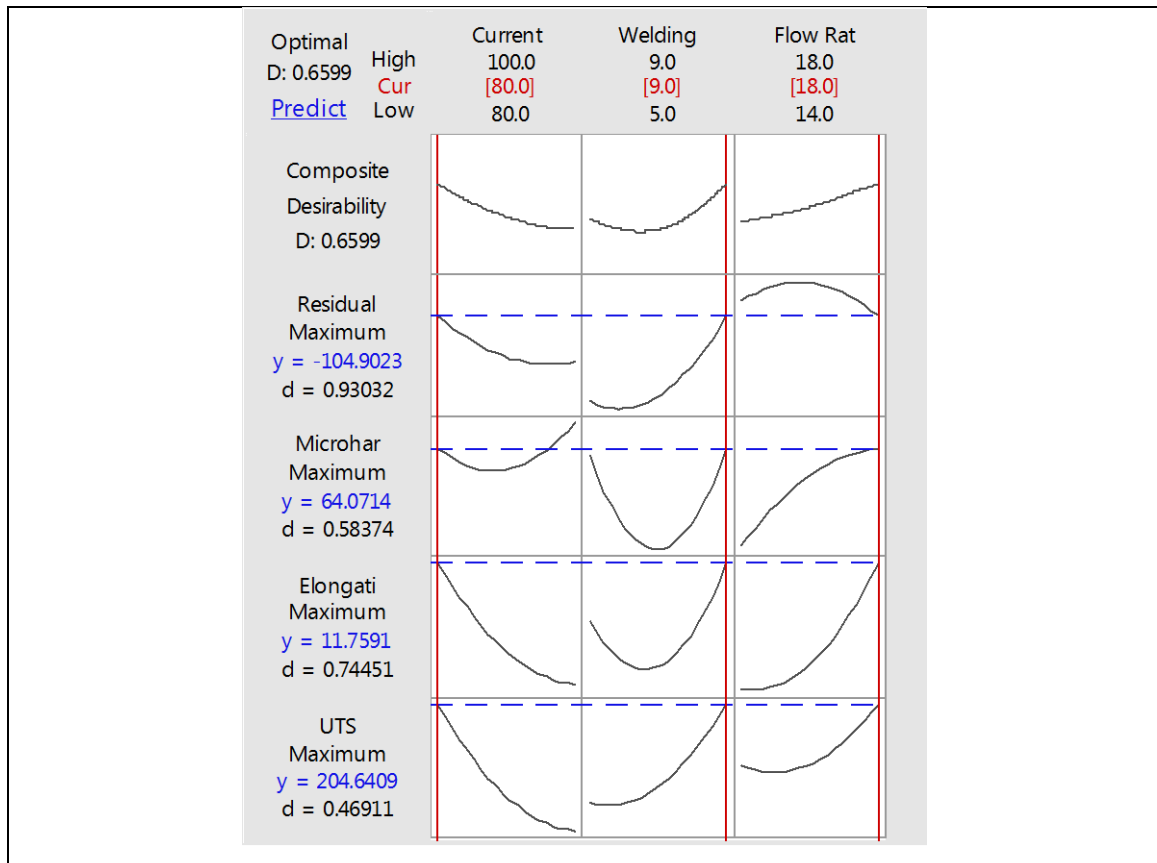


**Fig. 5.8** Optimal process parameters, responses and their desirability with using CCFCD of RSM

#### 5.2.4 Process parameter optimization using hybrid technique

For optimizing the data by GRA-PCA hybrid technique, firstly the responses having dissimilar units were converted into normalized dimensionless number as shown in Table 5.6.

<b>Table 5.6</b> Normalizing and deviation sequence table for GRA								
S.No.	Normalizing				Deviation Sequence			
	UTS	Elong.	MH	RS	UTS	Elong.	MH	RS
	(MPa)	(%)	(HV)	(MPa)	(MPa)	(%)	(HV)	(MPa)
1	0.2727	0.3448	0.1897	1.0000	0.7273	0.6552	0.8103	0.0000
2	0.4318	0.7586	0.5690	0.9643	0.5682	0.2414	0.4310	0.0357
3	0.0455	0.1034	0.4741	0.8036	0.9545	0.8966	0.5259	0.1964
4	0.1591	0.1724	0.4828	0.6786	0.8409	0.8276	0.5172	0.3214
5	0.0682	0.3448	0.6724	0.7321	0.9318	0.6552	0.3276	0.2679
6	0.1136	0.1379	0.1638	0.7500	0.8864	0.8621	0.8362	0.2500
7	0.1364	0.1379	0.0000	0.3929	0.8636	0.8621	1.0000	0.6071
8	0.0909	0.0690	0.2414	0.4821	0.9091	0.9310	0.7586	0.5179
9	0.0000	0.0000	0.1552	0.4286	1.0000	1.0000	0.8448	0.5714
10	0.0909	0.1034	0.1379	0.4643	0.9091	0.8966	0.8621	0.5357
11	0.0455	0.0345	0.0431	0.4107	0.9545	0.9655	0.9569	0.5893
12	0.1364	0.1724	0.2328	0.5000	0.8636	0.8276	0.7672	0.5000
13	0.0227	0.0345	0.1983	0.4464	0.9773	0.9655	0.8017	0.5536
14	0.1364	0.3448	0.1724	0.2500	0.8636	0.6552	0.8276	0.7500
15	0.1591	0.2759	0.4483	0.3036	0.8409	0.7241	0.5517	0.6964
16	0.2045	0.3793	0.4655	0.7500	0.7955	0.6207	0.5345	0.2500
17	0.1364	0.5172	0.5517	0.5179	0.8636	0.4828	0.4483	0.4821
18	0.2500	0.6207	0.6293	0.4286	0.7500	0.3793	0.3707	0.5714
19	1.0000	1.0000	1.0000	0.0536	0.0000	0.0000	0.0000	0.9464
20	0.5909	0.8966	0.9138	0.0000	0.4091	0.1034	0.0862	1.0000

Larger the better phenomenon is used for all the responses, as residual stress is compressive (negative sign) the larger the better is applied for reducing the residual stress at an optimal



level. After normalizing the data, deviation sequence is computed as displayed in Table 5.6. For GRC,  $\xi$  is in the range of 0 to 1, it is an identification coefficient which is usually taken as 0.5 for GRA analysis. The PCA technique is coupled with GRA for finding the exact weights of the response parameter. Weights are calculated by eigen analysis of the correlation matrix and eigenvectors as shown in Table 5.7. Eigen vectors, principal components and their contribution or weights are shown in Table 5.8. In this, the weighting contribution of each response attribute is achieved by the sum of the principal component values of the respective eigen vectors. The variance in input for PC1 that characterizes the four response characteristics is the greatest as shown in Fig. 5.9.

<b>Table 5.7</b> Eigen analysis of the Correlation Matrix				
	UTS	% E	HV	RS
Eigen value	2.7917	0.8658	0.2559	0.0866
Proportion	0.698	0.216	0.064	0.022
Cumulative	0.698	0.914	0.978	1

<b>Table 5.8</b> Eigenvectors, principal components and contribution					
Variable	PC1	PC2	PC3	PC4	% Contribution
UTS (MPa)	0.558	0.038	-0.638	0.529	31.1364
% E	0.57	0.2	-0.14	-0.785	32.49
HV/0.3	0.535	0.24	0.746	0.317	28.6225
RS (MPa)	-0.277	0.949	-0.134	0.064	7.6729

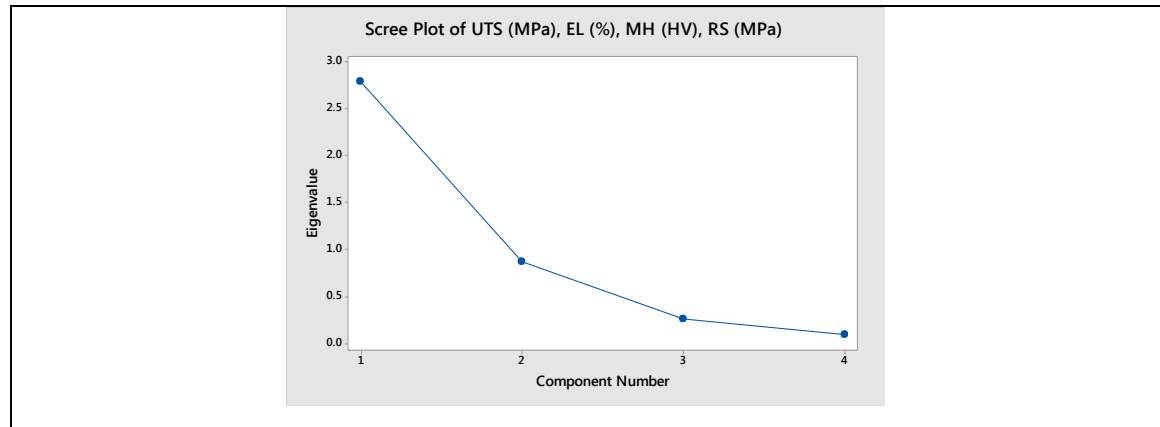


**Fig. 5.9** Screen plots of response with 4 principal components

So the weights are achieved by squaring the values of PC1 for each response. Weights obtained via PCA for UTS, elongation, microhardness and residual stress are 31.1364, 32.49, 28.6225 and 7.6729 respectively. Once the weights are obtained for each of the responses using the PCA technique, then GRG is computed as shown in Table 5.9.

<b>Table 5.9</b> GRC, GRG and Rank table with PCA					
GRC				GRG with PCA weights	Rank
UTS	%E	HV/0.3	RS		
MPa	%	HV	MPa		
0.4074	0.4328	0.3816	1.0000	0.4534	8
0.4681	0.6744	0.5370	0.9333	0.5902	3
0.3438	0.3580	0.4874	0.7179	0.4179	10
0.3729	0.3766	0.4915	0.6087	0.4259	9
0.3492	0.4328	0.6042	0.6512	0.4722	5
0.3607	0.3671	0.3742	0.6667	0.3898	13
0.3667	0.3671	0.3333	0.4516	0.3635	17
0.3548	0.3494	0.3973	0.4912	0.3754	15
0.3333	0.3333	0.3718	0.4667	0.3543	19
0.3548	0.3580	0.3671	0.4828	0.3689	16
0.3438	0.3412	0.3432	0.4590	0.3513	20
0.3667	0.3766	0.3946	0.5000	0.3878	14
0.3385	0.3412	0.3841	0.4746	0.3626	18
0.3667	0.4328	0.3766	0.4000	0.3933	12
0.3729	0.4085	0.4754	0.4179	0.4169	11
0.3860	0.4462	0.4833	0.6667	0.4546	7
0.3667	0.5088	0.5273	0.5091	0.4694	6
0.4000	0.5686	0.5743	0.4667	0.5095	4
1.0000	1.0000	1.0000	0.3457	0.9490	1
0.5500	0.8286	0.8529	0.3333	0.7102	2

In this GRG is calculated using PCA weights followed by the ranks. The higher the value of GRG implies better quality characteristics. Experiment 19 (100 A-5 mm/sec-14 L/min having 352 J/mm heat input) is showing the highest value of GRG with PCA weights. The highest GRG value is 0.9490 with PCA weights respectively, which is ranked 1 among the other experiments. The optimum process parameters having highest GRG value or rank 1 is achieved from Table 5.9 are 100 A, 5 mm/sec and 14 L/min for current (I), welding speed (TS) and flow rate (Q) respectively. Table 5.10 shows the main effects on mean GRG with PCA which also shows the optimum process parameter as well. The variation of mean GRG value for each input parameters shifts from level 1 to level 3 demonstrates the optimum process parameters. The highest value of mean GRG corresponds to the optimal level. Thus, welding speed (TS) is the dominant input parameter on various responses followed by current (I) and the flow rate of shielding gas (Q). PCA technique is considered because of the distribution of the exact weight in which they are contributing for optimal process parameter done for each response that gives accurate and precise results.

<b>Table 5.10</b> Main effects on mean GRG with PCA					
Process parameter	Mean GRG with PCA weights				
	level 1	level 2	level 3	Max-Min (delta)	Rank
I (A)	0.472	0.388	0.595	0.206	2
TS (mm/sec)	0.619	0.376	0.472	0.242	1
Q (L/min)	0.529	0.393	0.527	0.136	3
Total mean GRG	0.486				

Table 5.11 shows the ANOVA table for GRG with PCA weights, clearly sums up the level of significance or dominance of a parameter. Welding speed is coming out to be the significant input parameter as compared to the other input parameter with approximately 65 % of the total contribution. Fig. 5.10 shows the residual plots for GRG.

<b>Table 5.11</b> ANOVA table results for GRG with PCA weights							
Source	SS	df	Mean	F-value	p-value	Remarks	Contribution (%)
A-Current	0.046703	2	0.023352	2.08	0.165	Insignificant	33.26
B-Welding speed	0.091039	2	0.045519	4.04	0.043	Significant	64.83
C-Flow rate	0.002681	2	0.001341	0.12	0.889	Insignificant	1.91

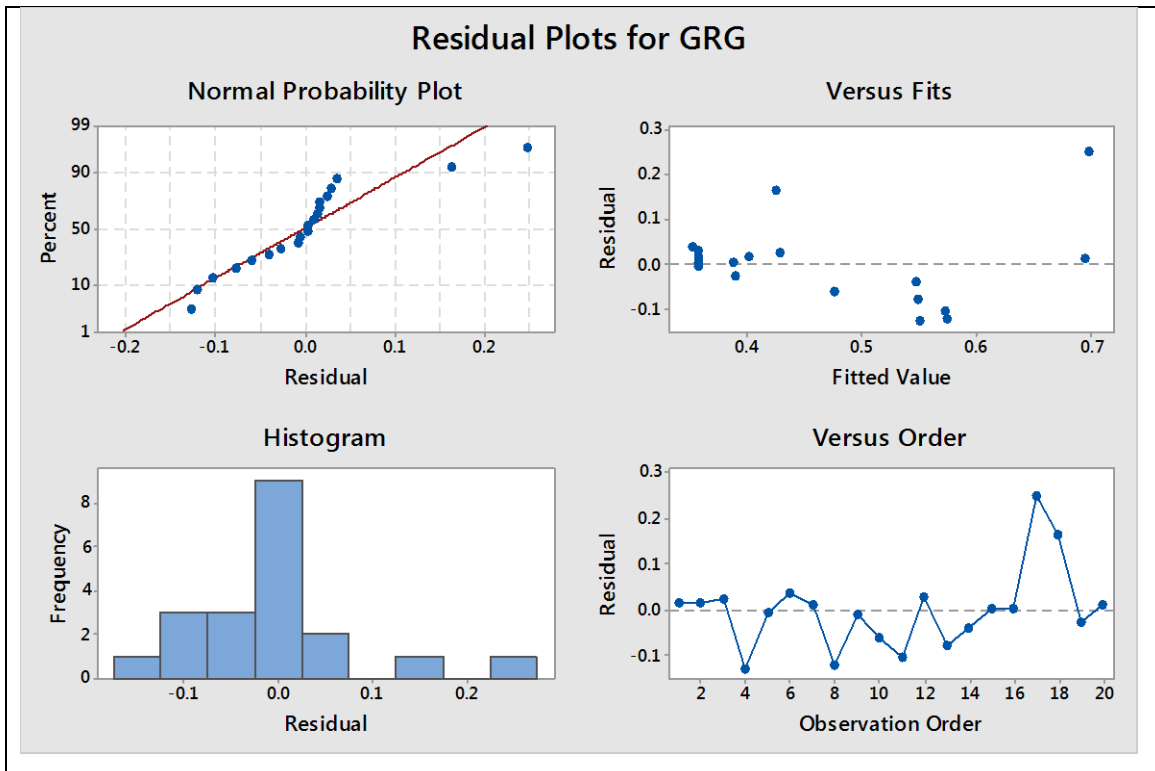


**Fig. 5.10** Residual plots for GRG

Fig. 5.11 shows the optimal process parameters obtained via GRA-PCA technique are 100 A, 5 mm/sec and 14 L/min for current (I), welding speed (TS) and flow rate (Q) respectively with 97.07 % desirability. The response parameters obtained are 226.0409 MPa, 12.5791 %, 68.7314 HV and -152.3023 MPa for UTS, elongation, microhardness and residual stress respectively. Compared to the initial optimal process parameters obtained via CCFCD, GRA-PCA technique significantly improved the levels of process parameters and desirability.

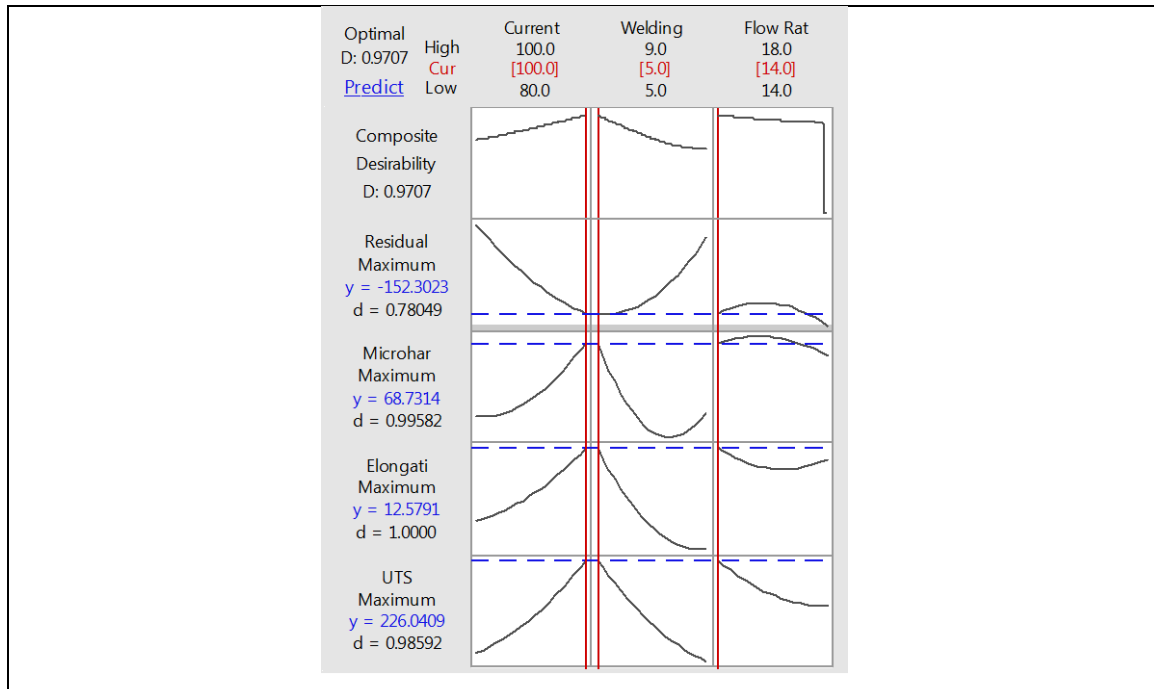


**Fig. 5.11** Optimal process parameters, responses and their desirability with using GRA-PCA technique

### 5.2.5 Confirmation Test

Confirmation runs are needed for reliability checks and also for the level of improvements in GRG. To validate the results, the experiment is tested with an optimized value of process parameters. Also, as shown in Table 5.12, the GRG at an optimum process parameter is improved by approximately 35 % relative to the initial best condition GRG.

<b>Table 5.12</b> Confirmation runs with GRA-PCA			
	Initial factor setting	Optimal welding parameters	
		Prediction	Experimental
Level	I1-TS3-Q3	I3-TS1-Q1	I3-TS1-Q1
UTS	203		226
%E	11.8		12.6
HV	63.9		68.7
RS	-103		-152
GRG	0.5902	0.771	0.8012
Improvement in GRG		0.211	

### 5.3 MICROSTRUCTURAL ANALYSIS ON CMT BUTT WELD

Macro-image of welded sample is shown in Fig. 5.12, which corresponds to five different positions: A = BM of AA6082-T6, B = FL of AA6082-T6 side, C = weld zone (WM), D = FL of AA6061-T6 side and E = BM of AA6061-T6 where microstructure is seen by optical microscope and FESEM.

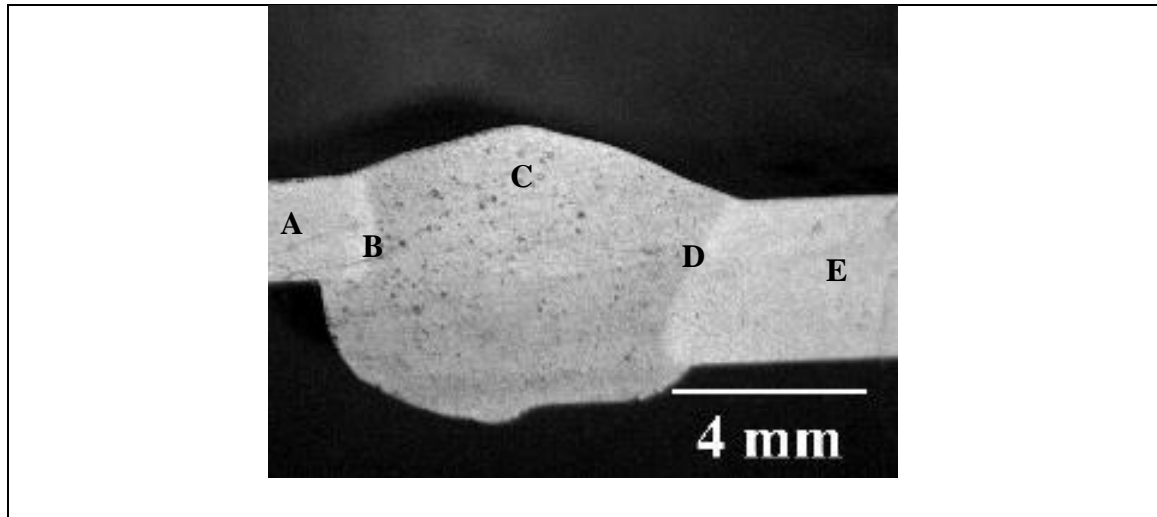


**Fig. 5.12** Macro-image of welded sample indicating the points

Fig. 5.13, 5.14 and 5.15 shows the microstructural images obtained by optical microscope at the indicated points for 163 J/mm, 227 J/mm and 369 J/mm respectively. It is seen that the interface of AA6082-T6 is rich in  $Mg_2Si$  which weakens the HAZ due to brittle intermetallics. On the other hand, interface of AA6061-T6 is having Al-Si eutectic structure which strengthens the bond and HAZ. There is a heterogeneous segregation structure formed in the WM, due to different composition of filler wire as compared to the BM and due to faster cooling rates which are assisted by low heat input in the welded sheets. The WM and fusion line (FL) of 6061-T6 is composed of dendrites with a solid solution of aluminium ( $\alpha$ -Al) and an Al-Si eutectic structure as depicted in Fig. 5.16 (b) & (f) [Liang et al., 2018].

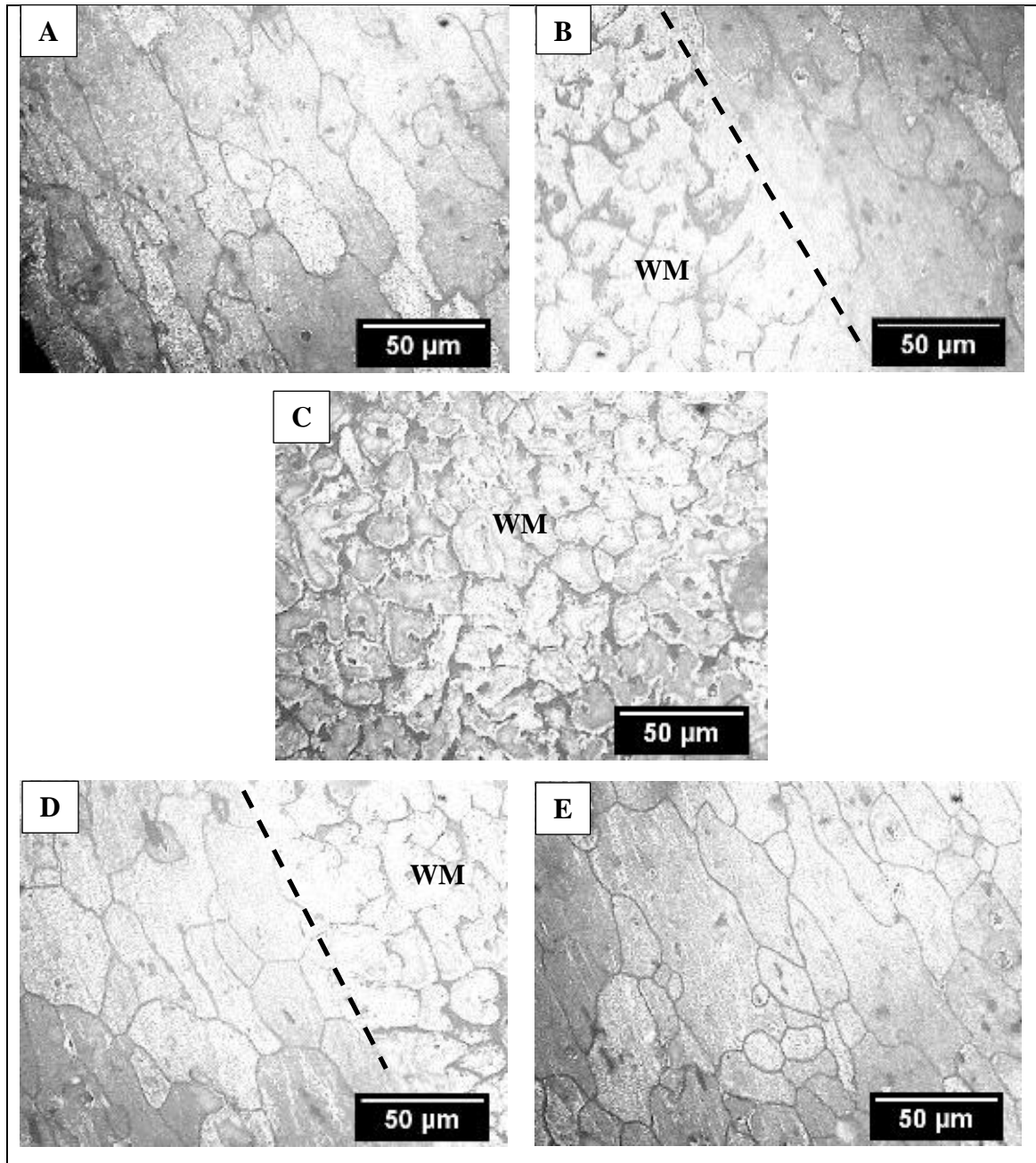


**Fig. 5.13** Microstructures at the indicated positions for 163 J/mm heat input

Al-Si eutectic structure is a low melting point segregation phase with a lamellar, aggregate, or distinct morphology along the  $\alpha$ -Al grain boundary [Nie et al., 2018]. Al-Si eutectic structure is surrounded by a dendritic structure of  $\alpha$ -Al in the WM and FL of 6061-T6 aluminium alloy. Al-Mg phase is existing in the WM as depicted in Fig. 5.16 (e).

Intermetallic compounds could be formed are Al-Mn ( $\text{Al}_2\text{Mn}_3$ ), Fe-Si ( $\text{Fe}_2\text{Si}$ ) and Mg-Si ( $\text{Mg}_2\text{Si}$ ).

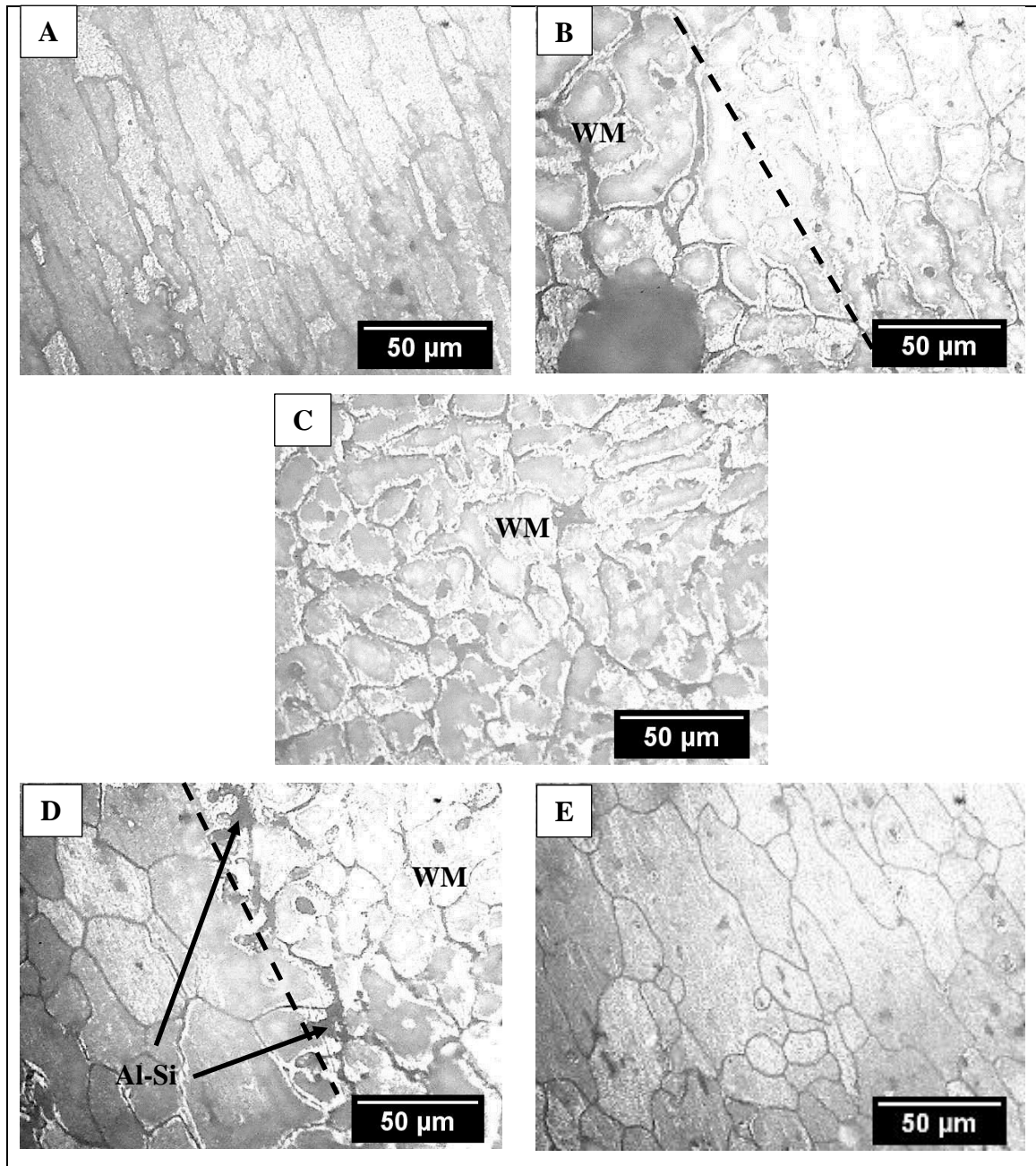
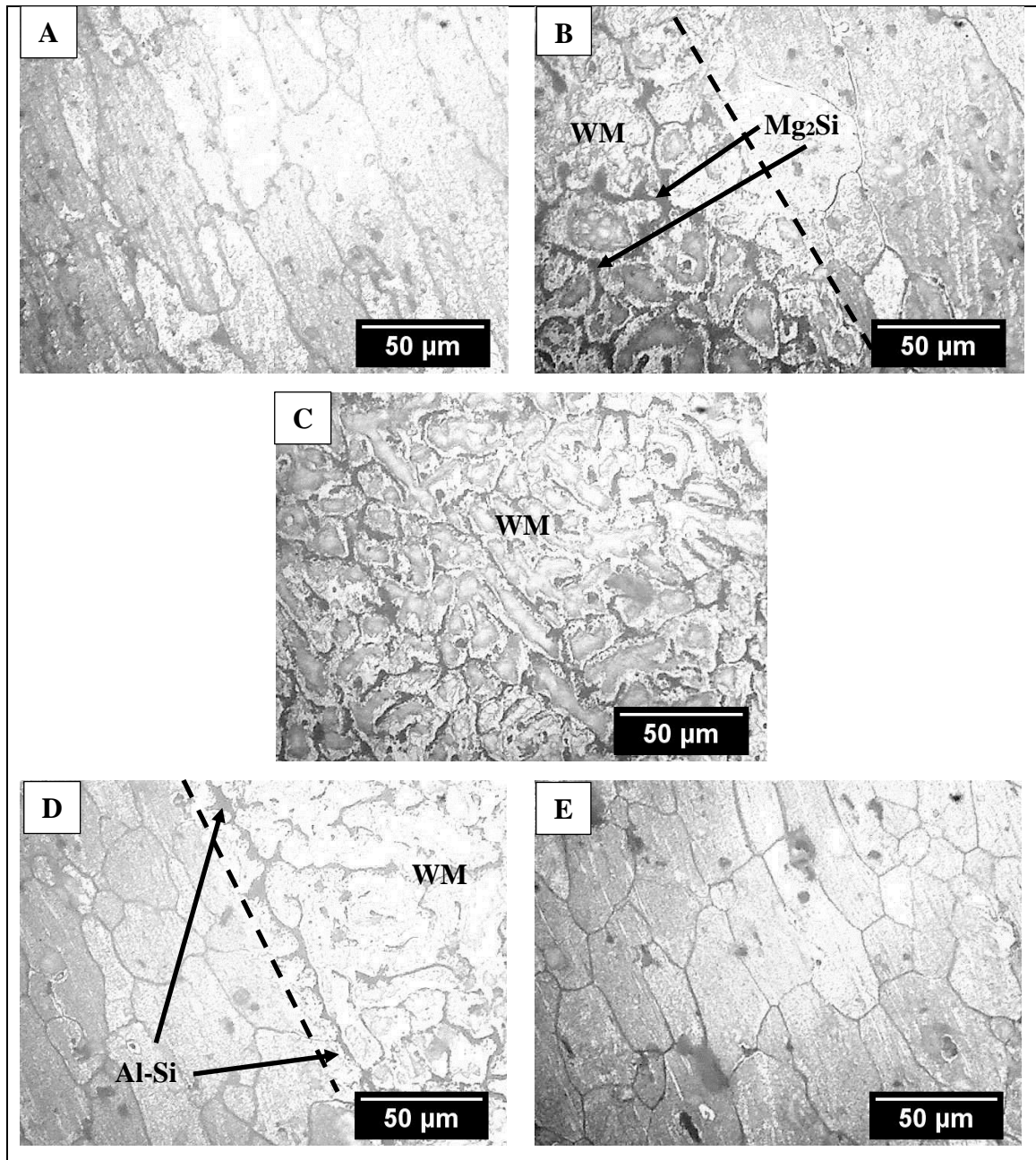


**Fig. 5.14** Microstructures at the indicated positions for 227 J/mm heat input

$\text{Mg}_2\text{Si}$  precipitate is formed in the FZ and not in the WM as depicted in Fig. 5.16 (d), due to the presence of a high amount of Mg and Si (primary elements) in both the substrate and

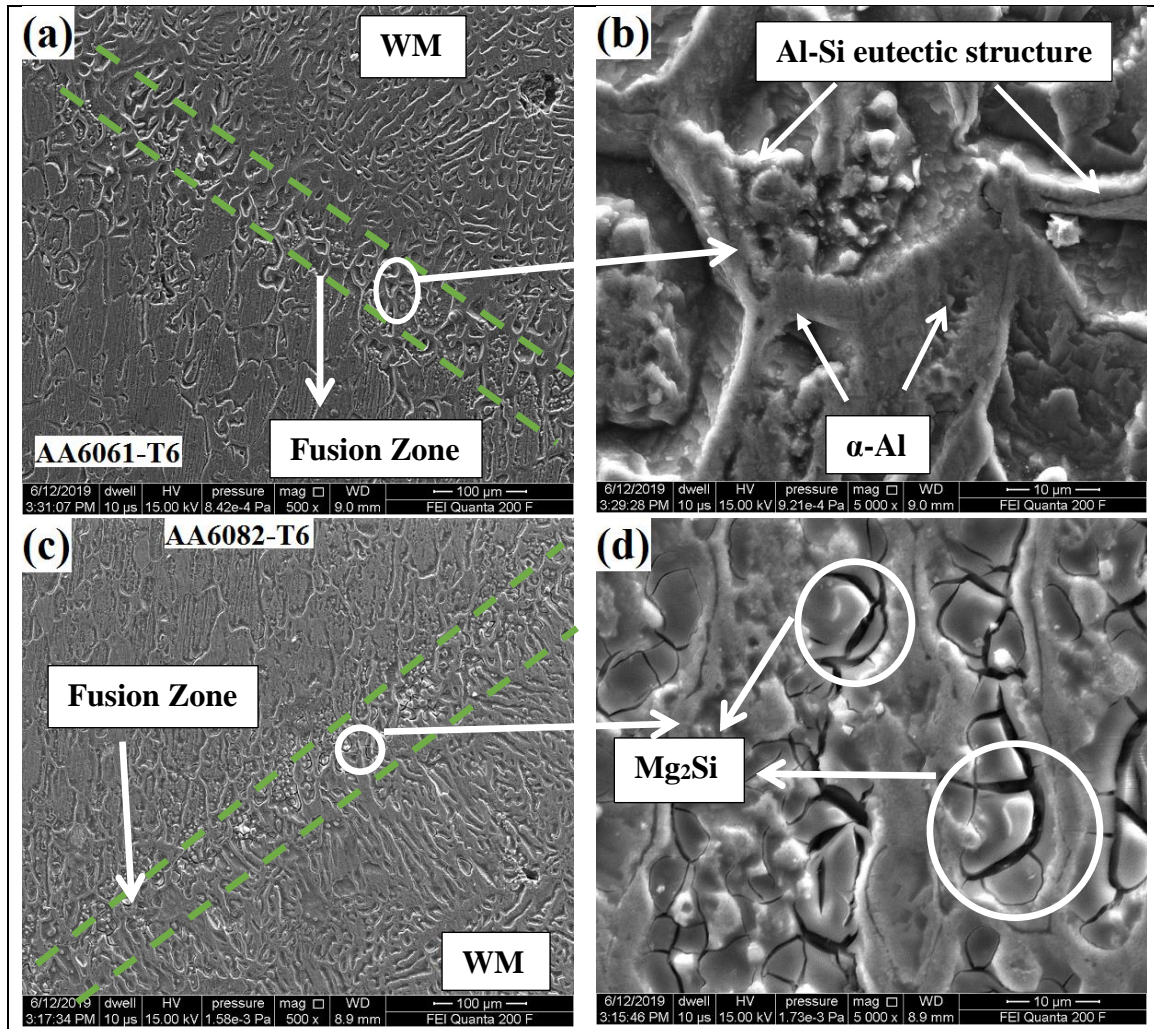


filler material (ER4043 wire), which is detrimental to ductility. During fusion welding, in the weld pool, vaporization of alloys takes place, which could cause the loss of alloy elements. Mg being highly evaporative element within such extreme temperature limits (during fusion welding) it usually escapes partially from the weld pool.



**Fig. 5.15** Microstructures at the indicated positions for 369 J/mm heat input

The rest of the Mg reacts with a large amount of Si to form  $Mg_2Si$  precipitate. Spectrum 10 (Fig. 5.17) provides the EDX result for the welded sample where the Mg content is considerably reduced to 0.3% (wt.%). So, as compared to BM,  $Mg_2Si$  precipitate is lower in WM when 6XXX aluminium alloy series is welded with ER4043 filler wire. Iron is also added as an impurity in most of the commercial 6XXX series alloys. As a result, Al-Fe, Al-Mg, Al-Mg-Mn [Elrefaey and Ross 2015; Eskin 2008 and Mondolfo 1976],  $Al_{0.7}Fe_3Si_{0.3}$ , FeNi,  $AlFe_{0.23}Ni_{0.77}$  and  $Fe_2Si$  possible intermetallic phases could be formed which deteriorates the mechanical properties. Fig. 5.18 shows the XRD and EDX result of sample 2<sup>nd</sup>, with 80A-9mm/sec-18 L/min having heat input of 168 J/mm.



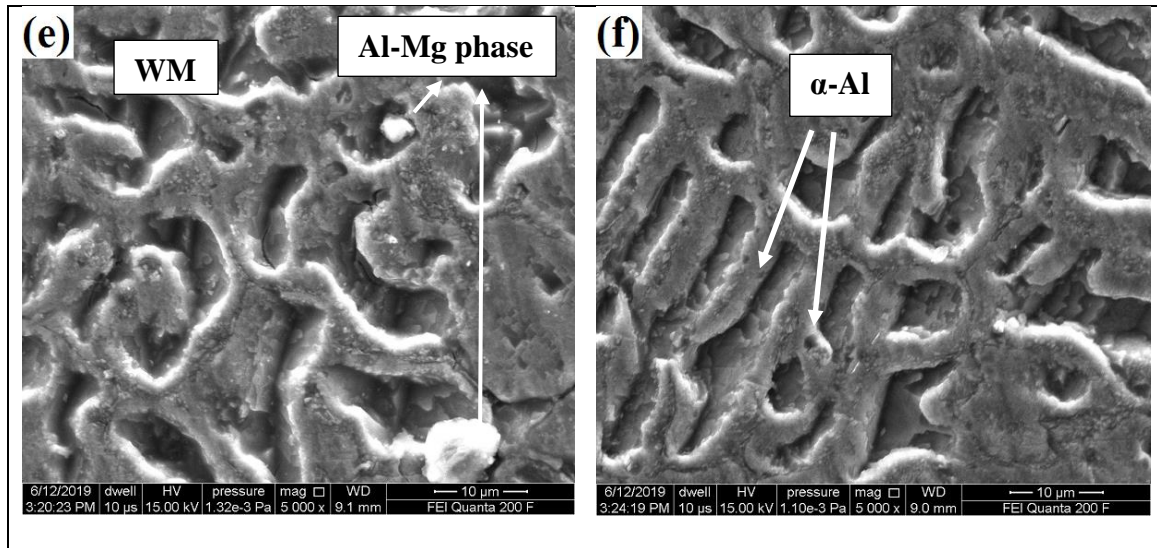


**Fig. 5.16** FESEM images at 163 J/mm (80A-9mm/sec-14L/min) (a)&(b) FL of AA6061-T6 side (c)&(d) FL of AA6082-T6 side (e) & (f) Weldment (WM)

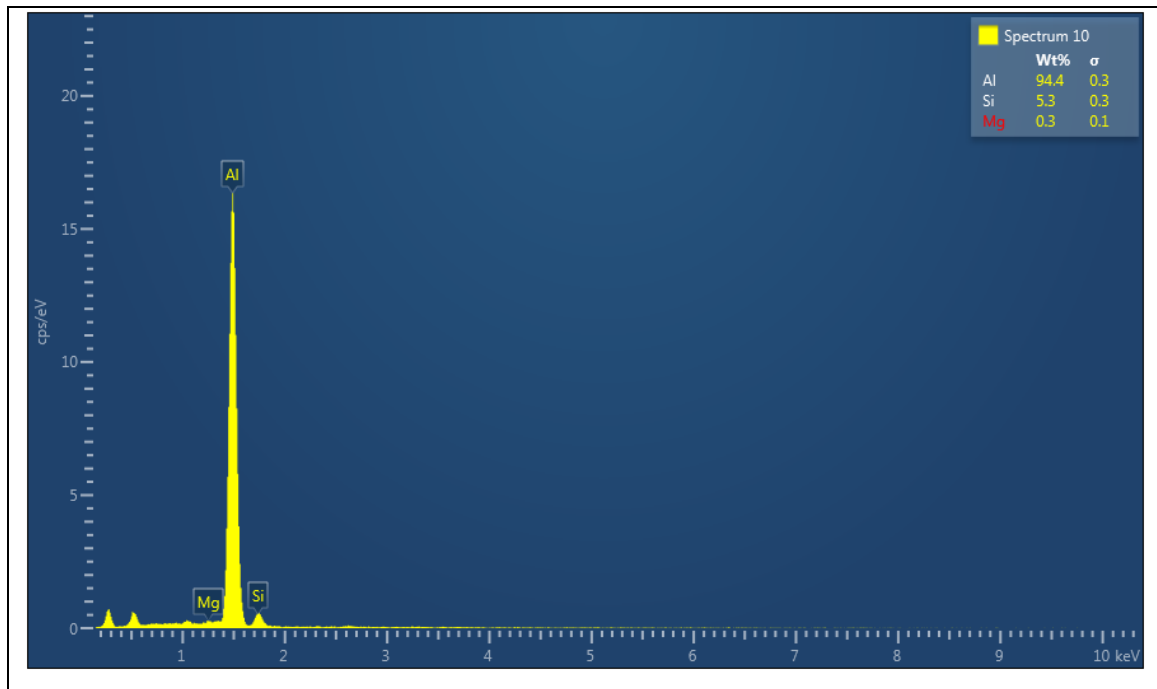


**Fig. 5.17** EDX spectroscopy of sample (Magnesium wt. %)

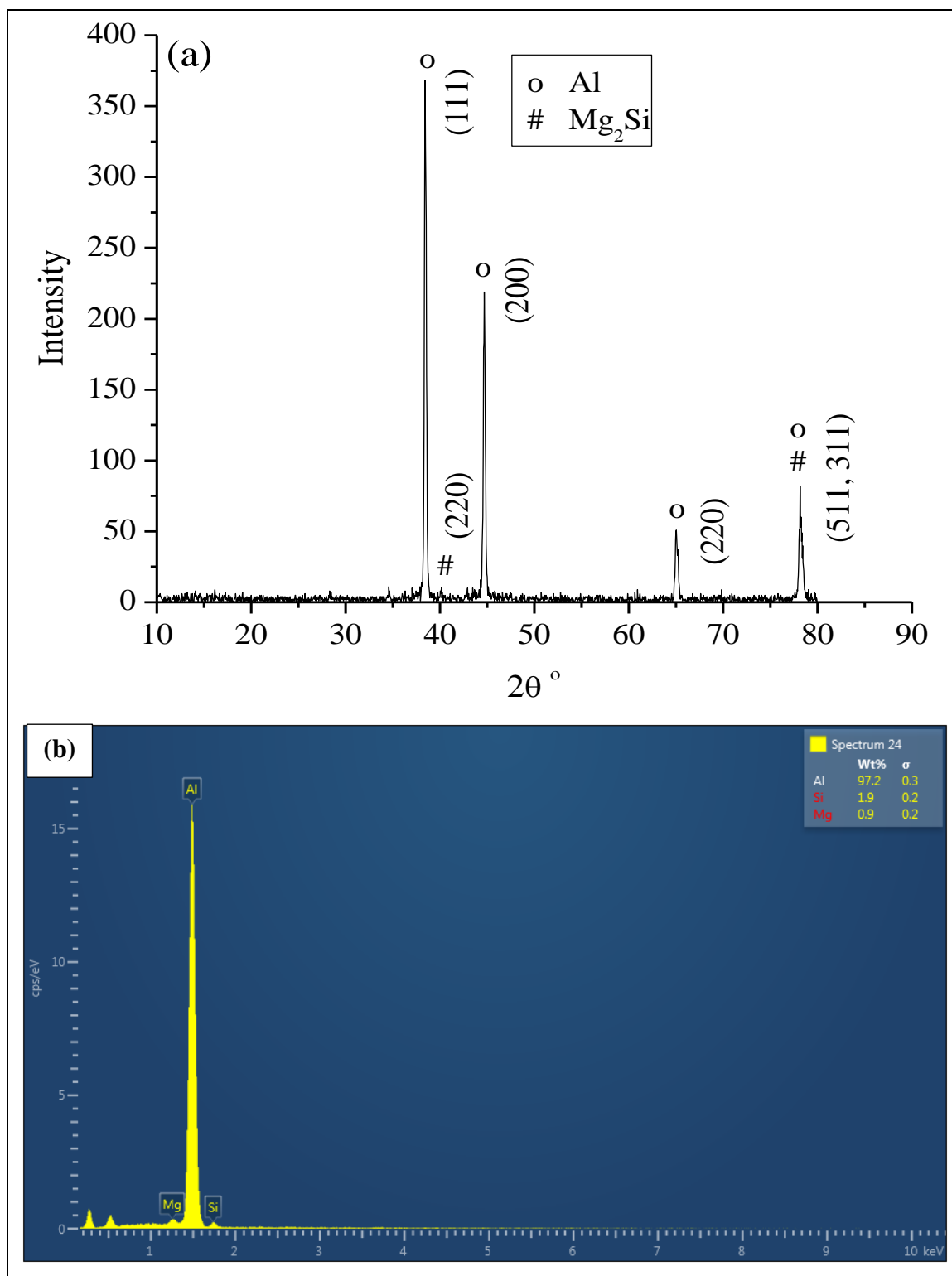


**Fig. 5.18** Experiment 2<sup>nd</sup> with 80A-9mm/sec-18L/min (168J/mm) plots (a) XRD (b) EDX



## 5.4 MECHANICAL PROPERTIES ON CMT BUTT WELD

### 5.4.1 Ultimate Tensile Strength

The samples were made at same thickness for tensile test i.e. the thicker side (AA6061-T6, 3.18 mm) was made equal to the thinner side (AA6082-T6, 2mm) by machining the thicker surface to get the exact tensile properties of the welded butt joint. UTS is in the range of 184 - 228 MPa depending on the process parameters or heat input. Fig. 5.19 (b) shows the tensile specimens after breaking with respect to heat input as per the design experiment. It is distinctly visible from the Fig. 5.19 that all the tensile specimens having fracture at the HAZ of 6082-T6 aluminium alloy side.

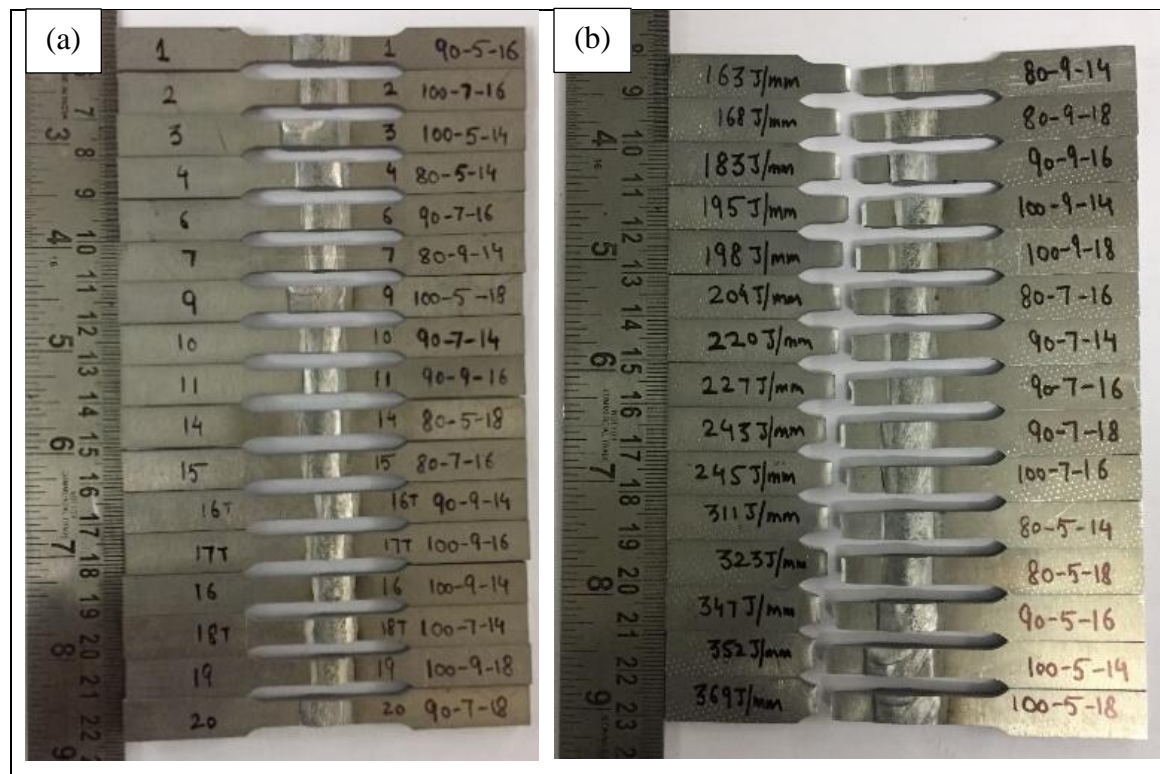


**Fig. 5.19** Tensile specimen (a) before UTM (b) after UTM

During welding, the HAZ side of 6082-T6 aluminium alloy gets more intermetallic phases like  $Mg_2Si$  which is highly detrimental to the strength of the joint.  $Mg_2Si$  is a brittle intermetallic compound which is formed because of high wt. % of Mg and Si elements in the 6082-T6 aluminium alloy and the ER4043 filler wire. Whereas the HAZ of 6061-T6 aluminium alloy is composed of dendrites with a solid solution of aluminium ( $\alpha-Al$ ) and

an Al-Si eutectic structure which makes the HAZ of 6061-T6 much stronger than the HAZ of 6082-T6 aluminum alloys. Fig. 5.20 shows the UTS and percentage elongation graph vs heat input.

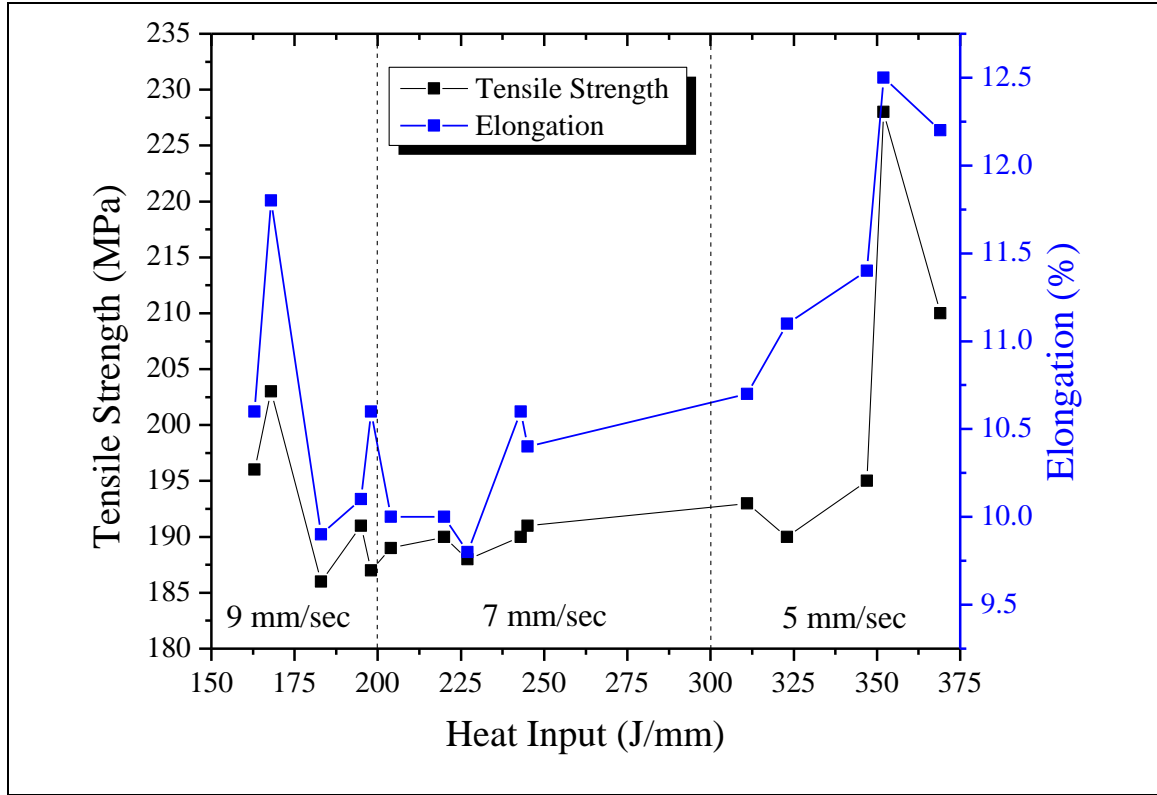


**Fig. 5.20** Tensile strength and elongation curve vs heat input

Stress-strain curve as per heat input is displayed in Fig. 5.21. This illustrates that the elongation (%) is in the range of 9.8 to 12.5 %. The maximum tensile stress is 228 MPa (having heat input 352 J/mm) whereas the minimum is 186 MPa (having heat input 183 J/mm). When compared with the base metal (AA6061-T6), the butt joint strength is about 65-80 %. It can be stated that the joint efficiency is 65-80% of the base metal, which is a good result considering fusion welding. Tensile specimen after breaking shows a honeycomb structure which anticipates maximum strength having a large number of dimples and voids which is depicted in Fig. 5.22. Fig. 5.22 (a) shows higher amounts of voids as compared to Fig. 5.22 (b). As the heat input increases, these fracture voids reduce resulting in higher percentage elongation.

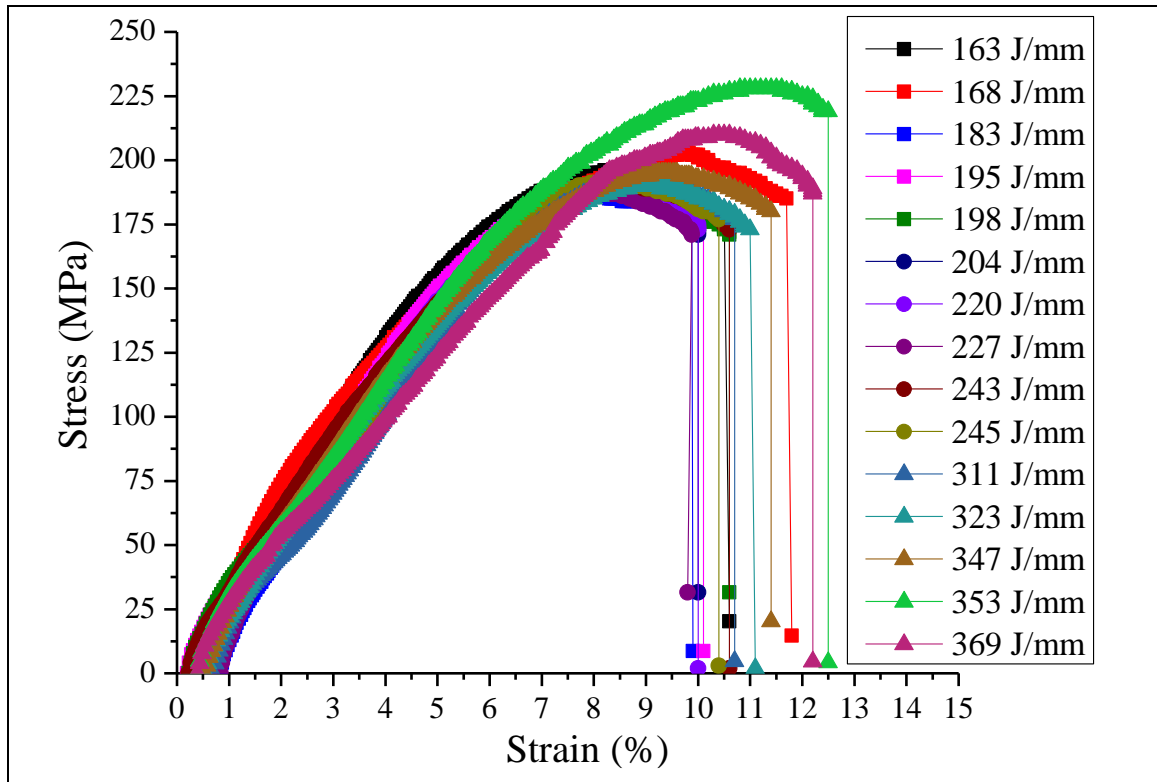


**Fig. 5.21** Stress vs strain curve

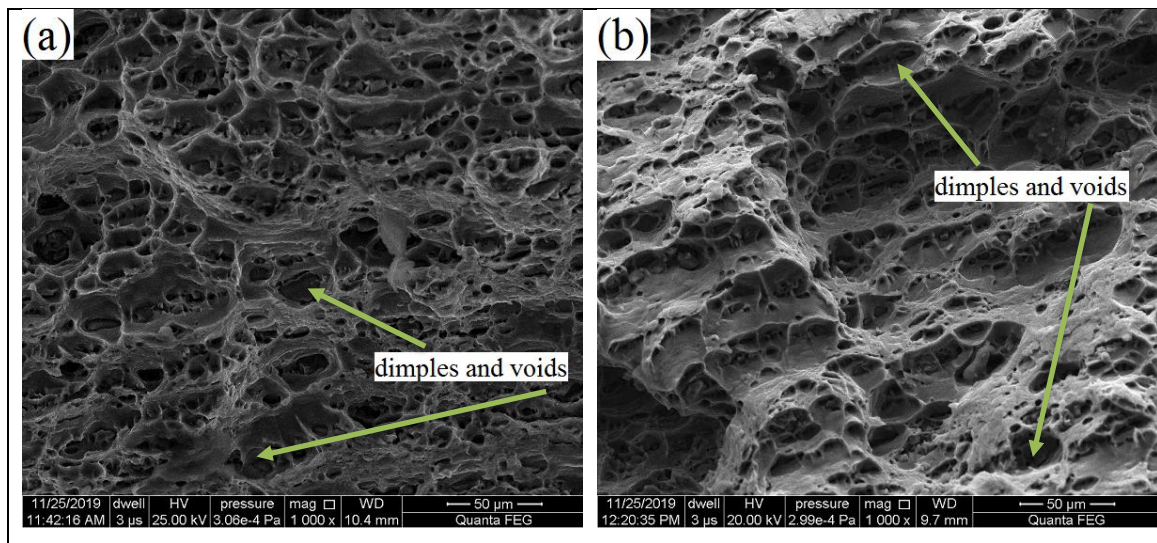


**Fig. 5.22** Fractography FESEM image (a) Sample 3 (90A-9mm/sec-16L/min) (183 J/mm)  
(b) Sample 10 (100A-7mm/sec-16L/min) (245 J/mm)

#### 5.4.2 Microhardness

Microhardness of the dissimilar welded samples is measured along the line, which is depicted in Fig. 5.23. Seven points are considered along the hardness measurement line i.e. BM, HAZ, FL of 6061-T6 side, WM, FL, HAZ, BM of 6082-T6 side. At least five indentations of each sample are taken and then the average values were utilized to calculate microhardness at a specific zone of that sample.

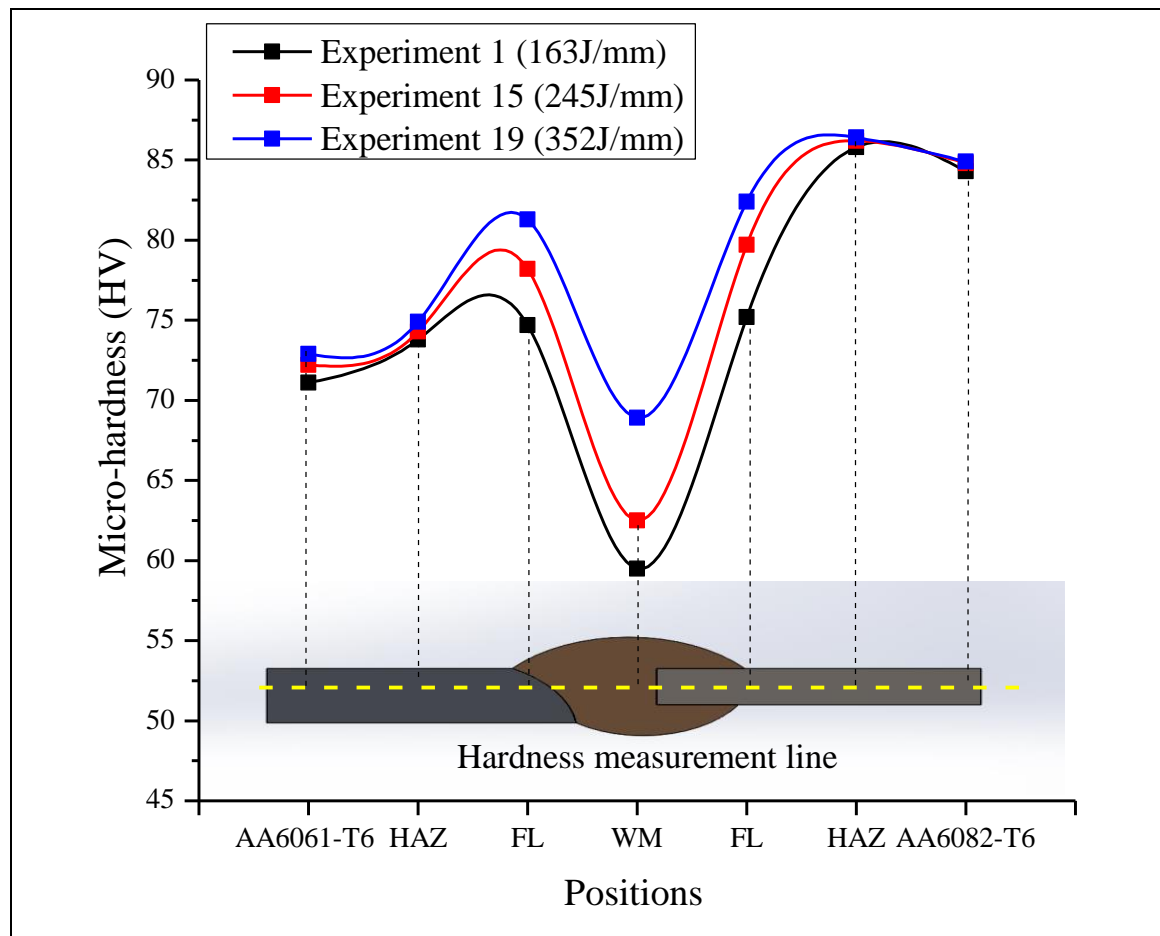


**Fig. 5.23** Microhardness at various position

Almost all the samples are having approximately similar micro-hardness in their respective zones. Microhardness is varying according to the process parameters or the amount of heat input on the welded sample as shown in Fig. 5.24. This variation is due to brittle intermetallic compound formation like  $Mg_2Si$ , precipitate formation, grains formation and



softening effect [Anyalebechi, 1995]. According to the experiments, the mean microhardness is 61.790 HV which is higher as compared to MIG welding (52 HV) obtained by Ishak et al., (2015). Highest microhardness is 68.9 HV which is experienced in the second highest heat input (352 J/mm). The deviation in micro-hardness majorly depends on the different zone on the welded sample due to possible reasons like softening of HAZ, coarse or large grain structure, precipitate formation, brittle intermetallic compound formation etc. During the solidification of FZ, the metal usually eludes its original strength due to strain-hardening effect (SHE). Development of intermetallic compounds (IMC) like  $Mg_2Si$  which is brittle in nature, in the FZ excites a growth in micro-hardness specifically in aluminum alloys.

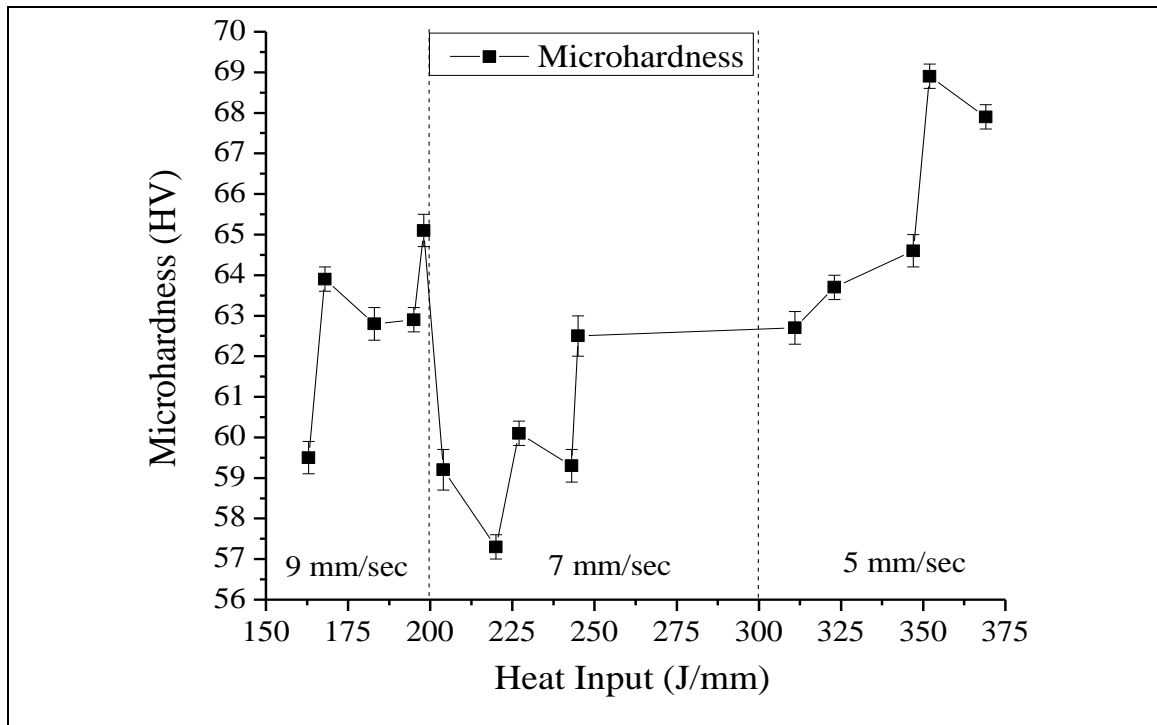


**Fig. 5.24** Microhardness vs heat input

As possibility of precipitate formation of  $Mg_2Si$  is more in FZ and HAZ as contrasted to BM, which results in slight decrease in microhardness. Softening behavior in HAZ and FL of aluminium alloys also changes the microstructure due to which it is called as the weakest zone of the joint [Nie et al., 2018]. In FZ of 6082-T6 aluminum alloy side, there is the existence of  $Mg_2Si$  after welding whereas in FZ of 6061-T6 aluminium alloy side the

Mg<sub>2</sub>Si phases dissolve which results in development of large precipitate and coarsening of grains [Ahmad and Bakar 2011; Maisonnnette et al., 2011]. Therefore, the microhardness of FZ and HAZ of 6082-T6 side is higher than FZ and HAZ of 6061-T6 aluminum alloy. It can be inferred from the above discussion that 6061-T6 is more heat sensitive than 6082-T6 aluminium alloy [Nie et al., 2018]. Due to grain size refinement (coarser grains), the microhardness of WM is lower (approximately 30%) as compared to HAZ. Due to rapid cooling rate, the grains are becoming finer (as moved from WM to BM of both the substrate material) for enhancement of the microhardness values in the HAZ and FL. The rise in microhardness values at HAZ and FL is due to rapid cooling rate (as heat input decrease from going WM to BM) heading to the development of reduced grain size.

#### 5.4.3 Residual Stress

Generally, two types of residual stress are experienced i.e. tensile and compressive. Tensile residual stress is not favorable because it leads to crack formation resulting in lower mechanical properties. Compressive residual stress is more favourable. Compressive residual stress is measured at the weld bead which keeps on increasing with heat input. The residual stress is in compressive nature which is better than the tensile residual stress since it helps to minimize the cracks on the surface of the sample which results in avoiding mechanical failure. In addition, compressive residual stresses are intentionally induced to boost mechanical parts' fatigue behaviour, whereas attempts to reduce residual tensile stress are made using different methods such as post-weld heat treatment, shot peening, spot heating, etc. Since tensile residual stress causes crack nucleation and further crack propagation under tensile load conditions and resulting in tensile failure. Higher compressive stress is also not suitable because it deteriorates the grain structure of the sample which could lead to distortion and mechanical failure. The experimental results of residual stress are in the range which is a positive outcome due to CMT process. Fig. 5.25 shows the residual stress curve at various points for different heat inputs. It shows that at the FZ and WM, the residual stress is compressive in nature. As the curve moves to the base metal on either side, the residual stress tends to zero and eventually some tensile stress is experienced. Higher the heat input, more the compressive residual stress is experienced.

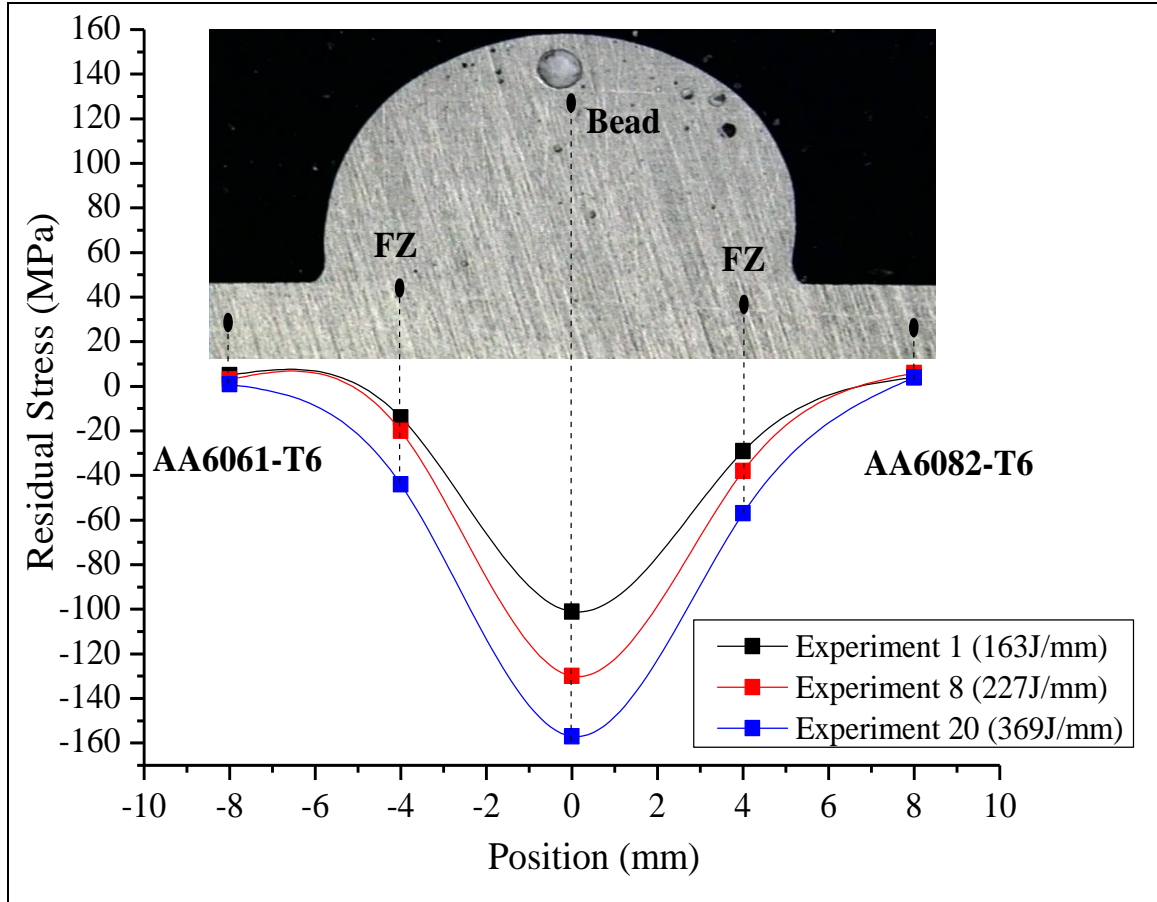


**Fig. 5.25** Residual stress at various positions

Fig. 5.26 shows the Debye Scherrer ring (3D), distortion and profile curve of residual stress at lower (163 J/mm), medium (227 J/mm) and high (369 J/mm) heat input as per the experiments. Debye Scherrer ring (3D) signifies the concentration of residual stress at weld bead, which is demonstrated by converting red (at the tip) to blue shade (at the bottom) at all the heat inputs. Red shade indicates that there is more concentration of residual stress in that region whereas blue shade reveals the negligible concentration of residual stress. The position of the Debye rings, which is a direct measure of strain, can accurately measure residual stress. With the help of Debye ring's spotted position, the extent of the strain is governed. The distortion image acquired in 369 J/mm indicates that high amount of destruction i.e. structural variations occurred in the sample because of the high amount of compressed residual stresses, indicated by the profile peak in the profile image. Due to low heat input provided by CMT machine, the residual stresses are within range as per fusion

welding. When compared to MIG, CMT results in lesser residual stress due to its lower heat input characteristics. As the welding speed reduces from 9 mm/sec to 5 mm/sec the residual stress increases significantly.

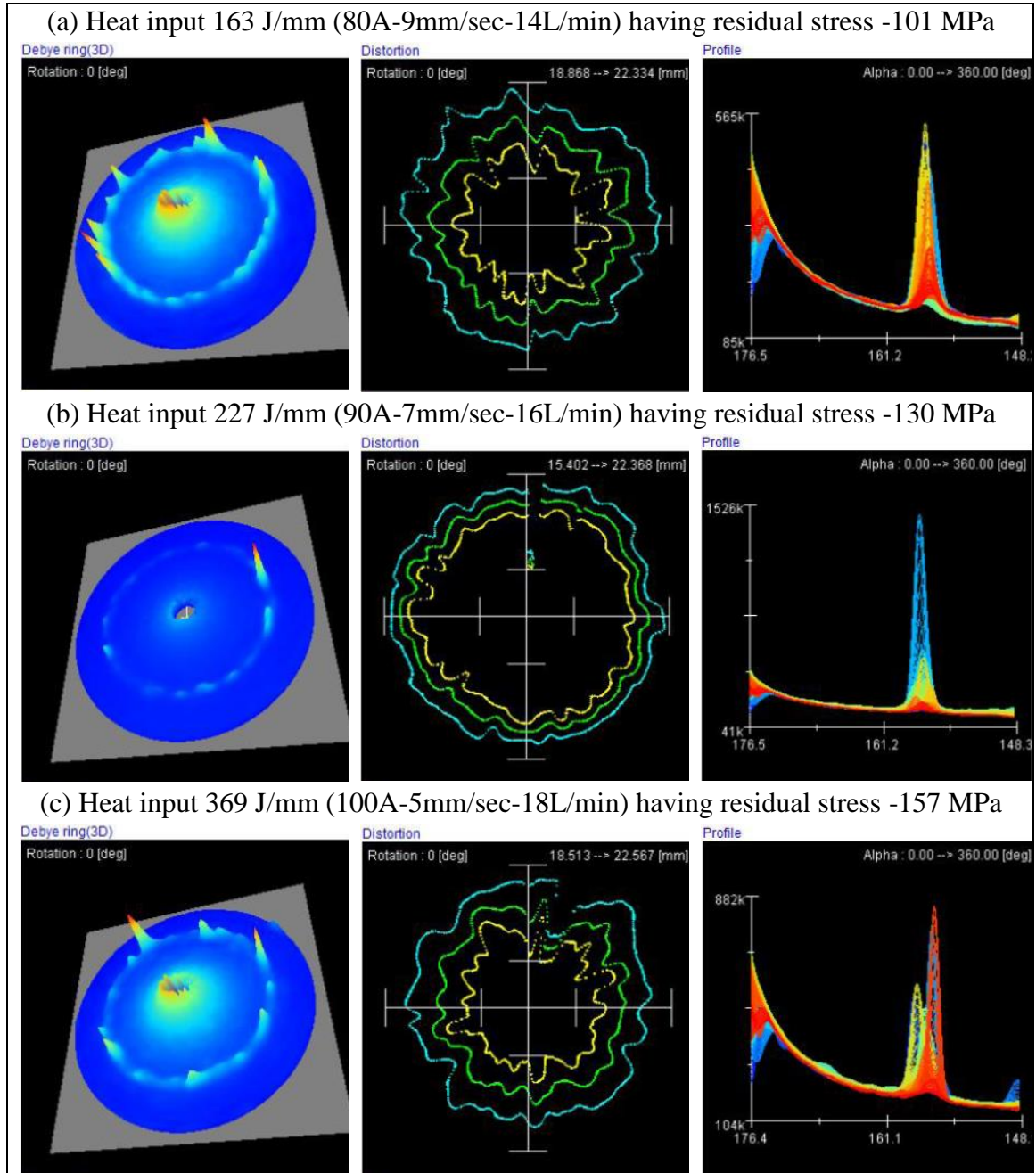


**Fig. 5.26** Debye ring (3D), Distortion and profile of residual stress at various heat input  
(a) 163 J/mm (b) 227 J/mm (c) 369 J/mm

Approximately 28 % increase in residual stress is experienced when welding speed is reduced from 9 mm/sec to 7 mm/sec with increase in current of 80 A to 90 A respectively (Heat input increased from 163 J/mm to 227 J/mm). Similarly, around 20 % increase in residual stress is experienced when welding speed is reduced from 7 mm/sec to 5 mm/sec with increase in current of 90 A to 100 A respectively (Heat input increased from 227 J/mm to 369 J/mm). This comparison shows that current and welding speed both are majorly affecting the residual stress.

## **5.5 SUMMARY**

This chapter is based on CMT butt joining of dissimilar aluminium alloys having different thickness at various heat inputs as per the design matrix. Macrostructural images of CMT butt joints at various heat inputs are illustrated and their weld dimensions are discussed briefly. Optimization of process parameters for the processed joints is carried out by GRA-PCA hybrid technique and the results are compared with CCFCD. Responses chosen are UTS, percentage elongation, microhardness and residual stress which are discussed briefly. Microstructural analysis of CMT butt weld at various heat input and various positions are illustrated.

## CHAPTER 6 : RESULTS AND DISCUSSION ON U-CMT BUTT JOINTS

---

### 6.1 INTRODUCTION

Nowadays, industries are replacing GMAW with CMT for welding of thin plates (<5 mm) due to low heat generation during welding, which is suitable for welding of lower thickness material. CMT offers the meticulous technique of material deposition with low THI by integrating a pioneering wire feed system and combined with high-speed DPC [Pickin et al., 2011]. CMT welded joints are fabricated without spatter, negligible deformation and promotes gap bridging ability in thin sheets [Feng et al., 2009]. Thin aluminium sheets are extensively used in manufacturing sector due to its lightweight to higher strength, durable and recyclability. Recent days, automobile industries are adopting this trend (lightweight to higher strength) rapidly for developing thin aluminum alloy sheets for their products and these manufactured products are already achieving a positive response in the market [Feng et al., 2009 and Fang et al., 2013]. Major drawback of welding aluminium alloys (6061-T6 and 6082-T6) in liquid state is intensity of porosity and these alloys are susceptible for absorption of hydrogen gas in fusion state as discussed by various researchers. The solubility of hydrogen gases escalates in liquid aluminium which creates voids in the joints, as a results of porosity formation. The grain structure of weld metal is coarsened during arc welding processes, resulting in deprivation of the mechanical properties of weld material [Ahmed, 2005]. The grain coarsening structure can enhanced by giving a ultrasonic vibrations during welding process, which leads to grain refining through cavitation and acoustic streaming [Puga et al., 2013 and Tian et al., 2018]. Increasing the degree of molten weld pool convection by actively stirring it with an acoustic wave which increases the liquid weld pool's thermal conductivity as heat transfer in the molten weld pool becomes more efficient [Kau, 1987]. It enables nuclei to survive in the molten weld pool and thus encourages the formation of equiaxed grains in the fusion region. Ultrasonic vibrations during welding not only boost the grain refining but also helps in enhancing the tensile strength, microhardness, wear resistance and porosity of welded joint [Tian et al., 2018 and Haghayeghi et al., 2015]. Tian et al., (2018) uses ultrasonic vibrations on the

welded joints of Al alloys in the CMT process and depicted that number of pores are reduced by increasing the Al-Si eutectic lamellar spacing. [Dai, \(2003\)](#) testified that grain refinement and hardness enhancement with high-intensity ultrasonic wave emissions in AA7075-T6 during gas tungsten arc welding (GTAW). [Puga et al., \(2013\)](#) uses indirect ultrasonic vibrations on Al-Si-Cu alloy and studied that cavitation and acoustic steaming created by ultrasonic vibrations are responsible for microstructure and mechanical properties optimization. [Fang et al., \(2017\)](#) carried out ultrasonic-assisted rheo-squeeze casting process on quasicrystal-reinforced Mg-Zn-Y alloy. Ultrasonic vibration with a high frequency and amplitude has been discovered to be a physical and mechanical way to enhance microstructures and mechanical properties. [Kumar et al., \(2017\)](#) gives a status review on applications of ultrasonic vibration on welding and metal processing. It has been stated that ultrasonic vibrations can aid in the fusion welding process because the mechanical energy of high frequency vibrations is transformed into heat. It is very clear that ultrasonic vibrations provide tremendous benefits when used in welding and other manufacturing processes in terms of enhanced mechanical properties, adequate surface strength, superior material flow and homogenous grain growth etc.

Emphasis in this chapter is on improving mechanical properties such as tensile strength, microhardness, etc., and grain refining through the use of ultrasonic vibrations during CMT welding.

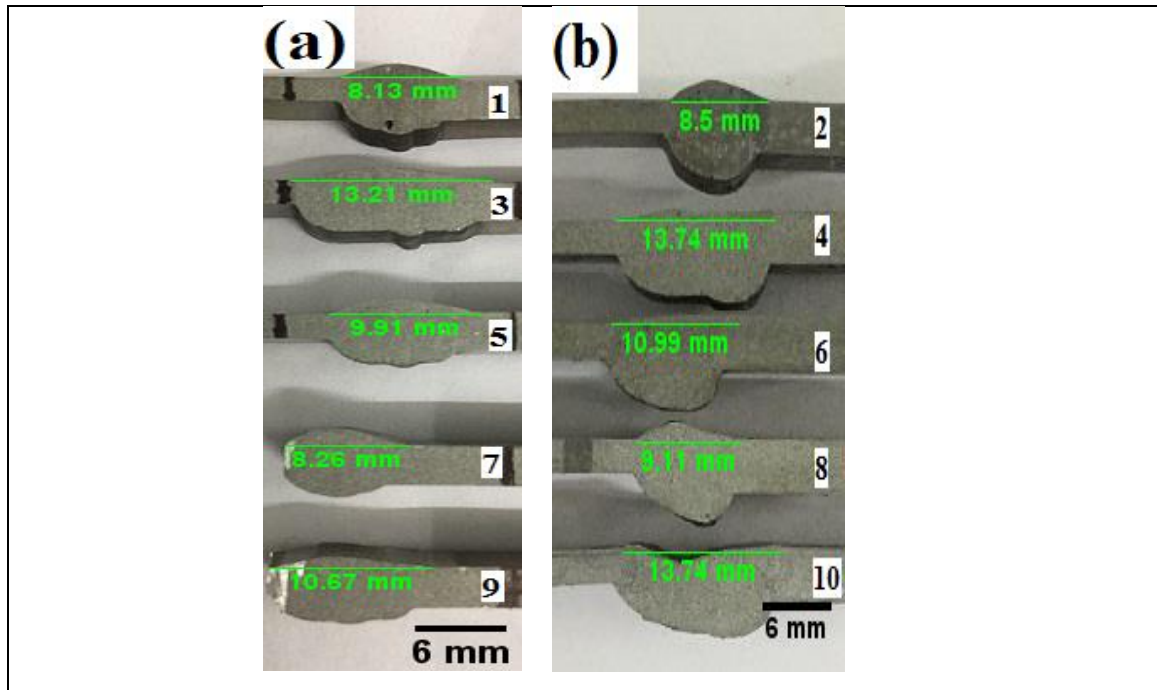
## **6.2 COMPARISON BETWEEN CMT AND U-CMT BUTT JOINTS**

### **6.2.1 Effect of ultrasonic vibrations on weld bead dimensions**

Ultrasonic vibrations at certain frequency with a specific amplitude has a key effect on the size of weld bead dimensions. Fig. 6.1 (a) and (b) displays the cross sections of the welded joints made with and without ultrasonic vibration receptively. The weld width is increased in U-CMT welded sample as compared to CMT welded samples. Ultrasonic vibrations expand the time of solidification of the molten weld pool, which allows more base metal to fuse with the filler wire. This increases the weld width & penetration depth and simultaneously decreases the contact angle in U-CMT welded joints which is shown in Fig. 6.2. Similar type of results are reported by [Tian et al., \(2018\)](#) who uses ultrasonic vibrations

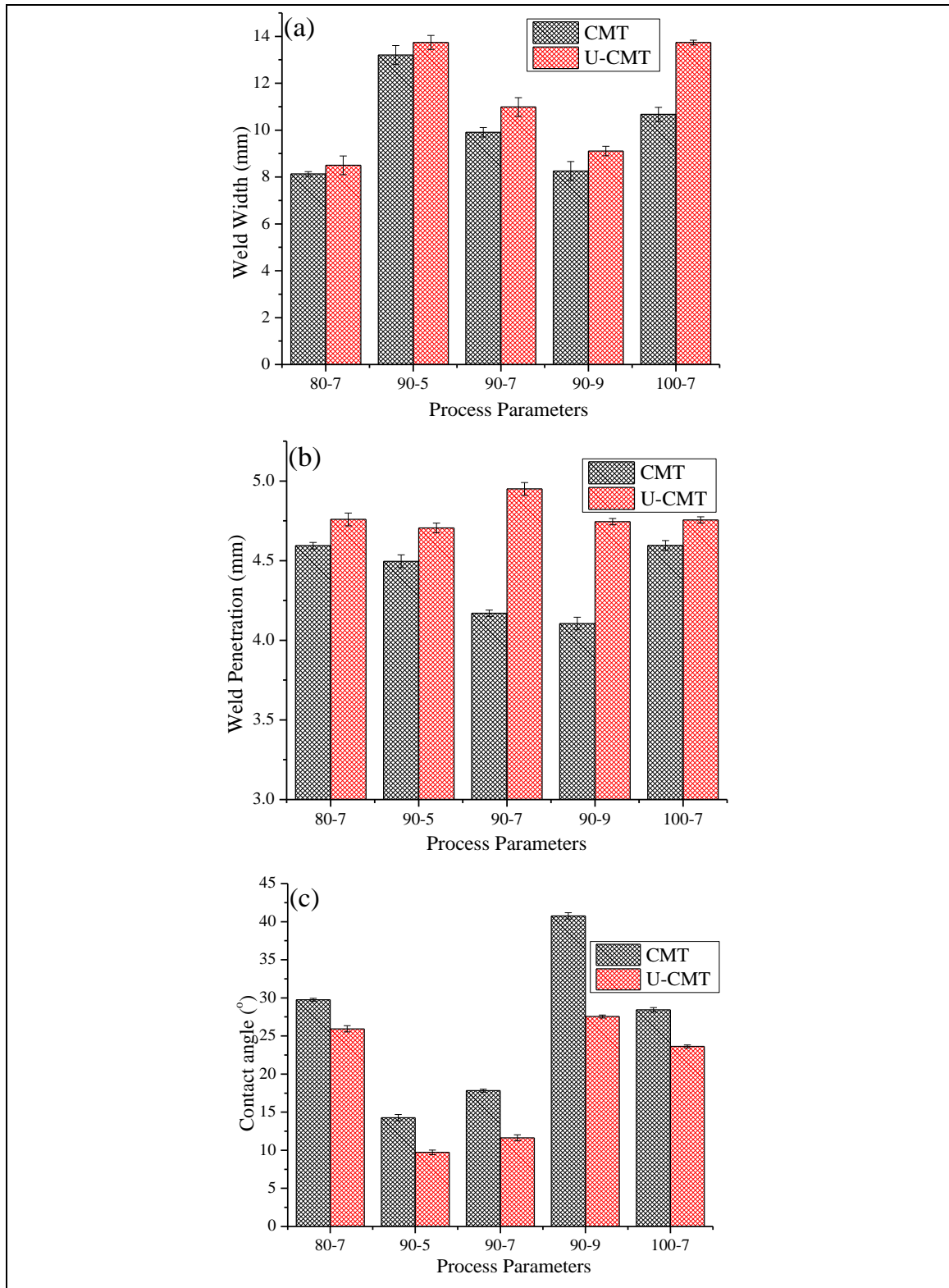


during CMT welding to weld aluminium alloys. Fig. 6.2 (a) displays the difference in the weld width of samples welded with CMT and U-CMT process, the enhancement of weld width observed in the U-CMT samples due to high thermal heat input (THI). As the current increases and welding speed decreases simultaneously the THI increases resulting in higher weld width and lower contact angle. Penetration doesn't show a massive change in the values, but it does have a progressive change which is shown in Fig. 6.2 (b). The difference in penetration values between S-1 and S-2 is 0.165 mm, S-3 and S-4 is 0.209 mm, S-5 and S-6 is 0.780 mm, S-7 and S-8 is 0.640 mm and finally S-9 and S-10 is 0.159 mm. It shows that the difference in the penetration value of the two welding processes (CMT and U-CMT) at same parameter increases at first, attains a maximum value and then decreases to some extent with the given process parameters. Increasing the weld bead dimensions may signify that higher deposition rate can be achieved with ultrasonic assisted cold metal transfer welding.



**Fig. 6.1** Cross-sectional view of welded samples indicating weld width (left side is AA6082-T6 and right side is 6061-T6) (a) CMT (b) U-CMT

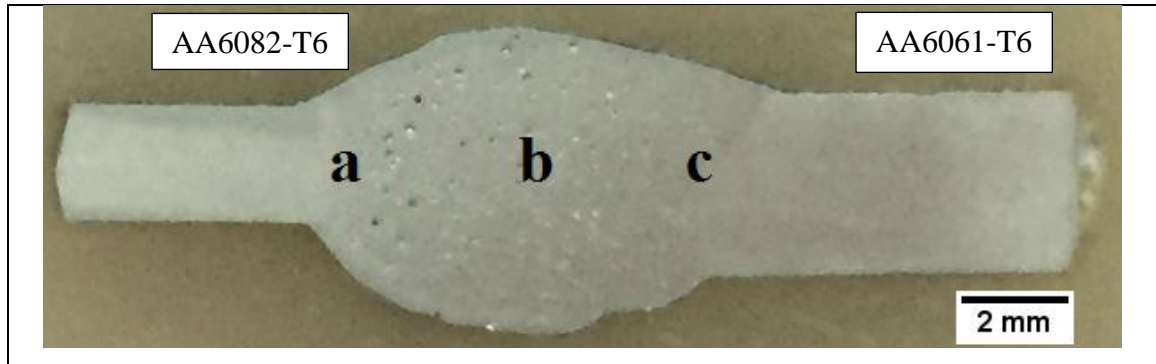




**Fig. 6.2** Effect of ultrasonic vibrations on CMT and U-CMT welded Joints (a) Weld width (b) Weld depth penetration (c) Contact angle

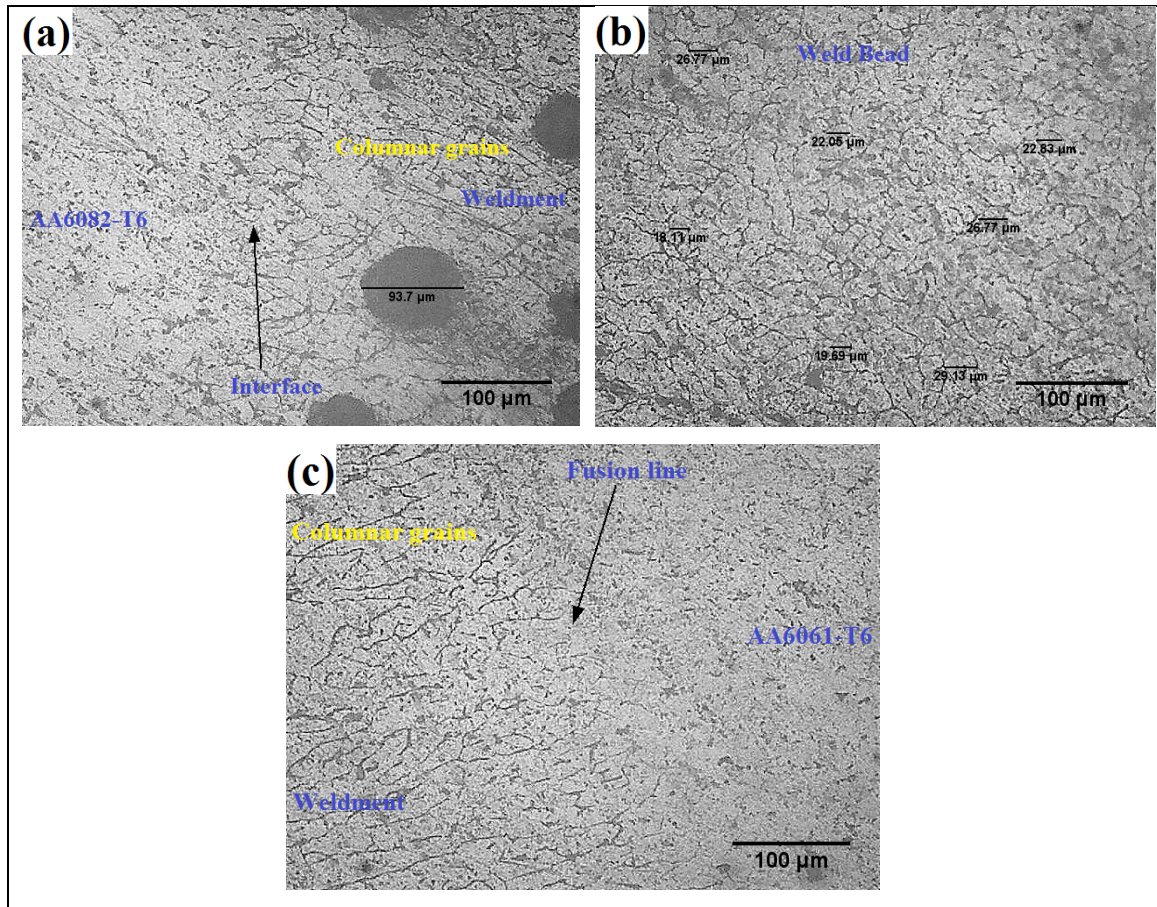
### 6.2.2 Effect of ultrasonic vibrations on the microstructure

Fig. 6.3 shows the macro-image of weld bead consisting various points for microstructural analysis. Point 'a' shows the interface of AA6082- T6/weld bead, 'b' shows the middle of the weld bead and 'c' shows the interface of weld bead/AA6061-T6.



**Fig. 6.3** Macro-image of weld bead consisting of various points for microstructural analysis

The microstructure image of AA6082-T6/weld bead interface is shown in Fig. 6.4 (a). The fusion of dissimilar materials is clearly visible in the interface and some of porosities occurred due to hydrogen entrapment. The average grain size of base material is 28  $\mu\text{m}$  for AA6061-T6 and 26  $\mu\text{m}$  for AA6082-T6. Fig. 6.4 (b) shows the microstructure at the center of the weld bead. Grain size is depicted in the image itself with the help of ImageJ software, which is in the range of 16-36  $\mu\text{m}$ . As this weldment grain size is larger than the base metal which means that the microhardness is lower in the weld bead core. Similarly interface of weld bead/AA6061-T6 is displayed in Fig. 6.4 (c) which clearly shows the different zones in welding separated by fusion line. The average grain size of the CMT weld bead joints is 25  $\mu\text{m}$  which is exhibited in Fig. 6.6 (a). Fig. 6.5 illustrates the microstructural image at different regions of sample welded with ultrasonic assisted CMT. The good bonding takes place between dissimilar alloys and the interface of AA6082-T6/weld bead & weld bead/AA6061-T6 are shown in Fig. 6.5 (a) and Fig. 6.5 (c) respectively. Fig. 6.5 (b) shows the microstructure at the center of the weld bead for U-CMT, which has the grain size in the range of 6-20  $\mu\text{m}$ . The average grain size is around 10  $\mu\text{m}$  in the center of the weld bead zone as shown in Fig. 6.6 (b).

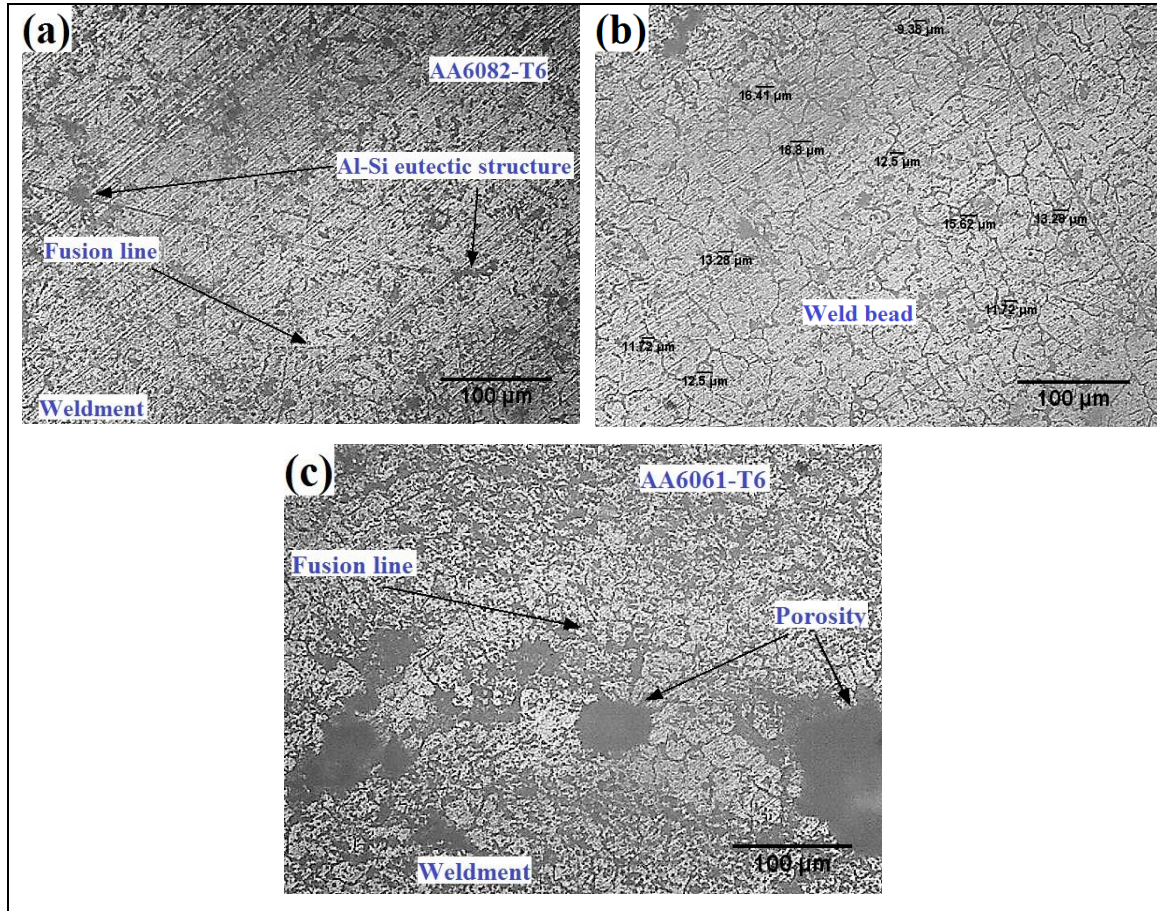


**Fig. 6.4** Microstructure of sample 7 (CMT) (a) Interface of AA6082-T6/weld bead (b) Weld bead (c) Interface of weld bead/AA6061-T6

Similar results are achieved by [Tian et al., \(2018\)](#). It is shown that the average grain size is smaller in case of joints welded with the help of ultrasonic vibrations as compared to joints welded without ultrasonic vibrations. The grain size is inversely proportional to the yield strength of the material according to the hall-petch relation. Ultrasonic vibrations during CMT welding causes the reduction in grain size at the weld bead that makes the joint stronger as compared to CMT welded joints without vibrations. High amount of Al-Si eutectic structures are seen with ultrasonic vibrations as depicted in Fig. 6.5 (a). As a result, it is evident that the welded joint fabricated by ultrasonic vibration is rich in Al-Si eutectic structure. [Tian et al., \(2018\)](#) also reported that eutectic structure of Al-Si is in the shape of globular grains owing to U-CMT as compared with long strips in CMT. That signifies the enrichment of Al-Si eutectic structure in U-CMT. [Srivastava et al., \(2017\)](#) also concluded

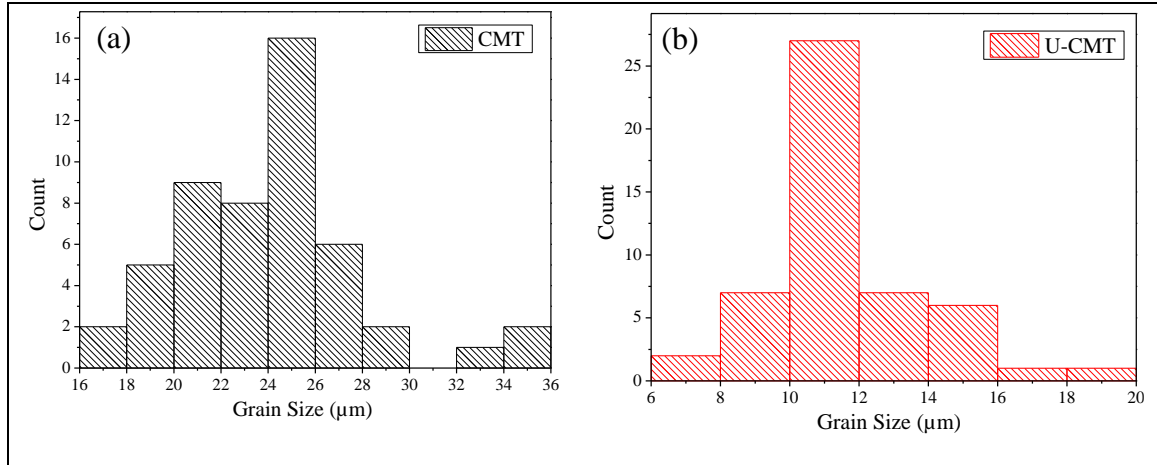


that refinement of eutectic structures is due to ultrasonic vibrations. FESEM image of the CMT and U-CMT welded sample is presented in Fig. 6.7.

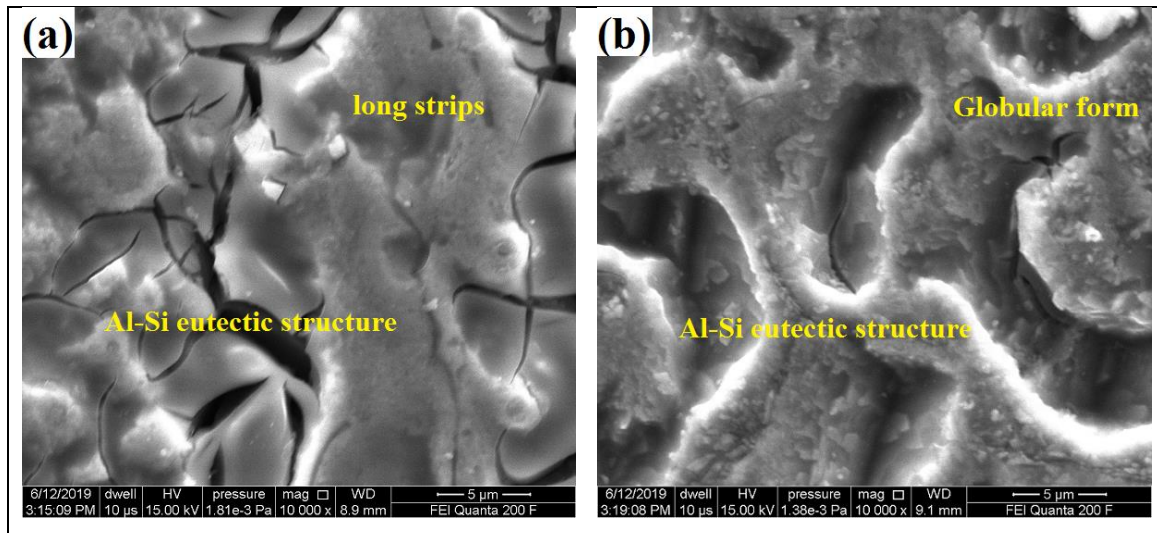


**Fig. 6.5** Microstructure of U-CMT (a) Interface of AA6082-T6/weld bead (b) Weld bead (c) Interface of weld bead/AA6061-T6

Significant amount of Al-Si eutectic structures is seen with U-CMT welded sample. The shape of grains in Al-Si eutectic structure is in globular forms in U-CMT welded sample and in the CMT welded sample long strip shape was detected. The ultrasonic vibrations enhances the enrichment of Al-Si eutectic structure in the weld material and main reason for formation of globular shape of grain size.



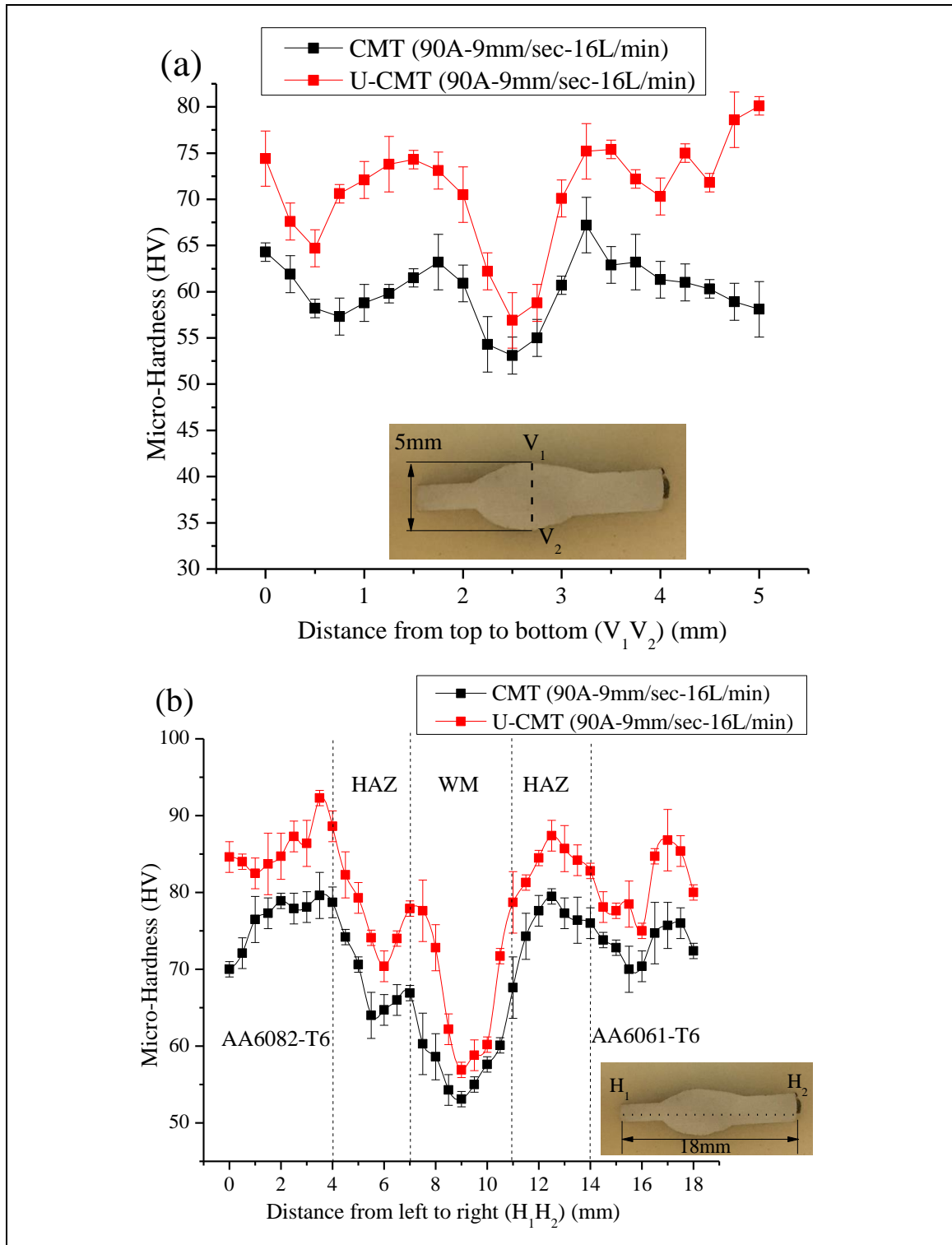
**Fig. 6.6** Grain size distributions at the weld bead (a) CMT (b) U-CMT



**Fig. 6.7** (a) FESEM image of CMT welded weld bead (b) FESEM image of U-CMT welded weld bead

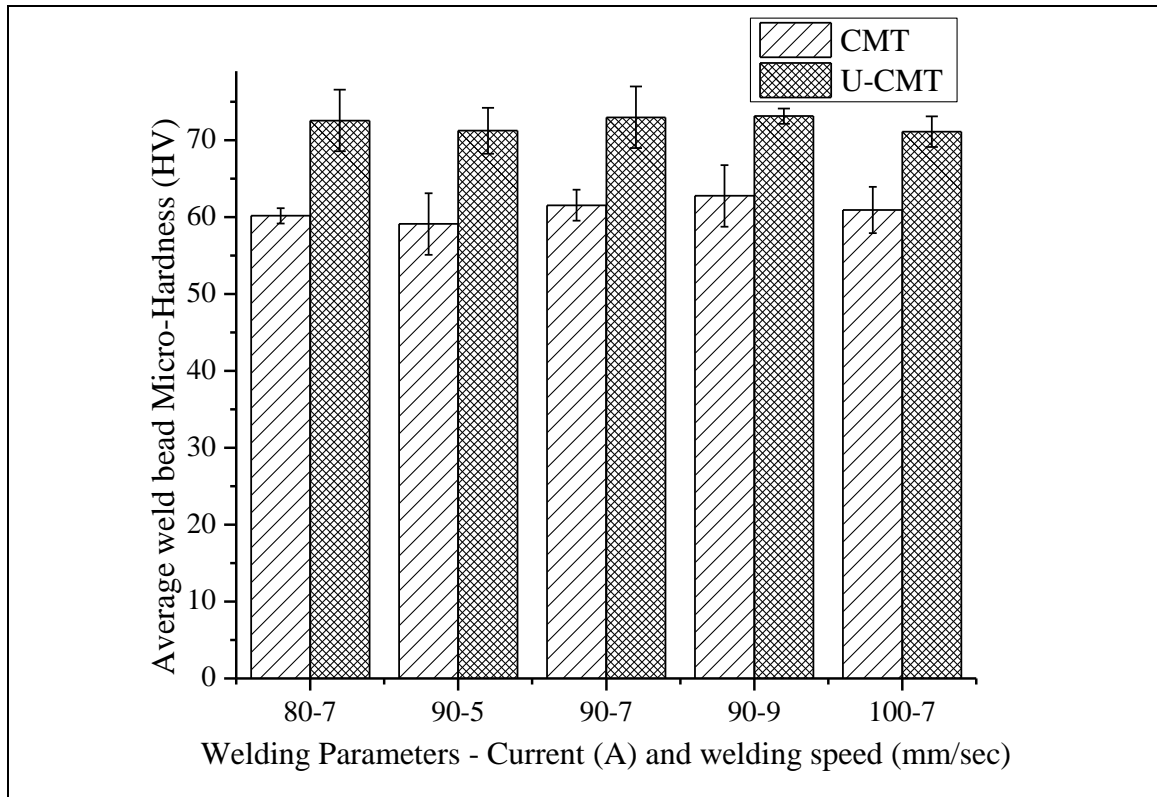
### 6.2.3 Effect of ultrasonic vibrations on the microhardness

Fig. 6.8 (a) and (b) displays the microhardness of the CMT & U-CMT cross section of weld bead sample measured in perpendicular ( $V_1V_2$ ) and parallel ( $H_1H_2$ ) direction respectively. From the top of the bead ( $V_1$ ), 0.1 mm gap is given for the first measurement and 0.25 mm gap is given in between the rest of the measurement for showing the variation in microhardness at the perpendicular section of the weld bead.



**Fig. 6.8** Microhardness of CMT and U-CMT of sample 7 and 8 respectively (a) Perpendicular ( $V_1V_2$ ) to cross-section of weld bead (b) Parallel ( $H_1H_2$ ) to cross-section of weld bead

From left end of the bead ( $H_1$ ), 0.1 mm gap is given for the first measurement and 0.5 mm gap is given in between the rest of the measurement for showing the variation in microhardness at the parallel section of the weld bead. It is understood from Fig. 6.8 (a), the microhardness is in the range of 53-67 HV from top of the CMT welded specimen whereas for U-CMT it ranges about 56-80 HV. As movement from  $V_1$  to  $V_2$ , slight decrease in microhardness was observed in both the CMT and U-CMT welded samples at the center zone. As movement from  $H_1$  to  $H_2$ , the microhardness increment is significant at every weld zone which is shown in Fig. 6.8 (b). The weld zone (WM) is having lowest microhardness in both CMT and U-CMT process because when the solidification of aluminium alloys in weld pool takes place, weld bead undergoes softening effect, which is common in aluminium alloys. The microhardness of the filler wire plays a major role for the values of microhardness in the weldment. The ER4043 filler wire is having an average hardness of 75 HV. Fig. 6.9 shows the average weld bead microhardness with respect to different welding parameters.



**Fig. 6.9** Average weld bead microhardness values for CMT and U-CMT

It shows the significant increase in microhardness value with the assist of ultrasonic vibrations. The average of 18.5 % increase in the microhardness value for U-CMT welded sample in comparison with CMT welded sample. [Tian et al., \(2018\)](#) experimentally found that with similar welding parameters, the joints welded with ultrasonic vibrations is having higher average microhardness values of 16 % as compared to the joints without ultrasonic vibration. Higher hardness simply correlates with the finer (small) grain size. The enhancement of hardness in the U-CMT samples is due to smaller grain size in the welded material. The refinement of the grains occurs in the welded sample due to the ultrasonic vibrations. The average grain size for CMT sample is 25  $\mu\text{m}$  whereas for U-CMT it is about 10  $\mu\text{m}$  according to Fig. 6.6. As per Hall-Petch relationship smaller the grain size higher the hardness value [Masumura et al., \(1998\)](#). Similar type of results was reported by [Dai, \(2003\)](#) for AA7075-T6 during GTAW. It is showed that by applying ultrasonic vibrations, the grains in the welds are refined by 15 %.

#### 6.2.4 Effect of ultrasonic vibrations on tensile strength

The tensile samples after tensile testing of CMT and U-CMT welded joints are shown in Fig. 6.10. It is distinctly visible from Fig. 6.10 that all the tensile specimens having fracture at the HAZ of AA6082-T6 side. Higher tensile strength is achieved with ultrasonic vibrations due to lower grain size of the welded samples. Sample 10 (100 A and 7 mm/sec) with U-CMT observed the fracture at the weld zone because of the higher heat input, which is measured using thermal imaging camera. Higher heat input incorporated with vibrations which creates a cavity, i.e. the weld bead aesthetics shows a concave cavitation with increase amount of penetration. This slightly lowers down the tensile strength of the joint as shown in Fig. 6.11. Sample 10 (100 A and 7 mm/sec) experiences the maximum heat input as compared to the other samples. So, as a result, its tensile strength is lower by 1% in CMT and approximately 8 % in U-CMT as compared with the maximum tensile strength of the other samples. In U-CMT the variation is larger for tensile strength reduction because of its vibrational heat. Stress vs strain curve is shown in Fig. 6.12. All the CMT samples are depicted in Fig. 6.12 (a), which is in the range of 188 – 194 MPa. As U-CMT samples shows relatively higher tensile strength than CMT samples which is shown in Fig. 6.12 (b). It shows the maximum tensile strength sample (202 MPa) in U-CMT which is higher than



all the samples of CMT. S-8 (UCMT 90A-9mm/sec) also has higher percentage elongation which improves its ductility as compared to S-7 (CMT 90A-9mm/sec).

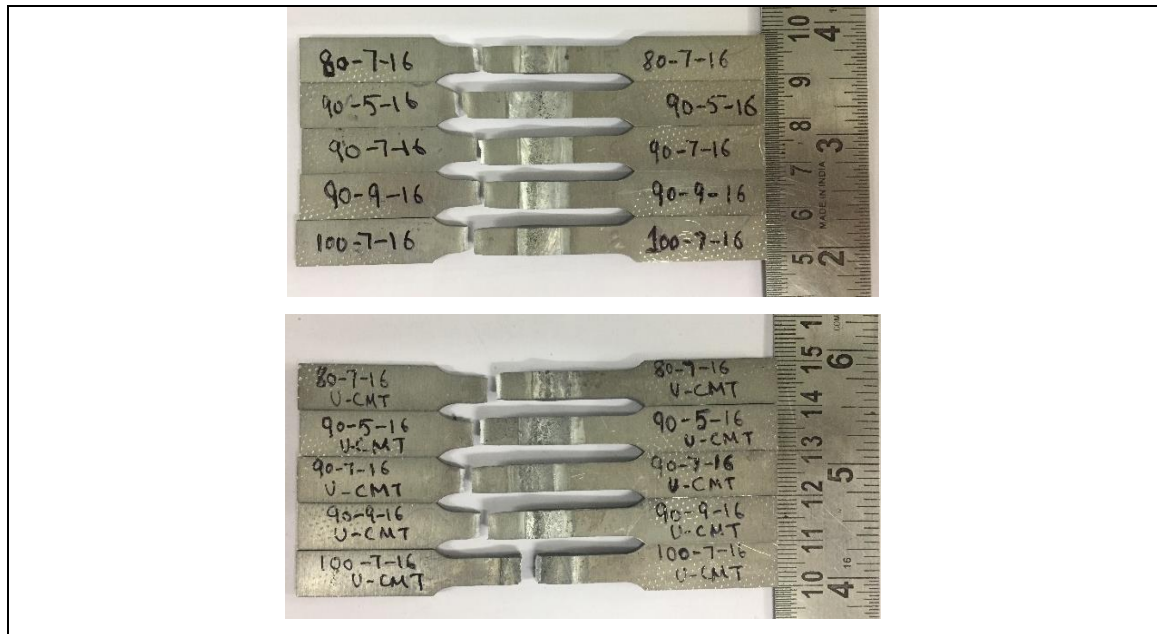


**Fig. 6.10** Fracture location of tensile specimens (a) CMT (b) U-CMT

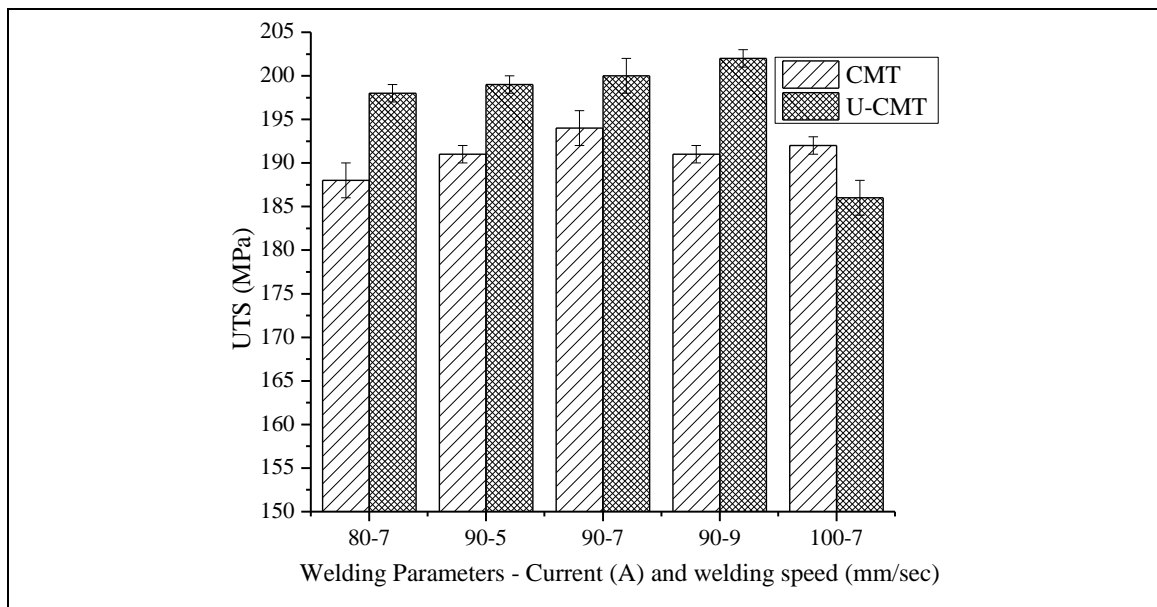


**Fig. 6.11** Tensile strength of welded samples for with and without ultrasonic vibrations welded samples

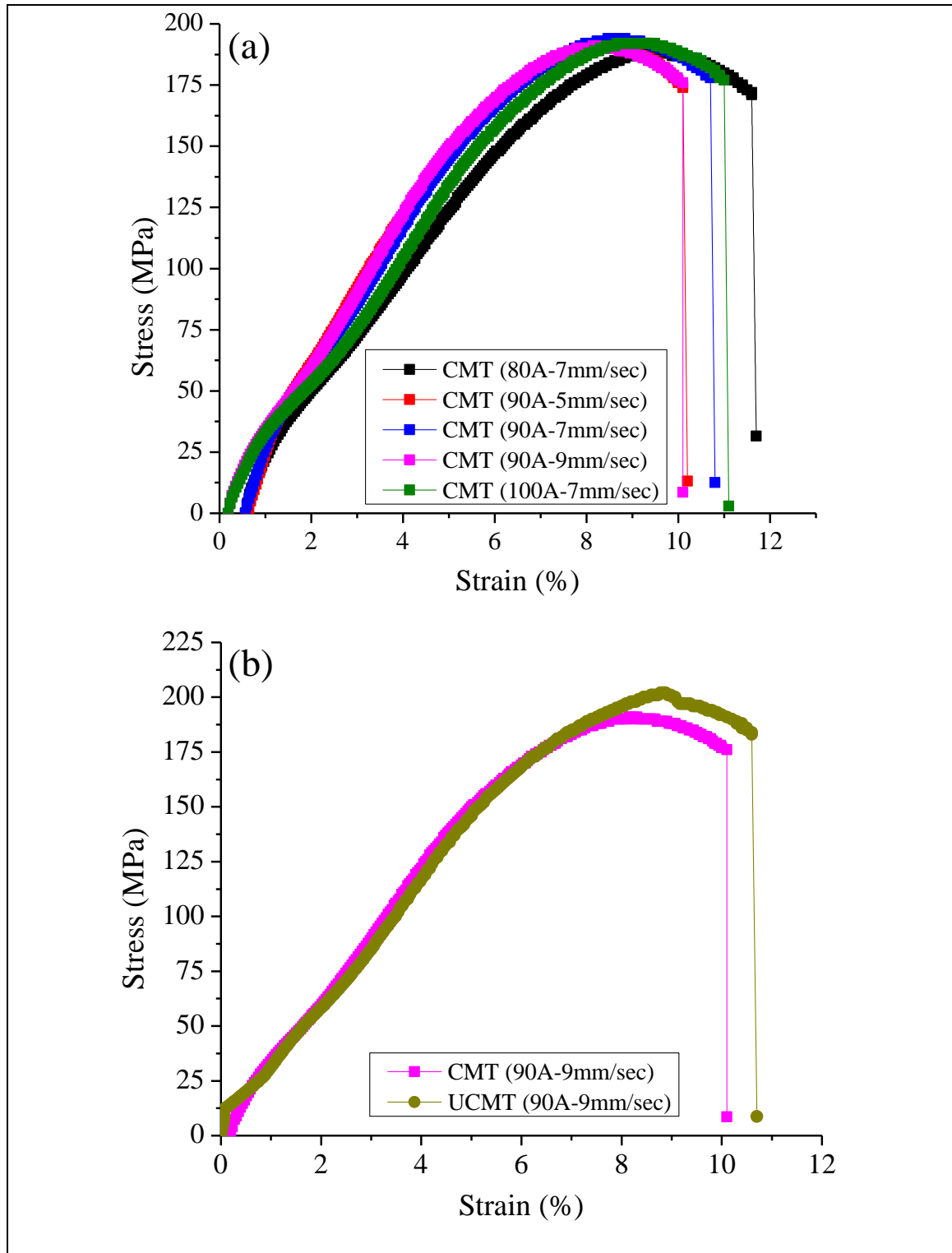


**Fig. 6.12** Stress vs strain curve (a) All CMT samples (b) CMT and U-CMT comparison

The tensile fracture surface of CMT and U-CMT welded sample are shown in Fig. 6.13. Dimples and voids are clearly visible in the tensile fracture surface of CMT welded sample.

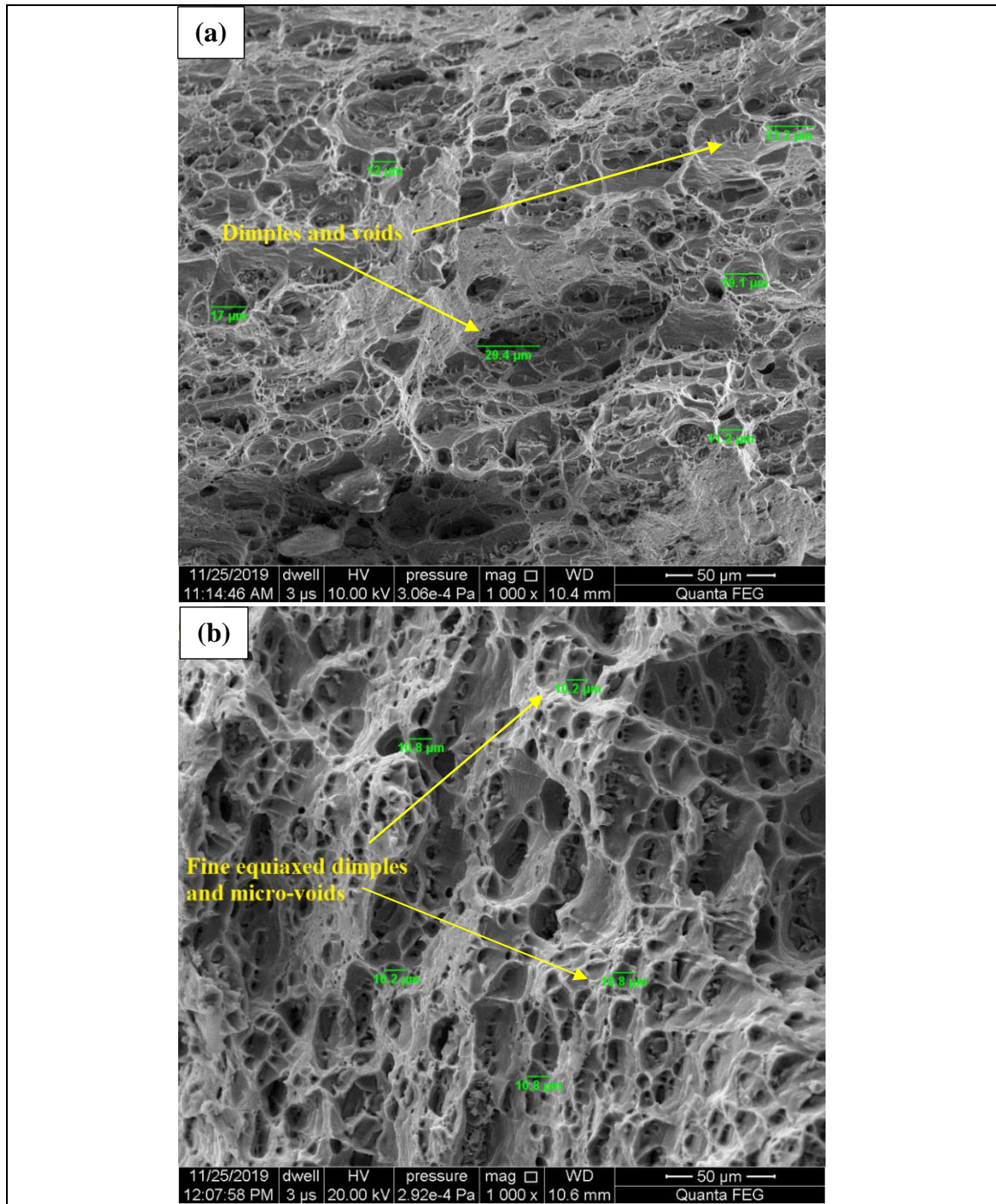


**Fig. 6.13** FESEM image of tensile fractured surface (a) CMT sample 7 (90A-9mm/sec)  
(b) U-CMT sample 8 (90A-9mm/sec)

In the U-CMT welded tensile fracture surface fine equiaxed dimples and micro-voids are observed due to refinement of grains. Honeycomb like structure also seen in the Fig. 6.13 which anticipates maximum strength. The EDX analysis of tensile fractured surface of selective regions of CMT welded sample and U-CMT welded sample are displayed in Fig. 6.14 and Fig. 6.15 respectively. The elements and their weight percentage of the fracture surface of both samples are similar, majorly consisting of Al and Si. [Tian et al., \(2018\)](#) reported that the Al-Si eutectic structure is primarily composed of Al and Si, with small quantities of other elements.

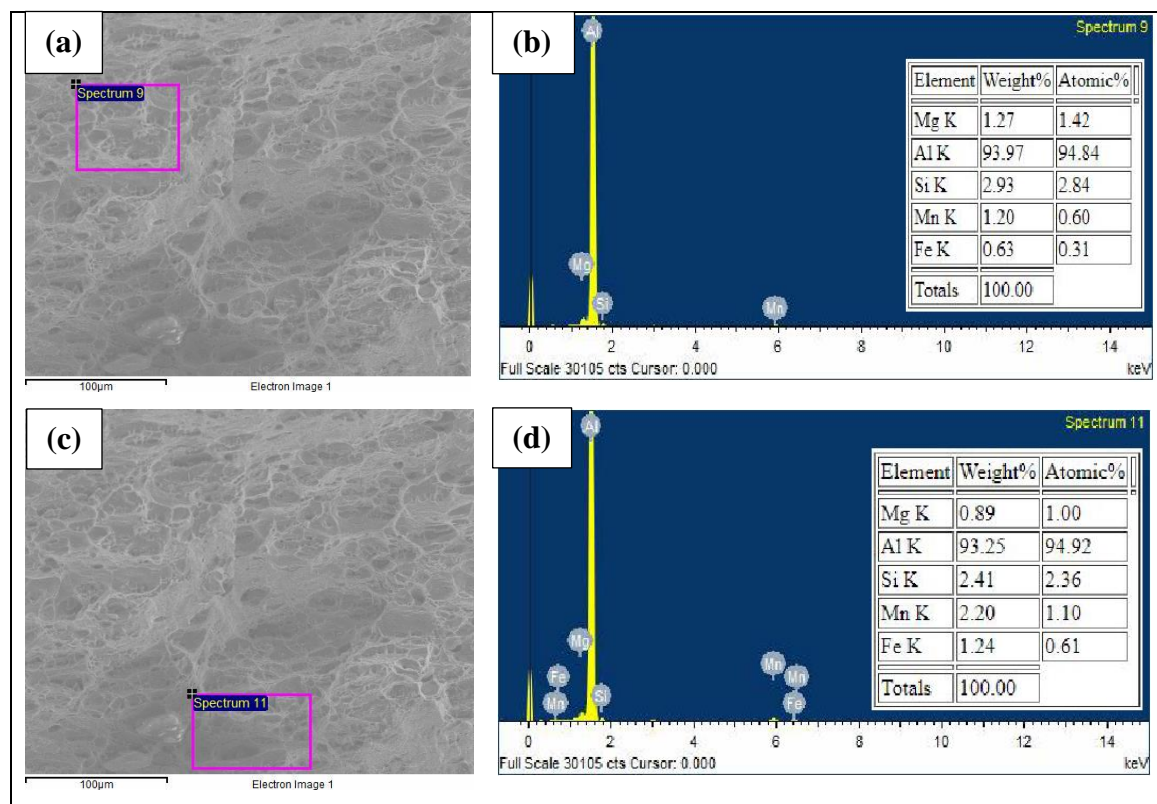


**Fig. 6.14** EDX image tensile fractured surface of CMT (a) & (b) spectrum 9 (c) & (d) spectrum 11



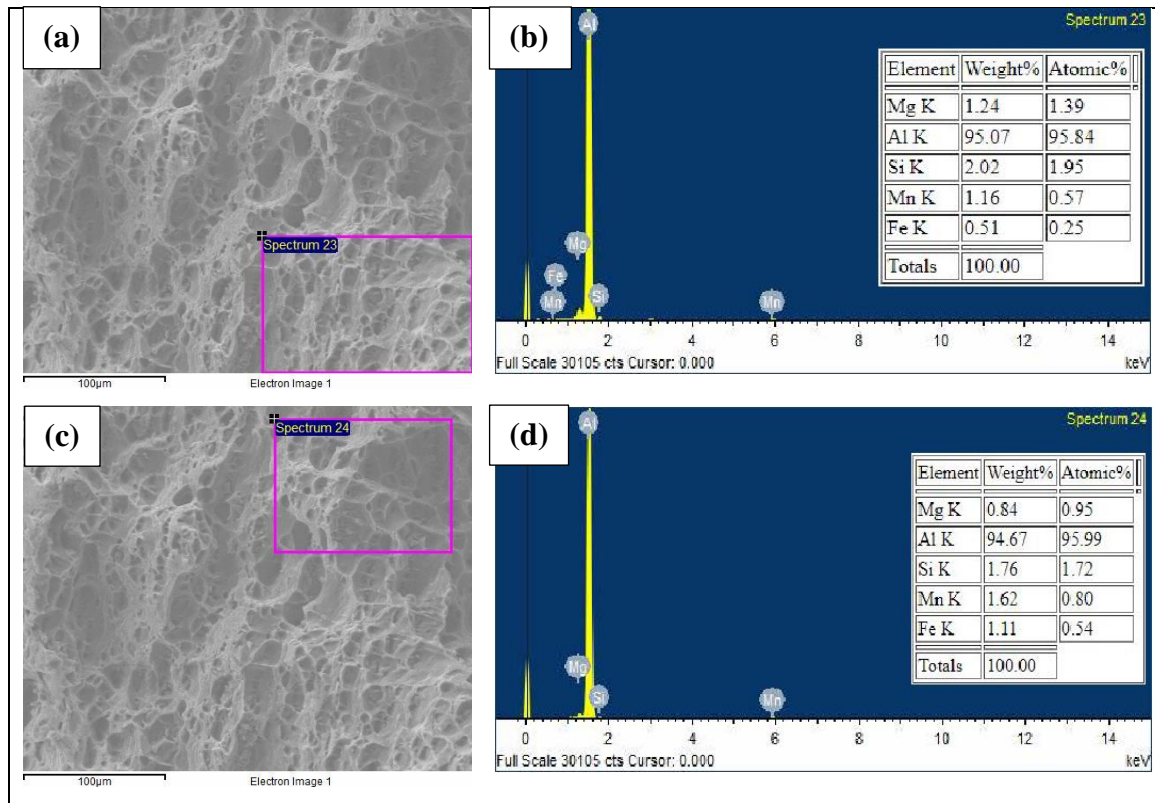


**Fig. 6.15** EDX image tensile fractured surface of U-CMT (a) & (b) spectrum 23 (c) & (d) spectrum 24

### 6.2.5 Effect of ultrasonic vibrations on porosity

Radiography inspection testing of welded samples are carried out as per ASME Sec. - V: 2017. Radiography inspection image of CMT and U-CMT welded specimens are shown in Fig. 6.16 (a) and (b) respectively. In the CMT welded images the porosity is easily noticeable and encircled in yellow color. Two major pores are not in the acceptable range which is present in the welded joint and close to points A and B. The U-CMT welded plated is free from porosity like weld defects which is clearly seen from the Fig. 6.16 (b). With the application of ultrasonic vibrations during CMT process defect free joint observed due to grain refining through cavitation and acoustic streaming [Puga et al., 2013; Tian et al., 2018 and Kumar et al., 2016]. At the end of the weld in U-CMT specimens there is a minor lack of fusion is experienced due to the ultrasonic probe which was touching the welded plate for generating the vibrations. Kou, (1987) reported that by directly stirring the weld pool with an acoustic wave, increasing the magnitude of the weld pool convection. This

increases the thermal conductivity of the liquid pool as heat transfer in the weld pool becomes more efficient. This allows nuclei to live in the weld pool and thus facilitates the creation of equiaxed grains in the fusion zone. The porosity reduction mechanism can be described as follows: Firstly, nucleation, floating and growth are included in the porosity formation process. Ultrasonic vibration influences the movement of gas bubbles. Secondly, the continuous vibrations at high frequency causes weld pool agitation, facilitating upward floating and escape of gas bubble [Tian et al., \(2018\)](#).

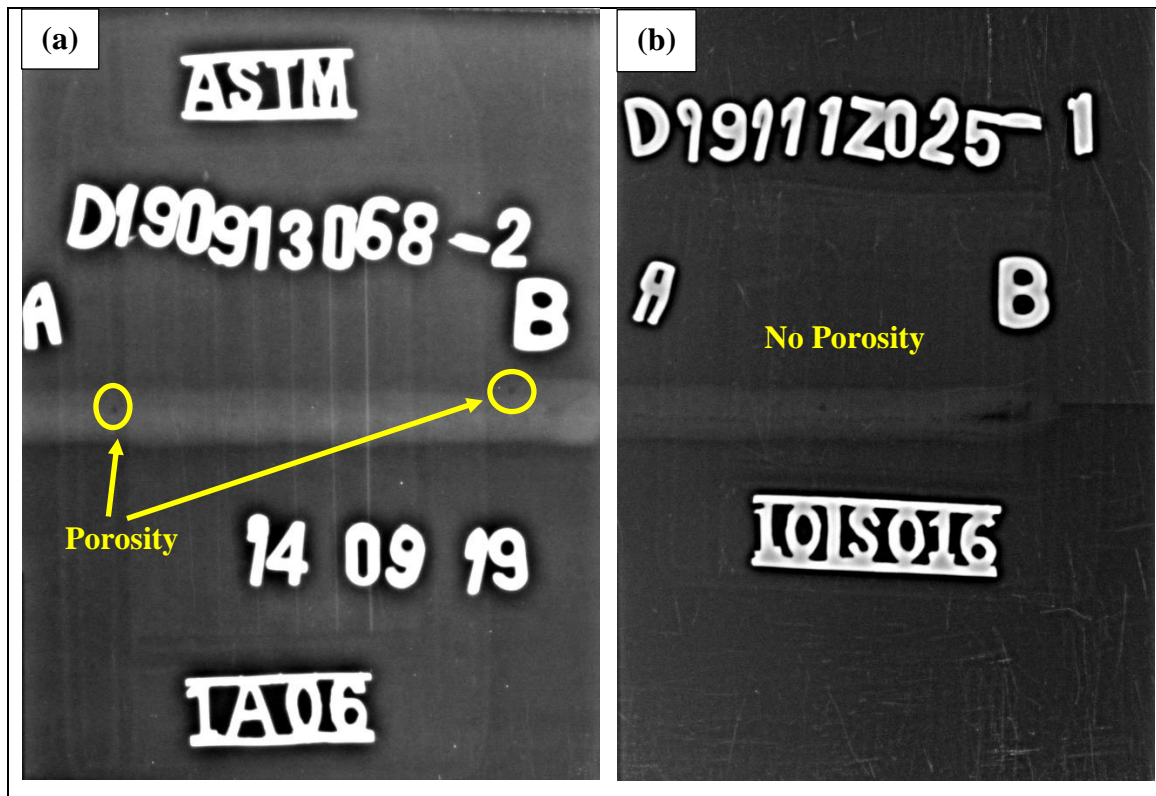


**Fig. 6.16** Radiography weld image of (a) CMT process (S-7) (b) U-CMT process (S-8)

### 6.3 SUMMARY

This chapter is based on comparative analysis between CMT and U-CMT butt joints. Comparison is based on weld bead dimensions, microstructures, microhardness, tensile strength including fractography and porosity. Results showed that ultrasonic vibrations during CMT welding improves mechanical properties. Grain refinement is also illustrated through the use of ultrasonic vibrations during CMT welding.

## CHAPTER 7 : CONCLUSIONS AND SCOPE FOR FUTURE WORK

---

### 7.1 CONCLUSIONS

This chapter gives the major conclusions which is derived from the results and discussions from the above chapters.

#### 7.1.1 Bead-on-Plate

- CMT has relatively lower penetration for the same current and welding speeds compared to MIG pulse synergic and MIG manual, which helps to weld thin sheets. For better joint efficiency, a good amount of penetration and dilution with low heat input is needed.
- High heat input and rapid cooling in the molten pool produce high residual stresses that are seen on the bead's surface in the form of cracks, which ultimately reduces the joint strength. These cracks are experienced by MIG pulse synergic and MIG manual, which CMT prevents due to low heat input. As a result, compared to MIG Pulse and MIG Manual, CMT has low residual stresses.
- At the beads, CMT shows a decrease in residual stress of 6-12 % and 21-29 % compared to MIG Pulse synergic and MIG Manual respectively and in the fusion zone, CMT is experiencing a decrease of 11-14 % and 17-25 % compared to MIG Pulse synergic and MIG Manual.
- A powerful tool for finding the optimal parameters is the CCFCD under RSM. The optimal process parameters for CMT are lower than MIG P and MIG M, but it still achieves a good penetration depth that is almost similar to MIG P and MIG M with low heat input.
- The optimal process parameters are 92.518A and 7.50mm/sec for CMT, 109.418A and 10.873mm/sec for MIG P, 110.847A and 11.527mm/sec for MIG M with 61.11%, 68.80% and 72.6% desirability, respectively for bead-on-plate experiments.
- With the optimal process parameters, the optimal penetration is 2.857mm, 2.852mm and 3.051mm for CMT, MIG P and MIG M respectively. Dilution is 43.118%,

52.120% and 59.606% for CMT, MIG P and MIG M respectively. Heat input is 132.999J/mm, 155.372J/mm and 161.381J/mm for CMT, MIG P and MIG M respectively.

- Current is directly proportional whereas welding speed is inversely proportion to the penetration. In terms of welding speed, the percentage increase in penetration is much higher than the current. Overall, CMT has relatively lower penetration for the same current and welding speeds compared to MIG pulse synergic and MIG manual, which helps to weld thin sheets.
- CMT is having high repeatability in terms of weld geometry as compared with MIG P and MIG M.
- CMT welding is spatter-free, negligible deformation of the plate, low heat input and forms an aesthetic bead for thin sheets compared to MIG pulse and manual welding.

#### 7.1.2 CMT Butt Joining

- Joining of dissimilar aluminium alloys with dissimilar thickness using cold metal transfer with the help of aluminium-silicon wire is achieved successfully.
- FESEM and optical microscope images of microstructure validate that the high amount of silicon and magnesium contents are present at weldment and fusion line of both the substrate side, which tends to form a brittle intermetallic compound ( $Mg_2Si$ ). As a result, a joint fracture can take place.
- Using RSM-GRA coupled with PCA technique, the most dominant input process parameter on multi-response was discovered to be the welding speed. The optimal process parameter acquired is I3-TS1-Q1 (current -100 A, welding speed - 5 mm/sec and flow rate - 14 L/min) which produces 226 MPa of ultimate tensile strength, 12.6 % of elongation, 68.7 HV of microhardness and -152 MPa of compressive residual stress.
- Using CCFCFCD of RSM, the optimal process parameters acquired is I1-TS3-Q3 (current - 80 A, welding speed - 9 mm/sec and flow rate - 18 L/min) which produces 204.64 MPa of ultimate tensile strength, 11.75 % of elongation, 64.07 HV of microhardness and -104.90 MPa of compressive residual stress.
- Desirability of GRA-PCA technique is significantly improved to 97.07 % which was initially at 65.99 % via CCFCFCD.



- The flow rate of shielding gas has a minimum or negligible contribution for affecting the response parameters, while welding speed is the dominant process parameter with approximately 65 % of contribution.
- More than 97 % of model significance is shown by the ANOVA table for each response. All the linear and quadratic interactions are significant with a high grade of adequate precision for each response.
- The actual weights obtained using principal component analysis for UTS, elongation, microhardness and residual stress are 31.1364, 32.49, 28.6225 and 7.6729 respectively.
- Confirmation runs helps in the improvement of grey relation grade by 0.211 and approximately by 35 % to the initial factor settings.

### 7.1.3 Ultrasonic-Assisted CMT Butt Joining

This chapter shows that with assist of ultrasonic vibrations in CMT welding, several improvements can be experienced that enhances the quality of weld.

- The bead dimensions enlarge when ultrasonic vibrations are introduced during the CMT process. Ultrasonic vibrations increase solidification time of the molten weld pool, which allows more base metal to fuse with the filler wire. This increases weld width & penetration depth and simultaneously shows a decrease in contact angle for U-CMT welded joints.
- Ultrasonic vibrations during welding have finer grains structure as compared to without ultrasonic vibrations.
- Tensile strength and microhardness have enhanced results with ultrasonic vibrations during CMT. It shows the maximum tensile strength sample (202 MPa) which is higher than the selected samples fabricated without ultrasonic vibrations. Results show the average increment of 18.5 % in microhardness values for U-CMT welded sample in comparison with the CMT welded sample.
- Fine equiaxed dimples and micro-voids are experienced in the fracture surface of the tensile specimen with the ultrasonic-assisted CMT welding due to refinement of grains. Honeycomb like structure is also observed which anticipates maximum strength.

Percentage elongation is also higher in U-CMT samples which ensures a ductile fracture.

- Radiography test proves that porosity is reduced in the welded samples with ultrasonic vibrations.

## **7.2 SCOPE FOR FUTURE WORK**

- The set up can be optimized for many other process parameters like different types of filler wire, contact tip to workpiece distance (CTWD), including laser energy for achieving higher mechanical properties etc.
- Aluminium composite can be fabricated with some natural or synthetic reinforcement and then welding can be carried out.
- Robotic CMT can be used to join the metals with high precision and accuracy.
- Spin arc welding can be done for achieving higher penetration low heat input.
- Optimization can be done using artificial neural network (ANN) with genetic algorithm (GA) for more precise results.

## REFERENCES

---

- [1]. Adak, D. K., Mukherjee, M., & Pal, T. K. (2015). Development of a direct correlation of bead geometry, grain size and HAZ width with the GMAW process parameters on bead-on-plate welds of mild steel. *Transactions of the Indian Institute of Metals*, 68(5), 839-849.
- [2]. Ahmad, R., & Bakar, M. A. (2011). Effect of a post-weld heat treatment on the mechanical and microstructure properties of AA6061 joints welded by the gas metal arc welding cold metal transfer method. *Materials & Design*, 32(10), 5120-5126.
- [3]. Ahmed, N. (Ed.). (2005). *New developments in advanced welding*. Elsevier. Woodhead Publishing Limited, Cambridge, England.
- [4]. Ahsan, M. R., Kim, Y. R., Kim, C. H., Kim, J. W., Ashiri, R., & Park, Y. D. (2016). Porosity formation mechanisms in cold metal transfer (CMT) gas metal arc welding (GMAW) of zinc coated steels. *Science and Technology of Welding and Joining*, 21(3), 209-215.
- [5]. Allison, A., & Scudamore, R. (2014). Strategic Research Agenda: Joining: Joining Sub-platform. Available from (<http://www.joining-platform.com/documents/Joining%20Sub-Platform%20SRA%20-%202014.pdf>)
- [6]. Anyalebechi, P. N. (1995). Analysis of the effects of alloying elements on hydrogen solubility in liquid aluminum alloys. *Scripta metallurgica et materialia*, 33(8), 1209-1216.
- [7]. Aslanlar, S., Ogur, A., Ozsarac, U., Ilhan, E., & Demir, Z. (2007). Effect of welding current on mechanical properties of galvanized chromided steel sheets in electrical resistance spot welding. *Materials & design*, 28(1), 2-7.
- [8]. Avinash, S., Balram, Y., Babu, B. S., & Venkatramana, G. (2019). Multi-response optimization of pulse TIG welding process parameters of welds AISI 304 and Monel 400 using grey relational analysis. *Materials Today: Proceedings*, 19, 296-301.
- [9]. Balasubramanian, M. (2016). Prediction of optimum weld pool geometry of PCTIG welded titanium alloy using statistical design. *Engineering Science and Technology, An International Journal*, 19(1), 15-21.
- [10]. Cao, R., Feng, Z., & Chen, J. H. (2014 A). Microstructures and properties of

- titanium–copper lap welded joints by cold metal transfer technology. *Materials & Design*, 53, 192-201.
- [11]. Cao, R., Feng, Z., Lin, Q., & Chen, J. H. (2014). Study on cold metal transfer welding–brazing of titanium to copper. *Materials & Design (1980-2015)*, 56, 165-173.
  - [12]. Cao, R., Wang, T., Wang, C., Feng, Z., Lin, Q., & Chen, J. H. (2014 B). Cold metal transfer welding–brazing of pure titanium TA2 to magnesium alloy AZ31B. *Journal of alloys and compounds*, 605, 12-20.
  - [13]. Cao, R., Wen, B. F., Chen, J. H., & Wang, P. C. (2013). Cold metal transfer joining of magnesium AZ31B-to-aluminum A6061-T6. *Materials Science and Engineering: A*, 560, 256-266.
  - [14]. Cao, R., Yu, G., Chen, J. H., & Wang, P. C. (2013 A). Cold metal transfer joining aluminum alloys-to-galvanized mild steel. *Journal of materials processing technology*, 213(10), 1753-1763.
  - [15]. Cary, H. B. (Ed.). (1988). *Modern Welding Technology Second Edition*. Prentice-Hall, Inc.. Englewood Cliffs, New Jersey.
  - [16]. Chandel, R. S., Seow, H. P., & Cheong, F. L. (1997). Effect of increasing deposition rate on the bead geometry of submerged arc welds. *Journal of materials processing technology*, 72(1), 124-128.
  - [17]. Chaudhari, R., Parekh, R., & Ingle, A. (2014, January). Reliability of dissimilar metal joints using fusion welding: A Review. In *International Conference on Machine Learning, Electrical and Mechanical Engineering (ICMLEME: 2014).*–2014.
  - [18]. Cook, G. E., & Eassa, H. E. D. E. (1985). The effect of high-frequency pulsing of a welding arc. *IEEE Transactions on Industry Applications*, (5), 1294-1299.
  - [19]. Dai, W. L. (2003). Effects of high-intensity ultrasonic-wave emission on the weldability of aluminum alloy 7075-T6. *Materials Letters*, 57(16-17), 2447-2454.
  - [20]. Dawes, C. T. (1992). *Laser welding: a practical guide*. Woodhead Publishing. New York.
  - [21]. Dong, H., Hu, W., Duan, Y., Wang, X., & Dong, C. (2012). Dissimilar metal joining of aluminum alloy to galvanized steel with Al–Si, Al–Cu, Al–Si–Cu and Zn–Al filler wires. *Journal of Materials Processing Technology*, 212(2), 458-464.
  - [22]. DuPont, J. N., & Marder, A. R. (1996). Dilution in single pass arc

- welds. *Metallurgical and Materials Transactions B*, 27(3), 481-489.
- [23]. Egerton, R. F. (2005). *Physical principles of electron microscopy : An Introduction to TEM, SEM, and AEM*. New York: Springer.
- [24]. Elemary, B. R. (2019). Evaluation and improvement of promising rubber recycling OT machine using fractional factorial and response surface design. *Communications in Statistics: Case Studies, Data Analysis and Applications*, 5(3), 168-188.
- [25]. Elrefaey, A., & Ross, N. G. (2015). Microstructure and mechanical properties of cold metal transfer welding similar and dissimilar aluminum alloys. *Acta Metallurgica Sinica (English Letters)*, 28(6), 715-724.
- [26]. Eskin, D. G. (2008). *Physical metallurgy of direct chill casting of aluminum alloys*. CRC press, Boca Roton.
- [27]. Fang, J., Gao, Y., Sun, G., & Li, Q. (2013). Multiobjective reliability-based optimization for design of a vehicledoor. *Finite Elements in Analysis and Design*, 67, 13-21.
- [28]. Fang, X., Wu, S., Lü, S., Wang, J., & Yang, X. (2017). Microstructure evolution and mechanical properties of quasicrystal-reinforced Mg-Zn-Y alloy subjected to ultrasonic vibration. *Materials Science and Engineering: A*, 679, 372-378.
- [29]. Feng, J., Zhang, H., & He, P. (2009). The CMT short-circuiting metal transfer process and its use in thin aluminium sheets welding. *Materials & Design*, 30(5), 1850-1852.
- [30]. Gery, D., Long, H., & Maropoulos, P. (2005). Effects of welding speed, energy input and heat source distribution on temperature variations in butt joint welding. *Journal of materials processing technology*, 167(2-3), 393-401.
- [31]. Ghosh, N., Pal, P. K., & Nandi, G. (2017). GMAW dissimilar welding of AISI 409 ferritic stainless steel to AISI 316L austenitic stainless steel by using AISI 308 filler wire. *Engineering science and technology, an international journal*, 20(4), 1334-1341.
- [32]. Goyal, H., Mandal, N., Roy, H., Mitra, S. K., & Mondal, B. (2015). Multi response optimization for processing Al-SiCp composites: an approach towards enhancement of mechanical properties. *Transactions of the Indian Institute of Metals*, 68(3), 453-463.
- [33]. Greyjevo, O. G. T. V. Z., & Metodo, A. I. T. (2009). Optimization of weld bead

- geometry in TIG welding process using grey relation analysis and Taguchi method. *Materiali in tehnologije*, 43(3), 143-149.
- [34]. Gunaraj, V., & Murugan, N. (1999). Prediction and comparison of the area of the heat-affected zone for the bead-on-plate and bead-on-joint in submerged arc welding of pipes. *Journal of Materials Processing Technology*, 95(1-3), 246-261.
- [35]. Gunaraj, V., & Murugan, N. (2002). Prediction of heat-affected zone characteristics in submerged arc welding of structural steel pipes. *Welding Journal-New York-*, 81(3), 45-s.
- [36]. Gungor, B., Kaluc, E., Taban, E., & Aydin, S. I. K. (2014). Mechanical and microstructural properties of robotic Cold Metal Transfer (CMT) welded 5083-H111 and 6082-T651 aluminum alloys. *Materials & Design (1980-2015)*, 54, 207-211.
- [37]. Haghayeghi, R., Heydari, A., & Kapranos, P. (2015). The effect of ultrasonic vibrations prior to high pressure die-casting of AA7075. *Materials Letters*, 153, 175-178.
- [38]. Haq, A. N., Marimuthu, P., & Jeyapaul, R. (2008). Multi response optimization of machining parameters of drilling Al/SiC metal matrix composite using grey relational analysis in the Taguchi method. *The International Journal of Advanced Manufacturing Technology*, 37(3), 250-255.
- [39]. Haragopal, G., Reddy, P. V. R., Reddy, G., & Subrahmanyam, J. V. (2011). Parameter design for MIG welding of Al-65032 alloy using Taguchi technique. *Journal of Scientific & Industrial Research*, 70, 844-850.
- [40]. Hermans, M. J. M., & Den Ouden, G. (1999). Process behavior and stability in short circuit gas metal arc welding. *WELDING JOURNAL-NEW YORK-*, 137-141.
- [41]. Hotelling, H. (1933). Analysis of a complex of statistical variables into principal components. *Journal of educational psychology*, 24(6), 417.
- [42]. Hu, S., Zhang, H., Wang, Z., Liang, Y., & Liu, Y. (2016). The arc characteristics of cold metal transfer welding with AZ31 magnesium alloy wire. *Journal of Manufacturing Processes*, 24, 298-306.
- [43]. Hunt, A. C., Kluken, A. O., & Edwards, G. R. (1994). Heat input and dilution effects in microalloyed steel weld metals. *WELDING JOURNAL-NEW YORK-*, 73, 9-s.

- [44]. Ibrahim, I. A., Mohamat, S. A., Amir, A., & Ghalib, A. (2012). The Effect of Gas Metal Arc Welding (GMAW) processes on different welding parameters. *Procedia Engineering*, 41, 1502-1506.
- [45]. İrizalp, A. O., Durmuş, H., Yüksel, N., & Türkmen, İ. (2016). Cold metal transfer welding of AA1050 aluminum thin sheets. *Matéria (Rio de Janeiro)*, 21(3), 615-622.
- [46]. Ishak, M., Noordin, N. F. M., Razali, A. S. K., Hakim, L., & Shah, A. (2015). The effect of filler ER4043 and ER5356 on weld metal structure of 6061 aluminium alloy by Metal Inert Gas (MIG). *methanol yield over Bi2S3/CdS photocatalyst*, 4, 68-75.
- [47]. Jácome, L. A., Weber, S., Leitner, A., Arenholz, E., Bruckner, J., Hackl, H., & Pyzalla, A. R. (2009). Influence of filler composition on the microstructure and mechanical properties of steel—aluminum joints produced by metal arc joining. *Advanced Engineering Materials*, 11(5), 350-358.
- [48]. Jing, S., Kehong, W., Qi, Z., Deku, Z., Jun, H., & Guangle, L. (2013). Microstructure characteristics and properties of Mg/Al dissimilar metals made by cold metal transfer welding with ER4043 filler metal. *Rare Metal Materials and Engineering*, 42(7), 1337-1341.
- [49]. Joseph, A., Harwig, D., Farson, D. F., & Richardson, R. (2003). Measurement and calculation of arc power and heat transfer efficiency in pulsed gas metal arc welding. *Science and Technology of Welding and Joining*, 8(6), 400-406.
- [50]. Jou, M. (2003). Experimental study and modeling of GTA welding process. *J. Manuf. Sci. Eng.*, 125(4), 801-808.
- [51]. Ju-Long, D. (1982). Control problems of grey systems. *Systems & control letters*, 1(5), 288-294.
- [52]. Kanakavalli, P. B., Babu, B. N., & Sai, C. P. V. (2020). A hybrid methodology for optimizing MIG welding process parameters in joining of dissimilar metals. *Materials Today: Proceedings*, 23, 507-512.
- [53]. Kang, M., & Kim, C. (2015). Joining Al 5052 alloy to aluminized steel sheet using cold metal transfer process. *Materials & Design*, 81, 95-103.
- [54]. Kaufman, J. G. (2000). Applications for aluminum alloys and tempers. *Introduction to Aluminum Alloys and Tempers; ASM International: Materials Park, OH, USA*, 87-118.

- [55]. Khanna, P., & Maheshwari, S. (2018). Development of mathematical models for prediction and control of weld bead dimensions in MIG welding of stainless steel 409M. *Materials Today: Proceedings*, 5(2), 4475-4488.
- [56]. Kou, S. *Welding Metallurgy*, 1987. A Wiley-Interscience Publication, New York, 29-59.
- [57]. Kumar, N. P., Vendan, S. A., & Shanmugam, N. S. (2016). Investigations on the parametric effects of cold metal transfer process on the microstructural aspects in AA6061. *Journal of Alloys and Compounds*, 658, 255-264.
- [58]. Kumar, S., & Singh, R. (2019). Optimization of process parameters of metal inert gas welding with preheating on AISI 1018 mild steel using grey based Taguchi method. *Measurement*, 148, 106924.
- [59]. Kumar, S., Grover, S., & Walia, R. S. (2018). Effect of hybrid wire EDM conditions on generation of residual stresses in machining of HCHCr D2 tool steel under ultrasonic vibration. *International Journal on Interactive Design and Manufacturing (IJIDeM)*, 12(3), 1119-1137.
- [60]. Kumar, S., Wu, C. S., Padhy, G. K., & Ding, W. (2017). Application of ultrasonic vibrations in welding and metal processing: a status review. *Journal of manufacturing processes*, 26, 295-322.
- [61]. Kuo, Y., Yang, T., & Huang, G. W. (2008). The use of grey relational analysis in solving multiple attribute decision-making problems. *Computers & industrial engineering*, 55(1), 80-93.
- [62]. Lakshminarayanan, A. K., & Balasubramanian, V. (2009). Comparison of RSM with ANN in predicting tensile strength of friction stir welded AA7039 aluminium alloy joints. *Transactions of Nonferrous Metals Society of China*, 19(1), 9-18.
- [63]. Lanc, Z., Štrbac, B., Zeljković, M., Živković, A., & Hadžistević, M. (2018). Emissivity of aluminium alloy using infrared thermography technique. *Materiali in Tehnologije*.
- [64]. Lee, J. I., & Rhee, S. (2000). Prediction of process parameters for gas metal arc welding by multiple regression analysis. *Proceedings of the Institution of Mechanical Engineers, Part B: Journal of Engineering Manufacture*, 214(6), 443-449.
- [65]. Li, J., Shen, J., Hu, S., Liang, Y., & Wang, Q. (2019). Microstructure and



- mechanical properties of 6061/7N01 CMT+ P joints. *Journal of Materials Processing Technology*, 264, 134-144.
- [66]. Liang, Y., Hu, S., Shen, J., Zhang, H., & Wang, P. (2017). Geometrical and microstructural characteristics of the TIG-CMT hybrid welding in 6061 aluminum alloy cladding. *Journal of Materials Processing Technology*, 239, 18-30.
- [67]. Liang, Y., Shen, J., Hu, S., Wang, H., & Pang, J. (2018). Effect of TIG current on microstructural and mechanical properties of 6061-T6 aluminium alloy joints by TIG–CMT hybrid welding. *Journal of Materials Processing Technology*, 255, 161-174.
- [68]. Li-li, G., Ling-shen, F., & Ming-yang, Z. (2012). Research on the line of laser tailor welded blanks. In *Information Engineering and Applications* (pp. 315-322). Springer, London.
- [69]. Lin, J., Ma, N., Lei, Y., & Murakawa, H. (2013). Shear strength of CMT brazed lap joints between aluminum and zinc-coated steel. *Journal of materials processing technology*, 213(8), 1303-1310.
- [70]. Lin, S. B., Song, J. L., Yang, C. L., Fan, C. L., & Zhang, D. W. (2010). Brazability of dissimilar metals tungsten inert gas butt welding–brazing between aluminum alloy and stainless steel with Al–Cu filler metal. *Materials & Design (1980-2015)*, 31(5), 2637-2642.
- [71]. Lindberg, R.A., (1998). Processes and materials of manufacture. Prentice Hall, 623-692.
- [72]. Little, R.L., (1994). Welding and welding technology. Tata McGraw Hill, 198-242.
- [73]. Liu, X., Frankel, G. S., Zoofan, B., & Rokhlin, S. I. (2007). In-situ observation of intergranular stress corrosion cracking in AA2024-T3 under constant load conditions. *Corrosion Science*, 49(1), 139-148.
- [74]. Lorenzin, G., & Rutili, G. (2009). The innovative use of low heat input in welding: experiences on ‘cladding’and brazing using the CMT process. *Welding International*, 23(8), 622-632.
- [75]. Lynch, S. P. (1988). Environmentally assisted cracking: overview of evidence for an adsorption-induced localised-slip process. *Acta Metallurgica*, 36(10), 2639-2661.
- [76]. Ma, T., & Den Ouden, G. (1999). Softening behaviour of Al–Zn–Mg alloys due to welding. *Materials Science and Engineering: A*, 266(1-2), 198-204.

- [77]. Madhavan, S., Kamaraj, M., Vijayaraghavan, L., & Rao, K. S. (2017). Cold Metal Transfer Welding of Dissimilar A6061 Aluminium Alloy-AZ31B Magnesium Alloy: Effect of Heat Input on Microstructure, Residual Stress and Corrosion Behavior. *Transactions of the Indian Institute of Metals*, 70(4), 1047-1054.
- [78]. Magudeeswaran, G., Nair, S. R., Sundar, L., & Harikannan, N. (2014). Optimization of process parameters of the activated tungsten inert gas welding for aspect ratio of UNS S32205 duplex stainless steel welds. *Defence technology*, 10(3), 251-260.
- [79]. Maisonnnette, D., Suery, M., Nelias, D., Chaudet, P., & Epicier, T. (2011). Effects of heat treatments on the microstructure and mechanical properties of a 6061 aluminium alloy. *Materials Science and Engineering: A*, 528(6), 2718-2724.
- [80]. Májlínger, K., Kalácska, E., & Spena, P. R. (2016). Gas metal arc welding of dissimilar AHSS sheets. *Materials & design*, 109, 615-621.
- [81]. Majumder, H., Paul, T. R., Dey, V., Dutta, P., & Saha, A. (2017). Use of PCA-grey analysis and RSM to model cutting time and surface finish of Inconel 800 during wire electro discharge cutting. *Measurement*, 107, 19-30.
- [82]. Martinsen, K., Hu, S. J., & Carlson, B. E. (2015). Joining of dissimilar materials. *CIRP Annals*, 64(2), 679-699.
- [83]. Masumura, R. A., Hazzledine, P. M., & Pande, C. S. (1998). Yield stress of fine grained materials. *Acta Materialia*, 46(13), 4527-4534.
- [84]. Mathers, G. (2002). The Welding Of Aluminium And Its Alloys(Book). *Woodhead Publishing Limited, Abington Hall, Abington, Cambridge, CB 1 6 AH, UK, 2002*.
- [85]. Mcauley, J. W. (2003). Global sustainability and key needs in future automotive design. *Environmental science & technology*, 37(23), 5414-5416.
- [86]. Mendez, P. F., & Eagar, T. W. (2001). Welding processes for aeronautics. *Advanced materials and processes*, 159(5), 39-43.
- [87]. Milani, A. M., Paidar, M., Khodabandeh, A., & Nategh, S. (2016). Influence of filler wire and wire feed speed on metallurgical and mechanical properties of MIG welding-brazing of automotive galvanized steel/5754 aluminum alloy in a lap joint configuration. *The International Journal of Advanced Manufacturing Technology*, 82(9-12), 1495-1506.

- [88]. Mondolfo, L. F. (1976). "Aluminium alloys: structure and properties", Boston: Butterworths, London, 1. *Ausgabe, S, 72.*
- [89]. Montgomery, D. C. (2017). *Design and analysis of experiments*. John Wiley & sons.
- [90]. Moreira, P. M. G. P., Santos, T., Tavares, S. M. O., Richter-Trummer, V., Vilaça, P., & De Castro, P. M. S. T. (2009). Mechanical and metallurgical characterization of friction stir welding joints of AA6061-T6 with AA6082-T6. *Materials & Design*, 30(1), 180-187.
- [91]. Mossman, M. M., & Lippold, J. C. (2002). Weldability testing of dissimilar combinations of 5000-and 6000-series aluminum alloys. *WELDING JOURNAL-NEW YORK-*, 81(9), 188-194.
- [92]. Moulton, J. A., & Weckman, D. C. (2010). Double-sided arc welding of AA5182-O aluminum sheet for tailor welded blank applications. *Weld J*, 89(1), 11-23.
- [93]. Nie, F., Dong, H., Chen, S., Li, P., Wang, L., Zhao, Z., ... & Zhang, H. (2018). Microstructure and mechanical properties of pulse MIG welded 6061/A356 aluminum alloy dissimilar butt joints. *Journal of materials science & technology*, 34(3), 551-560.
- [94]. Pang, J., Hu, S., Shen, J., Wang, P., & Liang, Y. (2016). Arc characteristics and metal transfer behavior of CMT+ P welding process. *Journal of Materials Processing Technology*, 238, 212-217.
- [95]. Patel, C. N., & Chaudhary, S. A. N. D. I. P. (2013). Parametric optimization of weld strength of metal inert gas welding and tungsten inert gas welding by using analysis of variance and grey relational analysis. *International journal of research in modern engineering and emerging technology*, 1(3), 48-56.
- [96]. Paulraj, S. (2018, February). Multi-response optimization of process parameters for GTAW process in dissimilar welding of Incoloy 800HT and P91 steel by using grey relational analysis. In *IOP Conference Series: Materials Science and Engineering* (Vol. 314, No. 1, p. 012023). IOP Publishing.
- [97]. Pearson, K. (1901). LIII. On lines and planes of closest fit to systems of points in space. *The London, Edinburgh, and Dublin Philosophical Magazine and Journal of Science*, 2(11), 559-572.
- [98]. Petroyiannis, P. V., Kamoutsi, E., Kermanidis, A. T., Pantelakis, S., Bontozoglou, V., & Haidemenopoulos, G. N. (2005). Evidence on the corrosion-induced hydrogen

- embrittlement of the 2024 aluminium alloy. *Fatigue & Fracture of Engineering Materials & Structures*, 28(6), 565-574.
- [99]. Pickin, C. G., Williams, S. W., & Lunt, M. (2011). Characterisation of the cold metal transfer (CMT) process and its application for low dilution cladding. *Journal of Materials Processing Technology*, 211(3), 496-502.
- [100]. Pinto, H., Pyzalla, A., Hackl, H., & Bruckner, J. (2006). A comparative study of microstructure and residual stresses of CMT-, MIG-and laser-hybrid welds. In *Materials science forum* (Vol. 524, pp. 627-632). Trans Tech Publications Ltd.
- [101]. Praveen, P., Yarlagadda, P. K. D. V., & Kang, M. J. (2005). Advancements in pulse gas metal arc welding. *Journal of Materials Processing Technology*, 164, 1113-1119.
- [102]. Puga, H., Barbosa, J., Costa, S., Ribeiro, S., Pinto, A. M. P., & Prokic, M. (2013). Influence of indirect ultrasonic vibration on the microstructure and mechanical behavior of Al-Si-Cu alloy. *Materials Science and Engineering: A*, 560, 589-595.
- [103]. Qin, G. L., Su, Y. H., & Wang, S. J. (2014). Microstructures and properties of welded joint of aluminum alloy to galvanized steel by Nd: YAG laser+ MIG arc hybrid brazing-fusion welding. *transactions of nonferrous metals society of china*, 24(4), 989-995.
- [104]. Quintino, L., Liskevich, O., Vilarinho, L., & Scotti, A. (2013). Heat input in full penetration welds in gas metal arc welding (GMAW). *The International Journal of Advanced Manufacturing Technology*, 68(9), 2833-2840.
- [105]. Ransley, C. E. (1948). The solubility of hydrogen in liquid and solid aluminium. *Journal of the Institute of Metals*, 74, 599-620.
- [106]. Saha, A., & Mondal, S. C. (2017). Experimental investigation and modelling of WEDM process for machining nano-structured hardfacing material. *Journal of the Brazilian Society of Mechanical Sciences and Engineering*, 39(9), 3439-3455.
- [107]. Saha, M. K., Hazra, R., Mondal, A., & Das, S. (2019). Effect of heat input on geometry of austenitic stainless steel weld bead on low carbon steel. *Journal of The Institution of Engineers (India): Series C*, 100(4), 607-615.
- [108]. Sakthivel, R., Venkadeshwaran, P., Sridevi, R., Meeran, R. A., & Chandrasekaran, K. (2016). Effect of welding current, arc voltage and gas flow rate on depth of penetration during MIG welding of AA2014 plate. *way*, 2, 30.

- [109]. Sankar, B. V., Lawrence, I. D., & Jayabal, S. (2018). Experimental study and analysis of weld parameters by GRA on MIG welding. *Materials Today: Proceedings*, 5(6), 14309-14316.
- [110]. Sapakal, S. V., & Telsang, M. T. (2012). Parametric optimization of MIG welding using Taguchi design method. *International Journal of Advanced Engineering Research and Studies*, 1(4), 28-30.
- [111]. Satyanarayana, V. V., Reddy, G. M., & Mohandas, T. (2005). Dissimilar metal friction welding of austenitic–ferritic stainless steels. *Journal of Materials Processing Technology*, 160(2), 128-137.
- [112]. Schierl, A. (2005). The CMT process a revolution in welding technology. *WELDING IN THE WORLD-LONDON-*, 49(I), 38.
- [113]. Shang, J., Wang, K., Zhou, Q., Zhang, D., Huang, J., & Li, G. (2012). Microstructure characteristics and mechanical properties of cold metal transfer welding Mg/Al dissimilar metals. *Materials & Design*, 34, 559-565.
- [114]. Shanmugarajan, B., Shrivastava, R., Sathiya, P., & Buvashekar, G. (2016). Optimisation of laser welding parameters for welding of P92 material using Taguchi based grey relational analysis. *Defence Technology*, 12(4), 343-350.
- [115]. Sharma, S. K., Maheshwari, S., & Singh, R. K. R. (2019). Effect of heat-input and cooling-time on bead characteristics in SAW. *Materials and Manufacturing Processes*, 34(2), 208-215.
- [116]. Shu, F., Lv, Y., Liu, Y., Xu, F., Sun, Z., He, P., & Xu, B. (2014). Residual stress modeling of narrow gap welded joint of aluminum alloy by cold metal transferring procedure. *Construction and Building Materials*, 54, 224-235.
- [117]. Silvayeh, Z., Vallant, R., Sommitsch, C., Götzinger, B., Karner, W., & Hartmann, M. (2017). Influence of filler alloy composition and process parameters on the intermetallic layer thickness in single-sided cold metal transfer welding of aluminum-steel blanks. *Metallurgical and Materials Transactions A*, 48(11), 5376-5386.
- [118]. Sivaraman, A., & Paulraj, S. (2017). Multi-response optimization of process parameters for MIG welding of AA2219-T87 by Taguchi grey relational analysis. *Materials Today: Proceedings*, 4(8), 8892-8900.
- [119]. Srivastava, N., Chaudhari, G. P., & Qian, M. (2017). Grain refinement of binary

- Al-Si, Al-Cu and Al-Ni alloys by ultrasonication. *Journal of Materials Processing Technology*, 249, 367-378.
- [120]. Sterjovski, Z., Bayley, C., Donato, J., Lane, N., & Lang, D. (2014). Weld-end solidification cracking in pulsed-tandem gas metal arc welding of naval steels. *Weld J*, 93, 145-s-152-s.
- [121]. Sun, Q. J., Li, J. Z., Liu, Y. B., Li, B. P., Xu, P. W., & Feng, J. C. (2017). Microstructural characterization and mechanical properties of Al/Ti joint welded by CMT method—Assisted hybrid magnetic field. *Materials & Design*, 116, 316-324.
- [122]. Sun, Y. L., Obasi, G., Hamelin, C. J., Vasileiou, A. N., Flint, T. F., Balakrishnan, J., Smith, M. C., & Francis, J. A. (2019). Effects of dilution on alloy content and microstructure in multi-pass steel welds. *Journal of Materials Processing Technology*, 265, 71-86.
- [123]. Sun, Z., Lv, Y., Xu, B., Liu, Y., Lin, J., & Wang, K. (2015). Investigation of droplet transfer behaviours in cold metal transfer (CMT) process on welding Ti-6Al-4V alloy. *The International Journal of Advanced Manufacturing Technology*, 80(9), 2007-2014.
- [124]. Taban, E., Gould, J. E., & Lippold, J. C. (2010). Dissimilar friction welding of 6061-T6 aluminum and AISI 1018 steel: Properties and microstructural characterization. *Materials & Design (1980-2015)*, 31(5), 2305-2311.
- [125]. Tian, Y., Shen, J., Hu, S., Wang, Z., & Gou, J. (2018). Effects of ultrasonic vibration in the CMT process on welded joints of Al alloy. *Journal of Materials Processing Technology*, 259, 282-291.
- [126]. Tosun, N., & Pihtili, H. (2010). Gray relational analysis of performance characteristics in MQL milling of 7075 Al alloy. *The International Journal of Advanced Manufacturing Technology*, 46(5), 509-515.
- [127]. Totten, G. E., & MacKenzie, D. S. (Eds.). (2003). *Handbook of aluminum: vol. 1: physical metallurgy and processes*. CRC press.
- [128]. Tseng, M. M., & Hu, S. J. (2014). Mass Customization, CIRP Encyclopedia of Production Engineering. Springer Berlin Heidelberg, 836-843.
- [129]. Utkarsh, S., Neel, P., Mahajan, M. T., Jignesh, P., & Prajapati, R. B. (2014). Experimental investigation of MIG welding for ST-37 using design of

- experiment. *International Journal of Scientific and Research Publications*, 4(5), 1-4.
- [130]. Wang, J., Feng, J. C., & Wang, Y. X. (2008). Microstructure of Al–Mg dissimilar weld made by cold metal transfer MIG welding. *Materials Science and Technology*, 24(7), 827-831.
- [131]. Wang, P., Hu, S., Shen, J., Liang, Y., & Pang, J. (2016). Effects of electrode positive/negative ratio on microstructure and mechanical properties of Mg/Al dissimilar variable polarity cold metal transfer welded joints. *Materials Science and Engineering: A*, 652, 127-135.
- [132]. Wang, Z., Zhu, L. I., & Wu, J. H. (1996). Grey relational analysis of correlation of errors in measurement. *Journal of Grey System*, 8(1), 73-78.
- [133]. Xia, M., Tian, Z., Zhao, L., & Zhou, Y. N. (2008). Fusion zone microstructure evolution of Al-alloyed TRIP steel in diode laser welding. *Materials transactions*, 49(4), 746-753.
- [134]. Xue, J., Li, Y., Chen, H., & Zhu, Z. (2018). Effects of heat input on wettability, interface microstructure and properties of Al/steel butt joint in laser-metal inert-gas hybrid welding-brazing. *Journal of Materials Processing Technology*, 255, 47-54.
- [135]. Yang, S., Zhang, J., Lian, J., & Lei, Y. (2013). Welding of aluminum alloy to zinc coated steel by cold metal transfer. *Materials & Design*, 49, 602-612.
- [136]. Zhang, C., Li, G., Gao, M., Yan, J., & Zeng, X. Y. (2013). Microstructure and process characterization of laser-cold metal transfer hybrid welding of AA6061 aluminum alloy. *The International Journal of Advanced Manufacturing Technology*, 68(5-8), 1253-1260.
- [137]. Zhang, H. T., Feng, J. C., He, P., Zhang, B. B., Chen, J. M., & Wang, L. (2009). The arc characteristics and metal transfer behaviour of cold metal transfer and its use in joining aluminium to zinc-coated steel. *Materials Science and Engineering: A*, 499(1-2), 111-113.
- [138]. Zhou, Y., & Lin, Q. (2014). Wetting of galvanized steel by Al 4043 alloys in the first cycle of CMT process. *Journal of Alloys and Compounds*, 589, 307-313.

## LIST OF PUBLICATIONS

---

### List of papers published in SCI/SCIE journals

- [1]. **Koli, Y.**, Yuvaraj, N., Vipin & Aravindan, S. (2020). Investigations on weld bead geometry and microstructure in CMT, MIG pulse synergic and MIG welding of AA6061-T6. *Materials Research Express*, 6(12), 1265e5. **(Impact factor- 1.929)**
- [2]. **Koli, Y.**, Yuvaraj, N., Aravindan, S., Vipin. (2020). Multi-response Mathematical Modeling for Prediction of Weld Bead Geometry of AA6061-T6 Using Response Surface Methodology. *Transactions of the Indian Institute of Metals*, 1-22. **(Impact factor- 1.205)**
- [3]. **Koli, Y.**, Yuvaraj, N., Aravindan, S., Vipin. CMT Joining of AA6061-T6 and AA6082-T6 and Examining Mechanical Properties and Microstructural Characterization. *Transactions of the Indian Institute of Metals*, 1-17. **(Impact factor- 1.205)**
- [4]. **Koli, Y.**, Yuvaraj, N., Aravindan, S., Vipin. Control of humping phenomenon and analyzing mechanical properties of Al-Si wire-arc additive manufacturing (WAAM) fabricated samples using Cold Metal Transfer (CMT) process. *Part C: Journal of Mechanical Engineering Science*. **(Impact factor- 1.386)**

### List of papers published in SCOPUS journals

- [1]. Akanksha Gupta, Vipin, N. Yuvraj, **Yashwant Koli** & Sushil Kumar, “Numerical simulation of CMT butt weld Of AA6061-T6 and AA6082-T6 using Ansys” *International Journal of Mechanical and Production Engineering Research and Development (IJMPERD)*, ISSN(P): 2249–6890; ISSN(E): 2249–8001, Vol. 10, Issue 3, Jun 2020, 11865-11874.

### List of papers communicated in SCI/SCIE journals

- [1]. **Koli, Y.**, Yuvaraj, N., Aravindan, S., Vipin. Enhancement of mechanical properties of 6061/6082 dissimilar aluminium alloys through ultrasonic assisted cold metal transfer welding. (Communicated to *Arabian Journal for Science and Engineering*) **(Impact factor- 1.711)**



- [2]. **Koli, Y.**, Yuvaraj, N., Aravindan, S., Vipin. Multi-response mathematical model for optimization of process parameters in CMT welding of dissimilar thickness AA6061-T6 and AA6082-T6 alloys using RSM-GRA coupled with PCA. (Communicated to *Advances in Industrial and Manufacturing Engineering*)

List of papers published in International Conferences

- [1]. **Y.Koli**, N.Yuvraj, Vipin, S.Aravindan, “Comparative investigations on mechanical properties in GMAW and CMT welding of AISI 304L and AISI 202 austenitic stainless steel” ICARI, ISSN: 2347-3258.
- [2]. **Koli Y.**, Yuvaraj N., Vipin, Aravindan S. (2021) Enhancement of Mechanical Properties for Dissimilar Welded Joint of AISI 304L and AISI 202 Austenitic Stainless Steel. In: Singari R.M., Mathiyazhagan K., Kumar H. (eds) *Advances in Manufacturing and Industrial Engineering. Lecture Notes in Mechanical Engineering*. Springer, Singapore. [https://doi.org/10.1007/978-981-15-8542-5\\_13](https://doi.org/10.1007/978-981-15-8542-5_13)

## **CURRICULUM VITAE**

---

Mr. Yashwant Koli has obtained his Bachelor's Degree (B.Tech) in Mechanical and Automation engineering (2010-2014) and Master's Degree (M.Tech) in Production engineering (2015-2017), both from Delhi Technological University (Formerly Delhi College of Engineering), Delhi, India. His main area of research includes gas metal arc welding (GMAW), cold metal transfer welding (CMT), wire-arc additive manufacturing (WAAM) and optimization techniques. He has published 4 SCI/SCIE, 2 SCOPUS and 11 conference papers at an international level. He also got Research Excellence Award (REA-2021) for commendable research on 15<sup>th</sup> February 2021 from Delhi Technological University.